

Controlling the Morphology of Spin coated Polymer Blend Films

Parvaneh Mokarian-Tabari

Presented for the degree of Doctor of Philosophy

Department of Physics and Astronomy

The University of Sheffield

January 2009

Declaration

I declare that this thesis is the result of my own work except where the work of others is cited, either explicitly or via the list of references. No part of this dissertation has been submitted for in whole or in part for any other degree or qualification at this university or any other institute.

Signed:

Parvaneh Mokarian-Tabari

January 2009

Acknowledgements

I would like to begin by thanking my supervisor Prof Richard A.L. Jones for teaching me the importance of clear thinking and seeing the bigger picture when conducting research into the nanoscale!

Many Thanks to Dr Mark Geoghegan for good discussions and encouragement during this project. I am grateful to Dr Sasha Heriot for the continuous support, Dr Johnathan Howse and Dr Cvetelin Vaslilev for good advice and practical support. I appreciate the help of fellow polymer physicists, Dr Simon Martin, Dr Andrew Parnell, Dr Alan Dunbar and Dr Tanya Mykhaylyk.

My special thanks go to Prof Ramin Golestanian whose knowledge I took advantage of in using Mathematica software. I am also grateful to Mr David K. Mohammad, Dr Ashley Cadby and Prof David Lidzey for their collaboration on the photovoltaic project.

Many thanks to Richard Nicholson in the central mechanical work shop for building the environmental cell and Trevor Gamble and Graham Dickinson for building the gadgets which I modified the experimental set up. Also, I would like to thank Mr John Newell, Ms Catherine Annabel and Mr Richard French.

Thanks to my friends specially (but not only) Warren for his constant optimism towards my project, Rita for having lots of Italian moments, Brett, Anna, Christa, Mike and CMA, Pierre, Mike, Andrew, Elham and Tom, Matt, Muneer, Lekshmi, Jo, Lorena, Johann, Frank and Anwasha who made my time in Sheffield enjoyable! I am grateful to my uncle Mostafa whom I had many cultural trips to Europe with!

I also appreciate Dorothy Hodgkin Postgraduate Awards through EPSRC and BP for sponsoring this project.

Finally, I would like to thank my family, specially my mum, Monireh Roudbarian for providing a priceless support throughout my life.

This thesis is dedicated to my grandparents; my grandfather who has been a great and passionate maths teacher for me and my grandmother whom I learned patience from.

Abstract

Thin films of polymer mixtures made by spin-coating can phase separate in two ways – by forming lateral domains, or by separating into two distinct layers. The latter situation – self-stratification or vertical phase separation – could be advantageous in a number of practical applications, such as polymer photovoltaics. In our experiments, we have used time-resolved small-angle light scattering and light reflectivity during spin coating to study the structure development in PS/PMMA and PFB/F8BT blends, solution cast in toluene. A sample cell was designed, made and mounted on the apparatus to manipulate the evaporation rate. Having solved the Meyerhofer equation for thinning rate and by fitting the model to the experimental data, we are able to extract the evaporation rate of toluene during spin coating. We demonstrate that, by controlling the evaporation rate during the spin-coating process, we can obtain either self-stratification or lateral phase separation in the same system. We relate this to a previously hypothesised mechanism for phase separation during spin coating in thin films, according to which a transient wetting layer breaks up due to a Marangoni-type instability driven by a concentration gradient of solvent within the drying film. Our results show that a high evaporation rate leads to a laterally phase separated structure, while reducing the evaporation rate suppresses the interfacial instability and leads to a self-stratified final film. Using the set up we developed to control the morphology through evaporation rate, we made preliminary photovoltaic devices. It is possible to control the efficiency of the polymer photovoltaics by means of process parameters such as evaporation rate.

Contents

1	Introduction	1
1.1	Overview and Motivation	1
1.2	Bibliography	9
2	Theory and Background	17
2.1	Thermodynamics of bulk polymer blends	17
2.1.1	Thermodynamics of ternary systems: polymer A-polymer B-Solvent	18
2.1.1.1	Pseudobinary solutions	19
2.1.1.2	Athermal system	19
2.1.1.3	Thermodynamics of an inhomogeneous ternary system	21
2.1.2	Practical limitation of Flory-Huggins theory	23
2.2	Phase Diagram	24
2.3	Mechanism of phase separation	27
2.3.1	Spinodal decomposition	28
2.3.1.1	Characterisation of the spinodal decomposition process	29
2.3.2	Nucleation and growth	30
2.3.3	Wetting	31
2.3.3.1	Wetting transition	33
2.4	Surface Effect on Phase Separation in Bulk and thin films	35
2.4.1	Surface- directed spinodal decomposition	36
2.4.2	Previous studies on interface in thin films	38
2.5	Spin coated thin films	40
2.5.1	Numerical model of spin coating	42

2.5.2	The effect of solvent and evaporation rate on film structure.....	47
2.6	Instability in thin films.....	51
2.6.1	Marangoni instability.....	51
2.6.2	Solvent evaporation rate.....	55
2.6.3	The effect of other parameters on film structure.....	59
2.6.3.1	The effect of molecular weight on surface energy	59
2.6.3.2	The effect of film thickness on the structure	61
2.7	Summary.....	62
2.8	Bibliography.....	66
3	Experimental Techniques	76
3.1	Small angle light scattering	76
3.1.1	The connection between light scattering and Fourier transform	78
3.1.2	Small angle light scattering with integrated spin coater	78
3.1.3	Fresnel equations	79
3.1.4	Specular reflection	82
3.1.4.1	Thickness-time profile	84
3.1.5	Off specular Scattering	86
3.2	The Environmental cell	87
3.3	Atomic force microscopy (AFM)	90
3.4	Optical microscopy	90
3.5	Polymers	90
3.5.1	PS/PMMA.....	91
3.5.2	PFB/F8BT	91
3.5.3	Solvents.....	91
3.6	Bibliography	92

4 Tuning the Optospinometer and Environmental cell	93
4.1 Improving the optics	93
4.1.1 Reducing the beam size	94
4.1.2 Focusing the scattering pattern	95
4.2 Characterising the performance of the environmental cell	96
4.2.1 An introduction to swelling	96
4.2.1.1 Thermodynamics of swelling equilibrium	99
4.2.2 Stability of the gas flow in the environmental cell	103
4.2.3 Swelling behaviour of polystyrene film	106
4.3 Summary	112
4.4 Bibliography	114
5 Evaporation Rate in Spin Coating	116
5.1 Introduction	116
5.2 Controlled vapour pressure atmosphere	117
5.3 Extracting the evaporation rate in spin coating	121
5.3.1 Solving Meyerhofer's equation	121
5.3.2 Governing mechanisms for film thinning during spin coating	123
5.4 Conclusion	123
6 Controlling Instabilities during Spin Coating through Evaporation Rate	127
6.1 Introduction	127
6.2 Design of the experiment	129
6.2.1 Analysing off specular data	130
6.3 Phase separation in PS/PMMA film	132
6.4 The effect of evaporation rate on film thinning	137

6.5	The effect of evaporation rate on interfacial instability	139
6.6	Bilayer formation.....	147
6.7	Summary and conclusions	149
6.8	Bibliography	151
7	Structure Development in Semiconducting Polymer Blends	
7.1	Introduction	152
7.1.1	The effect of the morphology on device performance	153
7.2	Case study: PFB/F8BT	156
7.3	Experiments	156
7.4	Results	157
7.4.1	Reflectivity–time data	157
7.4.2	Structure formation in PFB:F8BT: the effect of evaporation rate	161
7.5	Discussion and conclusion (Part I- silicon substrate)	173
7.6	Photovoltaic devices	178
7.6.1	The result of fluorescence microscopy and AFM	178
7.6.2	Photovoltaic device characterisation	184
7.7	Discussion and Conclusion (Part II- photovoltaics)	186
7.8	The effect of substrate on the morphology of PFB/F8BT	187
7.9	Bibliography	189
8	Conclusions and Future works	191
	Appendix I (Light scattering)	198

Chapter One

Introduction

1.1 Overview and Motivation

Immiscible polymers are widely used for many practical applications; so their phase behaviour, morphology and thermodynamics properties have been the object of intensive studies during the past two decades. Spin coating is a method used widely in the creation of highly uniform, sub-micrometer polymer films. It is used widely in industry to make thin films of photo-resists, sol-gel glasses and functional materials such as semiconducting polymers for use in polymer based field-effect transistors, light emitting diodes and photovoltaics [1]. The films of immiscible polymers can be made by spin coating; two immiscible polymers are dissolved in a common solvent, then the blend is spun cast and this leads to phase separation. The final structure of the blend films which is far from equilibrium can have many different morphologies depending on the history of the process. The process is affected by various parameters such as evaporation rate, solvent nature, spin rate, temperature, substrate chemistry, blend chemistry such as polymerization and concentration, film thickness etc. It is very important to have a deep understanding of the film formation process. Knowing that, we would be able to control the structure and

tailor the appropriate structure that is in favour of device efficiency. Currently there is no complete theory that accounts for the structure of a spin coated film. In this introductory section, I consider the many important factors that would have to be incorporated in such a theory. These factors would include:

- Bulk thermodynamics, both of binary polymer mixtures and of ternary polymer solutions.
- The mechanism by which phase separation takes place in bulk samples.
- The way surfaces and interfaces modify bulk thermodynamics in thin films.
- New mechanism of phase separation, mediated by surfaces and interfaces in thin film of binary polymer blends.
- The effect of solvent evaporation and hydrodynamics flow in the spin-coating of ternary polymer solution.
- The origin of interfacial instability, in particular Marangoni type instability in thin polymer films

In what follows, I discuss these factors.

Why are polymers hard to mix? Miscibility in polymer blends can be described in the frame-work of Flory-Huggins theory, based on a simple equation for the free energy of mixing which defines whether two species will mix or not. Polymers do not gain that much entropy by mixing. Thus, when two different polymers are blended, phase separation is likely to occur. There are two main ways to effect phase separation in a polymer blend: temperature quench and solvent quench. Temperature induced phase separation happens when molecular mobility is promoted by a temperature above the glass transition but inside the two-phase region. A Solvent quench occurs when a common solvent is added to the polymers. The latter happens in spin casting. In both cases, there are two main mechanisms, spinodal decomposition and nucleation followed by growth. The former is due to random fluctuations in composition in the unstable region of the phase diagram and the latter happens when the phase separation occurs in the metastable region of the phase diagram. Bulk

demixing of binary polymer mixtures [2-12] and ternary polymer solution [13-17] has been studied extensively during the last two decades. Phase separation in bulk samples of polymer blends generally leads to isotropic domain structures with a characteristic length scale increasing in the course of the process with no specific equilibrium value [18]. However, strongly anisotropic domain growth may be expected in the vicinity of the surfaces confining any bulk sample [19].

The surface is an important factor that can significantly affect the morphology of the blend film, particularly in its vicinity. In general, the coexisting compositions do not show the same interfacial energy value with the boundary surfaces. There is a preferential attraction between the confining surfaces and one of the components. Usually, the component with lower interfacial energy will segregate to the surface to decrease the total free energy. This leads to “near surface” or “enrichment surface” structure. The surface effect was considered for the first time by Reich and Cohn [20] in 1981. In their study they showed that boundaries and specific polymer-surface interactions can strongly affect the phase separation. Ten years later Ball and Essery [21] in a numerical study, simulated the phase behaviour of a binary mixture as a function of cooling rate. A strong dependency of domain morphology with cooling rate was observed and the effect was more apparent near the surface where as domains were formed preferentially parallel to the surface. Shortly after, Richard.A.L.Jones *et al* [22], experimentally detected the surface-directed spinodal decomposition for PEP/dPEP system. Jones’ experiment inspired many further investigation of this problem, including via experimental techniques [19] and theoretical and analytical development [23, 24].

In thin films, due to the confinement effect, there are additional surfaces and interfaces. External surfaces can significantly alter the phase decomposition of polymer blends in thin films [22] and break the translational and rotational symmetries. The break of the symmetry of the polymer mixture and preferential attraction of one of the blend components leads to the formation of

wetting layers [25-29] or surface-directed phase separation [19, 22, 30-32]. In thin films, due to the presence of additional surfaces, composition fluctuation is not random as it is in the bulk and is directed by the surface. The phase separation is due to surface-induced spinodal decomposition. This phenomenon which has been intensively studied [19, 22-24, 31, 33-46] may lead to domain morphologies and domain growth kinetics which significantly differ from those in bulk [13, 19, 20, 22, 35, 46-54]. Depending on both external surfaces, it is possible to obtain a different final phase domain morphology such as self stratified (multilayer) or column-like phase domains [55] with interfaces oriented parallel or perpendicular to the substrate.

The near surface structure, particularly in thin films, depends on various experimental parameters such as bulk composition, nature of the surfaces, wettability, quench depth etc. There are several theories that explain the formation of the typical blend structures and surface topographic structure in thin spin coated films [13, 18, 47, 56]. Among them the most versatile one is due to Walheim *et al* [1, 13] who considers the undulation on the surface of a binary blend as a function of solubility difference of the components in the common solvent. The theory has been latterly extended to ternary blends [57-59].

The nature of the solvent is the other variable which directly affects the morphology of the spin coated film. Solvent has a major role in undulation at the film surface [13, 57, 60-64]. Evaporation rate, which we shall pay intensive attention to in this thesis, has a major impact on film thickness and thus the final morphology. The occurrence of several defects such as striation [65, 66] and “chuck marks” [67, 68] has been attributed to the evaporation rate. These defects can cause failure in electronic devices. Therefore there is a huge motivation to understand how they are formed in order to avoid them. Research shows that evaporation and solvent related issues are the key parameters to control the striation formation [60, 66, 69, 70]. Recently, some important

factors like the interaction between polymer and solvent has been considered. Controlling evaporation rate is attractive in other industrial processes such as solvent annealing which is an alternative to temperature annealing [71, 72] and also is used to create different surface morphology [73-75]. In a systematic research by Lue *et al* [57] the effect of solvent type on the morphology of the thin film of PVK has been studied. The results show that the interaction between polymer chains and solvent is not as important as evaporation rate. In other words, no matter how good or how poor a solvent is, if it has low vapour pressure (like toluene), evaporation rate will be low and it would decrease the composition gradient near the surface and suppress the Marangoni instability. Conversely, exploiting a solvent with high evaporation rate during the spin coating will lead to a surface with high roughness due to the Marangoni effect.

In spite of much research and many proposed models for the spin coating process, there is not any universal theory to explain the mechanism of polymer film formation and predict the phase behaviour precisely. Therefore, it is not easy to design a processing route which reliably leads to a desired morphology. One possible reason could be that so far many of the studies have been restricted to analysis of the structure of the final film. As the process is non equilibrium, it is not very accurate to deduce complex details from the end point alone [1]. On the other hand, due to quick evaporation of solvent, it is very difficult to study the process during film formation. Until very recently, no technical method was developed to acquire information during the process. However in 2005, Jukes and Herriot [1, 76] for the first time have developed a technique that made it possible to study the process of phase separation in spin cast film *in situ* during formation. The method opened a new avenue to study the spin cast polymer film, but it is in an early phase of development.

In my project, I have developed this method which is based on time resolved small angle light scattering and light reflectivity and studied the structure evolution, in particular interfacial instability in thin polymer films during spin

coating. In previous experimental work in our group [1], strong evidence was found to support the model for the mechanism of film formation due to Walheim *et al* [13]. During spin casting, polymer blends initially form transient self-stratified layers due to preferential attraction of one of the components by the surface [1, 18, 19, 22, 28, 29, 35, 46, 51, 55, 77, 78]. These transient wetting layers subsequently break up due to instability. Our work, and that of other workers [1, 13], suggested a further hypothesis: that the instability leading to the break up of the layers was driven by a solvent concentration gradient inside the film. We speculated that a Marangoni type instability [79-81], driven by solvent concentration gradients within the layers is the governing mechanism for interfacial instability. During the spin coating, the solvent is removed from the system by evaporation from the surface. If the rate at which solvent is removed by evaporation exceeds the rate at which diffusion within the film equilibrates the solvent concentration, then a substantial solvent concentration gradient will be generated in the film. With the near-surface region being at a higher total polymer concentration, while near the substrate the solvent concentration will be higher. Since the energy of an interface between two immiscible polymers swollen by solvents is a strong function of the solvent concentration, this solvent gradient creates an effective potential for the interfacial position, which in some circumstances will make the interface physically unstable.

To probe the effect of solvent gradients within the film, I have studied the development of morphology in films spin cast in a sample cell with a controlled solvent vapour pressure. The environmental cell is designed and made to be mounted on the light scattering apparatus. Toluene vapour was introduced by blowing nitrogen inside a toluene bubbler. The bubbler was inside a water bath for temperature control. The saturated vapour pressure of a gas is a function of temperature only. So by changing the temperature, we were able to change the vapour pressure of the gas in the cell. The idea was that by increasing the vapour pressure of the gas inside the cell, the evaporation rate of

toluene from the film will decrease and this will weaken the surface tension profile in the film and therefore suppress Marangoni instabilities.

To establish a quantitative relationship between the process variables – the temperature of the solvent reservoir and the flow rates of the carrier gas – and the evaporation rates, we carried out a series of measurements of the time-evolution of the thickness of a film spun from pure solvent. From these, we were able to extract quantitatively the evaporation rate for a given set of process variables and spin speed. For this analysis, we used the model of Meyerhofer [82]. This builds on an earlier model of Emslie, Bonner and Peck (EBP) [83], which solves the hydrodynamics of the flow of a Newtonian fluid with viscosity η and density ρ on a plate spinning with angular velocity ω , by simply adding a term for a constant evaporation rate e per unit area.

The specular reflectivity-time was measured during the spin coating process for toluene at different saturated vapour pressures. The thickness-time profile was reconstructed. Our results show the expected outcome, the higher the nominal vapour pressure is inside the cell, the lower the evaporation rate.

To the prediction of the Meyerhofer theory, by fitting experimental thickness-time curves, we have extracted the evaporation rate for each vapour pressure. Our results are quantitatively accounted for by the theory. This suggests there are two stages of film thinning during spin coating; an early stage dominated by hydrodynamic thinning in which the solvent vapour pressure does not strongly affect the rate of thinning, and a second, evaporation rate dominated stage in which the rate of thinning can be systematically change by the solvent vapour pressure.

Having calibrated our apparatus to allow us to specify an evaporation rate for a given experiment, we turned to the results for films spun from mixtures of

polystyrene (PS) and polymethyl methacrylate (PMMA) to study the origin of interfacial instability. The polymers studied had molecular weights of 100000 Da (PS) and 96000 Da (PMMA). We tested our hypothesis by changing the concentration gradient in the film. Our results show that we are able to control the morphology by controlling the evaporation rate. There is a threshold for the evaporation rate, where above it, the interface becomes unstable and a laterally phase separated structure forms. Below the threshold the structure stabilises and a layered architecture forms.

We applied our hypothesis on a new blend system, PFB/ F8BT in toluene in order to create different morphologies. PFB and F8BT are both conjugated polymers from polyfluorene derivatives and have potential application in polymer photovoltaics. The morphology of the active layer in optoelectronic devices such as polymer based field-effect transistors[84-86], light-emitting diodes (LEDs) [87-92] and photovoltaic devices (PVs)[93-95] plays an important role in device efficiency. Charge generation and charge transfer happens in the interfaces in the active layer. It has been demonstrated that the morphology of the active layer can greatly enhance the device performance [96, 97]. This can be achieved by controlling the processing parameters such as solution and substrate temperature, spin-speed, solvent and solvent saturated atmosphere. We made a preliminary attempt to make photovoltaics by controlling the process parameter, evaporation rate here, and producing a range of morphologies. Then we studied the effect of the morphology on device efficiency. By controlling the evaporation rate during spin coating in our environmental cell we were able to produce different morphologies of PFB/F8BT without changing the composition of the blend. While the morphology of the film responds to variation in evaporation rate more or less systematically, understanding the device efficiency seems to be more complicated. Our results show that the layered structure doesn't necessarily lead to higher device efficiency. The efficiency of the device which is related

to charge generation and charge transfer (and the latter is believed to be more important) is far more complicated.

1.2 Bibliography

1. Heriot, S.Y. and R.A.L. Jones, *An interfacial instability in a transient wetting layer leads to lateral phase separation in thin spin-cast polymer-blend films*. *Nature Materials*, 2005. **4**(10): p. 782-786.
2. Qu, S., et al., *Dewetting dynamics at a polymer-polymer interface*. *Macromolecules*, 1997. **30**(12): p. 3640-3645.
3. Lifshitz, I.M. and V.V. Slyozov, *The Kinetics of Precipitation from Supersaturated Solid Solutions*. *Journal of Physics and Chemistry of Solids*, 1961. **19**(1-2): p. 35-50.
4. Siggia, E.D., *Late Stages of Spinodal Decomposition in Binary-Mixtures*. *Physical Review A*, 1979. **20**(2): p. 595-605.
5. Pincus, P., *Dynamics of Fluctuations and Spinodal Decomposition in Polymer Blends .2*. *Journal of Chemical Physics*, 1981. **75**(4): p. 1996-2000.
6. Schwahn, D., et al., *Critical Fluctuations and Relaxation Phenomena in the Isotopic Blend Polystyrene Deuteropolystyrene Investigated by Small-Angle Neutron-Scattering*. *Journal of Chemical Physics*, 1990. **93**(11): p. 8383-8391.
7. Rappl, T.J. and N.P. Balsara, *Does coarsening begin during the initial stages of spinodal decomposition?* *The Journal of Chemical Physics*, 2005. **122**(21): p. 214903-4.
8. Sigehuzi, T. and H. Tanaka, *Coarsening mechanism of phase separation caused by a double temperature quench in an off-symmetric binary mixture*. *Physical Review E (Statistical, Nonlinear, and Soft Matter Physics)*, 2004. **70**(5): p. 051504-8.
9. Demyanchuk, I., S.A. Wieczorek, and R. Holyst, *Percolation-to-droplets transition during spinodal decomposition in polymer blends, morphology analysis*. *The Journal of Chemical Physics*, 2004. **121**(2): p. 1141-1147.

10. Lefebvre, A.A., et al., *Determination of critical length scales and the limit of metastability in phase separating polymer blends*. The Journal of Chemical Physics, 2002. **117**(19): p. 9063-9073.
11. Wang, H., et al., *Early-stage compositional segregation in polymer-blend films*. Physical Review E, 2003. **67**(6).
12. Puri, S., *Kinetics of wetting for phase-separating binary mixtures*. Computer Physics Communications, 2002. **147**(1-2): p. 286-291.
13. Walheim, S., et al., *Structure formation via polymer demixing in spin-cast films*. Macromolecules, 1997. **30**(17): p. 4995-5003.
14. Wang, H. and R.J. Composto, *Wetting and phase separation in polymer blend films: Identification of four thickness regimes with distinct morphological pathways*. Interface Science, 2003. **11**(2): p. 237-248.
15. Cyganik, P., et al., *Phase decomposition in polymer blend films cast on substrates patterned with self-assembled monolayers*. Vacuum, 2001. **63**(1-2): p. 307-313.
16. Bergues, B., et al., *Phase decomposition in polymer blend films cast on homogeneous substrates modified by self-assembled monolayers*. Vacuum, 2001. **63**(1-2): p. 297-305.
17. Ma, Y.Q., *Phase separation in ternary mixtures*. Journal of the Physical Society of Japan, 2000. **69**(11): p. 3597-3601.
18. Budkowski, A., et al., *Surface-directed phase separation in nanometer polymer films: self-stratification and pattern replication*. E-Polymers, 2002.
19. Krausch, G., *Surface-Induced Self-Assembly in Thin Polymer-Films*. Materials Science & Engineering R-Reports, 1995. **14**(1-2): p. 1-94.
20. Reich, S. and Y. Cohen, *Phase-Separation of Polymer Blends in Thin-Films*. Journal of Polymer Science Part B-Polymer Physics, 1981. **19**(8): p. 1255-1267.
21. Ball, R.C. and R.L.H. Essery, *Spinodal Decomposition and Pattern-Formation near Surfaces*. Journal of Physics-Condensed Matter, 1990. **2**(51): p. 10303-10320.
22. Jones, R.A.L., et al., *Surface-Directed Spinodal Decomposition*. Physical Review Letters, 1991. **66**(10): p. 1326-1329.

23. Puri, S. and H.L. Frisch, *Surface-directed spinodal decomposition: Modelling and numerical simulations*. Journal of Physics-Condensed Matter, 1997. **9**(10): p. 2109-2133.
24. Binder, K., *Spinodal decomposition in confined geometry*. Journal of Non-Equilibrium Thermodynamics, 1998. **23**(1): p. 1-44.
25. Rysz, J., et al., *Wetting transition in a binary polymer blend*. Europhysics Letters, 2000. **50**(1): p. 35-40.
26. Rysz, J., et al., *Wetting transition in polyolefin blends studied by profiling techniques*. Macromolecular Symposia, 2000. **149**: p. 277-281.
27. Budkowski, A., *Interfacial phenomena in thin polymer films: Phase coexistence and segregation*, in *Interfaces Crystallization Viscoelasticity*. 1999. p. 1-111.
28. Geoghegan, M., et al., *Wetting in a phase separating polymer blend film: Quench depth dependence*. Physical Review E, 2000. **62**(1): p. 940-950.
29. Geoghegan, M. and G. Krausch, *Wetting at polymer surfaces and interfaces*. Progress in Polymer Science, 2003. **28**(2): p. 261-302.
30. Shuto, K., et al., *Molecular Aggregation Structure and Surface Morphology of 2-Dimensional Ultra Thin Film Prepared by Water Casting Method*, in *Advanced Materials '93, Ii - a & B - a: Biomaterials, Organic and Intelligent Materials; B: Information Storage Materials*, H. Aoki, et al., Editors. 1994. p. 615-618.
31. Rysz, J., et al., *Surface-directed spinodal decomposition modified by a surface active copolymer*. Europhysics Letters, 1997. **40**(5): p. 503-508.
32. Geoghegan, M., R.A.L. Jones, and A.S. Clough, *Surface Directed Spinodal Decomposition in a Partially Miscible Polymer Blend*. Journal of Chemical Physics, 1995. **103**(7): p. 2719-2724.
33. Budkowski, A., et al., *Surface enrichment-depletion duality in a binary polymer blend*. Europhysics Letters, 1998. **43**(4): p. 404-409.
34. Puri, S. and K. Binder, *Surface-directed phase separation with off-critical composition: Analytical and numerical results*. Physical Review E, 2002. **66**(6).
35. Bruder, F. and R. Brenn, *Spinodal Decomposition in Thin-Films of a Polymer Blend*. Physical Review Letters, 1992. **69**(4): p. 624-627.

36. Puri, S. and K. Binder, *Surface-Directed Spinodal Decomposition - Phenomenology and Numerical Results*. Physical Review A, 1992. **46**(8): p. R4487-R4489.
37. Scheffold, F., et al., *Surface phase behavior in binary polymer mixtures .1. Miscibility, phase coexistence, and interactions in polyolefin blends*. Journal of Chemical Physics, 1996. **104**(21): p. 8786-8794.
38. Scheffold, F., et al., *Surface phase behavior in binary polymer mixtures .2. Surface enrichment from polyolefin blends*. Journal of Chemical Physics, 1996. **104**(21): p. 8795-8806.
39. Puri, S. and K. Binder, *Power laws and crossovers in off-critical surface-directed spinodal decomposition*. Physical Review Letters, 2001. **86**(9): p. 1797-1800.
40. Bastea, S., S. Puri, and J.L. Lebowitz, *Surface-directed spinodal decomposition in binary fluid mixtures*. Physical Review E, 2001. **63**04(4).
41. Freed, K.F., *Analytic theory of surface segregation in compressible polymer blends*. Journal of Chemical Physics, 1996. **105**(23): p. 10572-10582.
42. Binder, K., S. Puri, and H.L. Frisch, *Surface-directed spinodal decomposition versus wetting phenomena: Computer simulations*. Faraday Discussions, 1999(112): p. 103-117.
43. Puri, S.J., *Surface-directed spinodal decomposition*. Journal of Physics-Condensed Matter, 2005. **17**(3): p. R101-R142.
44. Puri, S. and K. Binder, *Surface-Directed Spinodal Decomposition in a Thin-Film Geometry - a Computer-Simulation*. Journal of Statistical Physics, 1994. **77**(1-2): p. 145-172.
45. Takahara, A., et al., *Surface aggregation structure and surface mechanical properties of binary polymer blend thin films*. Macromolecular Symposia, 2000. **159**: p. 89-96.
46. Geoghegan, M., et al., *Lamellar Structure in a Thin Polymer Blend Film*. Polymer, 1994. **35**(10): p. 2019-2027.
47. Tanaka, K., A. Takahara, and T. Kajiyama, *Film thickness dependence of the surface structure of immiscible polystyrene/poly(methyl methacrylate) blends*. Macromolecules, 1996. **29**(9): p. 3232-3239.

48. Krausch, G., et al., *Self-Assembly of a Homopolymer Mixture Via Phase-Separation*. Applied Physics Letters, 1994. **64**(20): p. 2655-2657.
49. Affrossman, S., et al., *Surface topography and composition of deuterated polystyrene-poly(bromostyrene) blends*. Macromolecules, 1996. **29**(14): p. 5010-5016.
50. Kressler, J., et al., *Temperature-Dependence of the Interaction Parameter between Polystyrene and Poly(Methyl Methacrylate)*. Macromolecules, 1994. **27**(9): p. 2448-2453.
51. Krausch, G., et al., *Interference of Spinodal Waves in Thin Polymer-Films*. Macromolecules, 1993. **26**(21): p. 5566-5571.
52. Colombani, D. and P. Chaumont, *Chain Transfer by an Addition-Substitution-Fragmentation Mechanism .2. Preparation of Alpha,Omega-Difunctional Telomers through a Radical Transfer-Reaction on a Methacrylic-Type Cyclic Peroxyketal*. Macromolecules, 1994. **27**(21): p. 5972-5978.
53. Straub, W., et al., *Transient Wetting and 2d Spinodal Decomposition in a Binary Polymer Blend*. Europhysics Letters, 1995. **29**(5): p. 353-358.
54. Steiner, U., et al., *Complete Wetting from Polymer Mixtures*. Science, 1992. **258**(5085): p. 1126-1129.
55. Akpalu, Y.A., et al., *Suppression of lateral phase separation in thin polyolefin blend films*. Macromolecules, 2001. **34**(6): p. 1720-1729.
56. Ton-That, C., et al., *XPS and AFM surface studies of solvent-cast PS/PMMA blends*. Polymer, 2001. **42**(3): p. 1121-1129.
57. Luo, S.C., V. Craciun, and E.P. Douglas, *Instabilities during the formation of electroactive polymer thin films*. Langmuir, 2005. **21**(7): p. 2881-2886.
58. Walheim, S., M. Ramstein, and U. Steiner, *Morphologies in ternary polymer blends after spin-coating*. Langmuir, 1999. **15**(14): p. 4828-4836.
59. Cyganik, P., et al., *AFM/LFM surface studies of a ternary polymer blend cast on substrates covered by a self-assembled monolayer*. Surface Science, 2002. **507**: p. 700-706.
60. Strawhecker, K.E., et al., *The critical role of solvent evaporation on the roughness of spin-cast polymer films*. Macromolecules, 2001. **34**(14): p. 4669-4672.

61. Haas, D.E. and D.P. Birnie, *Evaluation of thermocapillary driving forces in the development of striations during the spin coating process*. Journal of Materials Science, 2002. **37**(10): p. 2109-2116.
62. Birnie, D.P., et al., *Effect of ramping-up rate on film thickness for spin-on processing*. Journal of Materials Science-Materials in Electronics, 2005. **16**(11-12): p. 715-720.
63. Chang, Y., W.C. Wu, and W.C. Chen, *Theoretical analysis on spin coating of polyimide precursor solutions*. Journal of the Electrochemical Society, 2001. **148**(4): p. F77-F81.
64. Birnie, D.P., *Rational solvent selection strategies to combat striation formation during spin coating of thin films*. Journal of Materials Research, 2001. **16**(4): p. 1145-1154.
65. Birnie, D., *Rational solvent selection strategies to combat striation formation during spin coating of thin films* J MATER RES 2001. **16**(4): p. 1145-1154
66. Daniels, B.K., et al. *Surface tension effects in microlithography—striations*. in *Advances in Resist Technology and Processing III*, Proc.SPIE 631. 1986.
67. Birnie, D.P., et al., *Film Substrate Vacuum-Chuck Interactions During Spin-Coating*. Optical Engineering, 1992. **31**(9): p. 2012-2020.
68. Birnie, D.P., B.J.J. Zelinski, and D.L. Perry, *Infrared Observation of Evaporative Cooling During Spin-Coating Processes*. Optical Engineering, 1995. **34**(6): p. 1782-1788.
69. Du, X.M., X. Orignac, and R.M. Almeida, *Striation-Free, Spin-Coated Sol-Gel Optical Films*. Journal of the American Ceramic Society, 1995. **78**(8): p. 2254-2256.
70. Kozuka, H., Y. Ishikawa, and N. Ashibe, *Radiative striations of spin-coating films: Surface roughness measurement and in-situ observation*. Journal of Sol-Gel Science and Technology, 2004. **31**(1-3): p. 245-248.
71. Elbs, H. and G. Krausch, *Ellipsometric determination of Flory-Huggins interaction parameters in solution*. Polymer, 2004. **45**(23): p. 7935-7942.
72. Voicu, N.E., et al., *Solvent-vapor-assisted imprint lithography*. Advanced Materials, 2007. **19**(5): p. 757-+.
73. Elbs, H., et al., *Thin film morphologies of ABC triblock copolymers prepared from solution*. Macromolecules, 2002. **35**(14): p. 5570-5577.

74. Buxton, G.A. and N. Clarke, *Creating structures in polymer blends via a dissolution and phase-separation process*. Physical Review E (Statistical, Nonlinear, and Soft Matter Physics), 2005. **72**(1): p. 011807-8.
75. Elbs, H., et al., *Microdomain morphology of thin ABC triblock copolymer films*. Macromolecules, 1999. **32**(4): p. 1204-1211.
76. Jukes, P.C., et al., *Time-resolved light scattering studies of phase separation in thin film semiconducting polymer blends during spin-coating*. Macromolecules, 2005. **38**(6): p. 2030-2032.
77. Genzer, J. and E.J. Kramer, *Wetting of substrates with phase-separated binary polymer mixtures*. Physical Review Letters, 1997. **78**(26): p. 4946-4949.
78. Krausch, G., et al., *Real-Space Observation of Dynamic Scaling in a Critical Polymer Mixture*. Physical Review Letters, 1993. **71**(22): p. 3669-3672.
79. Block, M.J., *Surface Tension as the Cause of Benard Cells and Surface Deformation in a Liquid Film*. Nature, 1956. **178**(4534): p. 650-651.
80. Pearson, J.R.A., *On Convection Cells Induced by Surface Tension*. Journal of Fluid Mechanics, 1958. **4**(5): p. 489-500.
81. Pearson, J.R.A., *On convection cells induced by surface tension*. Journal of Fluid Mechanics Digital Archive, 2006. **4**(05): p. 489-500.
82. Meyerhofer, D., *Characteristics of Resist Films Produced by Spinning*. Journal of Applied Physics, 1978. **49**(7): p. 3993-3997.
83. Emslie, A.G., F.T. Bonner, and L.G. Peck, *Flow of a Viscous Liquid on a Rotating Disk*. Journal of Applied Physics, 1958. **29**(5): p. 858-862.
84. Sirringhaus, H., N. Tessler, and R.H. Friend, *Integrated optoelectronic devices based on conjugated polymers*. Science, 1998. **280**(5370): p. 1741-1744.
85. Garnier, F., et al., *All-Polymer Field-Effect Transistor Realized by Printing Techniques*. Science, 1994. **265**(5179): p. 1684-1686.
86. Yang, Y. and A.J. Heeger, *A New Architecture for Polymer Transistors*. Nature, 1994. **372**(6504): p. 344-346.
87. Chappell, J., et al., *Correlating structure with fluorescence emission in phase-separated conjugated-polymer blends*. Nature Materials, 2003. **2**(9): p. 616-621.

88. Bernius, M.T., et al., *Progress with light-emitting polymers*. Advanced Materials, 2000. **12**(23): p. 1737-1750.
89. Morgado, J., R.H. Friend, and F. Cacialli, *Improved efficiency of light-emitting diodes based on polyfluorene blends upon insertion of a poly(p-phenylene vinylene) electron-confinement layer*. Applied Physics Letters, 2002. **80**(14): p. 2436-2438.
90. Wilkinson, C.I., et al., *Enhanced performance of pulse driven small area polyfluorene light emitting diodes*. Applied Physics Letters, 2001. **79**(2): p. 171-173.
91. Friend, R.H., et al., *Electroluminescence in conjugated polymers*. Nature, 1999. **397**(6715): p. 121-128.
92. Coffey, D.C. and D.S. Ginger, *Time-resolved electrostatic force microscopy of polymer solar cells*. Nature Materials, 2006. **5**(9): p. 735-740.
93. Arias, A.C., et al., *Vertically segregated polymer-blend photovoltaic thin-film structures through surface-mediated solution processing*. Applied Physics Letters, 2002. **80**(10): p. 1695-1697.
94. Halls, J.J.M., et al., *Efficient Photodiodes from Interpenetrating Polymer Networks*. Nature, 1995. **376**(6540): p. 498-500.
95. Chen, L.C., et al., *Excitation transfer in polymer photodiodes for enhanced quantum efficiency*. Advanced Materials, 2000. **12**(15): p. 1110-+.
96. Arias, A.C., et al., *Photovoltaic performance and morphology of polyfluorene blends: A combined microscopic and photovoltaic investigation*. Macromolecules, 2001. **34**(17): p. 6005-6013.
97. Greenham, N.C., X.G. Peng, and A.P. Alivisatos, *Charge separation and transport in conjugated-polymer/semiconductor-nanocrystal composites studied by photoluminescence quenching and photoconductivity*. Physical Review B, 1996. **54**(24): p. 17628-17637.

Chapter 2

Theory and Background

2.1 Thermodynamics of bulk polymer blends

Polymers are usually immiscible as they are made of relatively long chains and do not gain much entropy by mixing. It is desirable to blend materials as it generally provides a system with some properties of each component or totally distinctive characteristics. However, it is possible to make polymer blends by changing the temperature or composition. Heating polymers above their melting point (polymer melt) or dissolving them in a common solvent can sometimes lead to miscible or partially miscible blends. The condition that defines whether two polymers will mix is the free energy of mixing. This is given by the difference between the free energy of the mixture and the total free energy of two polymers when separate. Miscibility in polymer blends can be described in the framework of the well-known Flory-Huggins theory. This theory yields a simple equation for the free energy of mixing per lattice site.

$$\frac{\Delta G_{mix}}{k_B T} = \frac{\phi_A}{N_A} \log \phi_A + \frac{(1-\phi_A)}{N_B} \log(1-\phi_A) + \chi \phi_A (1-\phi_A) \quad (2.1)$$

ΔG_{mix} :	The free energy of mixing
ϕ_A :	Volume fraction of component A
N_A & N_B :	The number of lattice sites occupied per chain of component A and B
χ :	The interaction parameter
k_B :	Boltzmann constant

The first two terms describe translational entropy contribution and are suppressed relative to their values in binary small molecule mixtures by the factors N_A and N_B which are of the order of $10^3 - 10^4$ for high molecular weight polymers [1]. The last term represents the enthalpic component of free energy change on mixing. It can be positive (opposing mixing), zero (ideal mixtures) or negative (promoting mixing)[2]. In its simplest form, χ has an inverse dependence with temperature which represents a purely enthalpic interaction [3]:

$$\chi \propto \frac{1}{T} \quad (2.2)$$

However in particular the interaction parameters do not only vary with temperature but also with composition and in certain cases even with chain length [4-7].

2.1.1 Thermodynamics of ternary systems: polymer A-polymer B-Solvent

One way of mixing two immiscible polymers is by changing the composition. That is by dissolving them in a common solvent. In what comes next we shall study the thermodynamics behind the effect, i.e how the existence of a solvent can make two immiscible polymers become miscible.

The free energy of homogeneous ternary mixtures is the expansion of Flory-Huggins theory for binary systems [3, 8] and can be expressed as [9]:

$$g(\phi_1, \phi_2) = \frac{\phi_1}{N_1} \ln(\phi_1) + \frac{\phi_2}{N_2} \ln(\phi_2) + \frac{\phi_3}{N_3} \ln(\phi_3) + \chi_{12} \phi_1 \phi_2 + \chi_{23} \phi_2 \phi_3 + \chi_{13} \phi_1 \phi_3 \quad (2.3)$$

$g(\phi_1, \phi_2)$:	The free energy of mixing of three components
ϕ_i :	volume fraction of component i
N_i :	The number of lattice sites occupied per chain of component i
χ_{ij} :	The interaction parameter between component i and j

2.1.1.1 Pseudobinary solutions

If a solvent is good for both polymers, the ternary system can be treated as a pseudobinary system [10]. It means that polymer A and polymer B are mixed in units of blob A and blob B rather than segment A and segment B [11]. A good example of this system is polystyrene (PS)- toluene- polybutadiene (PB). Toluene is a good solvent for both of these polymers. Thus one can treat this system as a PS solution and a PB solution. The Flory-Huggins interaction parameters between PS and toluene and PB and toluene and PS and PB are given by $\chi_{PS-Tol} = 0.436$, $\chi_{PB-Tol} = 0.465$ and $\chi_{PS-PB} = 0.1$. The interaction parameters between “PS and toluene” and “PB and toluene” are approximately the same and therefore the solvent is divided equally between liquid phases. The solvent will act as a diluent to decrease the interaction parameters between PS and PB [11]. For more details on using the pseudo- binary approximation, see reference [11]. Therefore blending immiscible polymers in a good solvent is thermodynamically favourable as the enthalpic part of the free energy is reduced through the interaction parameter.

2.1.1.2 Athermal system

To define athermal behaviour we must first outline the assumptions made by Flory-Huggins theory. Flory- Huggins theory is based on a lattice model and predicts the free energy of mixing in polymer systems and solutions.

The free energy of mixing (ΔG_{mix}) has two parts, the combinatorial part (ΔG_{mix}^C) which depends on entropy and the residual part (ΔG_{mix}^R) which is an enthalpic term and is related to intermolecular forces between components.

$$\Delta G_{mix} = \Delta G_{mix}^C + \Delta G_{mix}^R \quad (2.4)$$

ΔG_{mix}^C : The combinatorial part, related to entropy

ΔG_{mix}^R : Residual part related to enthalpy

In a regular solution it is assumed that all components have the same size, therefore the entropy is negligible and a formula for the enthalpy contribution can be derived. However, for polymer solutions the condition is different and one can not ignore the effect of entropy. Initially it is assumed there is no energy interchange between polymers and the solvent. The free energy of mixing is derived based on the assumption that the change in enthalpy due to mixing is zero. The interaction parameter is now introduced to account for the contribution of enthalpy on the free energy of mixing.

When an amorphous polymer and solvent mix without any energetic effect, it is referred to as athermal behaviour. In an athermal solution the contribution of enthalpy due to mixing can be ignored. To fulfil this condition the components should have chemically similar substrates. A good example of this kind of system is polystyrene and toluene. Flory and Huggins showed that the change in Gibbs energy and entropy of mixing are given by:

$$-\frac{\Delta G^C}{RT} = \frac{\Delta S^C}{R} = -(N_1 \ln \phi_1 + N_2 \ln \phi_2) \quad (2.5)$$

The regular solution theory for molecules of similar size yields the following:

$$\frac{\Delta S_{mix}}{R} = -(x_1 \ln x_1 + x_2 \ln x_2) \quad (2.6)$$

x_1 and x_2 : The molar fraction of the components

Now, we can extend the athermal theory to a ternary system and study the effect of the solvent on mixing of two polymers. We assume that there is no energy interchange between polymer A and solvent and polymer B and solvent, i.e. $\chi_{AS} = \chi_{BS} = 0$, the last two terms in equation (2.7) will be zero. This means that the enthalpic contribution of free energy will be smaller. As there is less energy cost, mixing will be thermodynamically favourable for the system.

2.1.1.3 Thermodynamics of an inhomogeneous ternary system

In a system composed of three components, polymer A, polymer B and a solvent, one can not ignore the effect of concentration or thermal fluctuations in the system. In 1988 Hashimoto [11] showed that the contribution of concentration fluctuations on the free energy of mixing could be significant.

The total free energy of mixing in an inhomogeneous binary system can be written as [12]:

$$\Delta G_m = \int [g(\phi_1) + \kappa(\nabla\phi_1)^2] dV \quad (2.7)$$

ϕ_1 :	volume fraction of component A
$\nabla\phi_1$:	The spatial gradient of ϕ_1
$g(\phi_1)$:	The homogeneous contribution to the free energy
κ :	The gradient energy parameter

The gradient energy parameter (κ) has two contributions, enthalpic and entropic.

$$\kappa = \kappa_H + \kappa_S \quad (2.8)$$

The enthalpic part (κ_H) is an energetic term while the entropic part (κ_S) is related to the connectivity of the chains that constitute the polymer molecules [13]. These gradient coefficients have been estimated for small molecule,

polymer-solvent, polymer-polymer and polymer-polymer-solvent systems. For estimates of these coefficients see reference [13].

The entropic contribution for an inhomogeneous polymer-polymer system was presented by de Gennes [14]:

$$\kappa_S(\text{polymer} - \text{polymer}) = \frac{1}{6} \left[\frac{R_{G1}^2}{N_1 \phi_1} + \frac{R_{G2}^2}{N_2 \phi_2} \right] \quad (2.9)$$

R_{Gi} : The radius of gyration of polymer i

ϕ_i : The volume fraction of polymer i

N_i : Degree of polymerization of polymer i

The enthalpic gradient contribution for a polymer-solvent system has been calculated by Debye [15]:

$$\kappa_H(\text{polymer} - \text{solvent}) = \frac{1}{6} R_{G1}^2 \chi_{13} \quad (2.10)$$

χ_{13} : The Flory-Huggins interaction parameter between polymer-solvent

McMaster [16] extended Debye's approach for polymer-solvent systems and obtained the enthalpic gradient parameter for polymer-polymer systems.

$$\kappa_H(\text{polymer} - \text{polymer}) = \frac{1}{6} (R_{G1}^2 + R_{G2}^2) \chi_{12} \quad (2.11)$$

A similar approach was used to obtain the enthalpic contribution to the free energy in an inhomogeneous pseudobinary polymer-polymer-solvent system where fluctuations in solvent concentration are small [17].

$$\kappa_H(\text{polymer} - \text{polymer} - \text{solvent}) = \frac{1}{6} R_{G1}^2 \chi_{12} \quad (2.12)$$

χ_{12} : The Flory-Huggins interaction parameter between polymer-polymer

Balsara and Nauman [18] calculated the entropic gradient contribution for a polymer-solvent system by using a lattice approach:

$$\kappa_s(\text{polymer} - \text{solvent}) = \frac{1}{2} \frac{R_{G1}^2}{(1 - \phi_1)} \quad (2.13)$$

Aryapadi and Nauman [13, 19] extended Debye's approach to find κ_H for an inhomogeneous polymer-polymer-solvent system where the spatial fluctuation of concentrations of all the components is considered. Here is the equation:

$$\Delta G_m = \int [g(\phi_1, \phi_2) + \kappa_1 (\nabla \phi_1)^2 + \kappa_2 (\nabla \phi_2)^2 + \kappa_{12} (\nabla \phi_1)(\nabla \phi_2)] dV \quad (2.14)$$

Where $g(\phi_1, \phi_2)$ is the free energy of homogeneous ternary mixtures and is expressed as (rewritten from equation (2.3)) :

$$g(\phi_1, \phi_2) = \frac{\phi_1}{N_1} \ln(\phi_1) + \frac{\phi_2}{N_2} \ln(\phi_2) + \frac{\phi_3}{N_3} \ln(\phi_3) + \chi_{12} \phi_1 \phi_2 + \chi_{23} \phi_2 \phi_3 + \chi_{13} \phi_1 \phi_3$$

κ_1, κ_2 and κ_{12} defined as:

$$\kappa_1 = \frac{1}{6} R_{G1}^2 \chi_{13} \quad (2.15)$$

$$\kappa_2 = \frac{1}{6} R_{G2}^2 \chi_{23} \quad (2.16)$$

$$\kappa_{12} = \frac{1}{6} [R_{G1}^2 \chi_{13} + R_{G2}^2 \chi_{23} - (R_{G1}^2 + R_{G2}^2) \chi_{12}] \quad (2.17)$$

2.1.2 Practical limitation of Flory-Huggins theory

The Flory-Huggins theory is based on assumptions which may over simplify the problem of mixing in practice. For instance, it only describes the equilibrium status of polymers. But in reality polymers often do not have

enough time to reach their equilibrium. For instance, by going through their glass transition or by crystallising, the motion of the chains could be frozen long before equilibrium.

Flory-Huggins theory assumes weak forces between the polymers which may not be the case in all situations. It is also assumed that polymers are in a molten, random coil state [20]. If the equilibrium state of a polymer is crystalline or liquid crystal, there would be a strong tendency towards demixing.

Despite the shortcomings in Flory-Huggins theory, it still provides the most convenient framework for polymer blends. This is mainly due to the existence of the interaction parameter, χ , that varies with both temperature and composition [21].

$$\chi = A + \frac{B}{T} \quad (2.18)$$

Where the constant A represents an entropic contribution to χ , and B the enthalpic contribution. This essentially is a convenient way of parametrising the free energy.

2.2 Phase diagram

The Flory-Huggins model allows us to evaluate the Gibbs free energy as a function of a system's composition and therefore construct a phase diagram from the free energy curves. According to the shape of the curves in the free energy versus concentration plots, there are three distinct areas in the resulting phase diagrams, stable, metastable and unstable. Mathematically, the first derivative of free energy with respect to concentration reflects the condition of equilibrium through the equality of the chemical potentials of coexisting phases. The criterion for a stable one phase system in a binary mixture with composition φ at fixed temperature T and pressure p are:

$$\frac{\partial^2 G}{\partial \phi^2} > 0 \quad (2.19)$$

The line separating the unstable and the stable region is called the binodal (solid line in figure (2.1(c))). However if a certain part of the free energy curve is convex (figure 2.1(b)), the second derivative of the free energy with respect to concentration would be negative. This defines the unstable region in the phase diagram in which any thermally excited fluctuation in concentration will result in the lowering of the system's free energy.

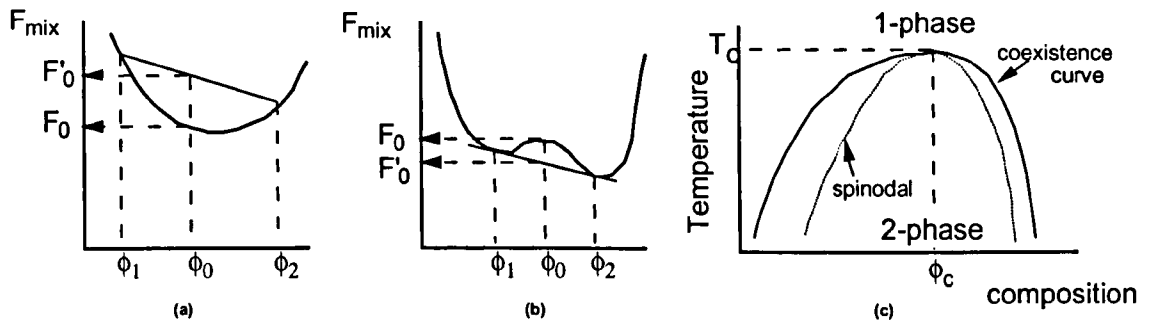


Figure (2.1) Free energy of mixing as a function of concentration where two species are (a) miscible, (b) immiscible, (c) Schematic phase diagram of an incompressible polymer solution. Richard A.L. Jones & Randal W. Richard, 1999 [21].

Spinodal regions are located inside the coexistence curve. The spinodal lines (dotted lines in figure (2.1(c))) separate the metastable from the unstable regime within the two-phase region. Binodal (coexisting curve) and spinodal lines meet at the critical point. At the critical point, the system can make large fluctuations in concentration with very little cost in free energy [22]. The thermodynamic condition for the critical point is given by:

$$\left(\frac{\partial^2 \Delta G_m}{\partial \phi^2} \right)_{p,T} = \left(\frac{\partial^3 \Delta G_m}{\partial \phi^3} \right)_{p,T} = 0 \quad (2.20)$$

For polymer blends the miscibility can only be achieved when $\chi < \chi_{cr}$. The χ_{cr} parameter at the critical point can be derived as follows:

$$\chi_{cr} = \frac{1}{2} \left(\frac{1}{\sqrt{N_A}} + \frac{1}{\sqrt{N_B}} \right)^2 \quad (2.21)$$

N_A and N_B are the number of polymer segments and are the degree of polymerization.

In binary systems, the phase diagram is plotted in terms of temperature (Y axis) and composition fraction (X axis). In ternary systems however the phase diagram is more complicated. It is made of three binary systems and is three dimensional, with temperature on the vertical axis. However, for simplicity it is common to use the two dimensional projection of the surfaces onto the base of a triangle (figure (2.2)). However, the exact calculation of the phase diagram of a ternary system consisting of at least one polymer component is difficult [9] and the calculated equilibrium curve sometimes deviates significantly from the experimental value.

For ternary systems, Dobry and Boyer-Kawenski [23] studied 78 polymer-polymer-solvent solutions using the cloud point isotherm method. They added solvent to two turbid immiscible polymers until the agitated solution became clear. To show the phenomenon is reversible, they evaporated the solvent from a clear mixture until it was cleared. Later on other methods were developed to plot the ternary phase diagram. In reference [24] some of the methods are mentioned. Figure (2.2) shows a ternary phase diagram of PS-PMMA-toluene.

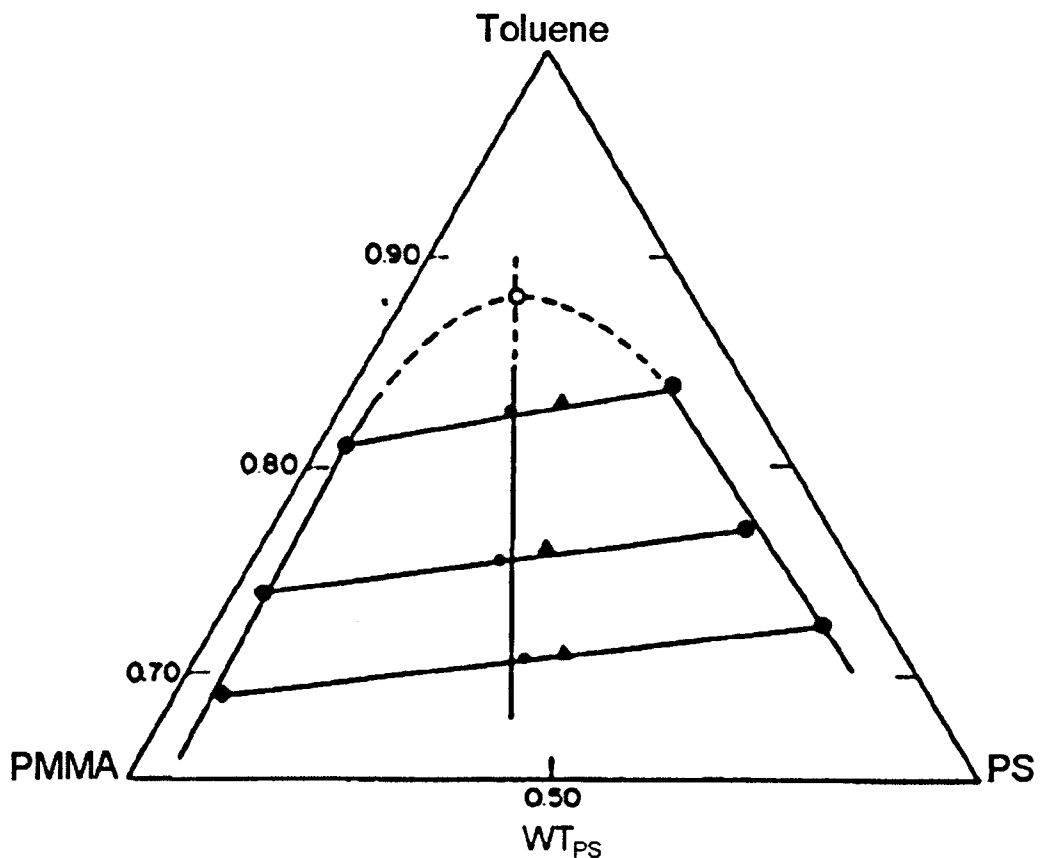


Figure (2.2) A typical Phase diagram of the system PS (100K)-PMMA (69K) - toluene at 23°C. A uniform blend of PS and PMMA was made by dissolving the polymers in toluene and shaking the sample. In a few days the mixture was separated into two distinct liquid phases. More than three weeks was given for the samples to reach equilibrium. Gel permission chromatography (GPC) was used to determine the composition of each phase. The solid triangles represent the mixed point of the starting PS-PMMA-toluene mixture. Taken from W.Y. Lau Wayne, 1984 [25].

2.3 Mechanism of Phase separation

Phase separation takes place when a single phase system suffers a change of composition, temperature or pressure that forces it to enter either the metastable or the spinodal region. Figure (2.3) illustrates three different phase separation path ways. In what follows, the common phase separation mechanisms will be discussed.

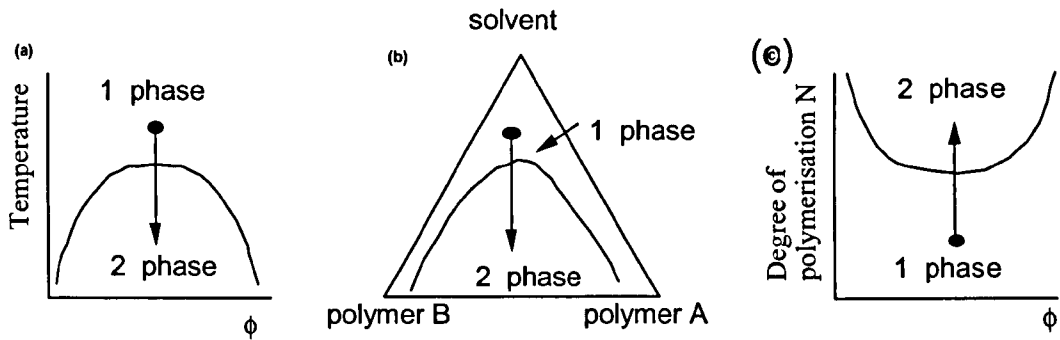


Figure (2.3) Schematic phase diagrams illustrating the different path which may lead to phase separation: (a) temperature quench: a mixture of two polymers undergoes phase separation on cooling. (b): solvent quench: two polymers are dissolved in a common solvent, and then phase separation happens after solvent evaporation. In (c) one or both of the components polymerises, causing phase separation to occur when a certain critical degree of polymerization has been reached. Taken from Richard A.L. Jones & Randal W. Richard, 1999 [21].

2.3.1 Spinodal decomposition

When a system is forced to jump from a single phase region into a spinodal region of immiscibility, the phases separate spontaneously by a mechanism called spinodal decomposition, which is based on the amplification of random composition fluctuations [21]. As it is shown in figure (2.1(b)), at any composition of ϕ_0 between ϕ_1 and ϕ_2 , phase separation of ϕ_0 to any composition close to ϕ_0 results in lowering the free energy of the system from F_0 to F'_0 . In the spinodal region any random, thermally induced concentration fluctuation will grow to form domains of the two coexisting phase [21, 26]. In the bulk, the unstable state decays by the growth of long wavelength fluctuations [27]. The length scale depends on molecular size of the polymer and the distance from the critical point. However concentration fluctuations grow at different rates [22]. On long length scales figure (2.4 (b)), the composition fluctuation can only grow in amplitude by transferring material from the troughs to peaks; this happens by diffusion, as the wavelength becomes longer, the fluctuations grow relatively slowly due to long distance of diffusion. On the other hand, a short wavelength fluctuation creates a sharp

concentration gradient (figure (2.4(c))). If the gradient is steep compared with the length scale of the radius of gyration of a polymer chain, there would be an energy penalty [21]. So, short fluctuations are suppressed as their growth would lead to the formation of excess interface, with an associated free energy cost which is thermodynamically unfavourable [21]. Thus there will be an intermediate dominant length scale of fluctuations (figure (2.4(a))) that grow the fastest and control the morphology of the phase separation in the early stages.

2.3.1.1 Characterisation of the spinodal decomposition process

Analysis of the spinodal decomposition process for isotopic polymer mixtures can be considered in four stages. The pictures of these stages are shown in figure (2.5) There are two important length scales. R , characterises the size of the domains and their average separation, and w , which characterises the width of the interface between domains. In the very early stages of SD both R and w are constant and are related to the fastest growing wavelength. They lead to the development of the peak in the scattering of structure factor at $q_m(0)$. The amplitude of the composition profile increases with time without any variation in q_m (figure (2.5(a))).

In the intermediate stage, q_m decreases and the fluctuation amplitude increases with time as is shown in figure (2.5(b)), until the latter approaches the coexisting composition. Then it enters the complicated transition stage, which is characterised by two time dependent length scales as indicated in figure (2.5(c)). As the R which characterises the size and separation of the domains, increases, the interfacial width $w(t)$ decreases towards its equilibrium value, $w(t) = w(\infty)$.

At the final stage the only length scale characterising the morphology is $R(t) \gg w(t)$, which characterises both the average size and the separation of the domains.

The late stage of the process is identical to a “nucleation and growth” mechanism [21, 26].

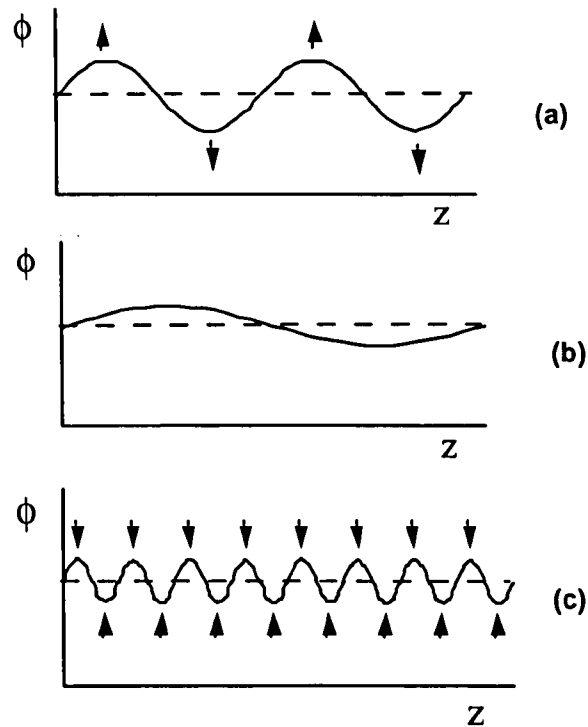


Figure (2.4) Spiodal decomposition. (a) In the stable part of phase diagram, the random concentration fluctuation grow quickly in amplitude (b) Long wave length fluctuation grow slowly due to long distance of diffusion (c) Short fluctuations are suppressed due to high free energy penalty associated with sharp concentration gradient. Richard A.L. Jones & Randal W. Richard, 1999, [21].

2.3.2 Nucleation and growth

When the system enters a metastable region from a single phase, any small composition fluctuation will raise the free energy of the system. To make phase separation happen, a droplet of the minority phase, greater than a critical size has to be nucleated. This slow nucleation followed by growth of phase separated domains is aptly known as “nucleation and growth”. The one and two phase regions are separated by the so-called binodal line.

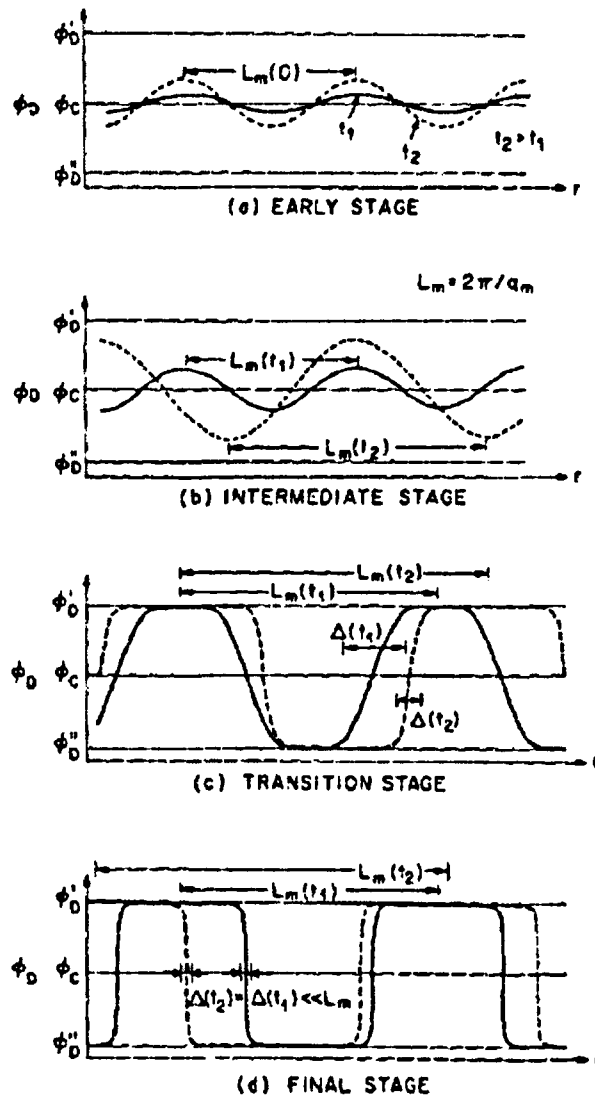


Figure (2.5) The behaviour of the interface width and average domain size at various stage of spinodal decomposition [49]. In each diagram the dashed curves represent the composition profile at a later time (t_2) than that given by solid curves (t_1). ϕ_D' and ϕ_D'' correspond to the equilibrium composition in each phase. F.S Bates, 1989 [26].

2.3.3 Wetting

So far we have only talked about the bulk situation. However, in the situation we consider experimentally, involving thin films, the role of the surfaces and interfaces is very important. Here we consider the role of interfaces in

thermodynamics of mixed polymer systems. The thermodynamic definition of wetting is based on the concept of surface energy or tension. Surface tension results from an imbalance of molecular forces in a liquid. To define the surface tension, temperature, volumes and chemical potential are assumed to be fixed. For one component system, we have:

$$\Omega = F - \mu N \quad (2.22)$$

- Ω : Grand potential
 F : Helmholtz free energy
 μ : Chemical potential
 N : Number of particles

The surface tension σ is derived from the thermodynamic differential:

$$d\Omega = \sigma dA - SdT - pdV - nd\mu \quad (2.23)$$

- A : The surface area
 S : The entropy
 T : Temperature
 p : Pressure
 V : Volume

The surface tension is defined as the excess free energy to enlarge the surface area by one unit. It also can be viewed as a force. Now consider a liquid drop on a solid surface. There are three different phases present and so three different surface tensions as follows; solid-vapour (σ_{sv}), solid-liquid (σ_{sl}) and liquid-vapour (σ_{lv}) (figure (2.6)). The relation between these three surface tensions is given by well-known Young equation:

$$\sigma_{sv} = \sigma_{sl} - \sigma_{lv} \cos \theta \quad (2.24)$$

- θ : The contact angle

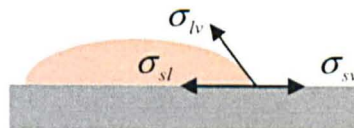


Figure (2.6) Force balance at the three phase contact line. The vectors indicate the surface tension between solid – vapour, Solid – liquid and liquid – vapour phases.

Wetting can be viewed as a direct consequence of Young's equation. When there is a droplet on the surface, as the surface is not totally covered by the liquid it is referred to as partial wetting (figure (2.7(a))). By changing some thermodynamic parameters like temperature, the surface tensions and contact angle will change. At a certain point when the sum of solid-liquid tension and liquid-vapour tension becomes equal to solid-vapour surface tension, the contact angle is zero and a uniform film covers the substrate. This situation is referred to as complete wetting (figure (2.7(b))). Analogously the contact angle can reach 180 degrees and total dewetting happens (figure (2.7(c))). In this case the liquid does not wet the solid and in equilibrium it remains separated from the substrate by a layer of vapour [28].



Figure (2.7) Wetting of a liquid drop on a solid substrate: (a) partial wetting, (b) complete wetting, (c) complete drying state.

2.3.3.1 Wetting transition

The wetting transition is a shift between partial and complete wetting. If the system is studied as a function of temperature, the transition temperature is called the wetting temperature, T_w . Due to the details of the intermolecular interaction this transition may be a first or second order transition (critical wetting). If a discontinuity occurs in the first derivative of the free energy, the transition is said to be first order. First order wetting implies a discontinuous jump to infinite film thickness at T_w , the film thickness jumps discontinuously from a microscopically thin to a thick film at the wetting transition temperature T_w [28] (figure (2.8 (a))).

If the first derivative of the free energy is continuous, the transition is called second order. These continuous transitions come in two different flavours: the so-called long- and short-range critical wetting transitions.

In long-range critical wetting (LRCW) transitions, the discontinuity is followed by a continuous divergence of the film thickness (figure (2.8(b))). The divergence is due to a change in sign of the net effect of the long-range van der Waals forces in the interaction energy between the two interfaces. As the transition is continuous and due to the long-range forces, this transition is called the long-range critical wetting (LRCW) transition [29].

This is an exceptional situation for which the long-range van der Waals forces can be neglected. As the transition is continuous and due to short-range forces, this transition is called the short-range critical wetting (SRCW) transition [30].

In this case the film thickness diverges continuously on approaching T_w .

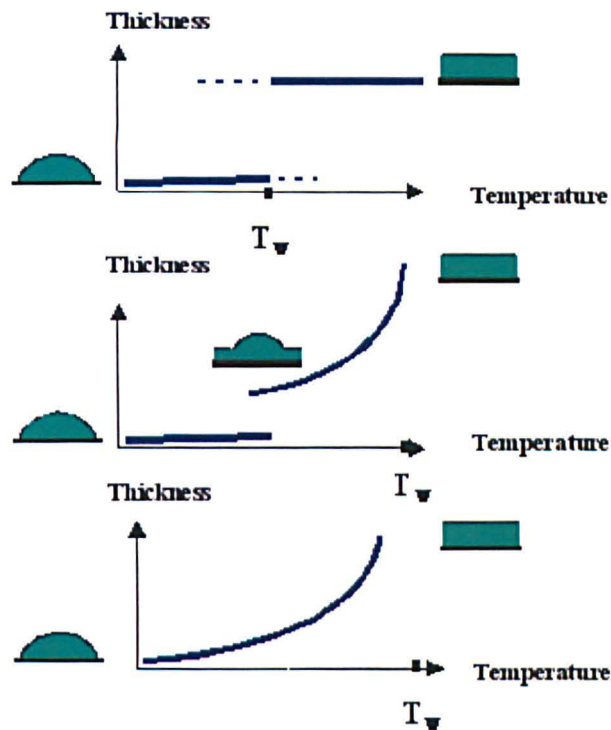


Figure (2.8) Schematic of variation of film thickness via temperature in (a) first order wetting transition, (b) long range order critical wetting and (c) short range order critical wetting.

2.4 Surface Effect on Phase Separation in Bulk and thin films

The morphology of a phase separated film is governed by the interplay between phase separation and phase segregation (wetting) [31]. Phase separation is controlled by χN , where χ is the Flory-Huggins interaction parameter and is the measure of the unfavourable polymer-polymer interaction, N is the number of segments of the polymers. On the other hand wetting is governed by the interaction of the polymers with the new boundary phases [28, 31, 32]. The effect of dewetting on pattern formation in polymer films and also in turn the dependence of dewetting on film thickness, temperature, sample geometry, composition, etc has been extensively studied [28, 32-44]. In the next section the thermodynamics of wetting will be explained.

Phase separation in bulk polymer films will lead to an isotropic domain structure (figure (2.9(a))). However in the vicinity of the surface confining the bulk, an anisotropic structure is expected [45]. The main reason for this happening is related to preferential attraction of one of the components by the surface. Essentially, the coexisting components have different interfacial values with the boundary surfaces. Thus, one of them, usually the component with lower surface energy will migrate to the surface to reduce the free energy of system. When the difference between surface energies is high, phase separation will lead to a layered structure with domains aligned parallel to the surface (figure (2.9(b))). So the final structure of the bulk consists of an isotropic structure distant from the free surface and an anisotropic and enriched structure near the surface. However these two structures will merge at some depth beneath the surface.

In thin films where the thickness of the sample is much smaller than its lateral extensions, the influence of the surfaces is very crucial and the entire domain morphology may be determined by the surfaces (figure (2.9(c))). However, at equilibrium the total interfacial area needs to be minimised; therefore, depending on the particular surface-polymer interaction and the wetting

behaviour of the existing components the layers are expected to coarsen thereby leading to a highly ordered bilayer or trilayer domain structure [45] (figure 2.9(d)).

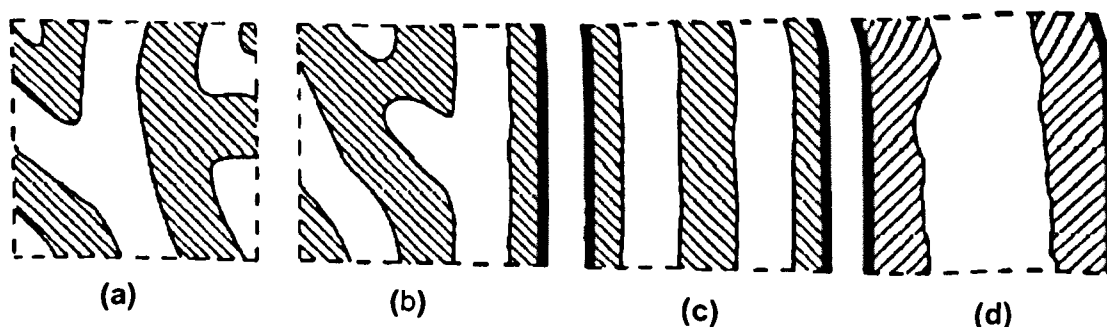


Figure (2.9) Schematic drawing of possible domain morphologies in phase separating binary polymer blends. (a) isotropic bulk situation, (b) preferential migration of the dark phase to the boundary surface, (c) situation in a thin film with two boundary surfaces attracting the same phase far from equilibrium and (d) situation as in (c) in equilibrium. Here, complete wetting of the dark phase is assumed for both boundary surfaces. G. Krausch, 1995 [45].

2.4.1 Surface- directed spinodal decomposition

In the bulk the concentration fluctuation governs the phase separation. In an unstable region of phase diagram as described before, these random fluctuations (figure 2.10(c)) lead to spinodal decomposition. In thin films, the presence of the two surfaces (polymer/air and polymer/substrate) breaks the translational and rotational symmetries. These additional surfaces modify the direction of compositional waves and make them directional (figure 2.10(d)). As the decomposition is derived by the surface, it is called surface-directed spinodal decomposition. In the bulk, surface-directed spinodal decomposition leads to a surface enriched structure. In thin films it can create self-organised ordered phase domain structures [46-49] or a laterally separated phase in the plane of the film [42, 45, 50-52].

For homogeneous surfaces this self-organisation can result in a self-stratified (multilayer) or column-like phase domain morphology [46] with the interfaces

between blend phases oriented (in general) parallel or perpendicular to the substrate, respectively [48] (figure (2.11)).

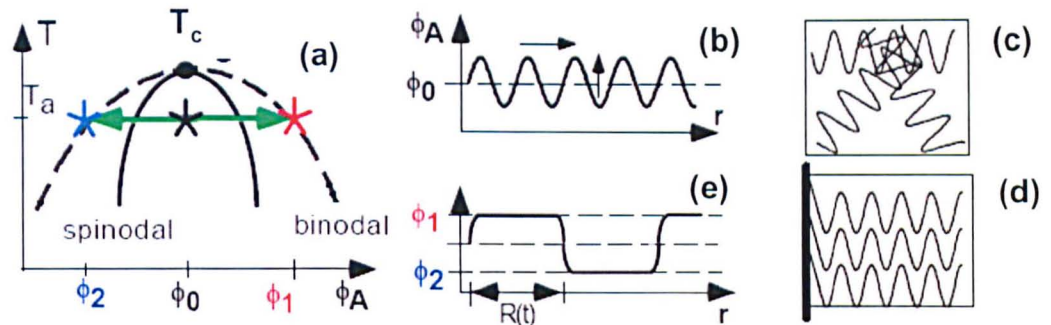


Figure (2.10) Bulk (c) and surface-directed (d) spinodal decomposition (a, b, e) of a binary mixture. Coexisting compositions are ϕ_1 and ϕ_2 , while the initial concentration is ϕ_0 . A. Budkowski *et al*, 2002 [48].

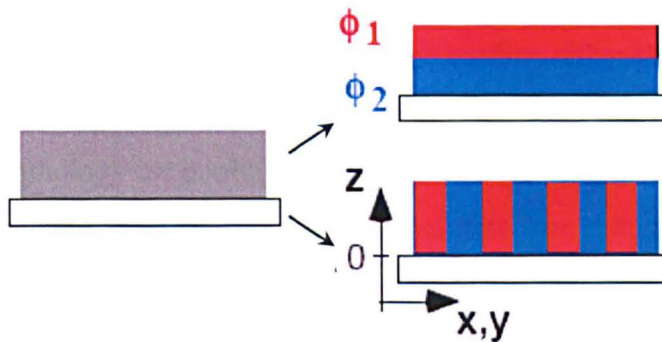


Figure (2.11) Self-organisation of thin polymer blends films. A homogeneous substrate can induce multilayer (self-stratification) or column-like-morphology of phase domains (ϕ_1 and ϕ_2). A. Budkowski *et al*, 2002 [48].

Studies on self-organisation in thin films composed of polymer blends are motivated by numerous technological applications. In addition to attractive aspects of self-assembly, specific phase domain morphologies can increase device efficiency. For instance, a self-stratified morphology is used in gas separating membranes [53] and polymeric photodiodes [54]. A column-like morphology is present in light emitting polymeric diodes with a variable colour or in anti-reflection coatings [55]. Patterned substrates are used in “all-polymer field transistors” to keep apart the phase regions of the source and drain [56].

2.4.2 Previous studies on interface effect in thin films

In 1981, Reich and Cohen [57] reported the first study of phase separation of polymer blends (melts) in thin films. The work was aimed to understand the effect of confining surfaces on phase separation behaviour. It was shown that both geometrical constraints on the chain conformations imposed by the boundaries and specific polymer-surface interactions strongly influenced the phase separation process. The influence increased with decreasing film thickness.

Ten years later, a numerical study was carried out by Hall and Essery [58] to understand the particular influence of boundary surfaces on the domain morphology in a phase separating binary mixture. They assumed that there is an established temperature gradient perpendicular to the sample surface. It was shown that in the near surface of off critical binary mixtures the domains are formed preferentially parallel to the surface rather than isotropically as usually observed in the bulk. In their simulation, a strong dependence of the domain morphology on cooling rate with the highest degree of surface induced order occurring at sufficiently low quench rate was obtained. A similar pattern was found to be generated by a boundary associated with a surface free energy.

Shortly after, R.A.L. Jones et al [27] experimentally observed the composition wave with a wave vector normal to the surface for PEP/dPEP system. They argued that these surface-directed spinodal decomposition waves are due to the preferential attraction of one of the polymers to the surface. They also studied laterally averaged composition profiles as a function of distance. The bulk is characterised by a randomly-oriented phase separation profile and the lateral average procedure does not yield a systematic behaviour. However the surface exhibits an enrichment layer of d-PEP followed by a depletion layer. This oscillatory profile is time-dependent and decays with a characteristic length to the bulk composition.

Jones' experiment motivated many further investigations of this problem. The experimental techniques and results have been reviewed by Krausch [45].

Following this experimental observation, Puri and Binder [59, 60] applied two special boundary conditions to conventional Cahn- Hillard equation theory for spinodal decomposition in the bulk. They took the preferential attraction of the components to the confining surface into account. Numerical solutions of their equations were very similar to experimental profiles obtained by Jones et al. For a good review of theoretical and numerical development of this problem see [61, 62].

In 1993, Lambooy et al [35] imaged the shapes of the growing hole and the interface between two polymers (PS/PMMA) and measured the dewetting velocity. According to them, the shape of the interface changes significantly with substrate viscosity and for the films thinner than 100 nm, a strong decrease of the dewetting velocity with decreasing the PMMA thickness was observed. This was due to the significant influence of silicon layer on the mobility of PMMA substrate layer.

All studies mentioned above are related to polymer melts. As we discussed earlier in this chapter, there is another way of making polymer blends by dissolving them in a common solvent and then spin coating. Spin coating is a quick way of making thin film of polymer blends. A good solvent decreases the free energy of mixing and therefore mixing is thermodynamically favoured.

In 1994 M. Geoghegan and R.A. L Jones *et al* [63] reported the lamellar structure formed in ternary system of polystyrene- polybutadiene spin cast from a toluene solution. Using neutron scattering technique they observed a very well defined layered structure with sharp interfaces. One year later in 1995 they [49] studied the effect of the surface and interface in a different system, polystyrene and *Poly(α - methyl - styrene)* thin film cast from toluene solution, using nuclear reaction analysis (NRA). Surface directed spinodal decomposition was observed. Also, the growth rate of the depletion layer near the surface and substrate was calculated. In 1997, Walheim et al [64] systematically studied the effect of solvent quality and substrate surface on domain structure of PS/PMMA. It was suggested that one important

mechanism for lateral phase separation was the creation of a transiently layered film by a process of wetting, followed by the break up of the layers because of an interfacial instability.

Different experiments were carried out to understand the interfacial effects in polymer thin film, in particular the influence of boundary surfaces on phase domain morphology and surface-directed spinodal decomposition has been intensively studied [45, 61, 65-69].

Most of these studies are done after film formation. However as it is a non equilibrium process, analysing the route from the end point does not provide precise information about the process itself. So, there is a huge motivation to develop a method to study the process in situ. In 2005, Heriot and Jukes [47, 70] for the first time developed a technique for in situ monitoring of the phase separation process. Using light scattering instruments, they could monitor the evolution of film thickness and the development of phase-separated structure as a function of time during the spin-coating process. Their results provided convincing direct evidence in favour of the Walheim hypothesis. Utilizing this device is in its early stage of development. Hopefully by developing the method, one would be able to deeply understand the process of film formation.

2.5 Spin coated thin films

Spin coating is a method used widely in the creation of highly uniform, sub-micrometer polymer films in CD manufacturing, field effect transistors, microlithography, photovoltaics, LEDs etc. To simply describe the process, a ternary system is made by dissolving the polymers in a common solvent. A few droplets are deposited on a rotating substrate and in less than a minute a uniform film is formed. It is believed that there are three main steps in spin coating. First, most of the polymer solution is flung away from the rotating substrate leaving a thin uniform film. This is followed by decrease in film thickness as a result of the balance between the centrifugal and viscous forces

acting on the film. During this stage phase separation occurs for immiscible blends. Since the polymers have different solubility in the solvent, different phases will solidify at different solvent concentrations. In the last stage the viscosity of the film becomes so high that it is frozen in the substrate and subsequent solvent evaporation takes place through the film surface. The final morphology depends on many parameters including polymer properties, solvent evaporation, solvent volatility and the precise casting conditions [47]. However, when the film formation is altered by a homogeneous surface, phase separation can occur in the direction perpendicular to the film plane, resulting in a self-stratified film [32, 47, 48, 63]. Alternatively it can happen in the plane of the film, resulting in a laterally patterned structure characterised by a length scale that depends on process history [47, 71-76]. Laterally phase separated domains are always accompanied by free surface undulations [61, 64, 77-79]. There are different theories, trying to relate the solvent effects to the phenomenon [64, 77, 79]. The most versatile one was published in 1997 and later in 1999 by Walheim et al [64, 78]. According to the authors, due to the difference in solubility of the blend components in the common solvent, the evaporation rate of the solvent from each polymer is different. It evaporates faster from the phase rich in less soluble polymers, which solidifies earlier. Consequently the phase rich in more soluble polymer is swollen. After final evaporation of the solvent from this phase, it collapses and forms a lower region of the free surface. This mechanism is claimed to take place during the third stage of spin coating (Figure (2.12 (d-f))) [64].

UNIVERSITY
OF SHEFFIELD
LIBRARY

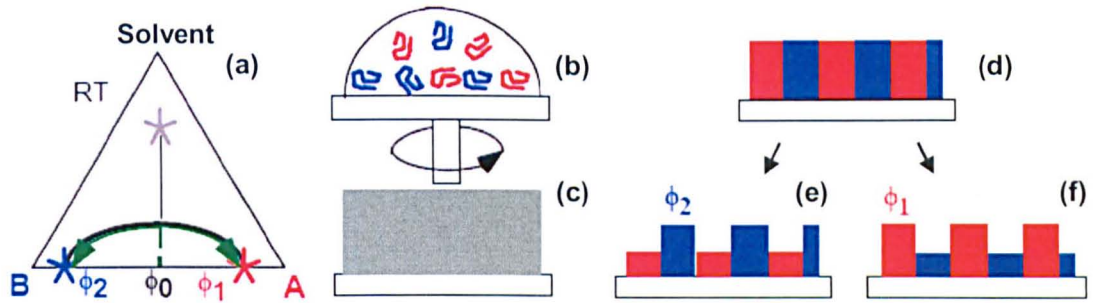


Figure (2.12) Phase separation (c-d) occurs in the course of the spin-casting process (b-f) for a certain range of decreasing solvent concentration (a) rather than at a fixed point of phase diagram. Surface undulations (e-f) are formed with the elevated phase rich in the polymer less soluble in a common solvent (ϕ_2 in (e), ϕ_1 in (f)). A. Budkowski *et al*, 2002 [48].

2.5.1 Numerical model of spin coating

Spin coating was first modelled by Emslie, Bonner and Peck (EBP) in 1958 [80]. Their model consists of a simple system of a viscous fluid. Hence there is no polymer, the viscosity remains constant during the process. They assumed that the solution shows Newtonian character i.e. viscosity and thickness are uniform over the spinning disk and the flow in the spin off stage is radial, rectilinear and slowly varying. In a Newtonian fluid, the shear stress changes linearly with shear strain. They set the transient point when the viscous (shear) force is balanced by the centrifugal force. Equation (2.25) shows the force balance and figure (2.13) schematically expresses the scheme.

$$-\eta \frac{\partial^2 v}{\partial z^2} = \rho \omega^2 r \quad (2.25)$$

η :	Fluid viscosity
v :	Radial velocity (in r direction)
z :	The coordinate normal to the disk surface (rotation axis)
ρ :	Fluid density
ω :	Rotation speed of the disk
r :	Radial coordinate

Integrating equation (2.25), we have:

$$\frac{\partial v}{\partial z} = -\frac{\rho\omega^2 rz}{\eta} + c \quad (c \text{ is constant of integration}) \quad (2.26)$$

Applying the boundary condition that at the free surface of the liquid ($z = h$), there is no shearing force ($\frac{\partial v}{\partial z} = 0$), we obtain the constant of integration:

$$c = \frac{\rho\omega^2 rh}{\eta} \quad (2.27)$$

By replacing c in equation (2.26) we have:

$$\frac{\partial v}{\partial z} = -\frac{\rho\omega^2 rz}{\eta} + \frac{\rho\omega^2 rh}{\eta} \quad (2.28)$$

Integrating equation above leads to:

$$v = -\frac{\rho\omega^2 rz^2}{2\eta} + \frac{\rho\omega^2 rhz}{\eta} + c' \quad (2.29)$$

Employing the boundary condition that at the surface of the disk ($z = 0$) the radial velocity is zero ($v = 0$), the value of the constant of integration will be zero ($c' = 0$) and therefore equation (2.30) will be obtained for the radial velocity:

$$v = -\frac{\rho\omega^2 rz^2}{2\eta} + \frac{\rho\omega^2 rhz}{\eta} \quad (2.30)$$

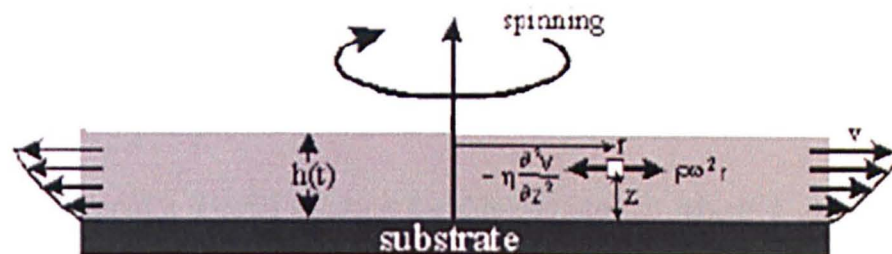


Figure (2.13) The balance between viscous force and centrifugal force during the spin coating. Taken from D.W Schubert *et al*, 2003 [81].

The radial flow (q) per unit length of circumference is:

$$q = \int_0^h u dz = \frac{\rho \omega^2 r h^3}{3\eta} \quad (2.31)$$

The equation below is the continuity equation in terms of radial flow per unit circumference (q):

$$\frac{\partial h}{\partial t} = -\frac{1}{r} \frac{\partial(rq)}{\partial r} \quad (2.32)$$

h : Film thickness at any time t during spinning

t : Time

q : Radial flow per unit circumference

Replacing (q) from equation (2.31) in equation (2.32), and by assuming that the viscosity is constant, we have:

$$\frac{\partial h}{\partial t} = -\frac{1}{r} \frac{\partial(rq)}{\partial r} = -\frac{1}{r} \frac{\partial\left(r \frac{\rho \omega^2 r h^3}{3\eta}\right)}{\partial r} = -\frac{1}{r} \frac{\partial(kr^2 h^3)}{\partial r} \quad (2.33)$$

$k = \frac{\rho \omega^2}{3\eta}$: Fluid constant

In the EBP system, the viscosity is constant (solvent only), therefore equation (2.33) can be rewritten as:

$$\frac{\partial h}{\partial t} = -\frac{k}{r} \frac{\partial(r^2 h^3)}{\partial r} \quad (2.34)$$

EBP considered a special solution for this equation in which h depends only on t . In this case [80]:

$$\frac{\partial h}{\partial t} = -2kh^3 \quad (2.35)$$

$$h = \frac{h_0}{\sqrt{1 + 4kh_0^2 t}} \quad (2.36)$$

h_0 : Initial height of the fluid layer

Equation (2.35) shows the film thinning rate during spin coating where there is no evaporation and therefore viscosity remains constant during spinning.

Meyerhofer [82] was the first to consider the evaporation phenomenon on spin coating model. He simply added e , the evaporation rate, to equation (2.35):

$$\frac{dh}{dt} = -2kh^3 - e \quad (2.37)$$

e : Evaporation rate

Meyerhofer didn't solve the equation above analytically. Instead he assumed there are two stages in spin coating. The early stage is flow dominated and the later stage is evaporation dominated. With this approach he could predict the final coating thickness in terms of several key solution parameters expressed in equation (2.38). Figure (2.14) shows film thickness as a function of spin speed and different solute concentration.

$$h_f = x \left[\frac{e}{2(1-x)k} \right]^{1/3} \quad (2.38)$$

e : Evaporation rate

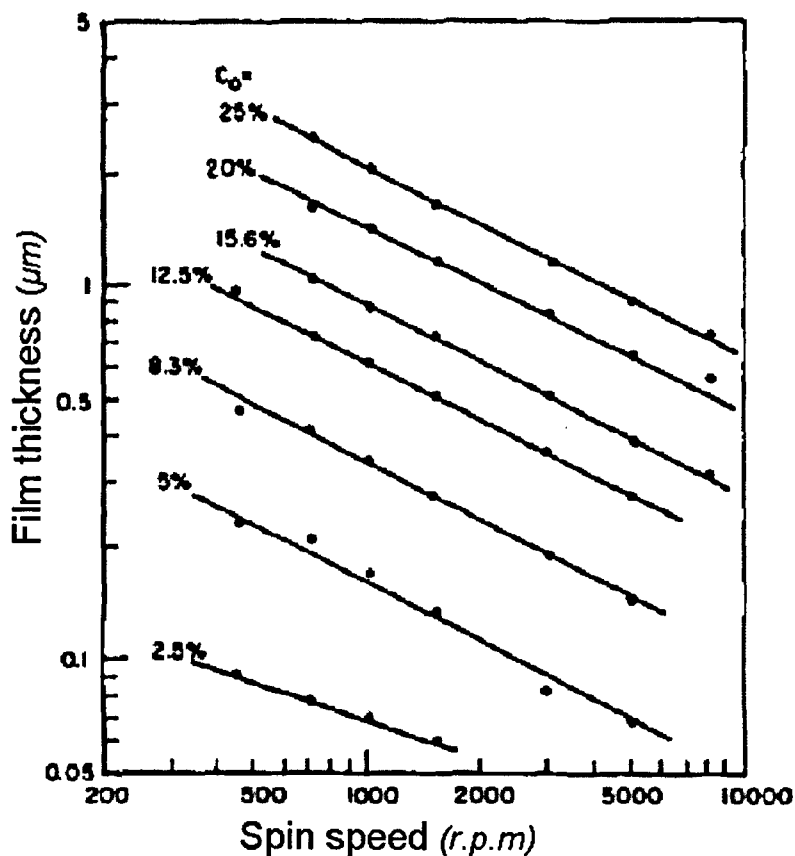


Figure (2.14) Meyerhofer's model for thickness via spin speed at different solute concentration. D.Meyerhofer, 1978 [82].

There have been several more attempts to predict the film thinning rate during spin coating. All these models [80, 82, 83] relied on the assumption of uniform solvent concentration during the spin coating. Later on, the model was improved by Bornside, Flack and Lawrence by taking the concentration profile into account [84-86] and also the effect of overlaying gas above the spinning disk [84]. Subsequent authors have generalised the work of Emslie et al [80] to include various additional physical effects including non Newtonian fluid behaviour, non polar substrate, surface roughness, evaporation and adsorption. Based on all these models the next attempt was extracting evaporation rate from the experiment. In the next section the impact of evaporation rate on the polymer film will be discussed.

2.5.2 The effect of solvent and evaporation rate on film structure

The effect of solvent on film structure can be considered from two different points of view. Firstly through solvent characteristics like vapour pressure, surface tension, volatility [37 of 345], viscosity and alternatively through the quality of solvent, i.e. the solubility of components in solvent, evaporation rate etc. However, in both cases fast evaporation of solvent during the spin coating process causes some instability in the interface. In chapter 6 we will show that this instability which is called a Marangoni instability plays an important role on the final structure in thin films.

Evaporation is an important part of the spin coating process in determining the final thickness as well as producing a uniform coating. The occurrence of several defects such as striation [87, 88] and “chuck marks” [89, 90] has been attributed to the evaporation rate. Daniels et al [88] eliminated the striations by spinning the film in a totally closed chamber in which the evaporation is eliminated. Strawhecker *et al* [91] studied the critical role of solvent evaporation on polymer film roughness. Du et al [92] reported reduction in striations by saturating the atmosphere with solvent vapour during spin coating. Kozuka et al [93] used alcohols with different boiling point to control the striations. According to authors, striations are present even for high boiling point alcohols (low evaporation rate). However striation disappeared during drying. Striations were observed even on a stationary substrate. This suggests that striation formation is independent of spinning [93].

The flow and evaporation behaviour of solvent during the spin coating has been measured mainly by Brinie and Hass [87, 94-96]. To implement different evaporation rates for the system, they employed solvents with different vapour pressures to make films and recorded reflectivity- time data during the spin coating by an optospinogram as shown in figure (2.15). Based on Braggs' law, they made thickness-time curve for different solvents. Figure (2.15) shows the result. Then, they used equation (2.13) and plotted the thinning rate $\left(\frac{dh}{dt}\right)$ as a

function of two times the cube of the film thickness ($2h^3$). The slope and intercept of the graph provides k and e respectively. See figure (2.17). The measured value of evaporation rate for different solvent can be seen in table (2.1).

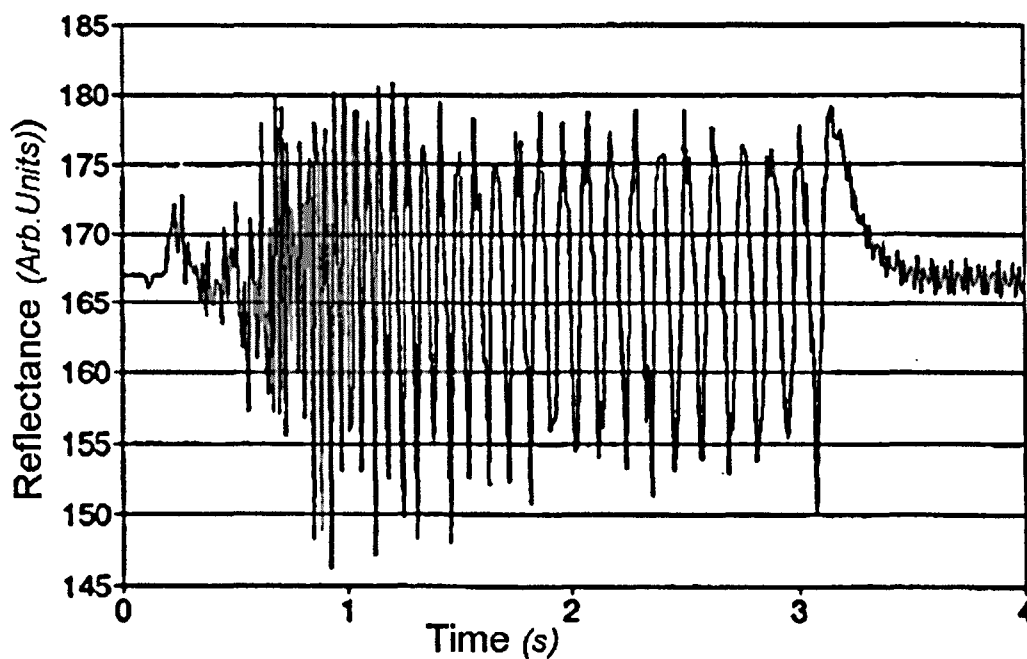


Figure (2.15) Intensity versus time plot for ethanol on silicon at 2000 r.p.m. Taken from Dunbar P. Birnie III and Manuel Manley, 1995 [95].

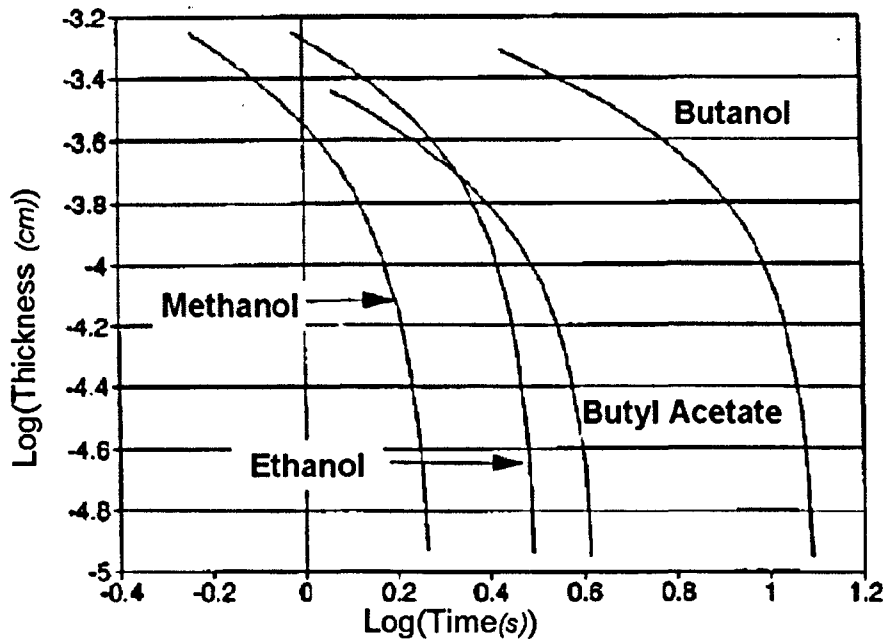
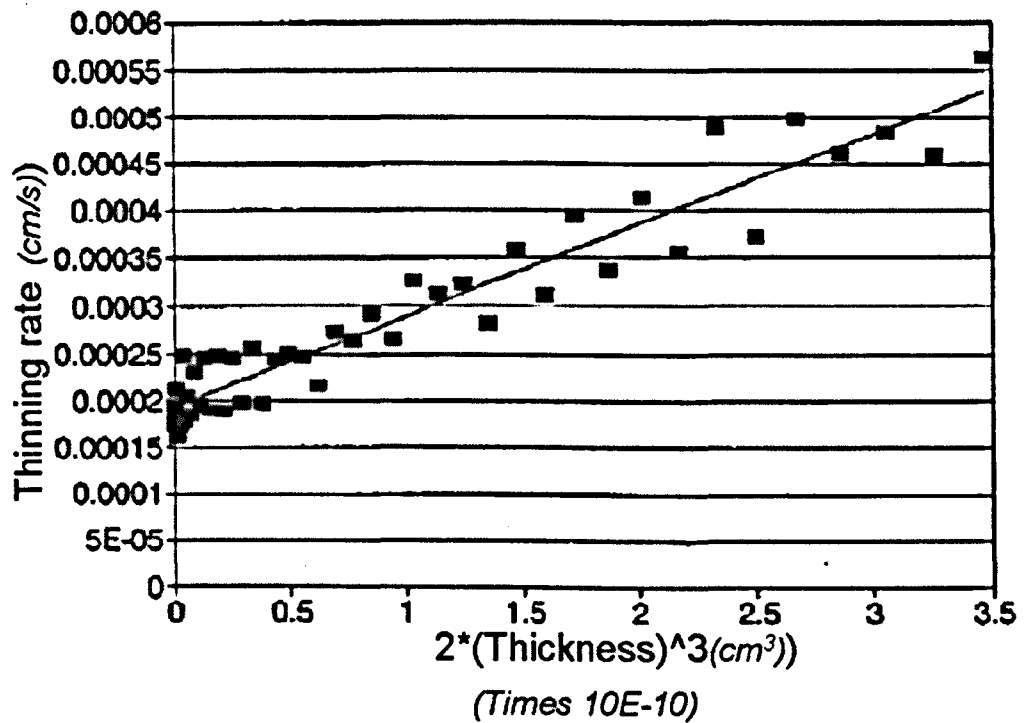


Figure (2.16) Thickness development for several volatile fluids at 2000 r.p.m. Taken from Dunbar P. Birnie III and Manuel Manley, 1995 [95].



Figure(2.17) Plot used for extracting evaporation rate and viscosity of ethanol spin coated at 2000 r.p.m. Taken from Dunbar P. Birnie III and Manuel Manley, 1995 [95].

Controlling the evaporation rate and the vapour environment is also important in post treatment of the samples. Temperature annealing is used in industry to induce mobility in the polymer to provide sufficient flow. However the narrow window between glass transition and the thermal-degradation temperature of most components limits the use of temperature annealing [97, 98]. Solvent annealing is an alternative to temperature annealing. It is also used to create different surface morphologies [99-101]. Nilsson et al [102] studied the effect of several parameters, one of them evaporation rate on phase segregation in polyfluorene/PCBM blends. Their results show that reduced evaporation rate causes a transition from a lateral structure with high roughness to a flat surface. However, there is no physical theory to explain the structure development in their experiment. Also there is no quantitative control of vapour pressure.

Table (2.1) Measured evaporation rate for different solvents as a function of spin speed [95].

Solvent	Spin speed r.p.m	Evaporation rate $\mu\text{m} / \text{s}$
Methanol	2000	3.11
Methanol	2000	3.03
Methanol	2000	3.09
Ethanol	500	0.82
Ethanol	1000	1.23
Ethanol	1500	1.58
Ethanol	1500	1.66
Ethanol	2000	1.94
Ethanol	2500	2.13
Ethanol	3000	2.26
Butyl acetate	2000	0.89
Butyl acetate	2000	0.93
1-Butanol	2000	0.35
1-Butanol	2000	0.35

2.6 Instability in thin films

Understanding the mechanism of film formation is an important part of designing cheap efficient optoelectronic devices. “Nucleation and growth”, spinodal decomposition and finally layering and subsequent instability are the different routes for film formation. I have already introduced the occurrence of layer formation during spin coating. Due to preferential attraction of one component with the substrate, one polymer wets the substrate first and the subsequent layers form afterwards. The interface between the layers becomes unstable and depending on the strength of the instability a laterally phase separated structure can form. In this section we will explain the potential mechanisms that makes the interface unstable and lead to a laterally phase separated structure.

In 2005, Heriot and Jones [47] have shown experimentally that PS/PMMA film goes through layering during spin coating. Hence the final structure is the well known laterally phase separated structure; it implies that at some point the interface between layers must have become unstable and led to a laterally phase separated structure. The question is now what makes the interface unstable? One potential mechanism for the interfacial instability in thin films is the Marangoni instability. In what comes next, I shall review the theory of the Marangoni instability theory and explain how this phenomenon could possibly be responsible for the origin of interfacial instability in spin cast thin films.

2.6.1 Marangoni instability

To understand the Marangoni instability as the major mechanism of interfacial instability in spin cast thin films, first we review the instability in liquid-liquid layers. Then this theory will be extended to spin cast films.

At the turn of the 20th century Henri Benard [103] studied the development of hexagonal patterns in thin layers of fluids that were open to the air and heated from below. See figure (2.18).The formation of the hexagonal cells was

initially attributed to buoyancy forces. Later on Lord Rayleigh [104] confirmed through linear stability analysis that the formation of convective cells is related to buoyancy forces. However, the conditions in his findings do not strictly apply to Benards' set up[105]. It took 50 years for Benards incorrect conclusion to be dismissed. It was shown experimentally by Block[106] and theoretically by Pearson[107] that those convection cells within fluids less than 1 *mm* are not strictly buoyancy driven and but rather are the result of changes in surface tension due to small variations in either temperature or concentration. This convection mechanism is usually named Marangoni convection in recognition of his previous work[105].

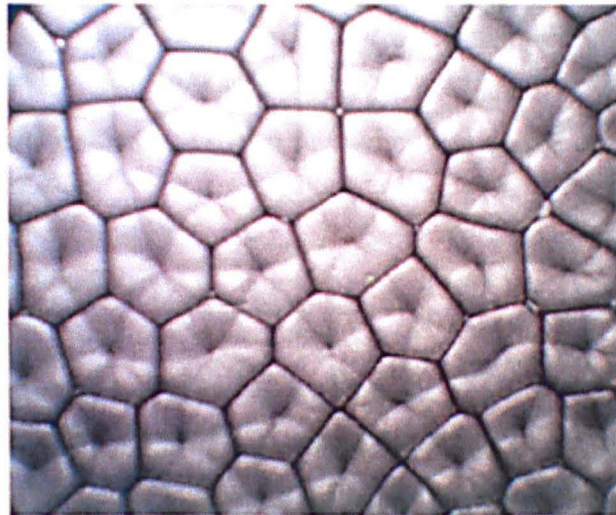


Figure (2.18) Honey-comb like cell pattern observed in Benard convection open to air. J.A Maroto *et al*, 2007 [105].

Surface tension is a function of temperature and concentration. Surface tension is higher in mixtures or at low temperatures. Figure (2.19) shows the effect of temperature on surface tension of selected liquids. The Marangoni effect is created when there is a gradient in surface tension in a solution. During the spin coating, the evaporation of the solvent from a solution can establish either a composition gradient or evaporative cooling; both these are based on a capillary effect. Solvent evaporates faster from the top than the bottom of the solution. Therefore the top of the solution has higher polymer concentration

than the bottom and also because the top of the solution is exposed to air, it is cooler than other regions. That is how the gradient is generated during the spin coating. Figure (2.20) illustrate the effect schematically. To minimise the free energy of the system, high tension regions (higher concentration or lower temperature) draw fluids away from lower tension regions generating a circulation effect and resulting in continuous convection. The convection flows make the air/fluid interface unstable. The magnitude of this instability when the thermocapillary forces are responsible can be expressed in Marangoni number [106-109]:

$$Ma = \frac{-(\partial\gamma/\partial T)H\Delta T}{\mu a} \quad (2.39)$$

$(\partial\gamma/\partial T)$: Temperature derivative of surface tension

ΔT : Temperature difference between the bottom and surface of the liquid

H : Film thickness

μ : Viscosity

a : Thermal diffusivity

For a value of Marangoni number bigger than 80, the film will be unstable [94, 107]. However in this model it is assumed that the temperature gradient is linear through the solution layer-i.e. that is the gradient is $\frac{\Delta T}{H}$. But during the spin coating due to the faster evaporation rate at the top surface, a non-uniform temperature gradient will form. Hass and Birnie [94] considered this transient surface temperature gradient by defining a new parameter, d , that represents the effective thermal penetration depth into the surface. The effects of thermocapillaries upon this development are expressed as follows [94]:

$$Ma = \frac{-(\partial\gamma/\partial T)H^2(\frac{\Delta T}{d})}{\mu a} \quad (2.40)$$

d : The effective thermal penetration depth near the surface

Due to the square dependence of the Marangoni number on the film thickness, it is possible to induce the thermocapillary-driven convection with a sufficiently thick solution layer of high evaporation rate [94]. For thin film, however, the thermocapillary-induced convection is unstable due to its small Marangoni number. Birnie [87] suggested that in thin films the concentration gradient (solutocapillary) has a more effective effect than temperature gradient (thermocapillary). Due to the square dependence of Marangoni number on H in equation (2.40), when the films reach about 10% of their initial thickness during spin coating there will be no practical susceptibility to thermocapillary instability. When the composition gradient is the dominant factor for gradient in surface tension's profile, equation (2.40) can be recast as [87]:

$$Ma = \frac{-(\partial\gamma/\partial C)H^2\nabla C}{\mu D} \quad (2.41)$$

C : Relevant composition variable

D : Diffusion rate of the component driving the composition dependent surface tension change

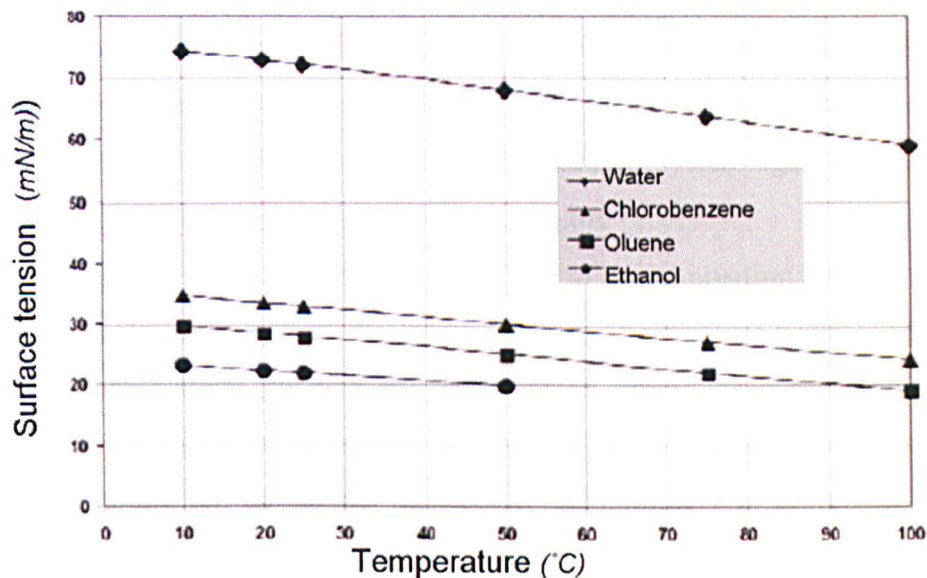


Figure (2.19) The surface tension of selective solvent as a function of temperature. General trend is for surface tension to lower with temperature. Taken from Dunbar P. Birnie III, 2001 [87].

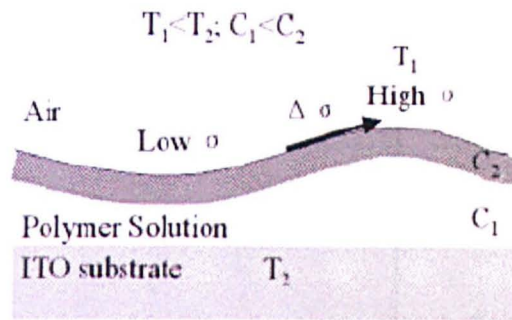


Figure (2.20) The Marangoni convection model (including composition- gradient-driven and temperature-gradient-driven processes) for the spin-coating process. T_1 and C_2 represent the temperature and solution concentration near the surface of the solution layer; T_2 and C_1 represent the temperature and solution concentration near the interface between the solution layer and the ITO substrate. S.C Lue, 2005 [109].

2.6.2 Solvent evaporation rate

Birnie [107] has shown the composition gradient can stabilise and destabilise the structure. Striation formation during spin coating arises as a result of the Marangoni effect, driven by the composition gradient of surface tension in the solution. A favourable solvent for a specific polymer should have a higher surface tension than the polymer itself. Therefore, by removing the solvent (high surface tension component) during spinning, the top surface tension will systematically decrease. This condition stabilises the system against striation as it suppresses the Marangoni instability. See figure (2.21).

Haas and Birnie [110] also studied the effect of radial position and spin speed on striation spacing in “spin- on- glass” coating. The striation wavelength, λ , is independent of radial position and is the same across the entire wafer. This disproves one of the mechanisms in which it is suggested striations are the radial stretching out of cellular patterns formed initially at the centre of the film. In figure (2.22) it is illustrated why stretch out of the cellular patterns can not be the right mechanism for striation formation.

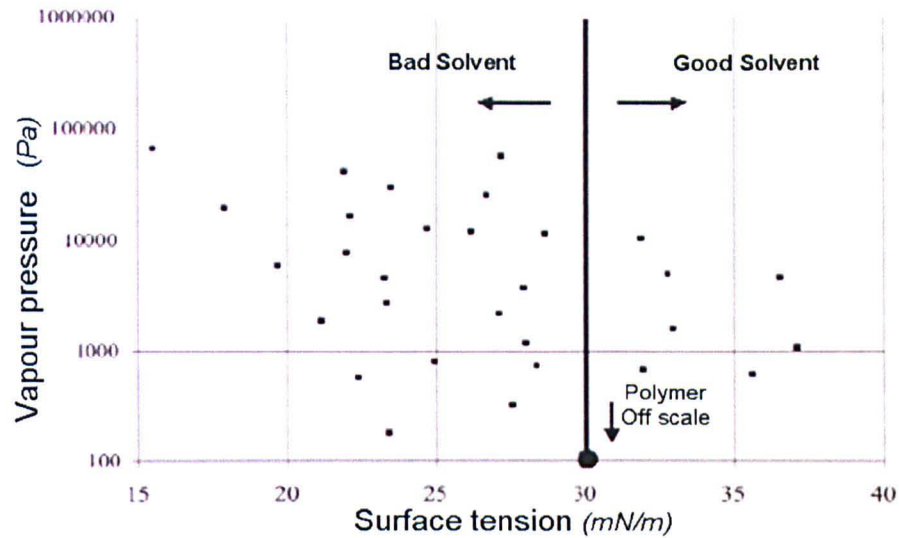


Figure (2.21) Selecting a favourable solvent to avoid striation formation for spin coating for a specific polymer. Favourable solvents will have surface tension higher than that for the solid itself. Evaporation of the solvent with higher surface tension is thermodynamically favourable as it lowers the free energy. Data taken from Dunbar P. Birnie III, 2001 [87].

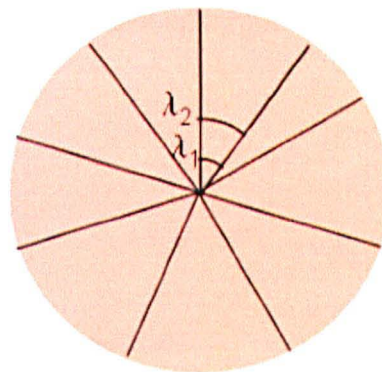


Figure (2.22) If the striations were the result of elongation of cellular pattern, formed initially near the centre of the film, one would expect spacing between lines to increase linearly with the radius. But the fact that λ is the same regardless of the position, rules out this mechanism.

According to the authors, cellular features form simultaneously everywhere on the wafer and are modified to decrease the surface tension at locations where shear field is high as it goes farther from the centre of the substrate, resulting in striations which are aligned with the fluid flow field [110].

The Marangoni effect has been recently studied by Luo [109] through a series of systematic experiments. The effect was studied for five different solvents on PVK film. The results show a strong dependence of film roughness on solvent evaporation rate due to Marangoni instabilities near the surface. Table (2.2) shows the characteristic data for various solvents. THF is a good solvent and toluene is a poor solvent for PVK, but both show a relatively low evaporation rate. According to Luo et al, the final structure of the films made from these two solvents is very smooth with no cell structure or striation near the surface. Roughness vs. evaporation rate data is plotted in figure (2.23). These results indicate that the Marangoni instability is minimal for low evaporation regardless of solubility [109]. When the evaporation rate is low, there is no sharp composition gradient along the film, so there is no Marangoni convection during the casting process. The fact that there is no obvious structure difference between good and bad solvents, suggests that the interaction between polymer chains and the solvent does not have an important role in dynamic instabilities.

Table (2.2) The characteristic data of different solvent [109].

Solvent	v_p (mmHg)	v	μ (D)	η (mPa s)	γ (mN/m)	ρ (g/cm ³)	θ
THF	129	8	1.75	0.456	26.40	0.889	*M
Chloroform	160	11.6	1.04	0.537	26.67	1.492	0.8
Benzene	75	5.1	0	0.604	28.88	0.874	0.18
Toluene	2	2.24	0.37	0.560	27.93	0.865	0.05
TCE	8	0.65	1.32	1.437	35.58	1.586	0.3

v_p , vapour pressure; v , relative evaporation rate (BuAc=1); μ , electric dipole moment; η , viscosity; γ , surface tension; ρ , density; θ , solubility (grams/100 g of water), *M, miscible.

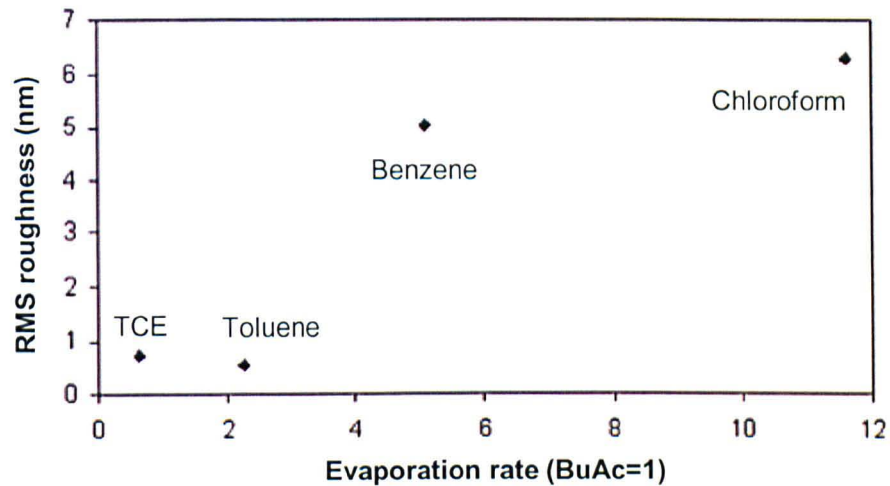


Figure (2.23) RMS roughness plotted as a function of evaporation rate of four solvents. Higher vapour pressure increases the roughness. Data taken from S.C Lue, 2005 [109].

Walheim et al [64] proposed a mechanism for undulation in (PS/PMMA) surface as a function of solvent quality and solubility of the component in it. Strawhecker et al [91] studied the evaporation rate in (PS/ PEMA) system.

They considered both volatility and film levelling. Films created by more volatile solvents are rougher due to flow instabilities and very long viscoelastic relaxation times for levelling [91]. In other words, they conclude that the roughness of the film is dictated by solvent evaporation rate and for slow evaporating solvent (with vapour pressure <0.1 bar) there is no Marangoni instability.

2.6.3 The effect of other parameters on film structure

Although spin casting is a simple process to produce immiscible polymer films, a deep understanding of the process of film formation, particularly thin films is not yet available. Up to twenty years ago phase separation in thin films was considered the same as that in the bulk. The reasons for this deficiency could be firstly related to technological limitations hampering the study of film formation as it happens. Secondly, many parameters such as spin speed, evaporation rate, temperature, substrate chemistry, solvent nature, blend chemistry such as polymerization and concentration, film thickness etc can have significant effects on the film and some of them are not easy to control. However, many of these factors have been studied. In the next part some of these parameters will be discussed.

2.6.3.1 The effect of molecular weight on surface energy

In general, in thin films most studies revealed that the lower surface free energy component is enriched at the air-polymer interface in order to minimize the magnitude of interfacial free energy [111]. Surface energy depends on many parameters such as polymer molecular weight (equation (2.42)). However, the dependence of surface enrichment on molecular weight and then surface energy is not always straightforward. Some anomalous behaviour has

been reported [111, 112] where the component with higher surface energy preferentially segregates to the air-polymer interface.

$$E = A - \frac{k}{M_w^{2/3}} \quad (2.42)$$

A & k : Constant

The surface chemical composition of polymer blends has been also extensively investigated in the past decades, both experimentally [111, 112] and theoretically [27]. Geoghegan et al [113] reported the effect of molecular weight on the morphology of as-cast (PS/PB) films. They showed that self stratified structure can be obtained by changing the molecular weight of the component and surface enrichment is dependent on the molecular weight. Tanaka et al [111] reported an anomalous behaviour for high molecular weight Polystyrene (PS) and low molecular weight Poly(methyl methacrylate) (PMMA), where the latter preferentially segregates at the air-polymer interface even though it has a higher surface energy. Hariharan's [112] numerical results also confirmed that the surface can be covered by lower molecular weight component. This is mainly due to the entropic penalty associated with the longer polymer chain at the surface. In other words, there is a compromise between end group surface tension and main part surface tension.

The behaviour of a spun cast (PS/PMMA) blend as a function of molecular weight in the range of 20K-100K has been studied in detail [64, 114, 115]. In 2003, Li et al [73] systematically studied the effect the surface morphologies and thermal stabilities of PS/PMMA blend film as a function of molecular weight of PS, varied from 2.9-129 K. Three different kinds of morphologies were detected in the range and the dependency of surface morphology on molecular weight was confirmed.

2.6.3.2 The effect of film thickness on the structure

Polymer dewetting of thin polymer film on a silicon substrate as a function of film thickness was studied previously [116]. Polymer films with thickness less than twice the gyration of an unperturbed chain, $2R_g$, are defined as two dimensional ultrathin films [117, 118]. The polymeric blend films with thicknesses less than $2R_g$ of the higher molecular weight component can be defined as two-dimensional ultrathin blend films [119] (figure (2.24)). It has been shown that the surface structure of multicomponent polymer systems like (PS/PMMA) is fairly different from that in the bulk. That is, a lower surface free energy component is generally enriched in the surface region in order to minimize the air-polymer interfacial free energy. Since polymeric chains at the interface, in general, are thermally unstable, the molecular aggregation structure in the two-dimensional ultrathin film of a binary polymer blend is different from that in the thick film. Tanaka et al [75] studied the (PS/PVMA) system. Although the blend was miscible in the bulk, in the ultra thin films, phase separation happened below the bulk phase separation temperature. According to the authors the negative spreading coefficient of PVME on the PS matrix and the remarkably reduced conformational entropy of a PVME chain due to stretching could be the potential cause for the occurrence. In another experiment [117] they showed that the surface structure of (PS/PMMA) film depends on film thickness. They attributed the formation of the surface structure to the possible chain conformation freezing, due to fast evaporation of the solvent. They conclude that the formation of the surface structure of (PS/PMMA) can be explained by the film thickness dependence of both the Flory-Huggins interaction parameters and the degree of entanglement among polymer chains.

Akpalu et al [50] investigated the suppression of lateral phase separation in thin polyolefin blends as a function of film thickness and temperature.

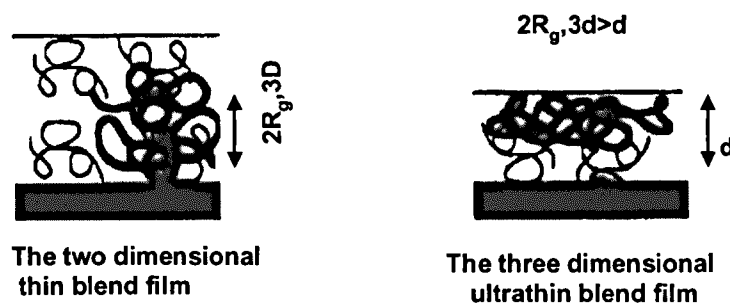


Figure (2.24) Schematic representation of the conformation of polymer chains in the thin film and the two-dimensional ultra-thin blend film. The image on the right hand side shows a polymeric films where thicknesses (d) are less than twice the radius of gyration of an unperturbed chain ($2R_g$). This is defined as two-dimensional ultrathin films. The polymeric blend films with thicknesses less than the dimension of $2R_g$, of the longest component can be defined as two-dimensional ultrathin blend films. K. Tanaka *et al*, 1995 [119].

2.7 Summary

So far, I have reviewed the thermodynamics of polymer blends in binary and ternary systems. Dissolving polymers in a common solvent favours the mixing as it lowers the enthalpic cost to free energy of the mixing. Thin polymer films can be made by spin casting polymer blends. The morphology of the film depends on many parameters. To control the morphology it is essential to understand the mechanism of film formation. Knowing that, we should be able to design tailored structures for specific applications. Despite intensive studies on spin cast thin polymer films, there is no general theory to explain the mechanism of film formation. This is due to the fact that film formation is a non equilibrium process and the proper way of studying the system is monitoring film characteristics during film formation (not afterwards). Unfortunately, the technology is not advanced enough for in-situ study of the non-equilibrium process of spin coating films.

However, in my project I have used a home made device in Sheffield called the Optospinometer which is based on small angle light scattering to probe the film formation during spin coating. Heriot and Jones [47] have shown during spin coating, first a transient wetting layer forms and is followed by an interfacial instability which leads to lateral phase separation.

The work presented in this thesis concentrates on the origin of the interfacial instability. For instance what makes the film unstable? The answer to this question is important because the formation of self stratified structure or lateral phase separation depends on this instability.

We have considered the Marangoni instability as a potential mechanism for interfacial instability. We have tested our hypothesis by controlling the evaporation rate during spin coating. The idea was that changing the evaporation rate can change the concentration gradient in the film which in turn is the driving force for the Marangoni instability. The question was then how to control the evaporation rate during spin casting? This was achieved by controlling the environmental conditions. To do that, we have designed and made an environmental cell mounted on the optospinometer. This experimental set up enables us to change the vapour pressure of the gas in the chamber while spin casting is in progress. Higher vapour pressure in the cell decreases the evaporation rate from the film. Lower evaporation rate will suppress the Marangoni instability and therefore a layered structure is expected to form. Higher evaporation rate will trigger the Marangoni instability and lead to lateral phase separation. In what follows I will briefly describe the content of each chapter.

Chapter 3

In chapter 3, I explain the experimental set up and different methods used to study the films made by spin casting, such as small angle light scattering, atomic force microscopy, optical microscopy, fluorescence microscopy etc. I will explain how the Fresnel equations have been used to model the reflectivity data and for plotting the thickness-time profile.

Chapter 4

In chapter 4, I will explain how I tuned my experimental set up. The first part of the chapter explains how the optics of the optospinometer have been modified. The second part is about controlling the vapour pressure inside the environmental cell. A series of swelling experiments were carried out by exposing the polystyrene films to toluene vapour at different vapour concentrations and rates. During the exposure, the reflectivity data was obtained by the optospinometer. The swelling behaviour was modelled using Fresnel's equations. The purpose of the experiments was to monitor stability of the gas flow in the cell and also controlling the concentration of the toluene vapour by changing the temperature of the gas or mixing it with nitrogen.

Chapter 5

In this chapter, I will describe how to change the evaporation rate during spin coating systematically by casting the film inside the environmental cell. Then I will explain how I extracted the value of evaporation rate for toluene by solving Meyerhofer's thinning rate equation during spin coating.

Chapter 6

Knowing the value of evaporation rate and how to control it, we applied it on PS/PMMA spin cast films to test the Marangoni instability. PS/PMMA films were made in the environmental cell at different vapour pressures and different evaporation rates. The hypothesis was that the higher evaporation rate causes a steep concentration gradient in the film. Therefore the interface will roughen to decrease the interfacial energy. This is a Marangoni instability. Conversely, slower evaporation rates will suppress the concentration gradient near the surface and therefore the Marangoni instability is driven by the concentration slope won't be strong enough to break to the surface of the film. As a result, a self stratified structure forms. The films made with different evaporation rates have different morphologies. The films were washed with selective solvents to

see if layering happens. The result confirms slow evaporation rates can create self stratified structure.

Chapter 7

In chapter 7, a new system composed of semiconducting polymers (F8BT/PFB) is studied. This blend is a potential material for active layer in photovoltaics. The efficiency of the device is strongly related to the morphology of the film. The ideal structure should provide enough interfaces to create excitons but it should supply a short and direct route for the charges to reach the electrodes. Using our experimental set up, we could produce variety of morphologies just by changing the evaporation rate in the environmental cell during the spin coating. The semiconducting blend films were first made on silicon substrates at different evaporation rates. They were characterised by optical microscopy, fluorescence microscopy and atomic force microscopy.

As a preliminary attempt, we made a real photovoltaic device by spin casting the active layer on ITO substrate. The devices were characterised by means of different methods. The data are presented as preliminary results. However, we achieved our goal to produce films with different morphologies and different efficiencies, but more experiments need to be done to properly characterise the devices and discuss the physics behind it.

Chapter 8

In conclusions and suggestion for future work.

2.8 Bibliography

1. Indrakanti, A., *Interplay between kinetics and apparent thermodynamics in thin polymer blend films*, in *Chemical Engineering*. 2004, The Pennsylvania State University: Pennsylvania p. 359.
2. Michael Rubinstein, R.H.C., *Polymer Physics*. 2006, New York: Oxford University Press.
3. Flory, P.J., *Principles of Polymer Chemistry*. 1953, Ithaca, NY: Cornell University Press.
4. Petri, H.M., N. Schuld, and B.A. Wolf, *Hitherto Ignored Effects of Chain-Length on the Flory-Huggins Interaction Parameters in Concentrated Polymer-Solutions*. *Macromolecules*, 1995. **28**(14): p. 4975-4980.
5. Petri, H.M. and B.A. Wolf, *Concentration-Dependent Thermodynamic Interaction Parameters for Polymer-Solutions - Quick and Reliable Determination Via Normal Gas-Chromatography*. *Macromolecules*, 1994. **27**(10): p. 2714-2718.
6. Schneider, A., et al., *On what terms and why the thermodynamic properties of polymer solutions depend on chain length up to the melt*. *Journal of Polymer Science Part B-Polymer Physics*, 2004. **42**(9): p. 1601-1609.
7. Schneider, A., M. Wunsch, and B.A. Wolf, *An apparatus for automated turbidity titrations and its application to copolymer analysis and to the determination of phase diagrams*. *Macromolecular Chemistry and Physics*, 2002. **203**(4): p. 705-711.
8. Huggins, M.L., *Theory of polymer fractionation efficiency*. *Journal of Polymer Science Part A-2: Polymer Physics*, 1967. **5**(6): p. 1221-1234.
9. Scott, R.L., *The Thermodynamics of High Polymer Solutions. V. Phase Equilibria in the Ternary System: Polymer 1---Polymer 2---Solvent*. *The Journal of Chemical Physics*, 1949. **17**(3): p. 279-284.
10. Hashimoto, T., K. Sasaki, and H. Kawai, *Time-resolved light scattering studies on the kinetics of phase separation and phase dissolution of*

- polymer blends. 2. Phase separation of ternary mixtures of polymer A, polymer B, and solvent.* *Macromolecules*, 1984. **17**(12): p. 2812-2818.
11. Hashimoto, T., *Dynamics in Spinodal Decomposition of Polymer Mixtures.* *Phase Transitions*, 1988. **12**(1): p. 47-119.
 12. Cahn, J.W. and J.E. Hilliard, *Free Energy of a Nonuniform System .I. Interfacial Free Energy.* *Journal of Chemical Physics*, 1958. **28**(2): p. 258-267.
 13. M. V. Ariyapadi, E.B.N., *Free energy of an inhomogeneous polymer-polymer-solvent system.* *Journal of Polymer Science Part B: Polymer Physics*, 1989. **27**(13): p. 2637-2646.
 14. de Gennes, P.G., *Reptation of a Polymer Chain in the Presence of Fixed Obstacles.* *The Journal of Chemical Physics*, 1971. **55**(2): p. 572-579.
 15. Debye, P., *Angular Dissymmetry of the Critical Opalescence in Liquid Mixtures.* *Journal of Chemical Physics*, 1959. **31**(3): p. 680-687.
 16. McMaster, L.P., *Aspects of Liquid-Liquid Phase-Transition Phenomena in Multicomponent Polymeric Systems.* *Advances in Chemistry Series*, 1975(142): p. 43-65.
 17. Nauman, E.B., et al., *Compositional Quenching - a Process for Forming Polymer-in-Polymer Microdispersions and Cocontinuous Networks.* *Chemical Engineering Communications*, 1988. **66**: p. 29-55.
 18. Balsara, N.P. and E.B. Nauman, *Spinodal Decomposition in Polymer-Polymer-Solvent Systems Induced by Continuous Solvent Removal.* *Abstracts of Papers of the American Chemical Society*, 1987. **194**: p. 133-PMSE.
 19. Ariyapadi, M.V. and E.B. Nauman, *Free-Energy of an Inhomogeneous Polymer Polymer Solvent System .2.* *Journal of Polymer Science Part B-Polymer Physics*, 1992. **30**(6): p. 533-538.
 20. Jones, R.A.L., *Interfacial aspects of semi-conduction polymer devices: chapter 2*, in *Semiconductin polymers:Chemistry, Physics and Engineering*, G.Hadziianou and M.G. G., Editors. 2006, Wiley-VCH.
 21. Jones, R.A.L.a.R., Randal W, *Polymers at Surfaces and Interfaces.* 1999, UK: Cambridge University Press.
 22. Jones, R., *Interfacial aspects of semi-conduction polymer devices. ???, ???: ???*

23. Dobry, A. and F. Boyerkawenoki, *Phase Separation in Polymer Solution*. Journal of Polymer Science, 1947. **2**(1): p. 90-100.
24. Geveke, D.J. and R.P. Danner, *Ternary Phase-Equilibria of Polystyrene with a 2nd Polymer and a Solvent*. Journal of Applied Polymer Science, 1993. **47**(4): p. 565-575.
25. Wayne W. Y. Lau, C.M.B.R.Y.M.H., *Compatibility of polystyrene and poly(methyl methacrylate) of various molecular weights in toluene*. Journal of Applied Polymer Science, 1984. **29**(5): p. 1531-1536.
26. Bates, F.S. and P. Wiltzius, *Spinodal Decomposition of a Symmetric Critical Mixture of Deuterated and Protonated Polymer*. Journal of Chemical Physics, 1989. **91**(5): p. 3258-3274.
27. Jones, R.A.L., et al., *Surface-Directed Spinodal Decomposition*. Physical Review Letters, 1991. **66**(10): p. 1326-1329.
28. Bonn, D. and D. Ross, *Wetting transitions*. Reports on Progress in Physics, 2001. **64**(9): p. 1085-1163.
29. Shahidzadeh, N., et al., *Sequence of two wetting transitions induced by tuning the Hamaker constant*. Physical Review Letters, 1998. **80**(18): p. 3992-3995.
30. Ross, D., D. Bonn, and J. Meunier, *Observation of short-range critical wetting*. Nature, 1999. **400**(6746): p. 737-739.
31. Genzer, J. and E.J. Kramer, *Pretransitional thinning of a polymer wetting layer*. Europhysics Letters, 1998. **44**(2): p. 180-185.
32. Geoghegan, M. and G. Krausch, *Wetting at polymer surfaces and interfaces*. Progress in Polymer Science, 2003. **28**(2): p. 261-302.
33. Muller-Buschbaum, P., *Dewetting and pattern formation in thin polymer films as investigated in real and reciprocal space*. Journal of Physics-Condensed Matter, 2003. **15**(36): p. R1549-R1582.
34. Wang, C., G. Krausch, and M. Geoghegan, *Dewetting at a polymer-polymer interface: Film thickness dependence*. Langmuir, 2001. **17**(20): p. 6269-6274.
35. Lambooy, P., et al., *Dewetting at the liquid-liquid interface*. Physical Review Letters, 1996. **76**(7): p. 1110-1113.
36. Qu, S., et al., *Dewetting dynamics at a polymer-polymer interface*. Macromolecules, 1997. **30**(12): p. 3640-3645.

37. Muller-Buschbaum, P., J.S. Gutmann, and M. Stamm, *Dewetting of confined polymer films: an X-ray and neutron scattering study*. Physical Chemistry Chemical Physics, 1999. **1**(17): p. 3857-3863.
38. Muller-Buschbaum, P., et al., *Dewetting of thin polymer-blend films examined with GISAS*. Physica B-Condensed Matter, 2000. **283**(1-3): p. 53-59.
39. Puri, S. and K. Binder, *Wetting and phase separation at surfaces*. Pramana-Journal of Physics, 2005. **64**(6): p. 881-892.
40. Wang, H. and R.J. Composto, *Wetting and phase separation in polymer blend films: Identification of four thickness regimes with distinct morphological pathways*. Interface Science, 2003. **11**(2): p. 237-248.
41. Geoghegan, M., et al., *Wetting in a phase separating polymer blend film: Quench depth dependence*. Physical Review E, 2000. **62**(1): p. 940-950.
42. Genzer, J. and E.J. Kramer, *Wetting of substrates with phase-separated binary polymer mixtures*. Physical Review Letters, 1997. **78**(26): p. 4946-4949.
43. Rysz, J., et al., *Wetting transition in a binary polymer blend*. Europhysics Letters, 2000. **50**(1): p. 35-40.
44. Rysz, J., et al., *Wetting transition in polyolefin blends studied by profiling techniques*. Macromolecular Symposia, 2000. **149**: p. 277-281.
45. Krausch, G., *Surface-Induced Self-Assembly in Thin Polymer-Films*. Materials Science & Engineering R-Reports, 1995. **14**(1-2): p. 1-94.
46. Bruder, F. and R. Brenn, *Spinodal Decomposition in Thin-Films of a Polymer Blend*. Physical Review Letters, 1992. **69**(4): p. 624-627.
47. Heriot, S.Y. and R.A.L. Jones, *An interfacial instability in a transient wetting layer leads to lateral phase separation in thin spin-cast polymer-blend films*. Nature Materials, 2005. **4**(10): p. 782-786.
48. Budkowski, A., et al., *Surface-directed phase separation in nanometer polymer films: self-stratification and pattern replication*. E-Polymers, 2002.
49. Geoghegan, M., R.A.L. Jones, and A.S. Clough, *Surface Directed Spinodal Decomposition in a Partially Miscible Polymer Blend*. Journal of Chemical Physics, 1995. **103**(7): p. 2719-2724.

50. Akpalu, Y.A., et al., *Suppression of lateral phase separation in thin polyolefin blend films*. *Macromolecules*, 2001. **34**(6): p. 1720-1729.
51. Krausch, G., et al., *Real-Space Observation of Dynamic Scaling in a Critical Polymer Mixture*. *Physical Review Letters*, 1993. **71**(22): p. 3669-3672.
52. Krausch, G., et al., *Interference of Spinodal Waves in Thin Polymer-Films*. *Macromolecules*, 1993. **26**(21): p. 5566-5571.
53. Bikson, B., J.K. Nelson, and N. Muruganandam, *Composite Cellulose-Acetate Poly(Methyl Methacrylate) Blend Gas Separation Membranes*. *Journal of Membrane Science*, 1994. **94**: p. 313-328.
54. Halls, J.J.M., et al., *Efficient Photodiodes from Interpenetrating Polymer Networks*. *Nature*, 1995. **376**(6540): p. 498-500.
55. Walheim, S., et al., *Nanophase-separated polymer films as high-performance antireflection coatings*. *Science*, 1999. **283**(5401): p. 520-522.
56. Sirringhaus, H., et al., *High-resolution inkjet printing of all-polymer transistor circuits*. *Science*, 2000. **290**(5499): p. 2123-2126.
57. Reich, S. and Y. Cohen, *Phase-Separation of Polymer Blends in Thin-Films*. *Journal of Polymer Science Part B-Polymer Physics*, 1981. **19**(8): p. 1255-1267.
58. Ball, R.C. and R.L.H. Essery, *Spinodal Decomposition and Pattern-Formation near Surfaces*. *Journal of Physics-Condensed Matter*, 1990. **2**(51): p. 10303-10320.
59. Puri, S. and K. Binder, *Surface-Directed Spinodal Decomposition - Phenomenology and Numerical Results*. *Physical Review A*, 1992. **46**(8): p. R4487-R4489.
60. Binder, K. and H.L. Frisch, *Dynamics of Surface Enrichment - a Theory Based on the Kawasaki Spin-Exchange Model in the Presence of a Wall*. *Zeitschrift Fur Physik B-Condensed Matter*, 1991. **84**(3): p. 403-418.
61. Puri, S. and H.L. Frisch, *Surface-directed spinodal decomposition: Modelling and numerical simulations*. *Journal of Physics-Condensed Matter*, 1997. **9**(10): p. 2109-2133.
62. Binder, K., *Spinodal decomposition in confined geometry*. *Journal of Non-Equilibrium Thermodynamics*, 1998. **23**(1): p. 1-44.

63. Geoghegan, M., et al., *Lamellar Structure in a Thin Polymer Blend Film*. *Polymer*, 1994. **35**(10): p. 2019-2027.
64. Walheim, S., et al., *Structure formation via polymer demixing in spin-cast films*. *Macromolecules*, 1997. **30**(17): p. 4995-5003.
65. Puri, S. and K. Binder, *Power laws and crossovers in off-critical surface-directed spinodal decomposition*. *Physical Review Letters*, 2001. **86**(9): p. 1797-1800.
66. Bastea, S., S. Puri, and J.L. Lebowitz, *Surface-directed spinodal decomposition in binary fluid mixtures*. *Physical Review E*, 2001. **63**04(4).
67. Puri, S.J., *Surface-directed spinodal decomposition*. *Journal of Physics-Condensed Matter*, 2005. **17**(3): p. R101-R142.
68. Puri, S. and K. Binder, *Surface-Directed Spinodal Decomposition in a Thin-Film Geometry - a Computer-Simulation*. *Journal of Statistical Physics*, 1994. **77**(1-2): p. 145-172.
69. Bollinne, C., et al., *AFM study of capillary wave fluctuations on and spinodal dewetting of thin polymer films*. *Abstracts of Papers of the American Chemical Society*, 2002. **224**: p. U409-U410.
70. Jukes, P.C., et al., *Time-resolved light scattering studies of phase separation in thin film semiconducting polymer blends during spin-coating*. *Macromolecules*, 2005. **38**(6): p. 2030-2032.
71. Prosycevas, I., S. Tamulevicius, and A. Guobiene, *The surface properties of PS/PMMA blends nanostructured polymeric layers*. *Thin Solid Films*, 2004. **453-54**: p. 304-311.
72. Dekeyser, C.M., et al., *Submicrometer-scale heterogeneous surfaces by PS-PMMA demixing*. *Polymer*, 2004. **45**(7): p. 2211-2219.
73. Li, X., Y.C. Han, and L.J. An, *Surface morphology control of immiscible polymer-blend thin films*. *Polymer*, 2003. **44**(26): p. 8155-8165.
74. Raczkowska, J., et al., *Surface patterns in solvent-cast polymer blend films analyzed with an integral-geometry approach*. *Macromolecules*, 2003. **36**(7): p. 2419-2427.
75. Ton-That, C., A.G. Shard, and R.H. Bradley, *Surface feature size of spin cast PS/PMMA blends*. *Polymer*, 2002. **43**(18): p. 4973-4977.

76. Ade, H., et al., *Phase segregation in polymer thin films: Elucidations by X-ray and scanning force microscopy*. Europhysics Letters, 1999. **45**(4): p. 526-532.
77. Ton-That, C., et al., *XPS and AFM surface studies of solvent-cast PS/PMMA blends*. Polymer, 2001. **42**(3): p. 1121-1129.
78. Walheim, S., M. Ramstein, and U. Steiner, *Morphologies in ternary polymer blends after spin-coating*. Langmuir, 1999. **15**(14): p. 4828-4836.
79. Takahara, A., et al., *Surface aggregation structure and surface mechanical properties of binary polymer blend thin films*. Macromolecular Symposia, 2000. **159**: p. 89-96.
80. Emslie, A.G., F.T. Bonner, and L.G. Peck, *Flow of a Viscous Liquid on a Rotating Disk*. Journal of Applied Physics, 1958. **29**(5): p. 858-862.
81. Schubert, D.W. and T. Dunkel, *Spin coating from a molecular point of view: its concentration regimes, influence of molar mass and distribution*. Materials Research Innovations, 2003. **7**(5): p. 314-321.
82. Meyerhofer, D., *Characteristics of Resist Films Produced by Spinning*. Journal of Applied Physics, 1978. **49**(7): p. 3993-3997.
83. Bornside, D.E., C.W. Macosko, and L.E. Scriven, *On the Modeling of Spin Coating*. Journal of Imaging Technology, 1987. **13**(4): p. 122-130.
84. Bornside, D.E., C.W. Macosko, and L.E. Scriven, *Spin Coating - One-Dimensional Model*. Journal of Applied Physics, 1989. **66**(11): p. 5185-5193.
85. Flack, W.W., et al., *A Mathematical-Model for Spin Coating of Polymer Resists*. Journal of Applied Physics, 1984. **56**(4): p. 1199-1206.
86. Lawrence, C.J., *The Mechanics of Spin Coating of Polymer-Films*. Physics of Fluids, 1988. **31**(10): p. 2786-2795.
87. Birnie, D., *Rational solvent selection strategies to combat striation formation during spin coating of thin films* J MATER RES 2001. **16**(4): p. 1145-1154
88. Daniels, B.K., et al. *Surface tension effects in microlithography—striations*. in *Advances in Resist Technology and Processing III, Proc.SPIE 631*. 1986.

89. Birnie, D.P., et al., *Film Substrate Vacuum-Chuck Interactions During Spin-Coating*. Optical Engineering, 1992. **31**(9): p. 2012-2020.
90. Birnie, D.P., B.J.J. Zelinski, and D.L. Perry, *Infrared Observation of Evaporative Cooling During Spin-Coating Processes*. Optical Engineering, 1995. **34**(6): p. 1782-1788.
91. Strawhecker, K.E., et al., *The critical role of solvent evaporation on the roughness of spin-cast polymer films*. Macromolecules, 2001. **34**(14): p. 4669-4672.
92. Du, X.M., X. Orignac, and R.M. Almeida, *Striation-Free, Spin-Coated Sol-Gel Optical Films*. Journal of the American Ceramic Society, 1995. **78**(8): p. 2254-2256.
93. Kozuka, H., Y. Ishikawa, and N. Ashibe, *Radiative striations of spin-coating films: Surface roughness measurement and in-situ observation*. Journal of Sol-Gel Science and Technology, 2004. **31**(1-3): p. 245-248.
94. Haas, D.E. and D.P. Birnie, *Evaluation of thermocapillary driving forces in the development of striations during the spin coating process*. Journal of Materials Science, 2002. **37**(10): p. 2109-2116.
95. Birnie, D.P. and M. Manley, *Combined flow and evaporation of fluid on a spinning disk*. Physics of Fluids, 1997. **9**(4): p. 870-875.
96. Birnie, D.P., *Combined flow and evaporation during spin coating of complex solutions*. Journal of Non-Crystalline Solids, 1997. **218**: p. 174-178.
97. Elbs, H. and G. Krausch, *Ellipsometric determination of Flory-Huggins interaction parameters in solution*. Polymer, 2004. **45**(23): p. 7935-7942.
98. Voicu, N.E., et al., *Solvent-vapor-assisted imprint lithography*. Advanced Materials, 2007. **19**(5): p. 757-+.
99. Elbs, H., et al., *Microdomain morphology of thin ABC triblock copolymer films*. Macromolecules, 1999. **32**(4): p. 1204-1211.
100. Buxton, G.A. and N. Clarke, *Ordering polymer blend morphologies via solvent evaporation*. Epl, 2007. **78**(5).
101. Elbs, H., et al., *Thin film morphologies of ABC triblock copolymers prepared from solution*. Macromolecules, 2002. **35**(14): p. 5570-5577.

102. Nilsson, S., et al., *Morphology and phase segregation of spin-casted films of Polyfluorene/PCBM blends*. *Macromolecules*, 2007. **40**: p. 8291-8301.
103. Benard, H., *Experimental studies on the movement of liquids propagated by heat by means of convection. Permanent system : Cellular turbulence*. *Comptes Rendus Hebdomadaires Des Seances De L Academie Des Sciences*, 1900. **130**: p. 1004-1007.
104. Rayleigh, L., *On convection currents in a horizontal layer of fluid, when the higher temperature is on the under side*. *Philosophical Magazine*, 1916. **32**(187-92): p. 529-546.
105. Maroto, J.A., V. Perez-Munuzuri, and M.S. Romero-Cano, *Introductory analysis of Benard-Marangoni convection*. *European Journal of Physics*, 2007. **28**(2): p. 311-320.
106. Block, M.J., *Surface Tension as the Cause of Benard Cells and Surface Deformation in a Liquid Film*. *Nature*, 1956. **178**(4534): p. 650-651.
107. Pearson, J.R.A., *On Convection Cells Induced by Surface Tension*. *Journal of Fluid Mechanics*, 1958. **4**(5): p. 489-500.
108. Pearson, J.R.A., *On convection cells induced by surface tension*. *Journal of Fluid Mechanics Digital Archive*, 2006. **4**(05): p. 489-500.
109. Luo, S.C., V. Craciun, and E.P. Douglas, *Instabilities during the formation of electroactive polymer thin films*. *Langmuir*, 2005. **21**(7): p. 2881-2886.
110. Haas, D.E., et al., *The effect of radial position and spin speed on striation spacing in spin on glass coatings*. *Journal of Materials Science Letters*, 2001. **20**(19): p. 1763-1766.
111. Tanaka, K., A. Takahara, and T. Kajiyama, *Surface molecular aggregation structure and surface molecular motions of high-molecular-weight polystyrene low-molecular-weight poly(methyl methacrylate) blend films*. *Macromolecules*, 1998. **31**(3): p. 863-869.
112. Hariharan, A., S.K. Kumar, and T.P. Russell, *A Lattice Model for the Surface Segregation of Polymer-Chains Due to Molecular-Weight Effects*. *Macromolecules*, 1990. **23**(15): p. 3584-3592.
113. Geoghegan, M., et al., *The Morphology of as-Cast Films of a Polymer Blend - Dependence on Polymer Molecular-Weight*. *Journal of Polymer Science Part B-Polymer Physics*, 1995. **33**(8): p. 1307-1311.

114. Ton-That, C., et al., *Effects of annealing on the surface composition and morphology of PS/PMMA blend*. *Macromolecules*, 2000. **33**(22): p. 8453-8459.
115. Harris, M., G. Appel, and H. Ade, *Surface morphology of annealed polystyrene and poly(methyl methacrylate) thin film blends and bilayers*. *Macromolecules*, 2003. **36**(9): p. 3307-3314.
116. Xie, R., et al., *Spinodal dewetting of thin polymer films*. *Physical Review Letters*, 1998. **81**(6): p. 1251-1254.
117. Tanaka, K., A. Takahara, and T. Kajiyama, *Film thickness dependence of the surface structure of immiscible polystyrene/poly(methyl methacrylate) blends*. *Macromolecules*, 1996. **29**(9): p. 3232-3239.
118. Shuto, K., et al., *Molecular Aggregation Structure and Surface Morphology of 2-Dimensional Ultra Thin Film Prepared by Water Casting Method*, in *Advanced Materials '93, Ii - a & B - a: Biomaterials, Organic and Intelligent Materials; B: Information Storage Materials*, H. Aoki, et al., Editors. 1994. p. 615-618.
119. Tanaka, K., et al., *Ultrathinning-Induced Surface Phase-Separation of Polystyrene Poly(Vinyl Methyl-Ether) Blend Film*. *Macromolecules*, 1995. **28**(4): p. 934-938.

Chapter 3

Experimental Techniques

To study the mechanism of film formation during spin coating we have used various techniques.

A Small angle light scattering device integrated with a spin coater was used to collect information during the film formation.

To study the source of interfacial instability, we designed and made an environmental cell that can be mounted on the spin coat chuck. Inside the cell, the vapour pressure of the inserting gas can be controlled. In this chapter the experimental set up will be explained in detail.

Atomic force microscopy (AFM), fluorescence and optical microscopy have been used to study the topography and structure of the films.

3.1 Small angle light scattering

Small angle scattering (SAS) is the collective name given to the techniques of small angle neutron (SANS), X-ray (SAXS) and light (SALS, or just LS) scattering. In each of these techniques, radiation is elastically scattered by a

sample and the resulting scattering pattern is analysed to provide information about the size, shape, molecular weight, poly dispersity and internal structure [1-4]. During the scattering process, any changes in structure would be reflected in the energy or momentum of the scattered beam. In light scattering, the energy transfer is negligible, so it works based on momentum transfer. Any changes in momentum would be mirrored in momentum transfer or scattering vector, Q , which is defined as the difference between the propagation vectors of the incident and scattered light. The magnitude of the scattering vector is:

$$|Q| = |K_f - K_i| = \frac{4n\pi}{\lambda} \sin \frac{\theta}{2} \quad (3.1)$$

- n : Refractive index of the medium
 λ : The wavelength of the beam
 θ : Scattered angle

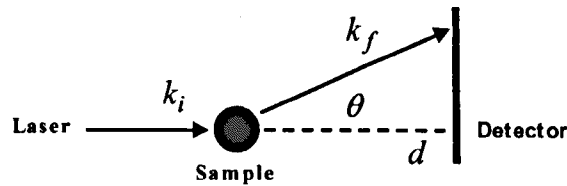


Figure (3.1) Schematic definition of scattering vector

By substituting equation (3.1) into Bragg's Law of Diffraction (3.2), we approach a useful expression which shows the relationship between Q and the distance of the sample from detector:

$$\lambda = 2d \sin \frac{\theta}{2} \quad (3.2)$$

$$d = \frac{2n\pi}{Q} \quad (3.3)$$

- d : Distance of sample from detector

3.1.1 The connection between light scattering and Fourier transform

When light is scattered from a small scattering object, the amount of scattering defines the scattering cross section. For a single scattering object, the intensity of the scattering object is expressed in equation (3.4).

$$F(\mathbf{s}) = \sigma \rho(\mathbf{x}) \exp(2\pi i \mathbf{x} \cdot \mathbf{s}) \quad (3.4)$$

$F(\mathbf{s})$: The intensity of the scattering object in direction s

σ : Scattering cross section

$\rho(\mathbf{x})$: Density at position x

Coherent scattering from a multiple source can be expressed in equation (3.5):

$$F(\mathbf{s}) = \int \rho(\mathbf{x}) \exp(2\pi i \mathbf{x} \cdot \mathbf{s}) d\mathbf{x} \quad (3.5)$$

$F(\mathbf{s})$: Wave scattered in direction s

$\rho(\mathbf{x})$: Scattering potential at position x

$$F(f(x)) = F(\omega) = \int f(x) \exp(-2\pi i \omega x) \quad (3.6)$$

F : Fourier Transform function

Comparing equation (3.5) with (3.6) which is the definition of Fourier transform shows that scattering produces the Fourier transform of an object. More detail about the scattering intensity can be found in appendix I.

3.1.2 Small angle light scattering with integrated spin coater

Small angle light scattering (SALS) is the main technique to study film formation in situ. The schematic image of this home made device made in Sheffield is shown in figure (3.2). A drop of the polymer blend is deposited on

the substrate which is placed on the stage of the spin coater, capable of reaching spin speeds in the range 0-10000 r.p.m within 200 *ms*. During spinning, a laser beam (He-Ne, 633 *nm*) incident on the sample is reflected and the reflected light is detected by two detectors. The first is a Si photodiode with a time resolution of 1 *ms* and measures the intensity of the specular reflection from the sample. Any scattered light out of the specular direction (off specular scattering) is projected on a screen and then imaged by a CCD camera which can capture 30 frames per second.

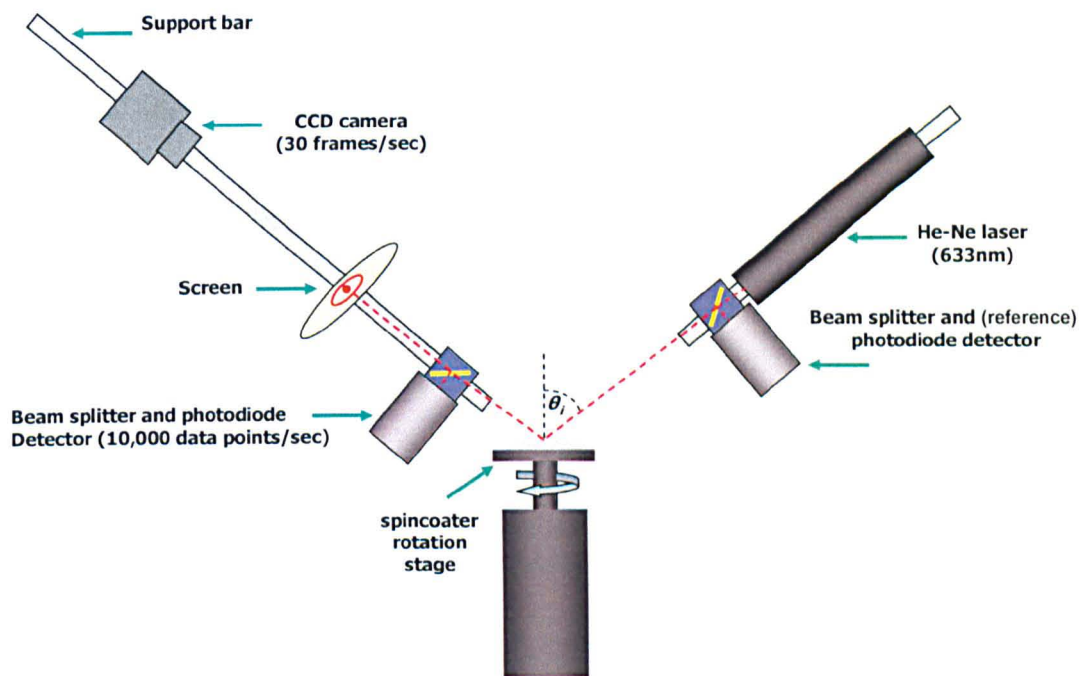


Figure (3.2) Schematic of light scattering device made in Sheffield

3.1.3 Fresnel equations

Fresnel equations describe the behaviour of light propagating in the media of different refractive index. When light is incident on an interface, a fraction of it is reflected and refracted, as long as the refractive indices of the two media are different. The extent to which radiation is reflected at a surface or interface

depends on wavevector. In vacuum, the z component of the wavevector (normal to the surface) is given by [3]:

$$k_{z,0} = (2\pi/\lambda)\sin\theta \quad (3.7)$$

θ : Grazing angle of incident

Subscript 0 indicates the vacuum. In any other environment, the equation (3.7) can be written as [3]:

$$k_{z,i} = (k_{z,0}^2 - k_{c,i}^2)^{1/2} \quad (3.8)$$

$k_{c,i}$: The critical value of $k_{z,i}$ below which total reflection occurs.

The reflection coefficient or reflectance at a sharp interface between two media, i and $i+1$ is given by:

$$r_{i,i+1} = \frac{(k_{z,i} - k_{z,i+1})}{(k_{z,i} + k_{z,i+1})} \quad (3.9)$$

In the case that polymer is in contact with air or vacuum, the reflection coefficient, $r_{0,1}$ and the reflectivity, R , are respectively defined by:

$$r_{0,1} = \frac{(k_{z,0} - k_{z,1})}{(k_{z,0} + k_{z,1})} \quad (3.10)$$

$$R = r_{0,1}r_{0,1}^* \quad (3.11)$$

R : Fresnel reflectivity at the interface

r^* : The conjugate of r

Now consider the case where a polymer film (medium 1) is in contact with vacuum (medium 0) and substrate (medium 2). The reflection coefficient from specimen/vacuum and from specimen/ substrate are $r_{0,1}$ and $r_{1,2}$ respectively.

Given that the film thickness is d , the reflectance can be determined as follows:

$$r = \frac{r_{0,1} + r_{1,2} \exp(2ik_{z,1}d)}{1 + r_{0,1}r_{1,2} \exp(2ik_{z,1}d)} \quad (3.12)$$

$k_{z,1}$: The scattering vector or momentum in the film

The reflectivity for such a specimen is given by:

$$R_{(z,0)} = rr^* = \frac{r_{0,1}^2 + r_{1,2}^2 + 2r_{0,1}r_{1,2} \cos(2k_{z,1}d)}{1 + r_{0,1}^2 r_{1,2}^2 + 2r_{0,1}r_{1,2} \cos(2k_{z,1}d)} \quad (3.13)$$

Now consider the specimen is composed of n layers, each with variable thickness on a substrate, and the $(n+1)$ th layer being the substrate and index 0 related to external surroundings (figure (3.3(b))). The reflectance of the specimen is the reflectance at air/specimen interface, i.e., $r_{0,1}$. This includes the internal reflection from each subsequent layer, starting from the substrate ($(n+1)$ th layer) and the layer closest to substrate (n th) layer. The reflectance between the $(n-1)$ th and n th layer is given by:

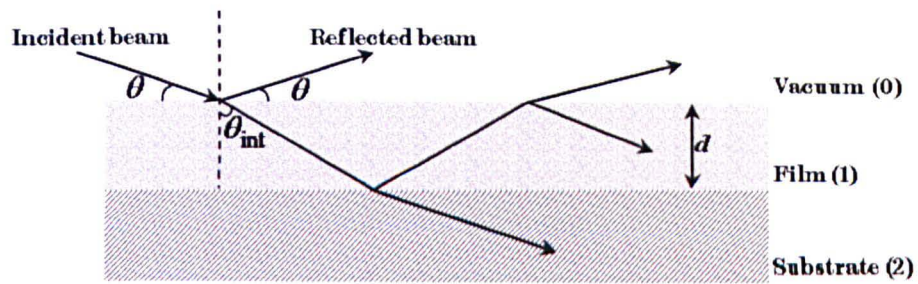
$$r_{n-1,n} = \frac{r'_{n-1,n} + r'_{n,n+1} \exp(2id_n k_n)}{1 + r'_{n-1,n} r'_{n,n+1} \exp(2id_n k_n)} \quad (3.14)$$

r' : Reflectance at the interfaces given by eq. 3.9

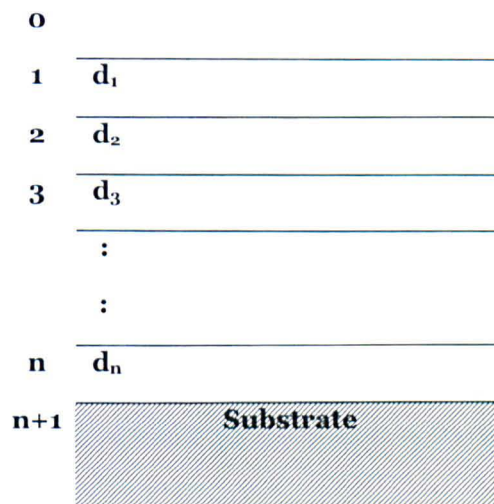
This reflectance, $r_{n-1,n}$, is used to calculate the reflectance for the next layer by:

$$r_{n-2,n-1} = \frac{r'_{n-2,n-1} + r_{n-1,n} \exp(2id_{n-1} k_{n-1})}{1 + r'_{n-2,n-1} r_{n-1,n} \exp(2id_{n-1} k_{n-1})} \quad (3.15)$$

This calculation is then continued until the reflectance of air/specimen, $r_{0,1}$, is obtained and then reflectivity can be calculated by $R = r_{0,1} r_{0,1}^*$.



(a)



(b)

Figure (3.3) (a) Reflection from surface of a media (b) Schematic of a n layer film each with variable thickness.

3.1.4 Specular reflection

When the laser beam is incident on the sample, it is reflected from the surface. Due to constructive and destructive interference of the reflected beam from air/solution and solution/substrate interfaces, fringes will form (figure (3.5)). The constructive interferences are the result of fulfilling Bragg's law. To apply Bragg's law, consider two waves C and D being scattered from top and bottom of a layer with thickness d (figure (3.4)). Because the refractive index of the two media is different, refraction will occur. However, the two waves are only in phase if the extra path length of wave D over C ($= AN+BN$) equals a whole

number of wavelengths. The equation for this path difference gives the Bragg law:

$$AN + BN = m\lambda \quad (3.16)$$

$$2d \cos \theta = m\lambda \quad (3.17)$$

θ : The internal angle regarding to the normal line

d : Film thickness

λ : Beam wavelength

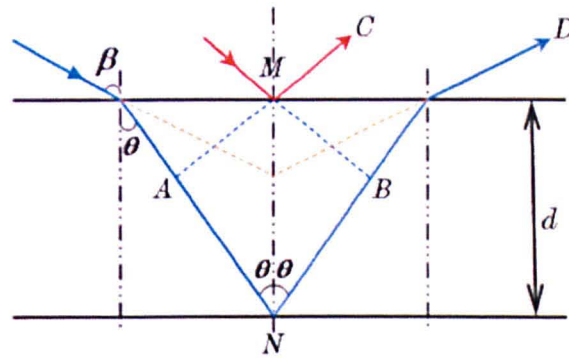


Figure (3.4) Reflection and refraction from a single layer.

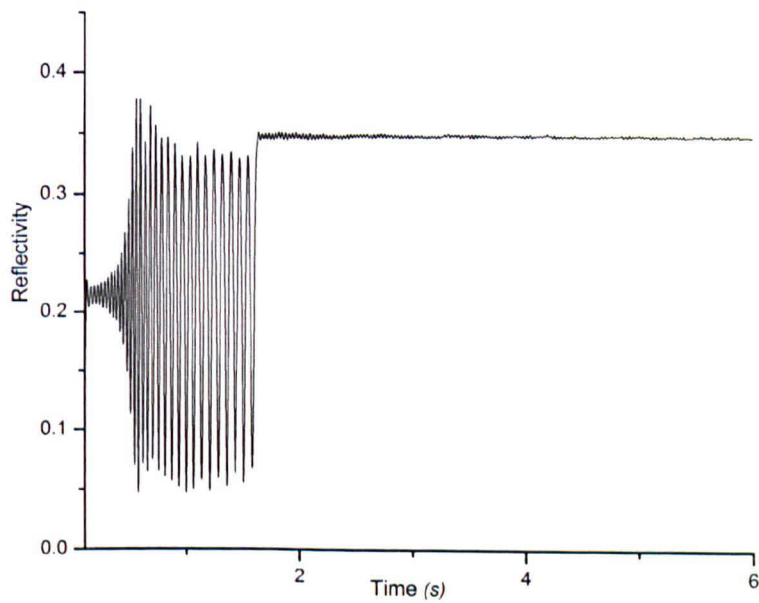


Figure (3.5) The fringe formation corresponding to constructive and destructive interference. The peaks are the result of Bragg's law.

3.1.4.1 Thickness-time profile

During spin coating, the reflectivity exhibits a series of peaks and troughs (figure (3.5)), corresponding to constructive and destructive interference of reflected light from the solution/air and solution/substrate interfaces. As the solvent is being removed from the system, the refractive index of the solution changes with time. It is assumed that the changes in reflective index with time for both the polymer and solution is linear at all time. So we have:

$$n_t = n_i + (\text{gradient} * t) \quad (3.18)$$

n_t : Refractive index of the film at time t

n_i : Initiative refractive index of the film

gradient: Gradient of linear plot of n vs t

Given equation (3.17), it can be seen that two adjacent peaks in the specular data will correspond to a thickness change of Δd :

$$\Delta d = \lambda/2n \cos \theta \quad (3.19)$$

θ : The internal angle regarding to the normal line

n : Refractive index of the film

According to Snell law we have:

$$n_1 \sin \beta = n_2 \sin \theta \quad (3.20)$$

$$\theta = \sin^{-1} \left(\frac{n_1 \sin \beta}{n_2} \right) \quad (3.21)$$

β : The incident angle regarding to the normal line

θ : Internal angle inside the film

n_1 & n_2 : Refractive index of media 1 and 2

By rearranging equation (3.19), we have:

$$d(t) = d(f) + (m - 1) * \left[\frac{\lambda}{2 * \cos(\theta) * n} \right] \quad (3.22)$$

$m - 1$: Peak number in specular data

$d(t)$: Film thickness at any time during film formation

$d(f)$: Final film thickness

By replacing n_i from equation (3.18) in (3.22), we obtain equation (3.23), it is possible to plot film thickness as a function of time.

$$d(t) = d(f) + (m - 1) * \left[\frac{\lambda}{2 * \cos(\theta) * (n_i + \text{gradient} * t)} \right] \quad (3.23)$$

Figure (3.6) shows the typical plot of thickness vs. time.

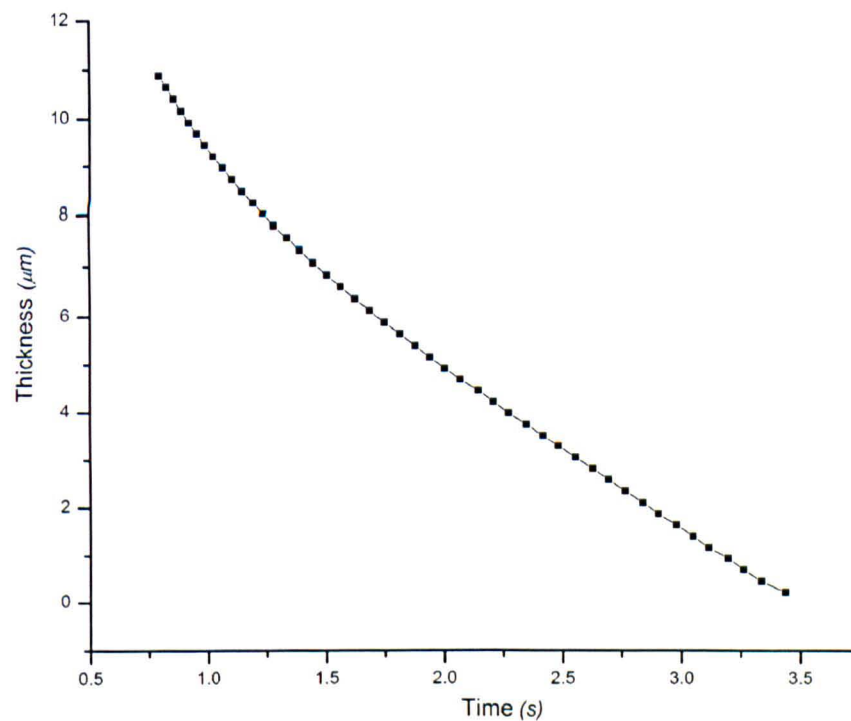


Figure (3.6) The typical plot of thickness vs. time for a PS/PMMA film during spin coating. The peak time and the number of peaks extracted from the relevant reflectivity-time graph were used in equation (3.23) to make this plot .

3.1.5 Off specular Scattering

Reflections off smooth surfaces are known as specular reflection or alternatively specular scattering. Reflections off rough surfaces are known as diffuse reflections or alternatively off-specular scattering. In thin films it happens when the film has structure at the surface or structure within the plane, as demonstrated in figure (3.7). Any fluctuations, either spatial or temporal, or a combination of these two, in the scattering length density will lead to non-specular or off specular scattering [5]. The scattered light is observed as a ring and by measuring the intensity of the cross-section of the ring, a plot of intensity vs. wave vector could be obtained (figure (3.7 (a))).

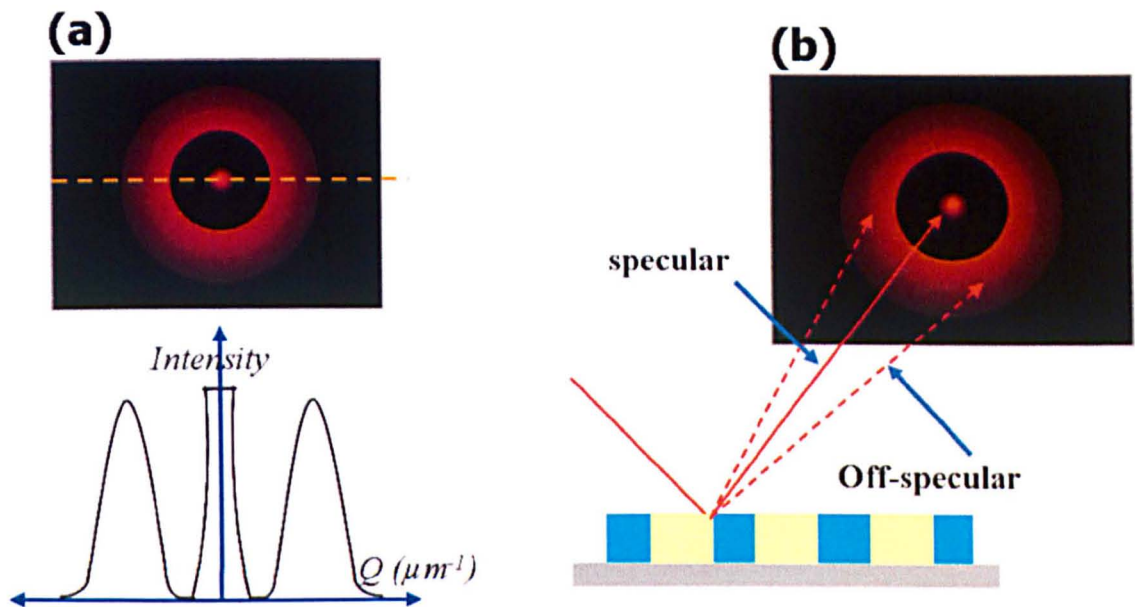


Figure (3.7) The specular and off specular reflection from film surface.

3.2 The Environmental cell

To study the interfacial instability in polymer thin films and testing our hypothesis (Marangoni instability) we have designed a chamber that can be mounted on top of the spin coater stage and can be used while collecting reflectivity-time and also off specular data from the optospinometer (figure (3.8)). UQG (ultra quality glass) was used for the windows to minimise the intensity loss. Figure (3.9) shows the intensity versus time plot for a silicon substrate both inside and outside of the cell. As is seen in figure (3.9) the intensity loss is small. Also because we do not use the absolute value of the intensity in our calculations, the slight reduction in intensity does not affect the data analysis.

Vapour pressure was quantitatively controlled in the cell. Toluene vapour was introduced by bubbling nitrogen through toluene. The bubbler is inside a water bath for temperature control (figure (3.10)). According to Clausius-Clapeyron relation, the saturated vapour pressure of a gas is a function of temperature only (equation 3.24).

$$\ln \frac{P_2}{P_1} = \frac{\Delta H_{vap}}{R} \left(\frac{1}{T_1} - \frac{1}{T_2} \right) \quad (3.24)$$

P_1 & T_1 : Corresponding vapour pressure and temperature

P_2 & T_2 : Corresponding vapour pressure and temperature in another point

ΔH_{vap} : Molar enthalpy of vaporization

R : The gas constant ($8.314 \text{ Jmol}^{-1} \text{ K}^{-1}$)

Therefore, by changing the temperature of the gas, we were able to achieve the desired vapour pressure. In chapter (5) we will explain how the evaporation rate of the toluene from the spinning film is extracted and also controlled inside the environmental cell. Figure (3.10) shows the experimental set up.

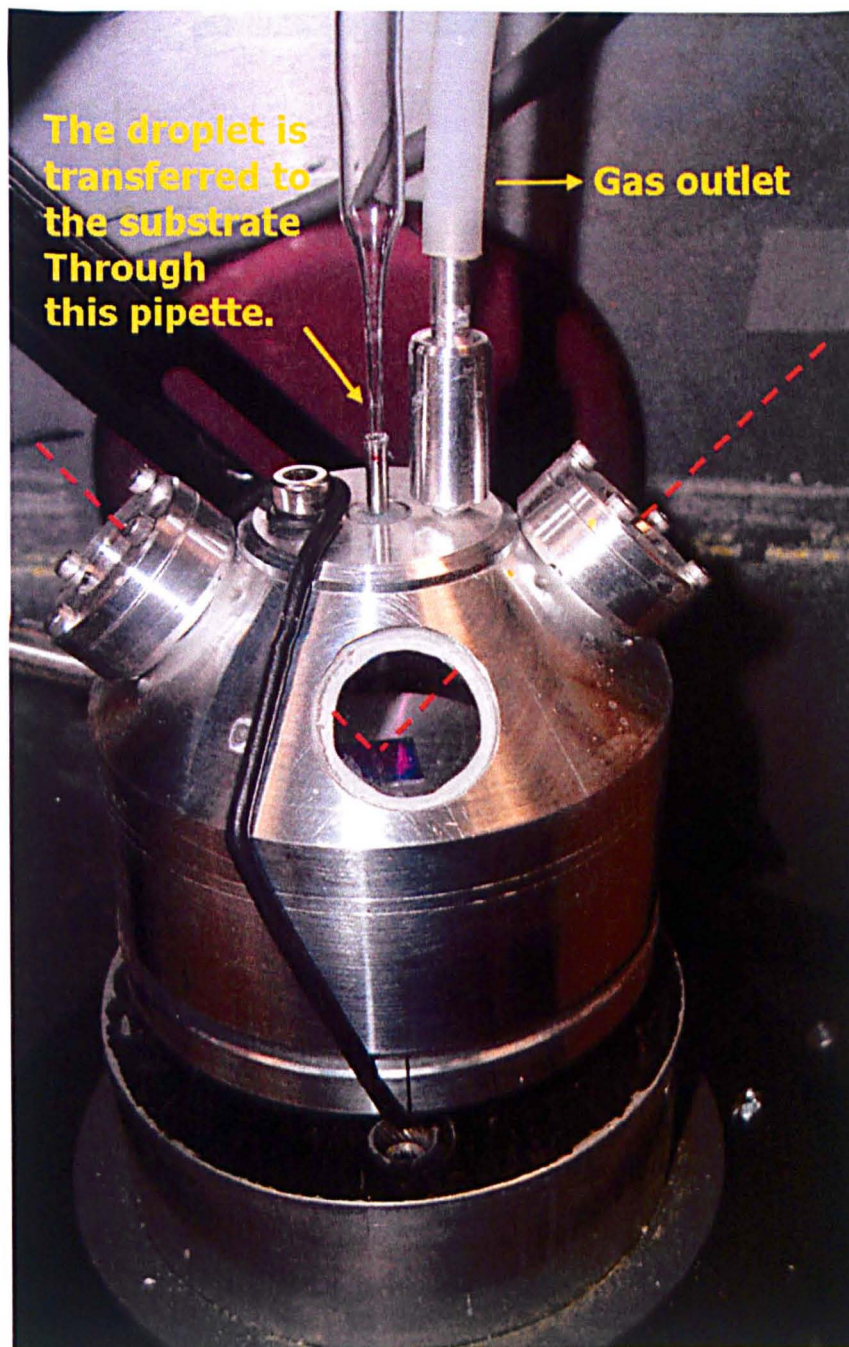


Figure (3.8) Environmental cell made of stainless steel mounted on spin coater chuck. Vapour pressure can be quantitatively controlled in the cell. The laser beam reflects from the sample through the side windows made of ultra quality glass. The gas outlet can either go through liquid paraffin or an exhaust pipe to avoid unwanted air entering the system. The inlet nozzle is bent (not seen here), as to avoid the direct blowing of gas onto the substrate.

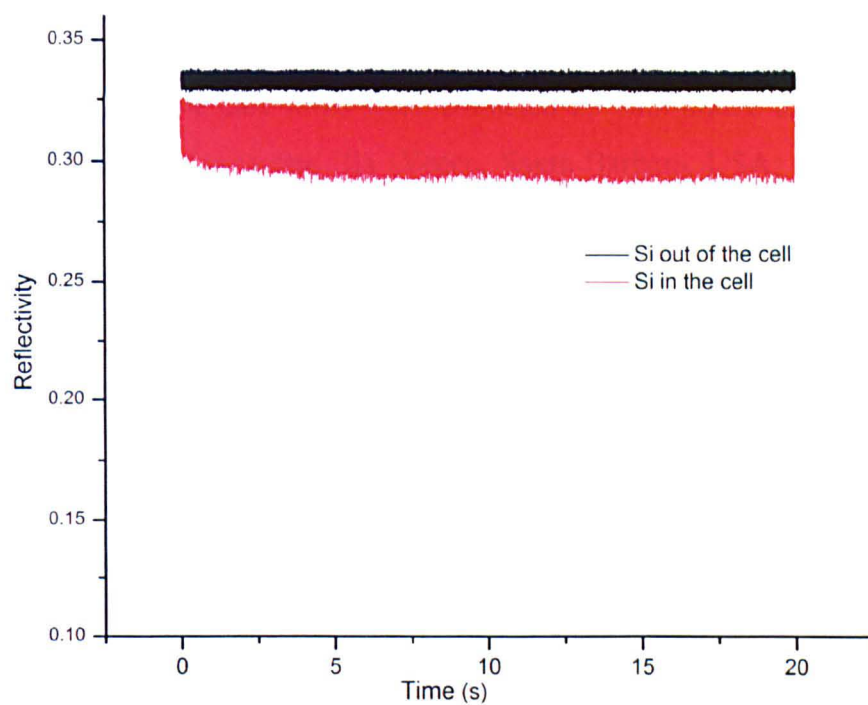


Figure (3.9) Silicon reflectivity inside and outside of the environmental cell.

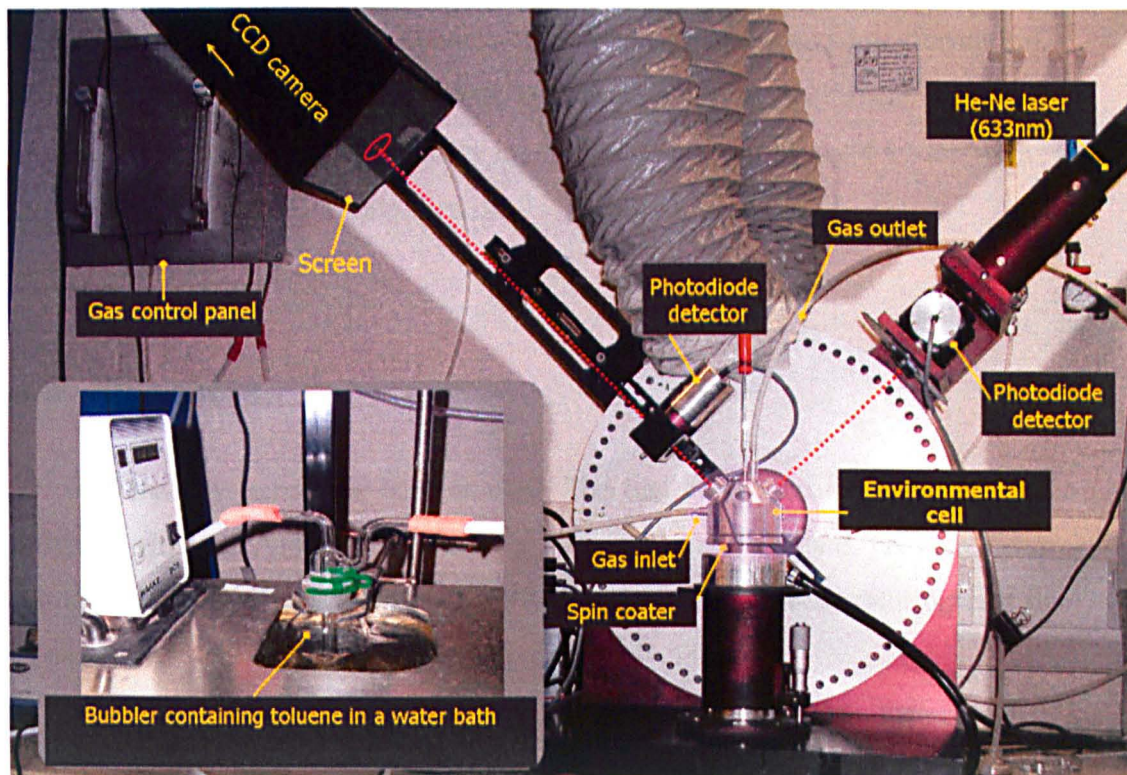


Figure (3.10) Experimental set up, including optospinometer, environmental cell, gas control panel and water bath with a bubbler containing toluene.

3.3 Atomic force microscopy (AFM)

The topography of the cast films were collected by Multimode atomic force microscope (AFM), Nanoscope IIIa (Veeco, Santa Barbara, USA) operated in tapping mode with OMCL silicon probe from Olympus. The cantilevers had a nominal spring constant of 40 N/m and resonant frequency of 300 kHz. Height and phase data were collected simultaneously. The images were analysed by Nanoscope software, version 5.12.

3.4 Optical microscopy

The optical microscope images have been used to study the sample surface morphology. The images were also used as input for Fast Fourier transform (FFT) analysis which provides information on the structure length scale. ImageJ software was used to obtain a two dimensional Fourier transformation. From this transformation an intensity distribution in reciprocal space is obtained. Usually a ring of intensity is present which can be used to determine the length scale on the sample surface.

3.5 Polymers

Two different systems have been studied. The first system was Polystyrene and polymethylmethacrylate (PS/PMMA). The second studied system was semiconducting polymer blend (PFB/F8BT). Both blends were solution cast in toluene.

3.5.1 PS/PMMA

Polystyrene (PS) with chemical formula $(C_8H_8)_n$ and polymethylmethacrylate (PMMA) with chemical formula $(C_5O_2H_8)_n$ were provided from Polymer lab and Polymer source. Table (3-1) shows the material specification.

Table (3.1) Specification of PS and PMMA

Polymer	# Sample	Source	M_p	M_w	M_w/M_n
PS	Part no:2013-5005	Polymer lab	96000	94650	1.03
PMMA	Part no:2023-5005	Polymer lab	100000	100300	1.04

3.5.2 PFB/F8BT

Conjugated polymers, PFB and F8BT were used to make active layer for photovoltaics. PFB poly((9, 9-dioctylfluorene)-alt-bis-N, N-(4-butylphenyl)-bis-N, N-phenyl-1, 4- phenylenediamine) and F8BT (Poly(2, 7-(9, 9-di-n-octylfluorene-alt-benzothiadiazole)) are both polyfluorene derivatives. PFB is a hole transporting polymer and F8BT is an electron acceptor in photovoltaic devices.

3.5.3 Solvents

Toluene was used as the main solvent to make blends for both PS/PMMA and PFB/F8Bt system. Solutions were made up to 10% polymer and 90% toluene by weight. Films were spun for 20 seconds at a speed of 2000 r.p.m.

Cyclohexane and acetic acid were used for selective washing of some components in the film.

3.6 Bibliography

1. Dawkins, R.A.P.J.V., *Modern Techniques for Polymer Characterisation*. 1999: John Wiley.
2. Julia S.Higgins, H.C.B., *Polymers and Neutron Scattering*. 1996: Oxford university Press Inc., New York.
3. T.P.Russell, *X-ray and neutron reflectivity for investigation of polymers*. Material science report, 1990(5): p. 171-271.
4. P.Lindner, T.Z., *Neutrons, X-rays and Light:Scattering Methods Applied to Soft Condensed Matter*. 2002: North Holland.
5. Penfold, J. and R.K. Thomas, *The Application of the Specular Reflection of Neutrons to the Study of Surfaces and Interfaces*. Journal of Physics-Condensed Matter, 1990. 2(6): p. 1369-1412.

Chapter Four

Tuning the Optospinometer and Environmental cell

This chapter has two parts. The first part explains how the optics in optospinometer was modified to obtain a more uniform beam spot and scattering pattern.

The second part is about the stability of the gas flow and equilibrium between film and vapour in environmental cell. To monitor this, we have done a series of swelling experiments by exposing previously made polystyrene films to toluene vapour at different conditions. Analysing the reflectivity-time data, we propose a model for thickness evolution of swelled films.

4.1 Improving the optics

The optospinometer set up and the physics behind it is explained in chapter 3. The main physical concept is reflection and scattering of laser light from a substrate. We have modified the optical set up in two steps. First reducing the

beam size and second eliminating the effect of any other interfering light source.

4.1.1 Reducing the beam size

The onset of instability in the film is revealed in scattered light. If the plane of the film roughens, it will scatter the light. To monitor this process clearly, we need to have a small beam footprint on the substrate and a high density of the scattered light. The scattered light forms a ring if there is a length scale within an isotropic structure. The formation of the ring and its subsequent movement provides valuable information on structure evolution. This will be discussed in chapter 6. A big size beam spot makes it very difficult to detect the scattering ring as they can merge as one spot (figure (4.1)).

To reduce the beam size, first we have tried multiple lenses and home made pin holes to converge the beam and reduce the size. The optical pin holes were not smooth enough around the edge and didn't provide a clean beam spot.

The next trial was using a beam expander and a diaphragm. A Beam expander reduces the intensity of the laser but creates a big spot size. Placing a diaphragm in front of the beam expander, the size of the beam was controlled. See figure (4.2).

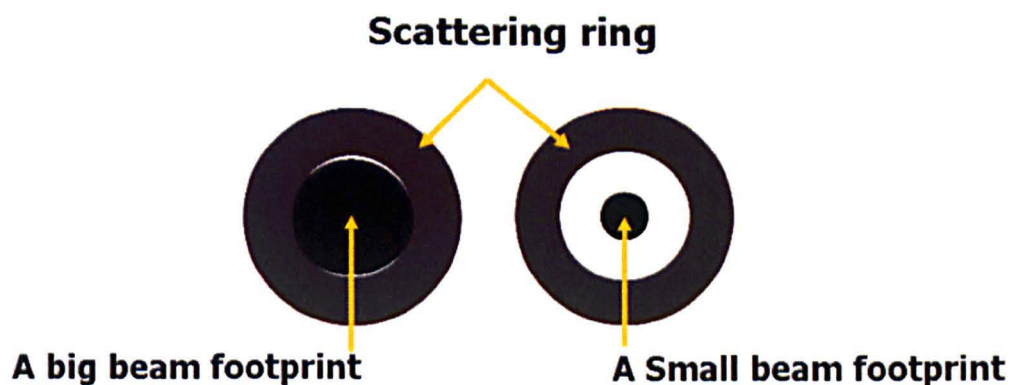


Figure (4.1) A big beam foot print will merge with the scattering ring and make it difficult to distinguish between the scattering and the small beam footprint.

4.1.2 Focusing the scattering pattern

To eliminate the interference of light from external sources with the scattered light, the light path between the screen and camera was isolated from the surrounding area. A sliding box was designed in which the camera is mounted at one end and a screen at the other end. To find the focus distance (length of the black box in figure (4.2)), first we opened both arms and aligned them horizontally. Then we removed the photodiode and put a paper with some text on the screen and then moved the camera along the rail till the text was clear. The distance between the camera and screen was measured ($\sim 37\text{ cm}$). The advantage of having a constant distance between camera and screen is that when we need to move the screen for example closer to the sample to detect smaller length scale, there is no need to adjust the camera as the distance is constant.

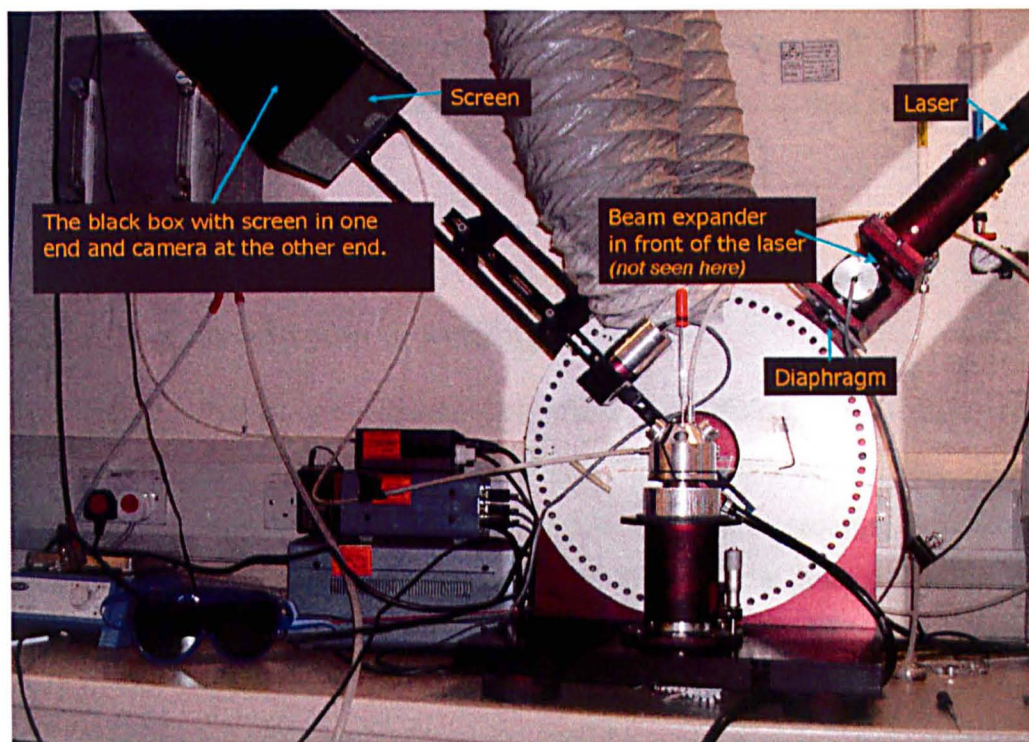


Figure (4.2) Optospinometer after the modification. The CCD camera and a glass screen are mounted at two ends of a black Aluminium box, in order to stop the light from the surroundings interfering with the scattered light. The supporting rail was modified to make the box slid easily. A beam expander and diaphragm, reduce the intensity and size of the beam. The environmental cell encloses the rotating chuck.

4.2 Characterising the performance of the environmental cell

In order to characterise the performance of the environmental cell, we carried out pilot experiments to investigate the uptake of the solvent by thin polymer films. Although the swelling of polymers lies outside the main focus of this thesis and these experiments were carried out mainly to characterise the apparatus, the phenomenon of polymer swelling is of interest in its own right and is introduced in the next section.

A series of polystyrene films with different thicknesses were spin cast. To produce different film thickness, polystyrene with different molecular weights were spin cast at different r.p.m. The thickness was at the range of 40 and 1400 *nm*. The PS films were exposed to toluene at different vapour pressures. The swelling of glassy polystyrene films exposed to toluene will be investigated by studying the reflectivity-time data. We will suggest an exponential model for thickness development. The model is then compared to experimental results.

4.2.1 An introduction to swelling

Swelling of polymers and phenomenon related to swelling such as diffusion, delamination and debonding of coatings from substrate [1] etc have technological importance in many areas such as emulsion, coating, adhesion, drug delivery etc. The swelling process in polymers is a combination of diffusion of the solvent to the free volume present in the porous structure of the polymer (mass uptake) and stretching of the polymer chains.

In a normal case, the mass transport can be described in the framework of Fick's first and second Laws. Fick's first law relates the flux of the material to the local concentration gradient of the diffusing species at any given point in the space.

$$F = D \frac{\partial c}{\partial x} \quad (\text{Fick's first law}) \quad (4.1)$$

F : The flux of matter

D : Diffusion coefficient ($m^2 s^{-1}$)

Fick's second law commonly known as the diffusion equation assumes that the concentration gradient is not constant and is changing with time.

$$\frac{dc}{dt} = \frac{d}{dx} \left(D \frac{dc}{dx} \right) \quad (\text{Fick's second law}) \quad (4.2)$$

Now consider a semi infinite system with constant diffusion coefficient where a material is deposited in a plane at $x = 0$ and is given enough time to diffuse in a film. In this situation, the solution for equation (3.2) can be written as:

$$c(x,t) = \frac{A}{\sqrt{t}} \exp\left(-\frac{x^2}{4Dt}\right) \quad (4.3)$$

Integrating the flux of the material over time gives the amount of mass that has left the plane as follows:

$$M(t) = C_0 \sqrt{\frac{Dt}{\pi}} \quad (4.4)$$

C_0 : Concentration of material deposited in the plan

Equation (4.3) forms the basis of diffusion experiment analysis. This kind of diffusion in which the mass of the diffusive species is determined as a function of time and is proportional to the square root of time is called Case I diffusion. This can be distinguished from Case II diffusion in which mass uptake changes linearly with time. When a non glassy polymer is exposed to a solvent or vapour, the solvent will diffuse to the polymer, following case I

diffusion. The chains will also move. The relaxation process which is involved with chain motion in the polymer film is much faster than the time the solvent/vapour can diffuse into the film. This is the characteristic of case I diffusion. In contrast, in case II diffusion, the relaxation time is much longer than the time associated with diffusion. This usually happens in glassy polymers.

When a glassy polymer is exposed to a good organic solvent/vapour, the weight of the polymer increases linearly with time. The polymer swells and as mentioned before a specific situation known as case II diffusion can happen. Case II diffusion has received considerable attention within the previous five decades [1-14]. It is characterized by linear kinetics and a sharp diffusion front [10] and can be described in two main stages:

- (a) The initiation stage in which the volume fraction of the solvent on the surface (φ_s) will increase until a critical value (φ_c) is reached. At this point a case II diffusion front forms.
- (b) The propagation stage, where the front moves through the polymer with uniform velocity.

The difference between actual volume fraction and the equilibrium volume fraction in stage (a) is a result of osmotic pressure that acts on semi-permeable surface of a glassy polymer. The osmotic pressure is resisted by the stress exerted by the chains in a glassy polymer. In glassy polymer films the chains are immobilised, therefore the relaxation of the chains happens slower than diffusion. This builds up stresses in the film and further diffusion of the solvent is possible only when the chains are relaxed. Crank [11] introduced the swelling stress to the diffusion equation. This led to the Thomas and Windle [10] model that describes the transport behaviour in case II diffusion based on the diffusion coefficient (D) and the flow viscosity of glassy polymers (η_0).

When the front is formed, the concentration of the penetrant in the front stays relatively constant while ahead of the front the concentration drops sharply. In

other words, the polymer ahead of the front is glassy but the material behind is highly plasticised. This has been shown by optical microscopy analysis (Thomas and Windle) [9] and Rutherford backscattering spectroscopy (Mills *et al*) [15]. The formation of the front is preceded by an induction period, during which the concentration of the solvent decreases as a function of depth in the film [16], see figure (4.3). Immediately after the induction period, the front is formed and moves at constant speed [17]. The velocity of the front may accelerate or decelerate at longer times[18].

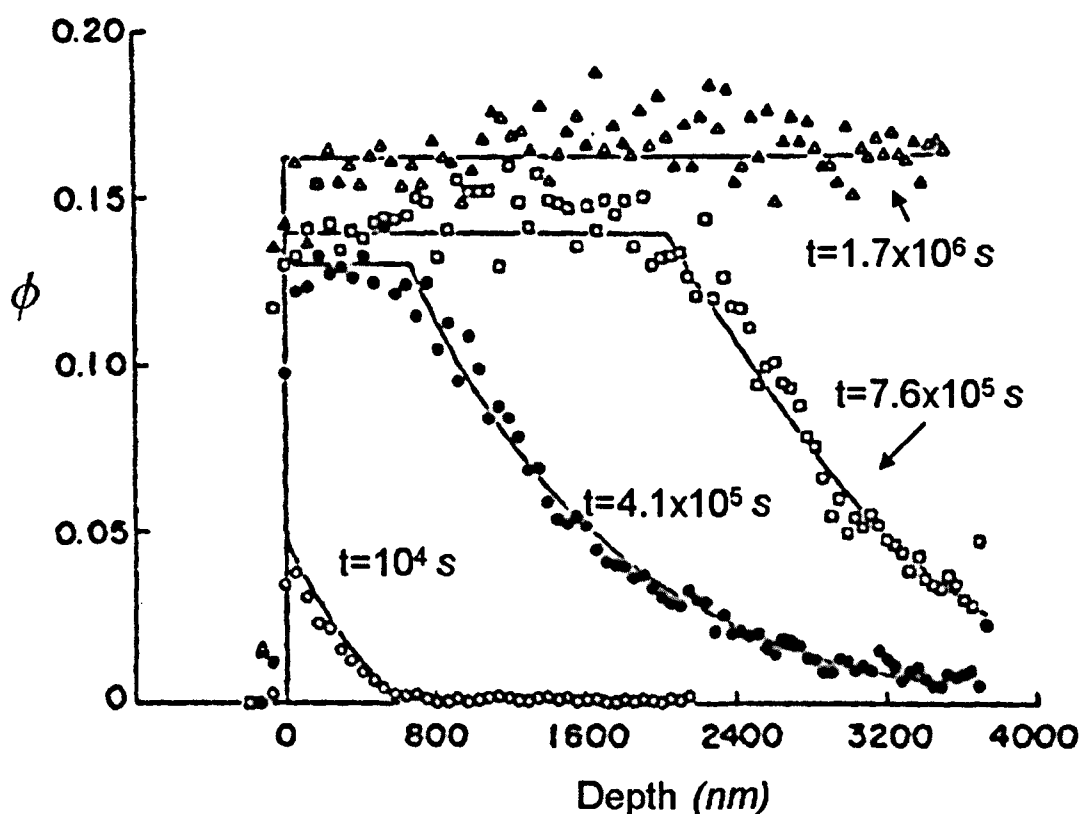


Figure (4.3) Isododecane volume fraction vs. depth profile in polystyrene after different exposure times. C. Y Hui *et al*, 1987 [17].

4.2.1.1 Thermodynamics of swelling equilibrium

The thermodynamics of equilibrium swelling of polymer films exposed to an organic solvent vapour can be described by the method of analysis proposed

by Flory- Huggins (more recently by Chen *et al*). It is based on equality of the chemical potential of the components at equilibrium. i.e. the chemical potential of the solvent vapour (μ_{vapour}) is equal to the chemical potential of the solvent in the film (μ_{pol}) when they are in equilibrium.

$$\mu_{vapour} = kT \ln a \quad (4.5)$$

a : Activity of the solvent vapour

a which is the activity of the solvent vapour is defined as the ratio of partial pressure of solvent vapour to the vapour pressure of the liquid at fixed temperature.

The chemical potential of the solvent in the film (μ_{pol}) can be derived from the Flory-Huggins theory of mixing[19, 20]

$$\mu_{pol} = kT \left((1 - \phi_s) \left(1 - \frac{1}{N} \right) + \ln \phi_s + \chi (1 - \phi_s)^2 \right) \quad (4.6)$$

ϕ_s : Volume fraction of solvent in the polymer film

N : The degree of polymerization

By equating equation (4.5) and (4.6) it is possible to describe the equilibrium behaviour of the vapour/ (polymer-solvent) in terms of χ the Flory-Huggins interaction parameters.

$$\ln a = (1 - \phi_s) \left(1 - \frac{1}{N} \right) + \ln \phi_s + \chi (1 - \phi_s)^2 \quad (4.7)$$

A plot of the fit to equation (4.7) from Sharp and Jones work is shown in figure (4.4). It shows as the relative pressure of the vapour (water here) increases, the amount of the solvent absorbed at the equilibrium will increase. The data taken from QCM (quartz crystal microbalance) in figure (4.5) show the same result. i.e. by increasing the vapour pressure, the initial rate of uptake

increases but along with that, the total equilibrium time increases as well. The increase of equilibrium time is not expected for diffusion in polymer material, because the diffusion coefficient is expected to increase with increasing the solvent content. In other words, diffusion in bulk films is different from thin films (films less than $2 \mu m$).

In a model suggested by Hui and co workers [16] it is assumed that swelling is driven by differences in osmotic pressure $\Delta\Pi$ across the polymer/vapour interface. Therefore the rate of change in volume fraction $(\frac{d\phi}{dt})$ can be written as:

$$\frac{d\phi}{dt} = \frac{\Delta\Pi}{\eta} \quad (4.8)$$

Π : Osmotic pressure

η : Elongational viscosity

Elongational viscosity (η) describes the response of the polymer to the osmotic pressure introduced by rapid swelling when it is exposed to a solvent vapour. The stresses are induced by swollen polymer and further uptake can only happen when the stresses have relaxed. The relevant relaxation time is set by η .

In our work in section (4.2.3), we will use a different approach to show there are different regimes during the swelling of a glassy polymer film. Using reflectivity-time data and by modelling the thickness-time, we demonstrate there is more than one stage in the kinetics of swelling of glassy films of polystyrene.

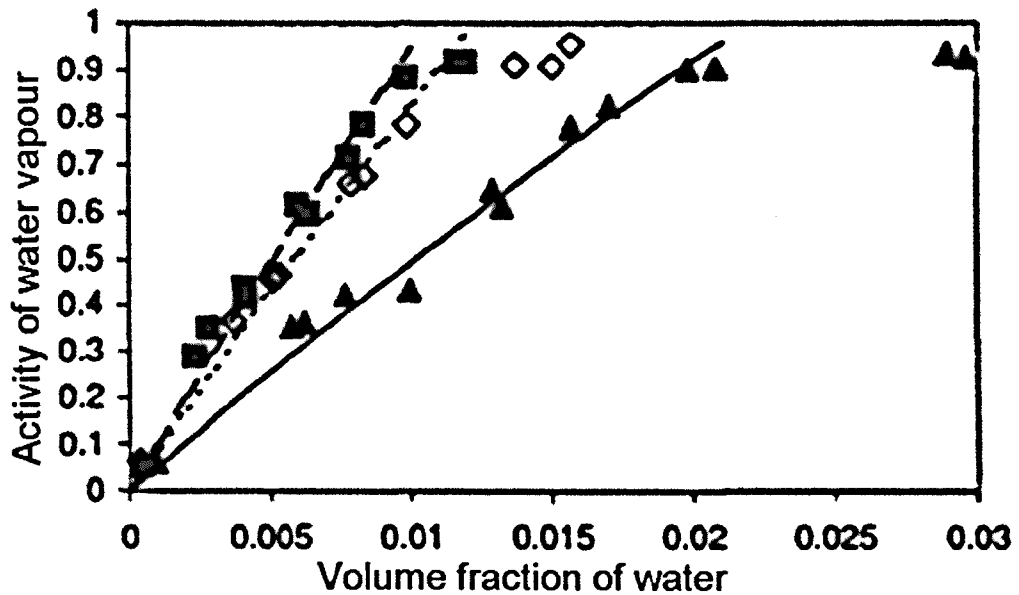


Figure (4.4) Dependence of the equilibrium volume fraction of water on the activity of water vapour in the air surrounding the films (with different molecular weights) [20]. Material used were (■) 80K Da PLA (poly (DL-lactide)), (◇) 12K Da PLA and (▲) 10K Da PLGA glycolic acid. Data taken from Sharp *et al*, 2001 [20].

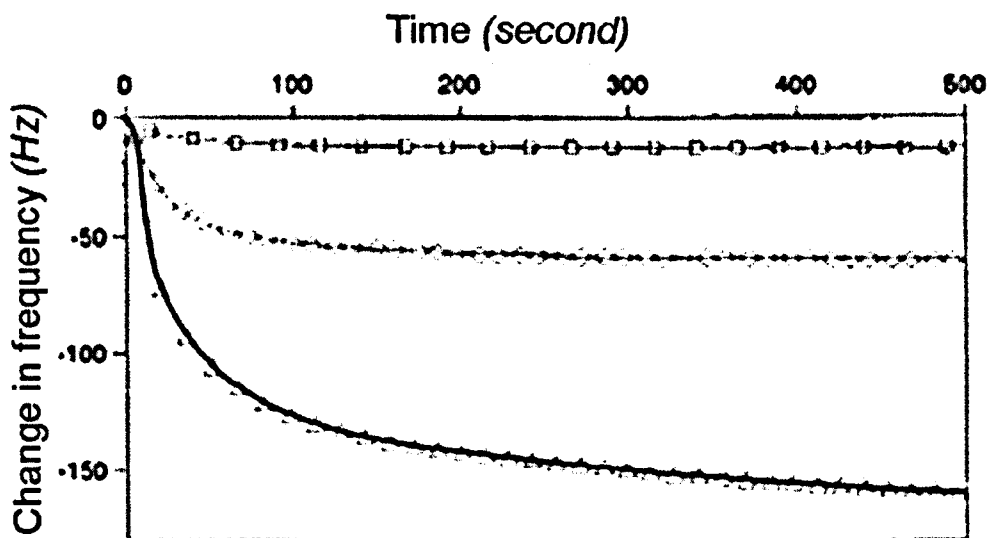


Figure (4.5) Kinetics of swelling on poly (DL-lactide) for polymers hydrated at relative humidities of (□) 6%, (◇) 37%, and (Δ) 78%. Data taken from Sharp *et al*, 2001 [20].

4.2.2 Stability of the gas flow in the environmental cell

The experimental set up for the environmental cell has been explained in chapter 3. In this part we will show that the set up is working and it is behaving as expected. The first experiment examined the stability of flow in the gas loop. Toluene at different vapour pressures was produced by blowing nitrogen gas through the solvent at different flow rates. The concentration of toluene is a function of temperature only. Therefore, changing the nitrogen flow rate, should not affect the concentration of the vapour in the cell and therefore no shift or volatility in reflectivity is expected. Figure (4.6) shows the situation in the environmental cell is very stable and that decreasing the flow rate of nitrogen does not alter the reflectivity

There are two methods to change the vapour pressure of the gas in the cell. The first method as mentioned before is changing the temperature. The higher the temperature of the gas, the higher the vapour pressure will be. The second method is mixing the toluene with another gas. This will dilute the vapour and reduce its pressure.

The result of the first technique (changing the vapour pressure by means of temperature) will be discussed in chapter 5. In what comes next, the second method (diluting toluene by nitrogen) in our set up will be inspected.

The concentration of toluene was controlled by mixing the toluene gas with nitrogen prior to entering the cell. Figure (4.7) shows the result. At the beginning when there is no exposure, the reflectivity is constant. Then the film is exposed to toluene at 18°C. This temperature provides the nominal vapour pressure of 19.61 *mmHg* and toluene concentration of $\frac{19.61}{760} * 100 = 2.6\%$ (760 *mmHg* is the saturated vapour pressure of toluene at

its boiling point). The reflectivity changes and after 5 minutes it increases slowly and reaches the equilibrium. At $t=15 \text{ min}$, toluene is mixed with nitrogen gas to reduce the concentration. The composition is (1:1) ratio of toluene to nitrogen. The concentration of toluene is halved to 1.3%. There is an immediate response to the change in concentration at $t=15 \text{ min}$. First the

intensity drops and then it starts to increase and reach the equilibrium. It takes less time to reach the equilibrium this time. This could be due to the fact that the film contains some toluene from the previous exposure and therefore is already swollen. Also because the vapour concentration is lower, the stress induced by osmotic pressure will be lower and therefore it takes less time to reach the equilibrium.

Figure (4.8) shows another multi exposure experiment. A PS film was exposed to toluene with vapour pressure of 19.61 mmHg for about 15 minutes and then the valve was closed to obstruct any gas flow. As seen in figure (4.8), the reflectivity drops. Then the valve was exposed to toluene with the same concentration value i.e. the vapour pressure of 19.61 mmHg at 18°C and toluene concentration of 2.6%. The reflectivity responds to the change. These outcomes are representative of many other experiments that show the set up is working in the expected way and that we are able to control the vapour pressure in the environmental cell.

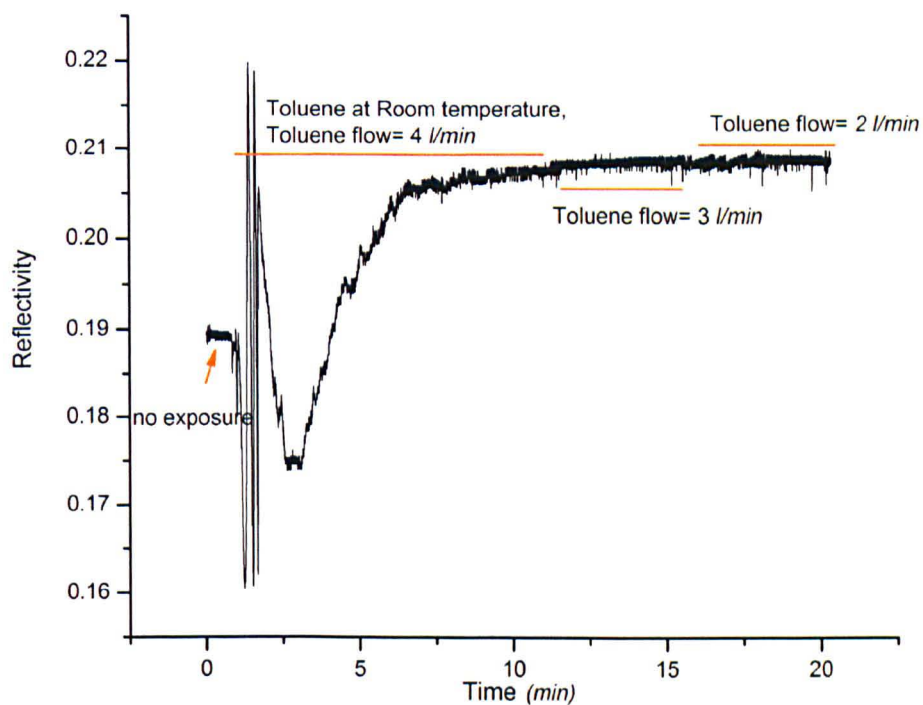


Figure (4.6) PS film is exposed to toluene at different nitrogen flow rate. Changing the flow rate from 4 l/min to 2 l/min does not make any change in reflectivity.

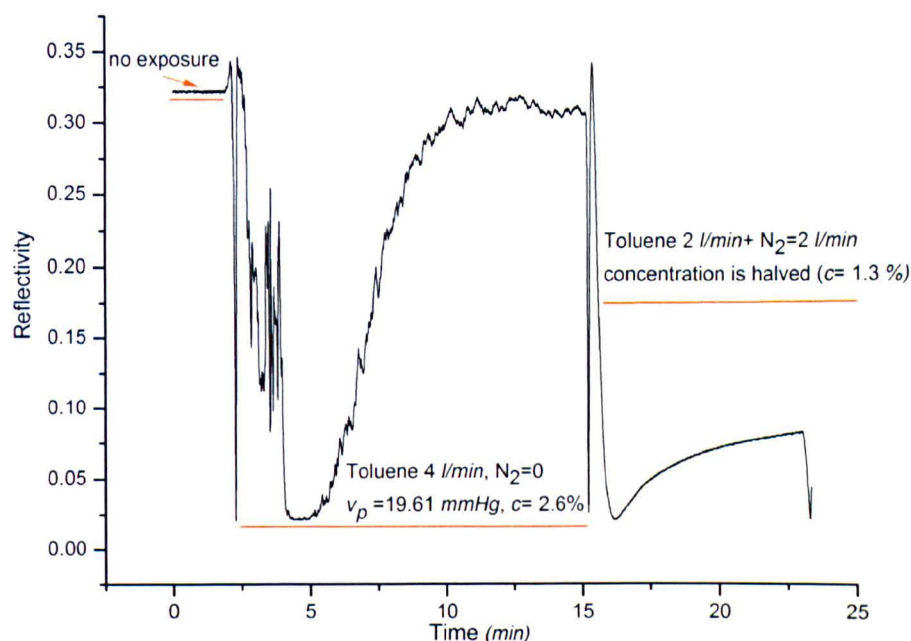


Figure (4.7) Reflectivity data of PS film responding to the reduction of toluene concentration in environmental cell. The film is exposed to toluene at room temperature (18°C) and swells. Then the concentration is halved by mixing the toluene with nitrogen gas. There is an immediate response to the change. Also at the second exposure, it takes less time for the film to reach the equilibrium.

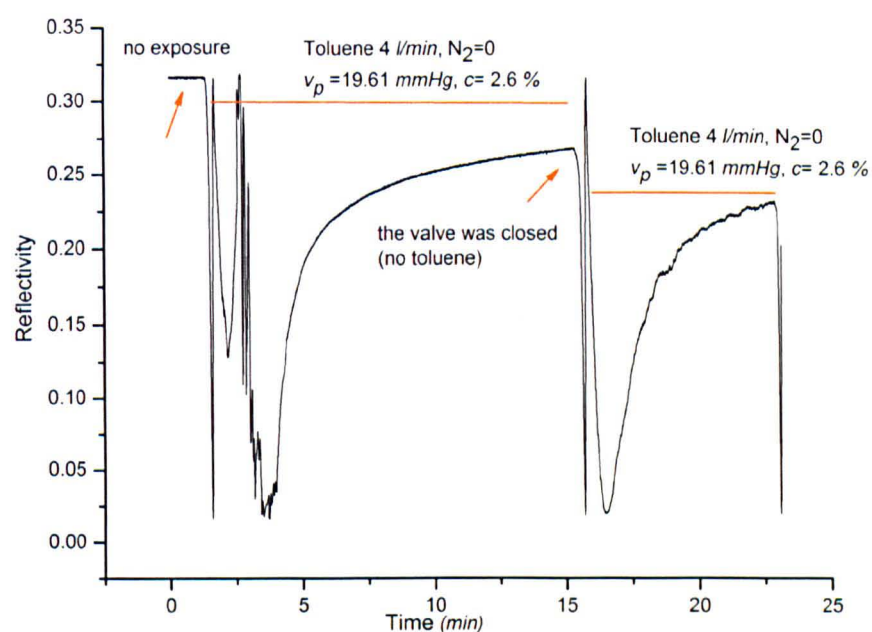


Figure (4.8) Monitoring the saturation condition in the environmental cell. PS is exposed to toluene gas with 2.6% concentration and fringes form due to swelling. Then the nitrogen gas valve is switched off after about 15 minutes. By decreasing vapour pressure, the reflectivity drops. After a couple of minutes, the film is exposed to toluene again, with the same concentration and reflectivity rises.

4.2.3 Swelling behaviour of polystyrene film

Satisfied with the stability of the gas flow and swelling response of the film, the films were exposed to toluene at 18 °C. We have tried to study the film swelling process by modelling the reflectivity- time data. In what follows we will explain the modelling step by step.

Figure (4.9) shows the reflectivity-time for a PS film with initial thickness of 1200-1400 nm exposed to toluene. Fringes appear due to absorption of the toluene in the film and changes in the film thickness and also changes in the refractive index of the film. At the beginning, the refractive index of the film is the refractive index of PS ($n_1 = n_{PS} = 1.59$). During swelling, the refractive index of the film will change to n_2 :

$$n_2 = n_{PS}v_{PS} + n_{sol}v_{sol} \quad (4.8)$$

n_2 : Refractive index of the swelling film

n_{PS} : Refractive index of pure PS (1.59)

v_{PS} : Volume fraction of PS

n_{sol} : Refractive index of toluene (1.5)

v_{sol} : Volume fraction of toluene

The volume fraction of the film can be written as a function of film thickness:

$$n_2 = n_{PS} \times \left(\frac{d_1}{d_2}\right) + n_{sol} \times \left(1 - \frac{d_1}{d_2}\right) \quad (4.9)$$

d_1 : Initial film thickness

d_2 : Final film thickness

The initial film thickness (d_1) was measured by either ellipsometry or AFM . However, the final film thickness could not be measured in the same way, because the film would collapse after being removed from the toluene atmosphere. Therefore, we had to calculate the film thickness.

Fringes are due to constructive and destructive interference of the reflected beam from the surface and interfaces of the film and substrate. Between each two subsequent peaks, the film thins by Δd which is given by equation (3.19) $\Delta d = \lambda/2n \cos \theta$. In our experimental set up, the incident angle is 45 degrees, the refractive index of polystyrene is 1.59 and the wavelength of the laser is 633 nm. θ is the internal angle and by applying Snell's law, we have $\cos \theta = 0.8898$. Using equation (3.16) and by substituting all values we obtain Δd as below:

$$\Delta d = \frac{633}{2 * 1.59 * 0.8898} = 229.48 \approx 230nm \quad (4.10)$$

We should mention that in our calculation for thickness change between two fringes, it is assumed that the refractive index is constant. But in reality the refractive index of the polystyrene film when toluene is introduced to the system, will change continuously according to equations (4.8) and (4.9). However, our assumption for having constant refractive index for calculation of Δd has very little effect on it. To make it more clear, even if the volume fraction of toluene reaches an extreme value of 0.9 ($v_1 = 0.1$ and $v_2 = 0.9$), in that case the value of n_2 will be $n_2 = 1.59 \times 0.1 + 1.50.9 = 1.51$ and, subsequently $\Delta d = 236nm$. The difference between our assumption and the extreme case of having 90% toluene in the swollen film introduces 6 nm difference in Δd which at this stage of modelling has a negligible consequence on the results and can be ignored.

Knowing the difference in thickness between each two subsequent fringes and by counting the number of fringes (full and fraction of fringes) and also

knowing the initial thickness, we are able to calculate the final film thickness after swelling.

In the next step we assume there is a linear relationship between refractive index and film thickness. Therefore we can write:

$$n[\text{thickness}] = n_1 + \left(\frac{n_2 - n_1}{d_2 - d_1}\right) \times \text{thickness} \quad (4.11)$$

n_1 & d_1 : Initial refractive index (1.59) and initial film thickness

n_2 & d_2 : Final refractive index and final film thickness

thickness: Film thickness during the swelling

The *thickness* is changing with time. If we have an equation for *thickness* as a function of time, we can replace it in the Fresnel equation. We suggest a one variable stretched exponential equation for thickness as a function of time as follows:

$$\text{thickness}[t] = d_2 + (d_1 - d_2) \times \exp\left(-\left(\frac{t}{a}\right)^2\right) \quad (4.12)$$

t : Swelling time (*min*)

a : Constant

And reflectivity according to Fresnel's equation reads:

$$R_{(z,0)} = rr^* = \frac{r_{0,1}^2 + r_{1,2}^2 + 2r_{0,1}r_{1,2} \cos(2k_{z,1}d)}{1 + r_{0,1}^2 r_{1,2}^2 + 2r_{0,1}r_{1,2} \cos(2k_{z,1}d)} \quad (4.13)$$

The different components of the equation above have been introduced in chapter 3. (d) in Fresnel's reflectivity equation (4.13) was replaced by suggested *Thickness*[t] from equation (4.12). By adjusting (a) for each set of experimental reflectivity-time data, the thickness evolution during the swelling was obtained. The model is done by Mathematica software and is

based on 2 layers (silicon substrate+ polystyrene film). Figures (4.9) - (4.11) show the reflectivity-time data and a plot of the fit to equation (4.13), with stretched exponential thickness function (equation (4.12)). As it is observed, there is good match between data and model at early stages; however this is not true at later stages. This outcome is expected and is in agreement with the theory of case II diffusion that suggests there are different regimes during swelling of the glassy polymer films. At the preliminary stage, there is a bigger driving force for mass uptake due to bigger difference in chemical potential of the vapour and the solvent in the film. The quick mass uptake and subsequent swelling, generates stress in response to the osmotic pressure. In glassy polymers, the chains attached to the substrate have different mobility in comparison to chains at the free surface. While the chains at the free surface are free to stretch in response to a good solvent, there are other areas on the film that show resistance to diffusion of the penetrating molecules. This barrier to the flow of the penetrant to glassy area of the film builds up an osmotic pressure and therefore a subsequent stress in the film. Relaxing of the chains comes with swelling and is a response to the induced stress. However, the diffusion of toluene to the glassy part of the polystyrene film occurs when the chains at the top layer of the film become stretched. This time delay introduces different swelling rates. Therefore, a single stage thickness evolution model can not fully describe the behaviour of the system.

Equation (4.12) is an empirical equation. To start, I tried a two variable stretched exponential equation for thickness as a function of time as follows:

$$thickness[t] = d_2 + (d_1 - d_2) \times \exp\left(-\left(\frac{t}{a}\right)^b\right) \quad (4.13)$$

a & b : Constant

I tried different values and combinations of a and b . The best general result was obtained with $b = 2$ and fitting a for different curves. The Mathematica programme, version 5.2 was used for modelling and fitting this equation to the

data. To find the best value for the constants in equation (4.13), different numbers were assigned to a and b and the programme was run to plot the curve. The author believes that the final version of Mathematica at this time (version 6) has an option to evaluate a big range of numbers at the same time. This option provides a better opportunity for fitting and makes it easier to find the best match between the data and the fit.

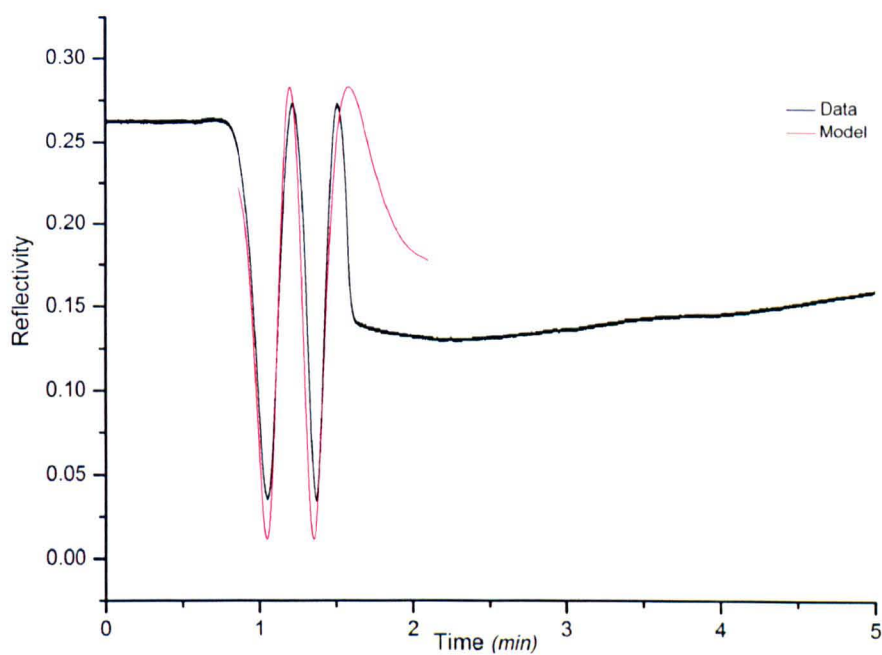


Figure (4.9) A polystyrene film of thickness 1150 nm was exposed to toluene at vapour pressure of 19.61 mmHg . The variable parameter (a) in equation (4.12) is 0.51 .

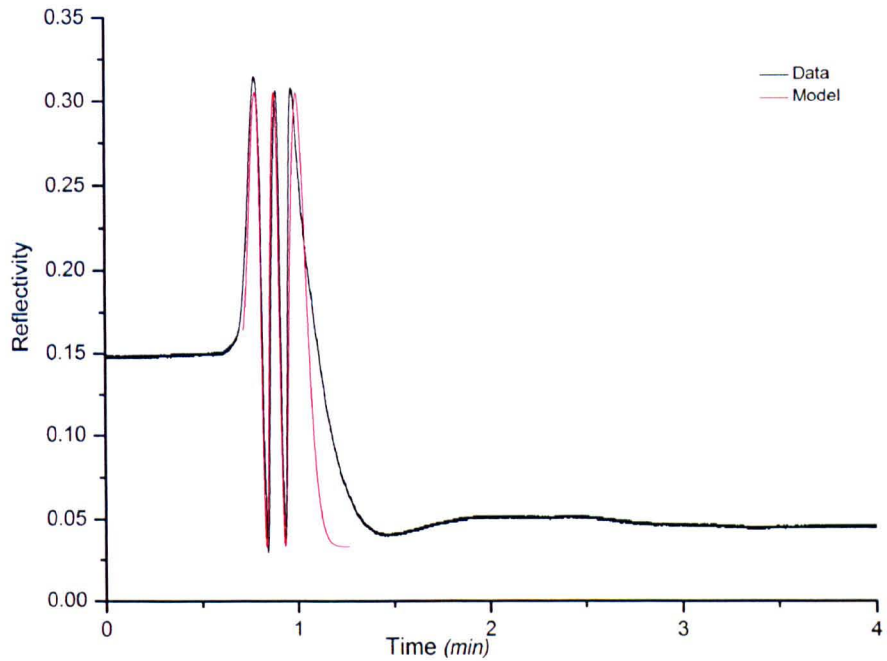


Figure (4.10) A polystyrene film of thickness 1270 nm was exposed to toluene at vapour pressure of 19.61 mmHg . The variable parameter (a) in equation (4.12) is 0.22 .

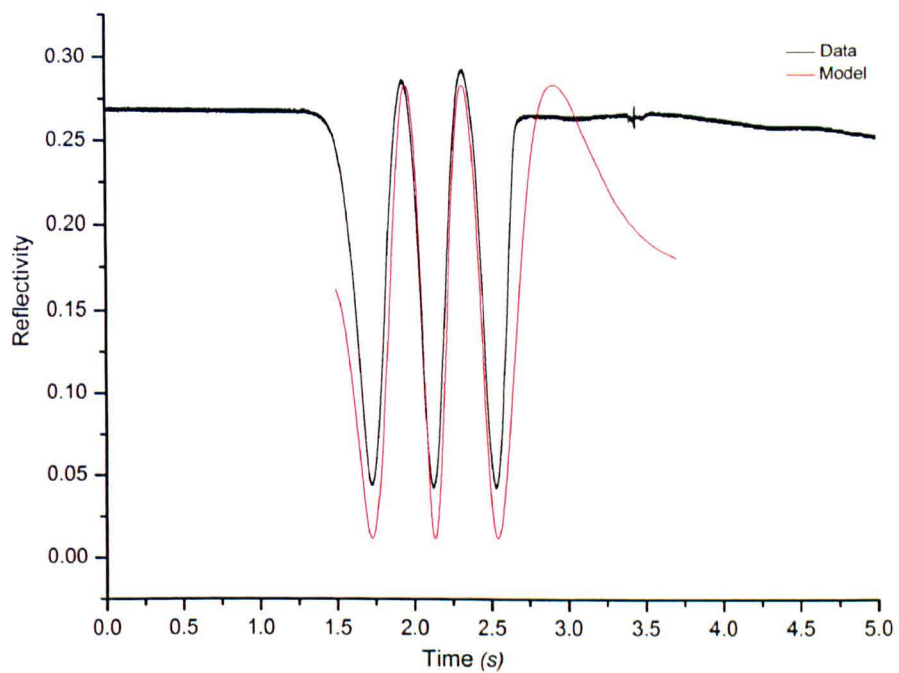


Figure (4.11) A polystyrene film of thickness 1400 nm was exposed to toluene at vapour pressure of 19.61 mmHg . The value of (a) in equation (4.12) is 0.92 .

4.3 Summary

In this chapter the optospinometer was modified by reducing the beam size by means of a beam expander and a diaphragm. To eliminate the effect of interference of the scattered laser beam and light from the surrounding environment the camera and the screen were mounted at the two ends of a black box made of aluminium. The box was painted black to avoid any reflection from a shiny surface.

The stability of the gas flow and uptake of toluene in environmental cell was examined by exposing the polystyrene film to toluene vapour and examining the equilibrium behaviour at different vapour pressures. Reflectivity was modelled by using the Fresnel equations and one variable stretched exponential model was suggested for thickness evolution during swelling

($thickness[t] = d_2 + (d_1 - d_2) \times \exp(-(\frac{t}{a})^2)$). Matching the model to the

experimental data shows that the thickness evolution has more than just one phase. In other words, stretching the chains happens with different rates as the swelling front proceeds. This is in agreement with the theory of case II diffusion for glassy polymers. Since the mobility of the chain is different with depth of the film, there is a time delay for the vapour molecules to diffuse through the whole thickness of the film. Therefore there is a front where behind it the polymer is highly plasticised and ahead of it still glassy. This builds up an osmotic pressure on the surface of the film. The swelling of the chains is a response to relax this stress. The solvent/vapour can diffuse further only when the chains are swollen by the solvent. In our model, a fit of the proposed thickness-time equation initially shows a good match with the experimental data. But before reaching the equilibrium there is a deviation in the model. This is possibly due to diffusion of the front towards the glassy region of the film.

Overall, the gas stability inside the environmental cell is in a good condition. In the next chapter we will spin cast toluene at different vapour pressures in

the environmental cell and establish a model to extract the evaporation rate during the spin coating.

4.4 Bibliography

1. Sharp, J.S. and R.A.L. Jones, Swelling-induced morphology in ultrathin supported films of poly(d,l-lactide). *Physical Review E*, 2002. 66(1).
2. Gall, T.P. and E.J. Kramer, Diffusion of Deuterated Toluene in Polystyrene. *Polymer*, 1991. 32(2): p. 265-271.
3. Gall, T.P., R.C. Lasky, and E.J. Kramer, Case-II Diffusion - Effect of Solvent Molecule Size. *Polymer*, 1990. 31(8): p. 1491-1499.
4. Alfrey, T., E.F. Gurnee, and W.G. Lloyd, Diffusion in Glassy Polymers. *Journal of Polymer Science Part C-Polymer Symposium*, 1966(12PC): p. 249-&.
5. Frisch, H.L., T.T. Wang, and T.K. Kwei, Diffusion in Glassy Polymers .2. *Journal of Polymer Science Part a-2-Polymer Physics*, 1969. 7(5PA2): p. 879-&.
6. Petropoulos, J.H., Sorption Longitudinal Swelling Kinetic Correlations in Polymer Film Vapor Systems. *Journal of Membrane Science*, 1984. 17(3): p. 233-244.
7. Peterlin, A., Diffusion in a Network with Discontinuous Swelling. *Journal of Polymer Science Part B-Polymer Letters*, 1965. 3(12PB): p. 1083-&.
8. Peterlin, A., Diffusion in a Glassy Polymer with Discontinuous Swelling .2. Concentration Distribution of Diffusant as Function of Time. *Makromolekulare Chemie*, 1969. 124(MAY): p. 136-&.
9. Thomas, N.L. and A.H. Windle, Diffusion Mechanics of the System Pmma-Methanol. *Polymer*, 1981. 22(5): p. 627-639.
10. Thomas, N.L. and A.H. Windle, A Theory of Case-II Diffusion. *Polymer*, 1982. 23(4): p. 529-542.
11. Crank, J., A Theoretical Investigation of the Influence of Molecular Relaxation and Internal Stress on Diffusion in Polymers. *Journal of Polymer Science*, 1953. 11(2): p. 151-168.

12. Thomas, N. and A.H. Windle, *Case-Ii Swelling of Pmma Sheet in Methanol. Journal of Membrane Science*, 1978. **3**(2-4): p. 337-342.
13. Astarita, G. and G.C. Sarti, *Class of Mathematical-Models for Sorption of Swelling Solvents in Glassy Polymers. Polymer Engineering and Science*, 1978. **18**(5): p. 388-395.
14. Sarti, G.C., *Solvent Osmotic Stresses and the Prediction of Case Ii Transport Kinetics. Polymer*, 1979. **20**(7): p. 827-832.
15. Mills, P.J., C.J. Palmstrom, and E.J. Kramer, *Concentration Profiles of Non-Fickian Diffusants in Glassy-Polymers by Rutherford Backscattering Spectrometry. Journal of Materials Science*, 1986. **21**(5): p. 1479-1486.
16. Hui, C.Y., et al., *Case-Ii Diffusion in Polymers .1. Transient Swelling. Journal of Applied Physics*, 1987. **61**(11): p. 5129-5136.
17. Hui, C.Y., et al., *Case-Ii Diffusion in Polymers .2. Steady-State Front Motion. Journal of Applied Physics*, 1987. **61**(11): p. 5137-5149.
18. Thomas, N. and A.H. Windle, *Transport of Methanol in Poly(Methyl Methacrylate). Polymer*, 1978. **19**(3): p. 255-265.
19. Jones, R.A.L.a.R., Randal W, *Polymers at Surfaces and Interfaces*. 1999, UK: Cambridge University Press.
20. Sharp, J.S., J.A. Forrest, and R.A.L. Jones, *Swelling of Poly(DL-lactide) and polylactide-co-glycolide in humid environments. Macromolecules*, 2001. **34**(25): p. 8752-8760.

Chapter 5

Evaporation Rate in Spin Coating

5.1 Introduction

As discussed previously there are two major stages in the spin coating process. First, the solution is spread on the substrate until the shear force balances the centrifugal force. Then at the second stage evaporation takes over and become the dominant mechanism of film thinning.

Despite the importance of evaporation rate on film quality, there is no systematic technique to study the effect of evaporation rate on the film thinning. So far, most studies have used different solvents with different vapour pressures to study the effect of evaporation rate on film morphology. The higher the vapour pressure is the higher the evaporation rate. We believe that employing different solvents is not an ideal way of studying the effect of evaporation rate during spin coating. Different solvents have different affinity or χ factor and solubility with polymers and different viscosity. These constraints can alter the kinetics of film formation. Therefore, by using different solvents, evaporation will not be the only factor influencing the system. In this chapter we will show how we determined the evaporation rate during spin coating at different vapour pressures.

To establish a quantitative relationship between the process variables – the temperature of the solvent reservoir and the flow rates of the carrier gas – and the evaporation rates, we carried out a series of measurements of the time-evolution of the thickness of a film spun from pure solvent. From this data, we were able to extract quantitatively the evaporation rate for a given set of process variables and spin speed. For this analysis, we used the model of Meyerhofer and by solving its equation we managed to extract a quantitative value for evaporation rate during the spin coating.

This calibration is then used in our subsequent experiments on the spin coating of blends in chapter 6.

5.2 Controlled vapour pressure atmosphere

The first sets of experiments were done by spinning liquid toluene at different vapour pressures in the environmental cell. The reflectivity- time data were collected and a typical graph is shown in figure (5.1).

Fringes are due to constructive and destructive interference of reflected beam from the surface and interfaces of the film and substrate. Between each two subsequent peaks film thins by Δd which is given by equation (3.16)

$\Delta d = \lambda/2n \cos \theta$. To calculate the internal angle (θ) we use Snell's law:

$$n_0 \sin \beta = n_1 \sin \theta \quad (5.1)$$

β : The incident angle regarding to the normal line

n_0 & n_1 : Refractive index of air and toluene respectively

θ : The internal angle

In our experimental set up, the incident angle is 45 degrees, the refractive index of toluene is 1.5 and the wavelength of the laser is 633 nm. By replacing these values

in equation (5.1), we have $1 \cdot \sin 45 = 1.5 \cdot \sin \theta$ and therefore $\cos \theta = 0.88191$. Using equation 3.16 and replacing all values we obtain Δd as below:

$$\Delta d = \frac{633}{2 \cdot 1.5 \cdot 0.881917} = 239.235 \text{ nm}$$

Knowing the difference in thickness between each two subsequent fringes and by counting back the number of fringes, we were able to plot thickness-time profile for toluene at each vapour pressure. It should be mentioned that when the reflectivity becomes constant, it means that no toluene is left and the thickness has reached zero. We call the corresponding time (t_f). Figure (5.2) shows a typical thickness-time curve for toluene.

The next step was to control the evaporation rate of the solvent. Toluene was spun cast in our environmental cell in controlled vapour atmosphere. Nitrogen gas was blown through a bubbler containing toluene in a water bath. By controlling the temperature of the bath, toluene vapour was produced at different saturated vapour pressures. If necessary, to reach a certain desired concentration of toluene, the vapour was mixed with nitrogen before entering the cell. Table (5.1) shows the vapour pressure and concentration of toluene at different temperatures. It is to be expected that the higher the vapour pressure inside the cell, the slower the evaporation of the toluene from the spinning substrate. To test our idea we filled the cell with gas at different vapour pressures and spin cast toluene while the reflectivity-time data was collected. Figure (5.3) shows the results for some selected vapour pressures. Increasing the vapour pressure shifts the end point time (t_f) towards longer times. These results prove that our experiment is working and we are able to manipulate the evaporation rate by controlling the environmental parameter.

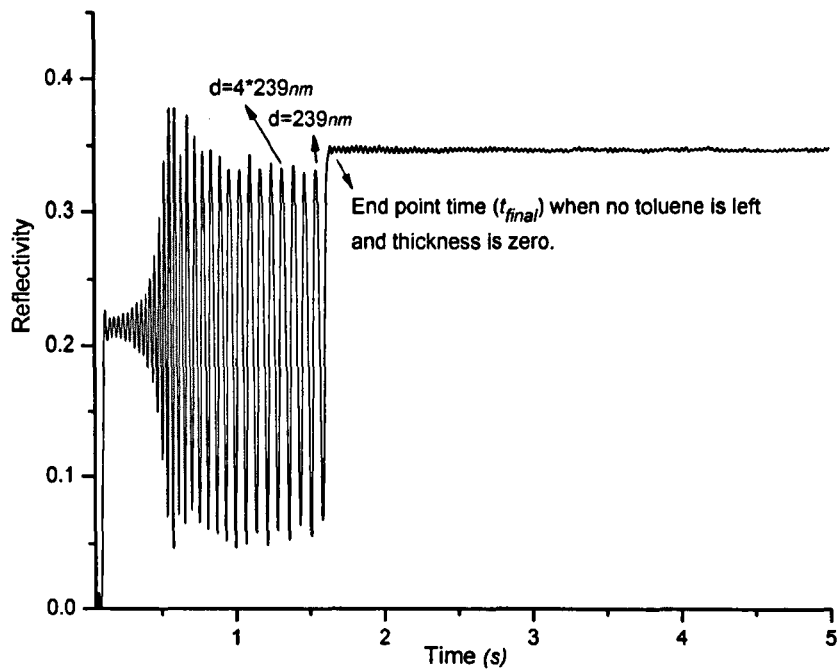


Figure (5.1) Reflectivity-time data for toluene during spin coating. The thickness change between every two subsequent fringes has been calculated ($\Delta d = 239\text{nm}$). By knowing that there is no toluene at $t = t_f$ and the thickness is zero and by counting back the number of fringes, thickness-time curve can be constructed. See figure (5.2).

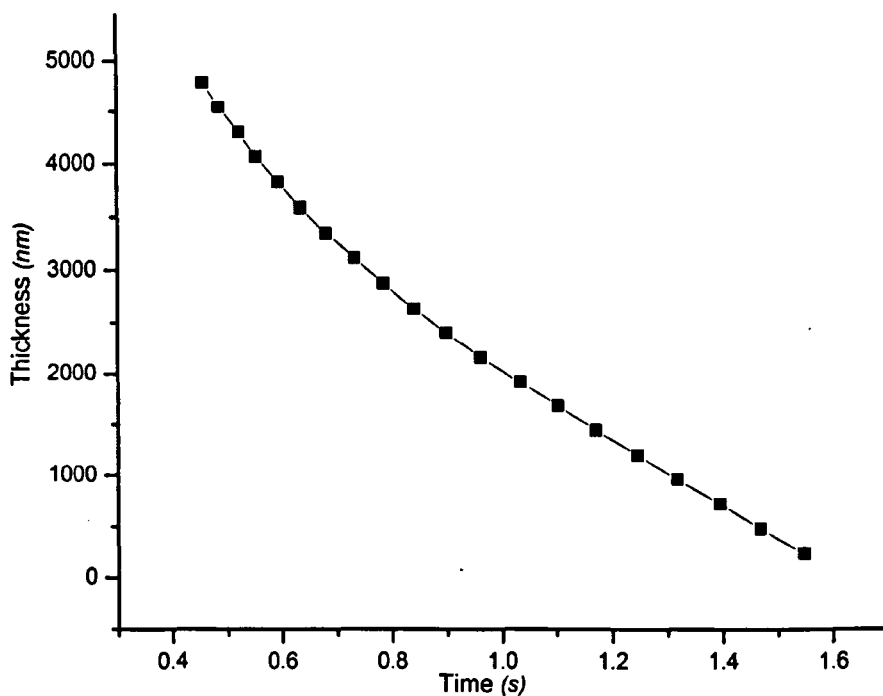


Figure (5.2) Thickness via time during spin coating of toluene. Data points extracted from figure (5.1).

Table (5.1) Vapour pressure and concentration of toluene at different temperature

Temperature (°C)	Vapour pressure (mmHg)	Concentration%
25	28.47	3.75
20	21.86	2.88
18	19.61	2.58
16	17.56	2.31
14	15.69	2.06
12	13.99	1.84
10	12.45	1.63
8	11.06	1.45
6	9.81	1.29
4	8.67	1.14
2	7.66	1.00
1	7.19	0.95
0.5	6.96	0.91

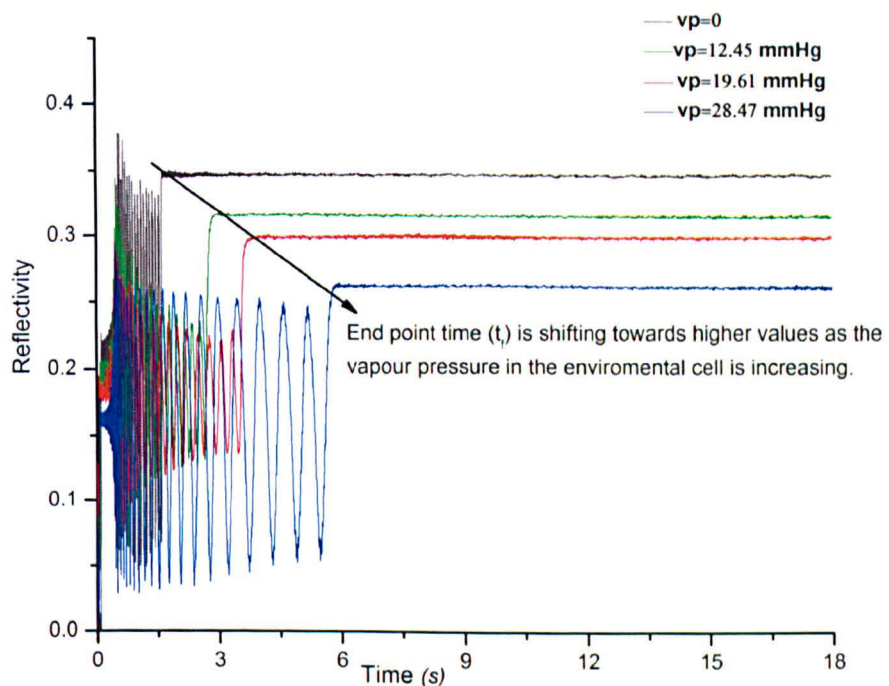


Figure (5.3) Comparing reflectivity-time plot for toluene at different vapour pressures. The black curve is when there is no toluene in the cell. By increasing the vapour pressure inside the cell, we can manipulate the thinning rate and make it evolve slower. v_p is indicative of nominal vapour pressure of toluene in the environmental cell.

5.3 Extracting the evaporation rate in spin coating

In the previous section we have shown that it is possible to control the evaporation rate. The next challenge was to extract the evaporation rate at each saturated pressure. We made our calculations based on the Emslie, Pecker and Boner (EPB) and Meyerhofer equation. To the knowledge of the author so far, this equation has not been solved analytically. We have solved Meyerhofer equation and extracted the evaporation rate value by fitting parameters for our experimental data. The details will be explained in the next section.

5.3.1 Solving Meyerhofer's equation

To extract the value of evaporation rate from these curves, we have used EPB and

Meyerhofer equation, $\frac{dh}{dt} = -2kh^3 - e$.

Using the reduced variables where $x = Ah$ and $s = Bt$, the above equation can be written as below provided that A and B fulfil relations (5.3) and (5.4):

$$\frac{dx}{ds} = -2x^3 - 1 \quad (5.2)$$

$$k = A^2 B \quad (5.3)$$

$$e = \frac{B}{A} \quad (5.4)$$

Rearranging equation (5.2), we have :

$$\int \frac{dx}{-2x^3 - 1} = \int ds \quad (5.5)$$

Which has the solution:

$$s = \frac{1}{\sqrt[3]{216}} \left[-\ln \frac{(1 + \sqrt[3]{2}x)^2}{1 - \sqrt[3]{2}x + \sqrt[3]{4}x^2} - 2\sqrt{3} \text{Arc tan} \left[\frac{-1 + \sqrt[3]{4^2}x}{\sqrt{3}} \right] \right] - C \quad (5.6)$$

Where the integration constant, C , related to the time t_{final} at which the film thickness becomes zero.

$$s = Bt = f[x] - C \quad (5.7)$$

$$C = f[0] - B * t_{final} \quad (5.8)$$

t_{final} can be read from reflectivity-time graph at each vapour pressure. By replacing C in equation (5.6), we obtain the relation below as Meyerhofer's equation answer.

$$s = \frac{1}{\sqrt[3]{216}} \left[-\ln \frac{(1 + \sqrt[3]{2}x)^2}{1 - \sqrt[3]{2}x + \sqrt[3]{4}x^2} - 2\sqrt{3} \text{Arc tan} \left[\frac{-1 + \sqrt[3]{4^2}x}{\sqrt{3}} \right] \right] - (f[0] - B * t_{final}) \quad (5.9)$$

By adjusting the constants A and B for each applied vapour pressure, we obtain good fits between equation (5.9) and our experimental data which is plotted in figure (5.4); from the fitted values of A and B we calculate the evaporation rate for each value of the applied vapour, which is plotted in figure (5.5). As expected, the higher the nominal vapour pressure is inside the cell, the lower the evaporation rate. Appendix A shows the details of what has been done for fitting.

5.3.2 Governing mechanisms for film thinning during spin coating

In Meyerhofer's calculation it was assumed that spin coating has two major stages and each step is governed by a different mechanism. At the beginning, the film thinning is governed by hydrodynamic flow in which shear and centrifugal forces compete until a viscous layer is formed. After this, the solvent starts to evaporate. Our results provide direct evidence in favour of Meyerhofer's theory.

Thickness-time profiles for toluene at different evaporation rates is shown in figure (5.4). The black curve shows when the film was made at ambient temperature and there is no gas flowing inside the cell. Here the evaporation rate is highest. Moving towards the blue curve the vapour pressure inside the cell is increasing and the blue curve shows when toluene is spin cast in the highest possible vapour atmosphere (low evaporation rate). This is the second evidence to suggest that by changing the vapour pressure of the flowing gas we can either decrease or increase the evaporation rate of the solvent. The predominant feature in this graph is that at the beginning of spinning, regardless of evaporation rate all curves fall on the same path clearly implying that hydrodynamic thinning is dominant at the beginning of spinning. However when the films reach about one third of their thickness, the evaporation becomes dominant and they behave differently as expected and show a variable thinning rate. This provides strong support for Meyerhofer's theory.

5.4 Conclusion

In this chapter, I have shown how to make a thickness-time profile when we have an evaporative solvent during spin coating. This is different from constructing a thickness-time profile for a spin cast film (polymer +solvent) as explained in chapter four. This is due to the fact that when we have only solvent in the system,

the thickness of the film will become zero when the solvent is totally evaporated. As no film is formed at the end, it is not possible to start from final film thickness and count back the number of fringes to construct the thickness-time profile. Instead we chose a different approach. Using Snell's law and Bragg's law, we calculated the thickness variation between two subsequent fringes and by knowing that the final thickness is zero, we constructed the thickness-time profile for toluene during the spin coating at different vapour pressures.

We extracted the evaporation rate of a solvent during the spin coating by using the Meyerhofer equation for the thinning rate of a spin cast film. By fitting the solution to the thickness-time profile modelled from reflectivity-time data, we extracted the value of evaporation rate for toluene at different vapour pressures. The results provide direct evidence in favour of Meyerhofer's theory; this suggests that film thinning happens in two different stages with at least two different mechanisms. At the beginning, the film thinning is governed by hydrodynamic flow in which shear and centrifugal forces compete until a viscous layer is formed. Evaporation becomes the main player at the second stage. The thickness-time profile shows that at the beginning of the spin coating, the thinning rate is almost the same for all films regardless of evaporation rate (hydrodynamic thinning). When the evaporation takes place, the rate of thinning is proportional to evaporation rate. The higher the evaporation rate is, the quicker the layer thins.

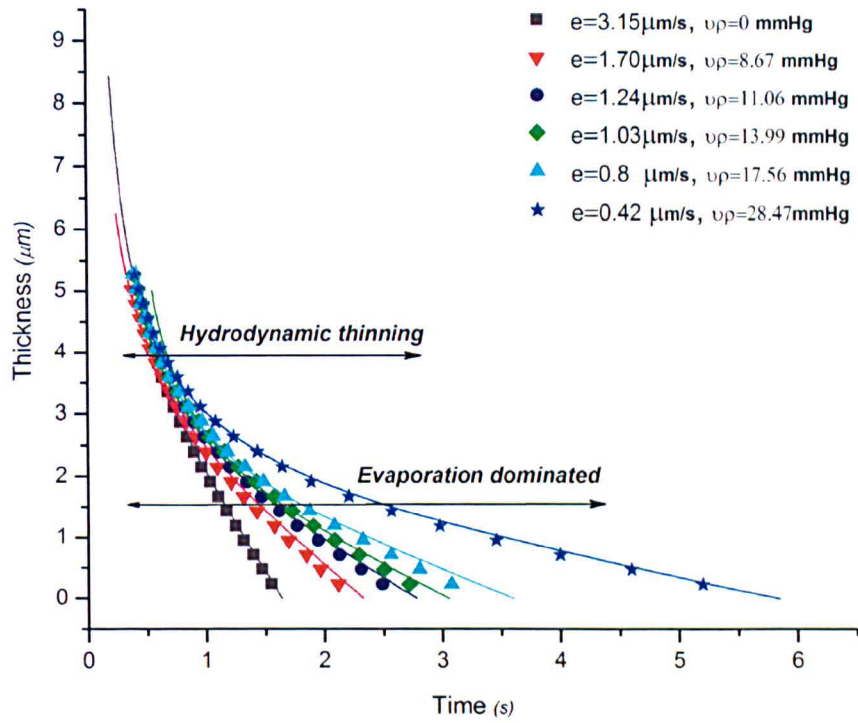


Figure (5.4) Thickness time profile for toluene at different saturated vapour pressure. The evaporation rate is controlled by changing the vapour pressure inside the cell. The black curve is related to highest evaporation rate. For the blue curve, it takes longest for the toluene to evaporate due to the higher saturated vapour pressure inside the cell and therefore slower evaporation rate.

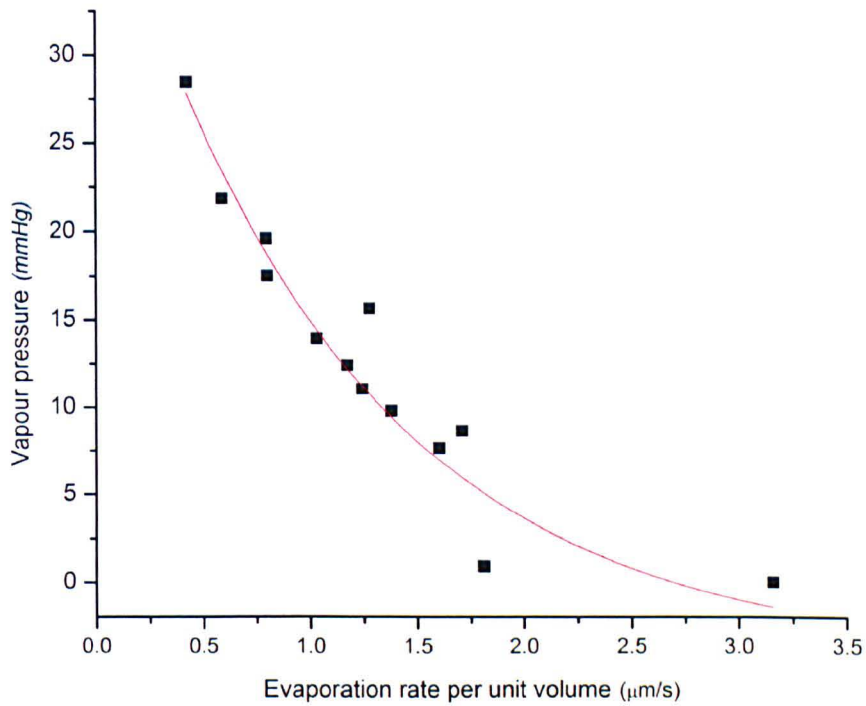


Figure (5.5) Evaporation rate of spin coated toluene on silicon substrate at different vapour pressure. The values have been extracted by fitting A and B in equation 4.9 for each set of experiment. The red curve is a guide to eye.

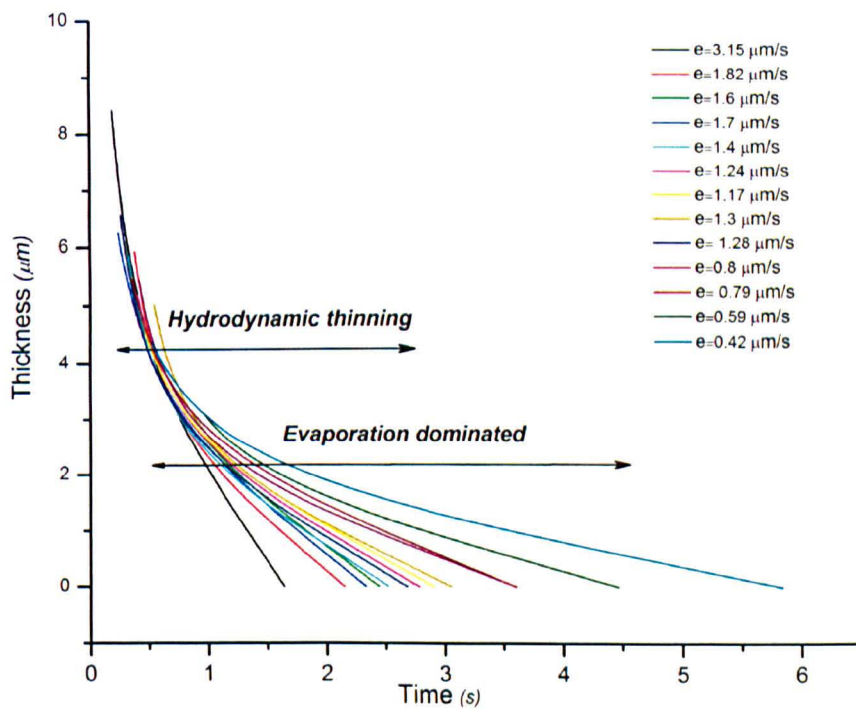


Figure (5.6) Thickness time profile for toluene at different saturated vapour pressure. Figure (5.4) with more plots.

Chapter 6

Controlling Instabilities during Spin Coating through Evaporation Rate

6.1 Introduction

Previous experimental work in our group shows strong evidence to support the model for the mechanism of film formation due to Walheim et al. During spin casting polymer blends initially form transient self-stratified layers due to preferential attraction of one of the components by the surface. The factor that determines if the film is self-stratified is if these layers subsequently break up due to instability at the interfaces between these layers. Usually the interface becomes unstable and will lead to a laterally phase separated structure figure (6.1).

In this chapter we will address the origin of the interfacial instability. Our hypothesis is that a Marangoni type instability[1-3], which we believe is driven

by a gradient of solvent evaporation from the substrate to the surface of the film, is the governing mechanism for interfacial instability.

One way to test this hypothesis is by changing the concentration gradient in the film. The concentration gradient is due to solvent evaporation. During the spin coating, the solvent is removed from the system by evaporation. If the rate of evaporation is greater than the diffusion of the solvent to make solvent concentration uniform through the film- then a concentration gradient will form causing a variation in interface tension profile in the film. The mechanism is schematically illustrated in figure (6.2).

Therefore if the generation of such a gradient across the film makes the interface physically unstable, it should be possible to see the difference in structure by changing the evaporation rate in a spin coating film.

In the previous chapter we have shown how to control and extract the evaporation rate from a spin cast film. It was shown that introducing toluene gas in the cell can suppress the evaporation rate from the spinning film. In this chapter, the evolution of the PS/PMMA film structure in vapour atmosphere i.e. different evaporation rate will be discussed and the Marangoni instability will be addressed.

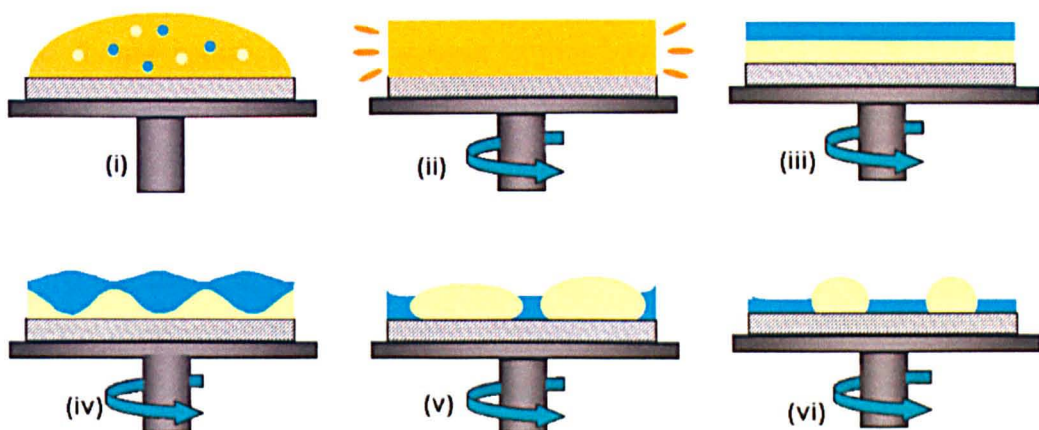


Figure (6.1) Proposed mechanism of film formation during spin coating of an immiscible blend [4].

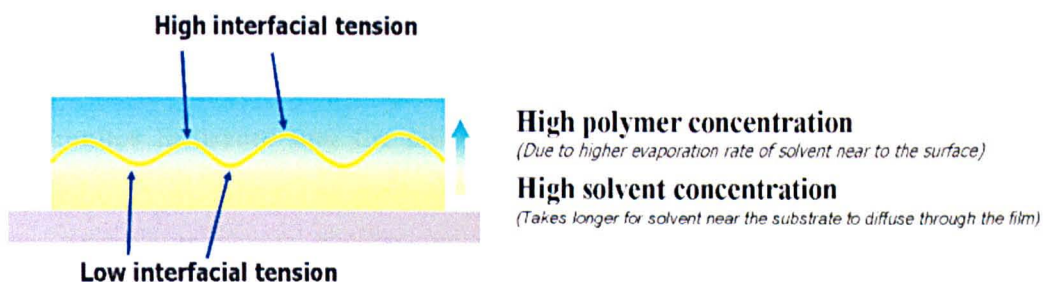


Figure (6.2) Schematic of concentration gradient during spin coating which creates an interfacial tension profile in the solution.

6.2 Design of experiment

To study the interfacial instability of polymer blend during the spin coating, we considered the Marangoni instability as the origin of this instability. The Marangoni instability happens as a result of a concentration gradient in the film. Therefore we had to find a method to control the concentration gradient. We tested the idea by controlling the evaporation rate in the environmental cell. The inspiration was that if the vapour pressure inside the cell is high, this will suppress the evaporation rate. Lower evaporation rate will let the diffusion suppress the solvent concentration gradient in the film. As a result the Marangoni instability will be repressed. Vice versa, increasing the evaporation rate should create a strong solvent concentration gradient and this in turn should trigger the Marangoni instability. Depending on if the instability is suppressed or enhanced we should be able to create a range of morphologies from self-stratified to laterally phase separated structure.

In the last two chapters, it is explained how we controlled the vapour pressure and the evaporation rate in the environmental cell.

A blend of 50:50, PS/PMMA, 10% concentration by weight in toluene was prepared. The silicon substrate was cleaned by plasma cleaning. After the substrate was placed on the spin coater chuck, the beam splitter was adjusted to obtain the true reflectivity for silicon and also the best image on the screen. The environmental chamber was positioned and filled with gas. The vapour

pressure of the gas was controlled by a water bath with a bubbler containing toluene. The full set up is explained in chapter 3. The waiting time was at least 3 minutes to assure that the cell was saturated with gas. The substrate was rinsed off with toluene to remove any dust or particles. A pipette assembled on top of the cell was used to dispense a few drops of the blend on the substrate and it was spun for 20 seconds at 2000 r.p.m. During spinning, the reflectivity and off specular data were collected and subsequently analysed by means of different methods.

6.2.1 Analysing off specular data

The scattered light is projected on a screen and recorded by a CCD camera which takes 600 images during 20 seconds of spin coating. Any instability in the film will be visible as off specular light (scattering). Any defined length scale in the film, will show an off specular ring. Evolution of this ring provides direct information on structure evolution and in particular length scale formation.

In what follows, the procedure to convert scattering images to length scale-time graph (q – space) will be explained. Each point in the ring is presented by its distance from the centre and the angle θ in figure (6.3(a)). Figure (6.3(b)) shows the cartoon of the unwrapped image of intensity. Due to the symmetric shape of the ring, half of it is considered for intensity calculation. This is schematically illustrated in figure (6.3(c)). A plot of intensity via pixel number at a time t is shown in figure (6.3(d)). These curves have been radially averaged over time. Radially averaged intensity data have been used to plot q via t . $Q(t)$ is related to length scale in reciprocal space (or q – space) and is equal to $q = \frac{2\pi}{d}$, where d is length scale. The system was calibrated by an AFM grid with 10 μm features. The distance between the screen and coating stage was 56 cm. Figure (6.4) is $q-t$ plot for PS/PMMA film during spin

coating. As seen, the onset of instability and structure evolution can be probed by means of this graph.

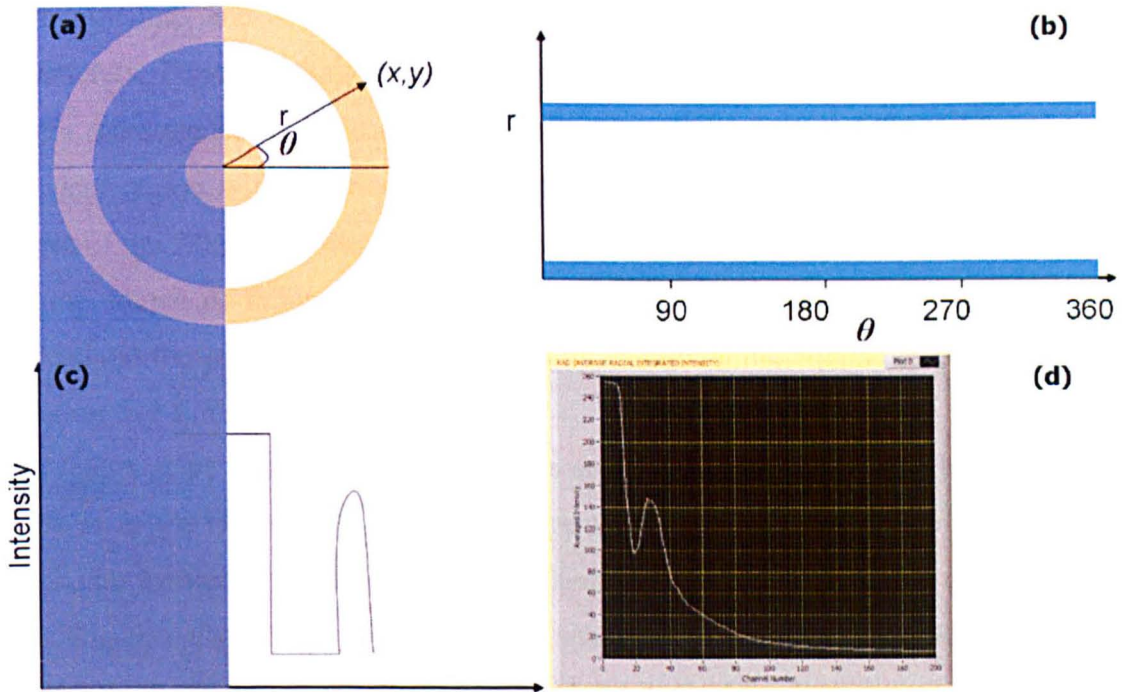


Figure (6.3) (a) Each point in the image is presented by r and θ . (b) unwrapped image of intensity. (c) Due to symmetric shape of the circle, only Intensity of half of the image is analysed. (d) A plot of intensity via pixel number/time frame at any time in lab view programme.

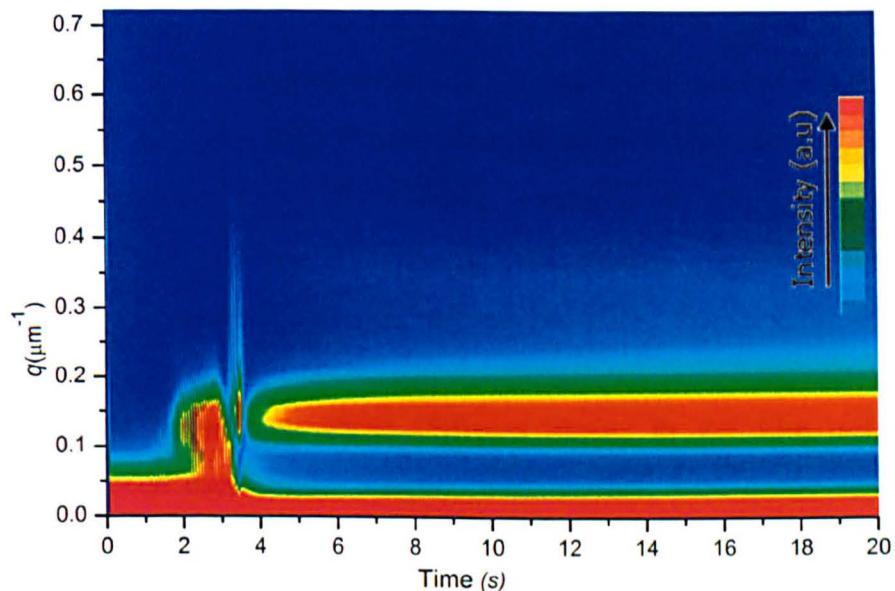


Figure (6.4) Structure development for PS/PMMA sample during spin coating. Different regions in this image are explained in figure (6.15). The colours represent the intensity as determined by the key on the plot.

6.3 Phase separation in PS/PMMA film

Film structure and topography of the film is affected by many different parameters. Figure (6.5(a)) shows the typical spin cast film structure. In the centre there are isotropic islands of PMMA in a cellular pattern followed by a transient region with striation towards the edge. The polygonal cells in the centre of the film are reminiscent of Benard-Marangoni pattern. The striations are the source of failure in devices. Therefore in addition of the interest to understand the physics behind it, there is an industrial motivation to produce striation free films.

The length scale of the striation pattern is approximately $50\ \mu\text{m}$, which is the same as in the isotropic centre. This suggests that the hydrodynamics simply break the symmetry of the instability when the shear field is large without affecting the physics that underlines the selection of a length scale. In other words, the formation of striations is not independent of the factors that control the overall film structure.

The CCD camera records the scattered light from the film. The scattering happens when there is a type of instability such as roughening in the film. The existence of the ring in scattering pattern is indicative of a specific length scale in the structure. Applying Fast Fourier Transform on the optical micrograph reveals a length scale of about $50\ \mu\text{m}$ which is same as the length scale of the scattered ring. It confirms that evolution of the scattering ring during the spin coating can in fact provide valuable information about the dynamic of film formation.

To obtain more information about different phases in the film, selective solvents have been used. Some samples were washed with acetic acid and cyclohexane. The former is a good solvent for PMMA and the latter is a good solvent for PS. Figure (6.6) is a topography AFM image of as cast PS/PMMA film. The bright islands are elevated columns of PMMA that disappeared after washing the sample with acetic acid (figure (6.7(a))). Washing the sample with

cyclohexane at the next stage, removes the PS rich phase from the film (figure (6.8)). PS has a lower surface tension and it is expected to be more abundant at the top surface of the film as this in theory should decrease the free energy of the system. However, the existence of any PMMA on the top surface of the film confirms that film formation is far from its equilibrium.

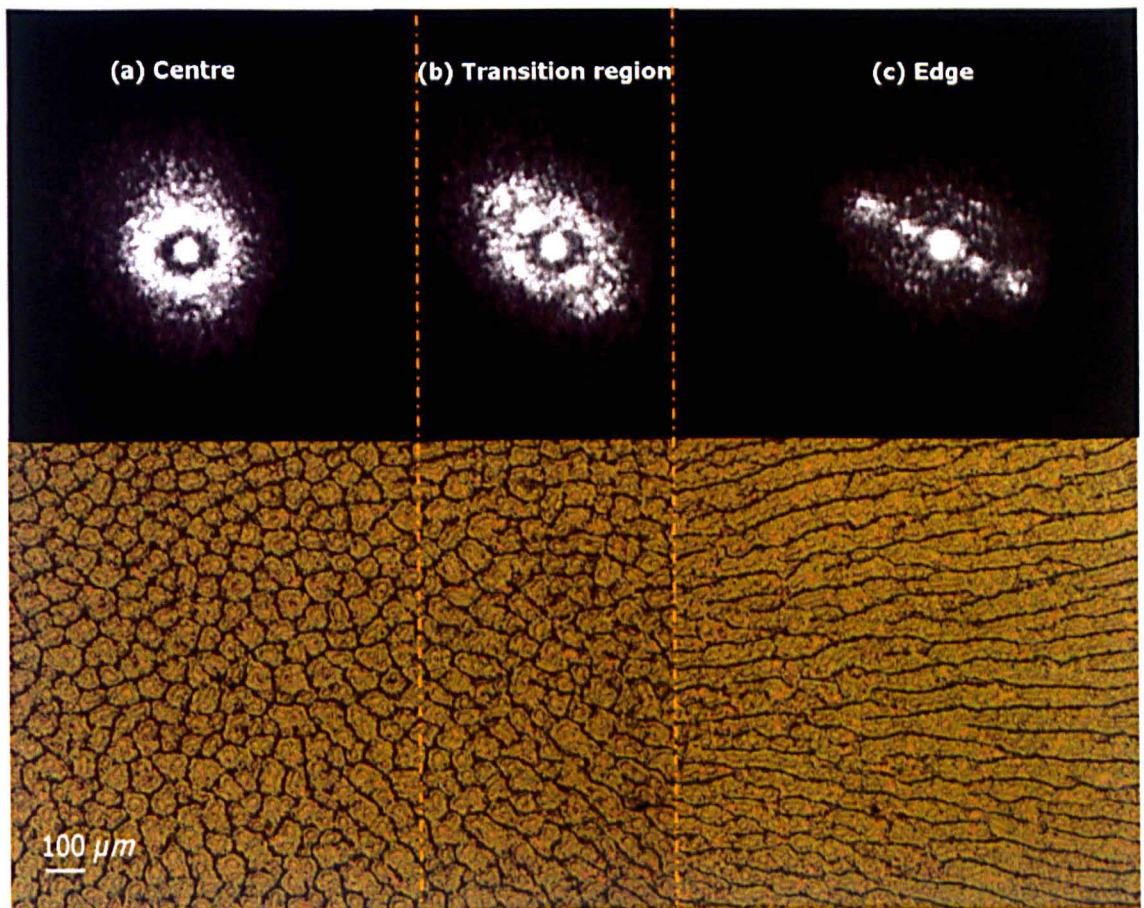


Figure (6.5) Optical micrographs and off specular intensity of a PS/PMA film (a) in the centre (b) transient region and (c) towards the edge of the substrate.

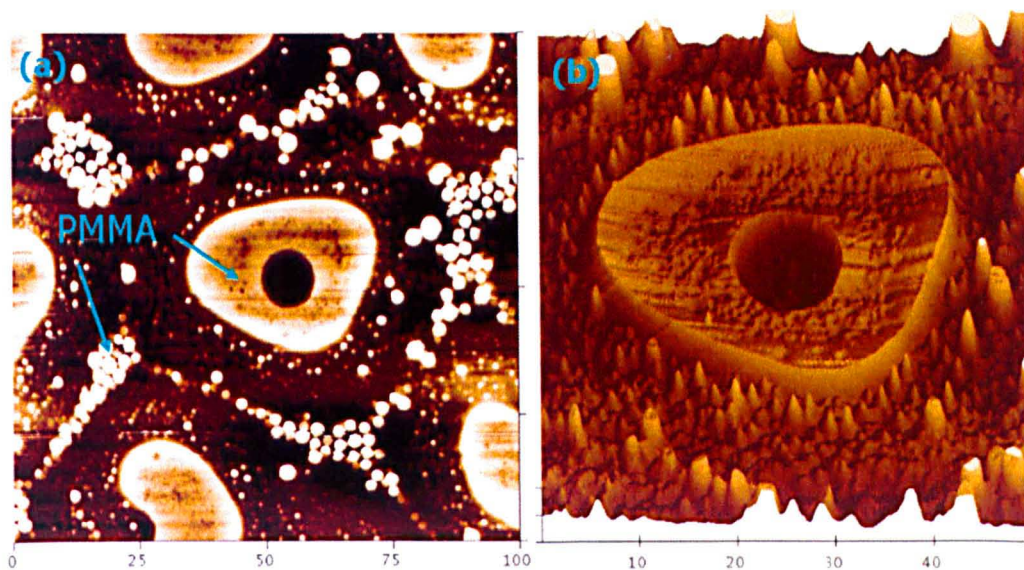


Figure (6.6) (a) A topography AFM image of a as cast PS/PMMA film. The structure is laterally phase separated. The circular domain of one phase is scattered in the matrix of other phase (b) Three dimensional image of the island in the centre of image (a). Features in the island. The surface is concave. The scale is in microns.

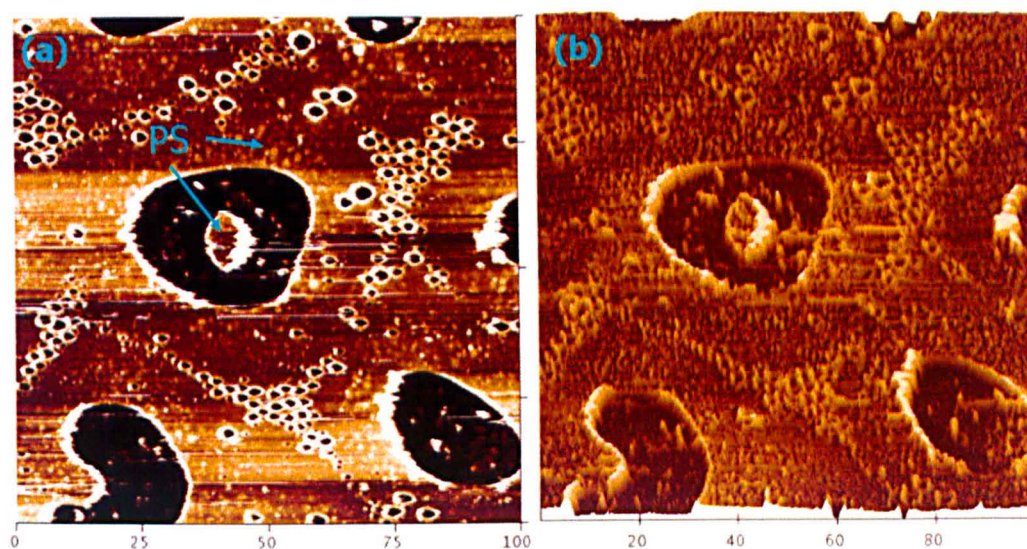


Figure (6.7) (a) A topography AFM image of the sample above after washing in acetic acid to dissolve the PMMA. The elevated islands have disappeared. This shows that they are made of PMMA (b) The three dimensional image of (a). The scale is in microns.

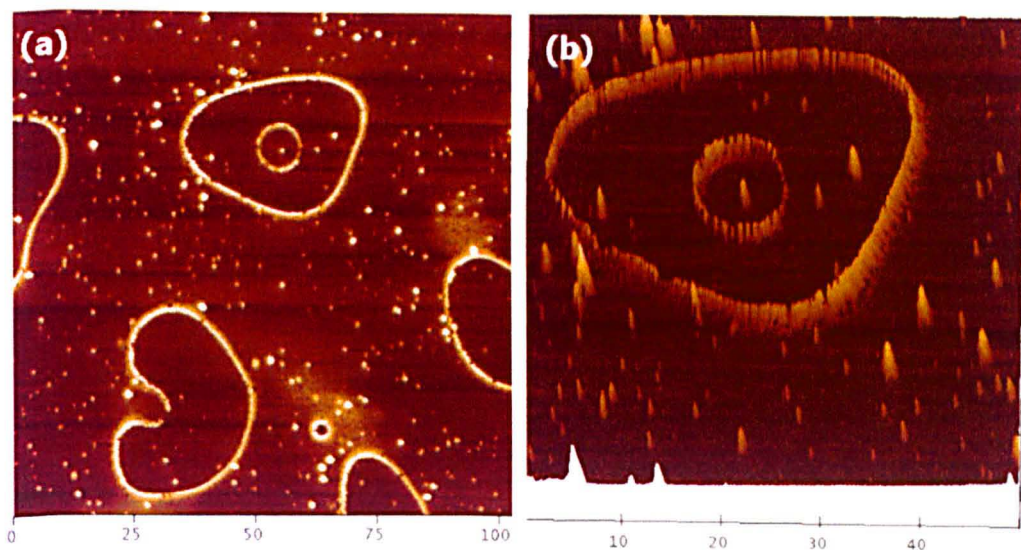


Figure (6.8) (a) The sample in figure (6.7) was washed with cyclohexane, this removed the PS rich phases, however the substrate is not clear yet. A rim is left behind. **(b)** The three dimensional image of the rim in (a). The scales are in microns.

We have repeated the selective washing experiment changing the sequence of washing (i.e the sample was first washed with cyclohexane and then with acetic acid). This was done as a supporting experiment. As expected there is not an obvious change in the morphology of the film washed with cyclohexane. All the PMMA islands are present at the surface as prior to the washing (figure (6.9 (b))). The background is slightly altered by washing. The second stage of washing with acetic acid has removed the islands but PS spikes are still present. See figure (6.9 (c)). Washing the sample one more time with cyclohexane removes the PS content from the film and leaves a shadow of PMMA island. This is seen in figure (6.10). However it should be mentioned that the molecular weights of the polymers in figures ((6.6)-(6.8)) are slightly different from the polymers in figure (6.9) and (6.10).

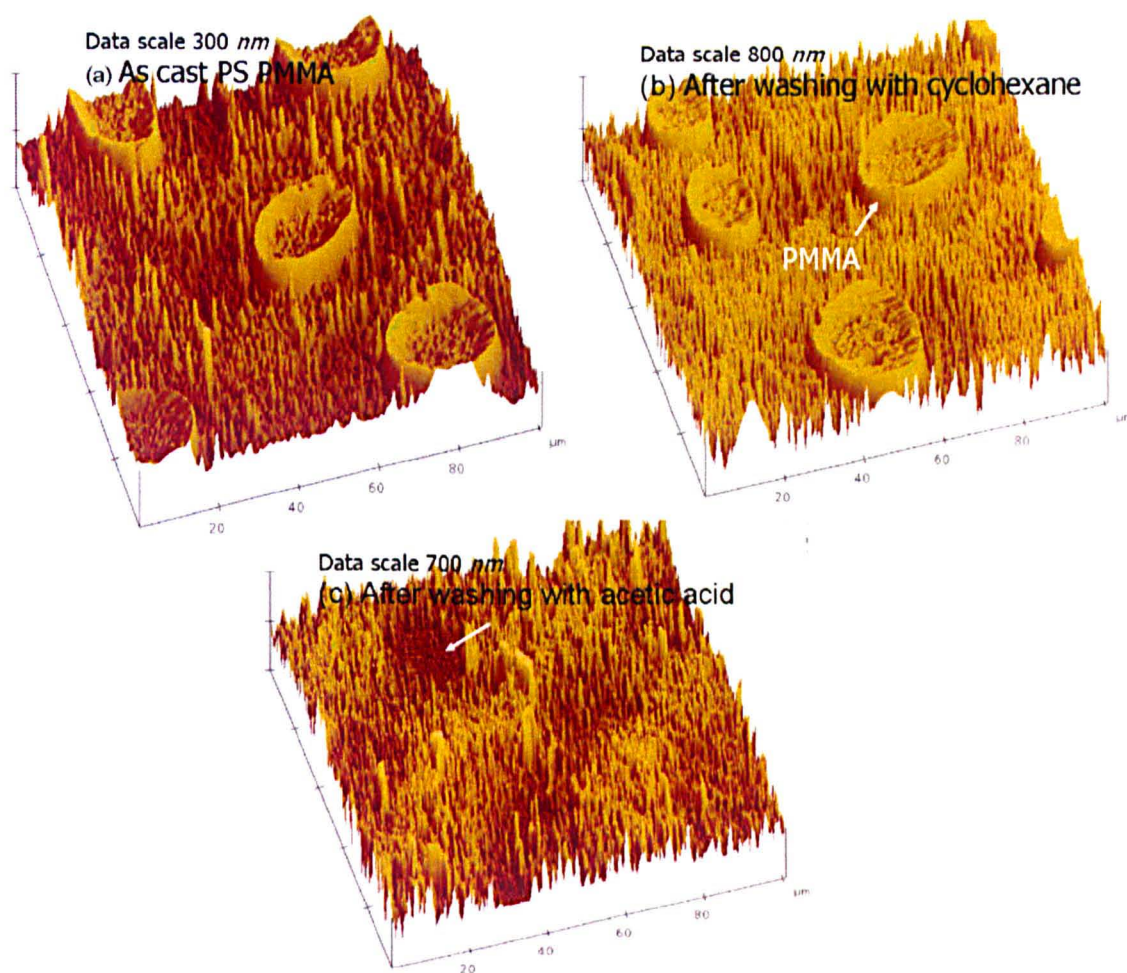


Figure (6.9) (a) 3-dimensional AFM image of as cast PS/PMMA (b) washing the sample with cyclohexane hasn't significantly changed the morphology. This suggests most of the top layer consists of PMMA. (c) Acetic acid has removed PMMA islands but PS is present at the background.

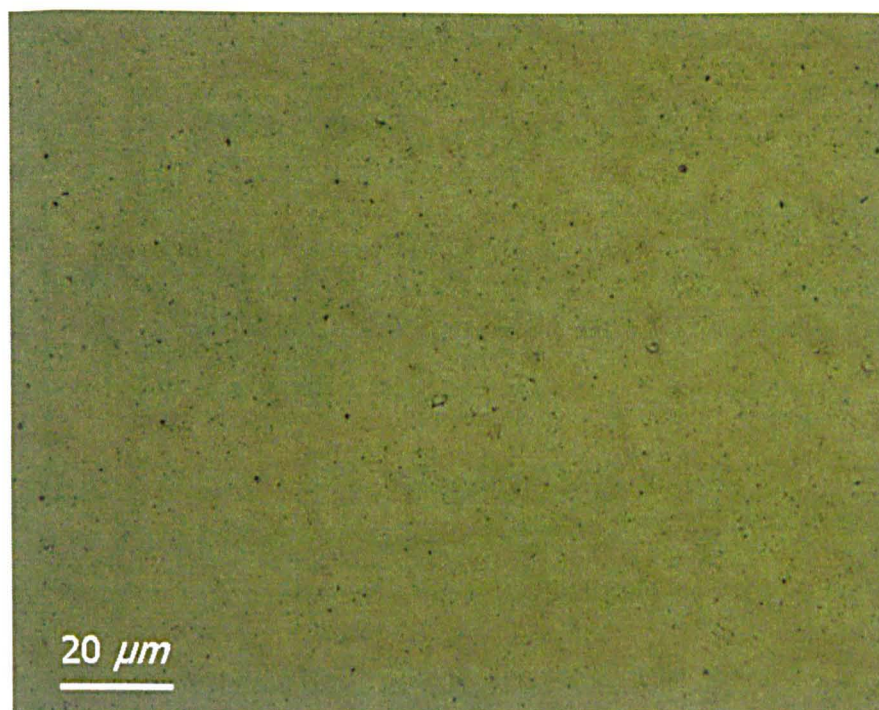


Figure (6.10) PS/PMMA film, first washed with cyclohexane, second with acetic acid and third with cyclohexane. On the substrate there is a shadow of cellular pattern seen at the top surface

6.4 The effect of evaporation rate on film thinning

In Chapter 3 we described how to plot the thickness-time profile for a film during spin coating. Figures ((6.11)-(6.13)) show the reflectivity-time plot for PS/PMMA film with different evaporation rates. The final time (t_f - when there is no toluene in the film) is consistent with the trend in evaporation rate. By measuring the final thickness of the film and applying Bragg's law, the thickness-time curves are plotted in figure (6.14). As expected, this plot is very similar to thickness-time plot for toluene. The initial part of all curves show similar behaviour as hydrodynamic thinning is the governing factor for film thinning at this stage. Later, when evaporation starts to dominate, films thin at different rates. At higher evaporation rates the thinning rate is higher.

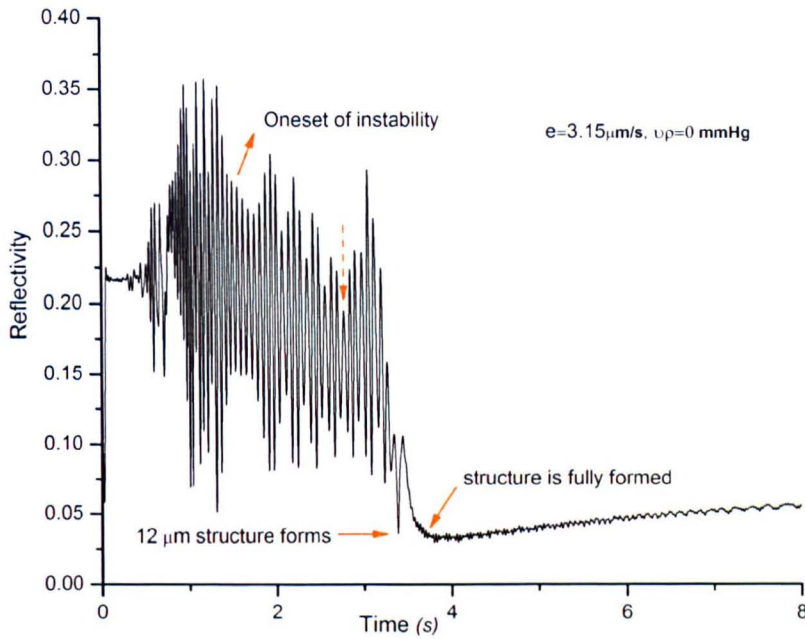


Figure (6.11) Reflectivity time for PS/PMMA film made at atmosphere pressure. The indicated specific time are read from $q-t$ graph in figure (6.15(a)).

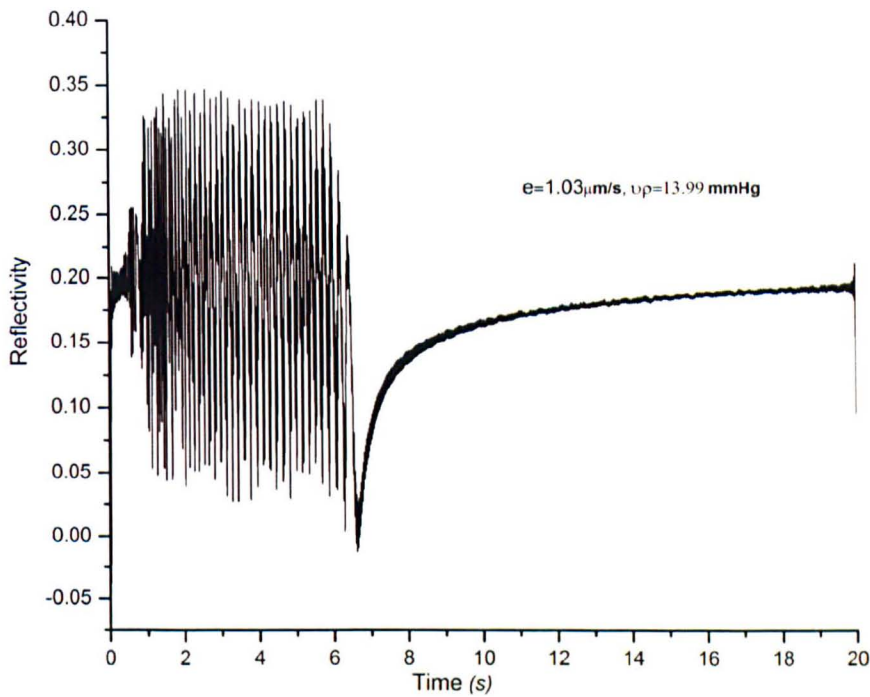


Figure (6.12) Reflectivity time for PS/PMMA film made at higher vapour pressure (13.99 mmHg). Due to lower evaporation rate, it takes longer for toluene to evaporate and therefore the final time (t_f) is higher.

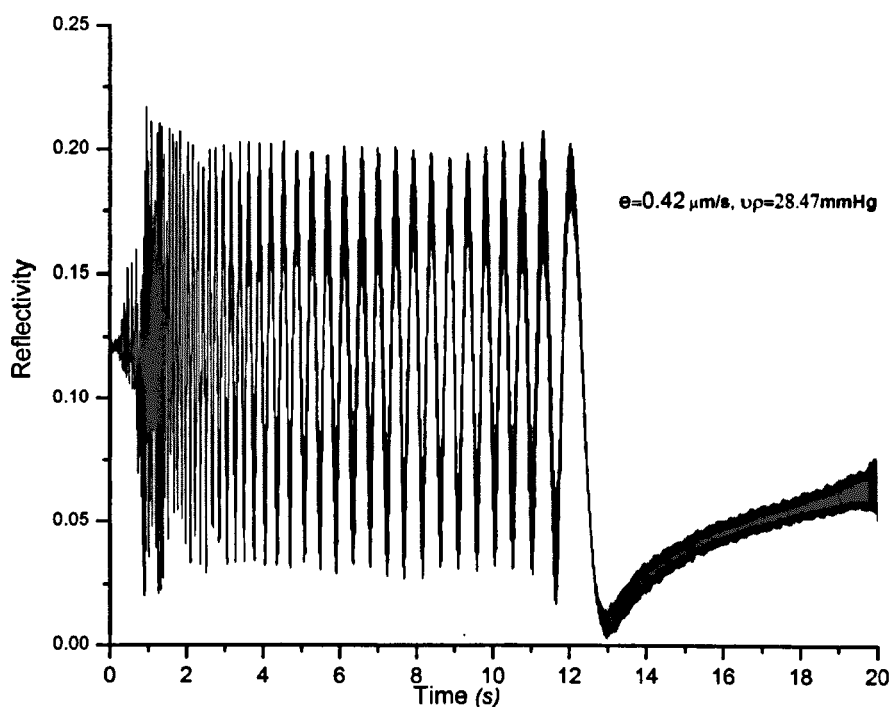


Figure (6.13) Reflectivity time for PS/PMMA film made at highest possible vapour pressure atmosphere before condensation. The final time (t_f) is approximately 13 seconds.

6.5 The effect of evaporation rate on interfacial instability

To study the Marangoni type instability in the liquid-liquid interface of PS/PMMA films, we spin cast the films in the environmental cell exposed to toluene gas at various vapour pressures.

Figure (6.15(a)) is a contour plot showing the radially averaged intensity of the scattered light out of the specular direction for the blend film made in ambient conditions with the highest evaporation rate ($e = 3.15 \mu\text{m}/\text{s}$). There are three distinctive regions on the plot. After 1.5 seconds the instability initiates with q shifting towards the higher value of scattering vector, indicative of formation of smaller length scale structure. This is followed by breaking up of the

structure and formation of a pattern of approximately $12 \mu\text{m}$. Finally a fixed pattern with length scale of about $50 \mu\text{m}$ forms and the scattering ring remains intact till the end of the spinning. The relevant times are indicated on $R-t$ graph in figure (6.11) which on its own, can not supply the same information provided by off specular data. While reflectivity-time gives information about layering and thickness changes during spin coating, the scattered beam provides information on instability and structure development.

The evaporation ends in less than 4 seconds and the film is settled. Figures (6.15(b)) and (6.15(c)) are the optical micrographs of the centre with a cellular pattern and edge of the film with the familiar striation with a periodicity of about $50 \mu\text{m}$.

In the next stage the evaporation rate of the solvent from the film has been decreased by increasing the overhead vapour pressure. As seen in figure (6.16), the onset of instability and the film settlement time is delayed due to slower the evaporation rate in the cell. The cellular pattern and striations are bigger than the previous sample but less predominant.

In figure (6.16(a-c)), at ($e = 1.03 \mu\text{m}/\text{s}$) we can see there is a change in the final structure as well as the scattering pattern. Most of PMMA islands are appeared towards the edge and also striations begin to disappear. There is no dominant q vector and also no scattering ring and it takes longer to develop a fixed structure (6.5s instead of 3.5s).

If we exploit lower evaporation rates, the above trend continues and at one extreme ($e = 0.42 \mu\text{m}/\text{s}$) there is no lateral phase separation. As shown in figure (6.19(a)), the $q(t)$ profile does not reveal any dominant q value, indicating a lack of a specific length scale in the film. It is clearly seen that evaporation rate in this film is very slow as it takes 13s for the toluene to evaporate. Comparing the final time (t_f) at highest evaporation rate ($e = 3.15 \mu\text{m}/\text{s}$ & $t_f = 3.5\text{s}$) with the lowest evaporation rate ($e = 0.42 \mu\text{m}/\text{s}$ & $t_f = 13\text{s}$) shows that thinning time is roughly 270% longer.

We speculate that due to a low evaporation rate, the concentration gradient in the film is not big enough to trigger (or initiate) the Marangoni instability. The oscillation of the scattered light in figure (6.19(a)) is similar to the fringes seen in reflectivity-time data (figure (6.13)). This is due to thickness variation during the spin coating. Perhaps the magnitude of the instability is never sufficient enough to break through to the surface and form any structure with defined length scale. We intend to consider if a layered type structure is formed. Washing the samples with selective solvents verifies our deduction. This will be discussed in the next section.

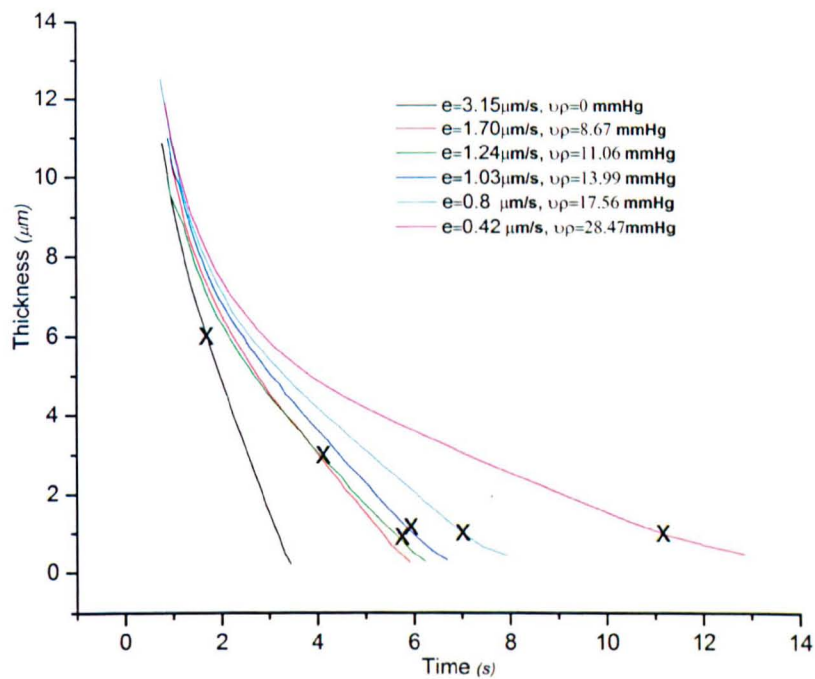


Figure (6.14) Thickness-time plot for PS/PMMA film with different evaporation rate. The X sign indicates the onset of instability in films. The values are extracted from $q - t$ graphs in figures ((6.15)-(6.19)). However at low evaporation rate there is not any obvious instability till the very end stage when toluene is completely evaporated.

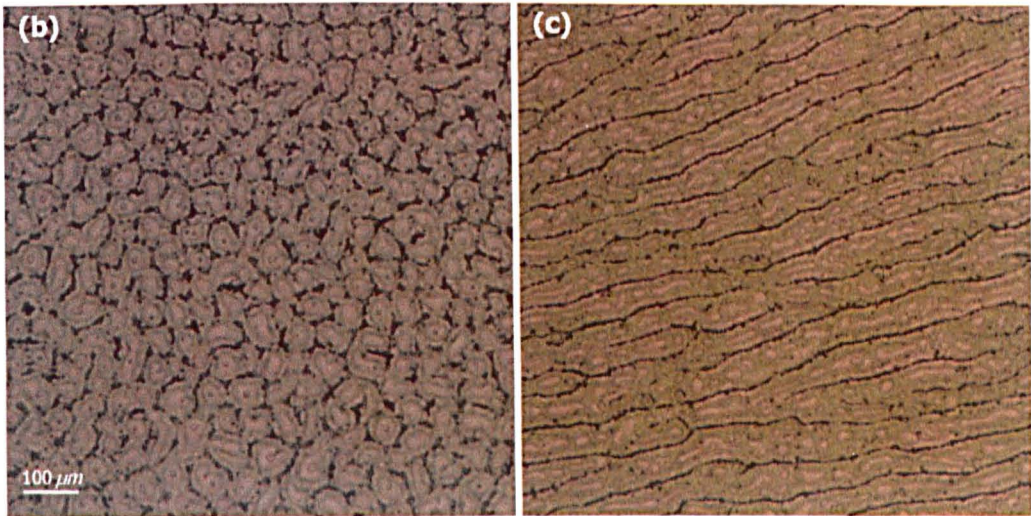
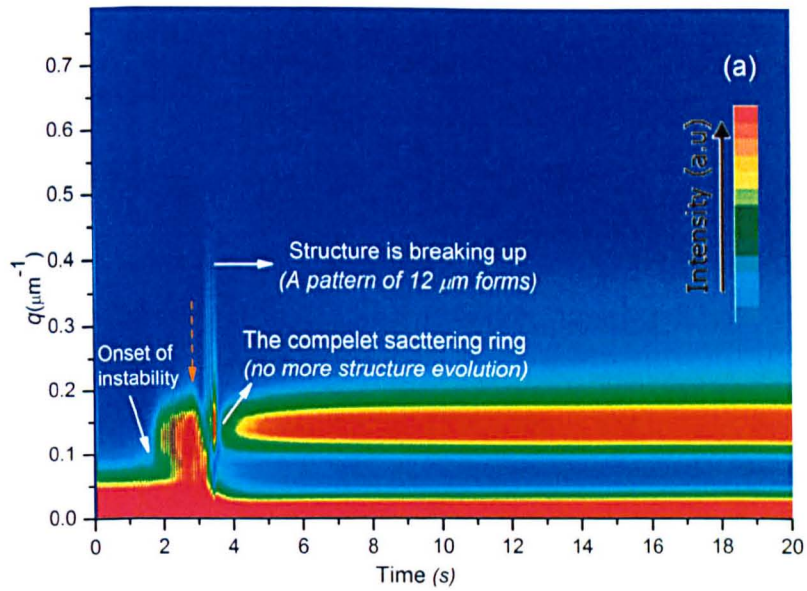


Figure (6.15) (a) The off-specular scatter $q(t)$ profile shows the structural evolution when there is no overhead gas pressure and the solvent evaporation rate is at its highest ($e = 3.15 \mu\text{m}/\text{s}$). There are 3 different stages; firstly smooth layering occurs, then the structure breaks up with features on many length scales and finally at ($t > 3.5 \text{ s}$) a fixed pattern with a length scale of $\sim 50 \mu\text{m}$ forms. Optical micrographs taken at (b) the centre of the sample and (c) the edge of the sample show a laterally phase separated structure ($\sim 50 \mu\text{m}$) with radial striations towards the edge of the sample.

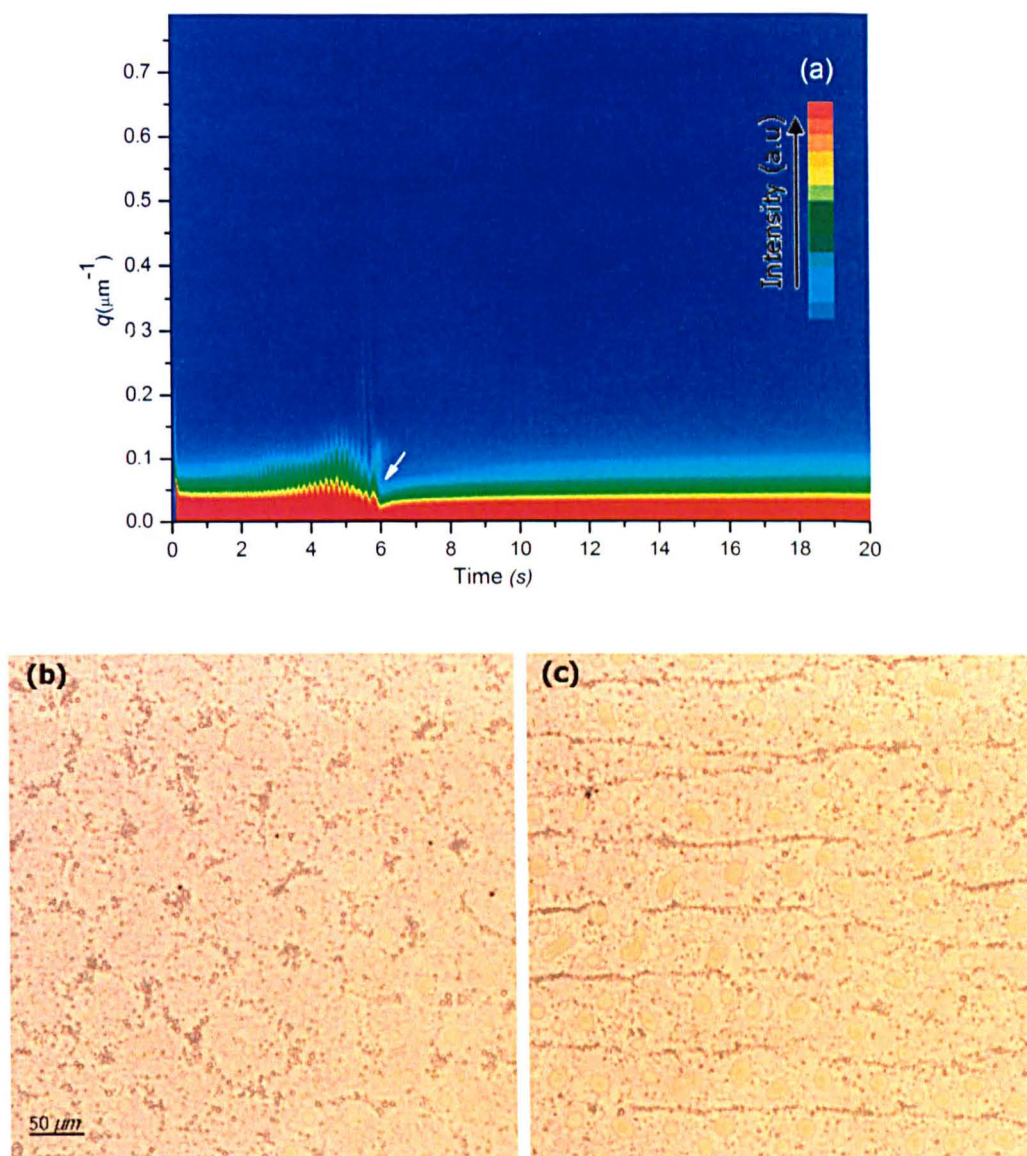


Figure (6.16) (a) Film is made in environmental cell with a saturated gas pressure of 8.64 mmHg which slowed down the evaporation rate from the film. It takes longer for toluene to evaporate; therefore t_f is longer than the previous sample (~ 6 seconds). (b) Optical micrograph of the centre region with a larger but less defined length scale. (c) Striations towards the edge of the sample.

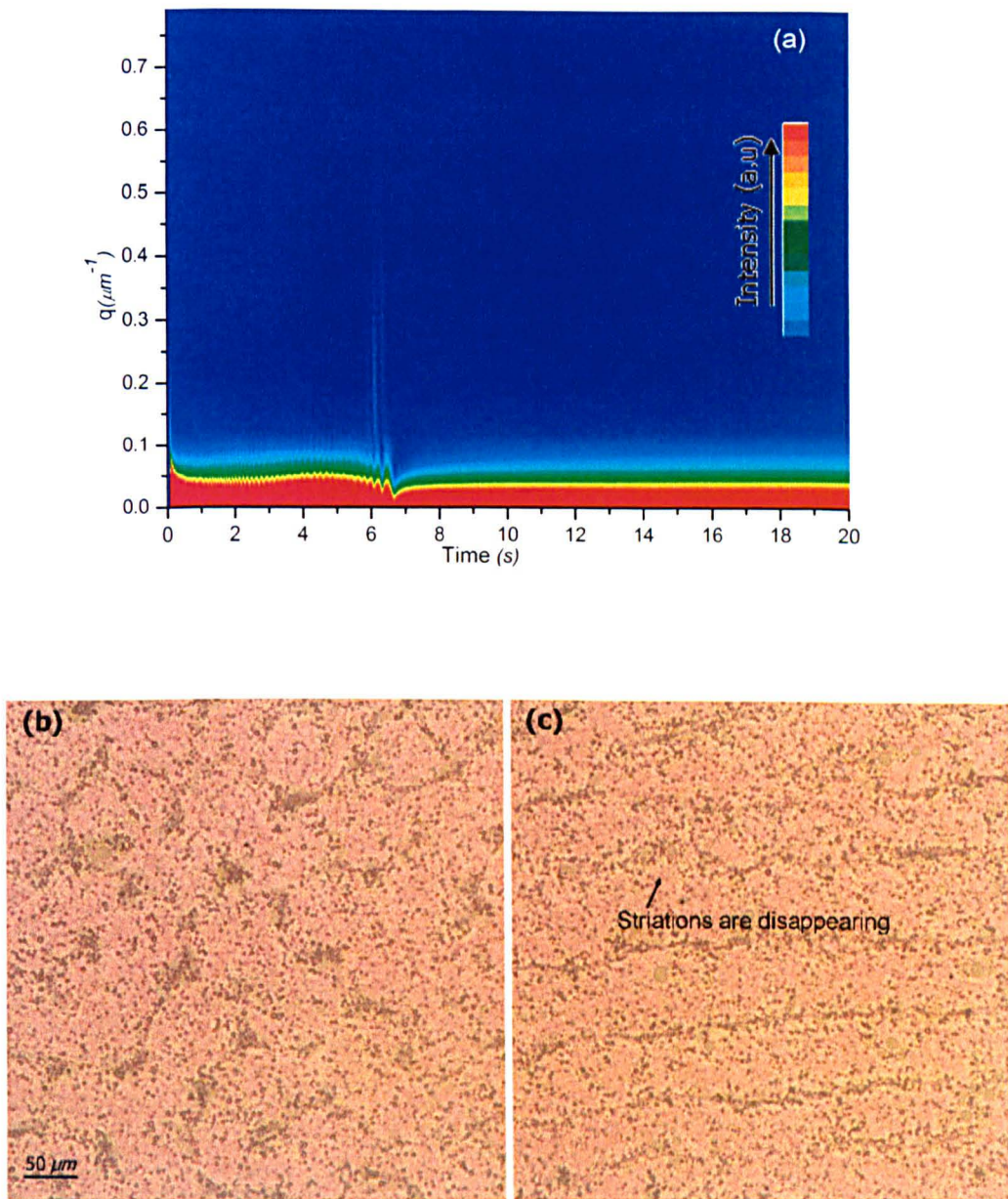


Figure (6.17) (a) due to a lower evaporation rate in this sample, the Marangoni-like instability is weaker and does not completely break through to the surface. Therefore, considerably less off-specular scattering is observed. The film evolves more slowly becoming fixed after 6.5 s. In the optical micrographs (b) and (c) there is no cellular pattern and the striations are less dominant.

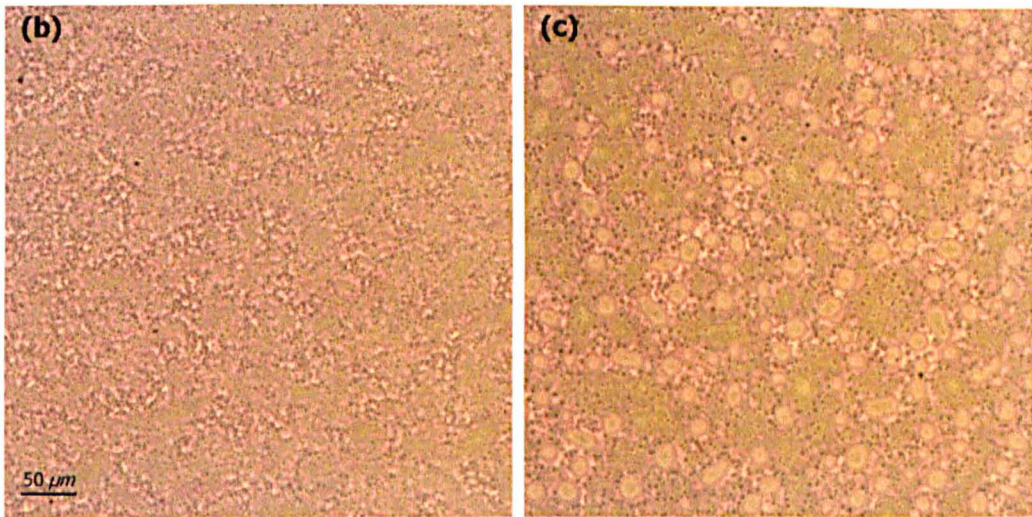
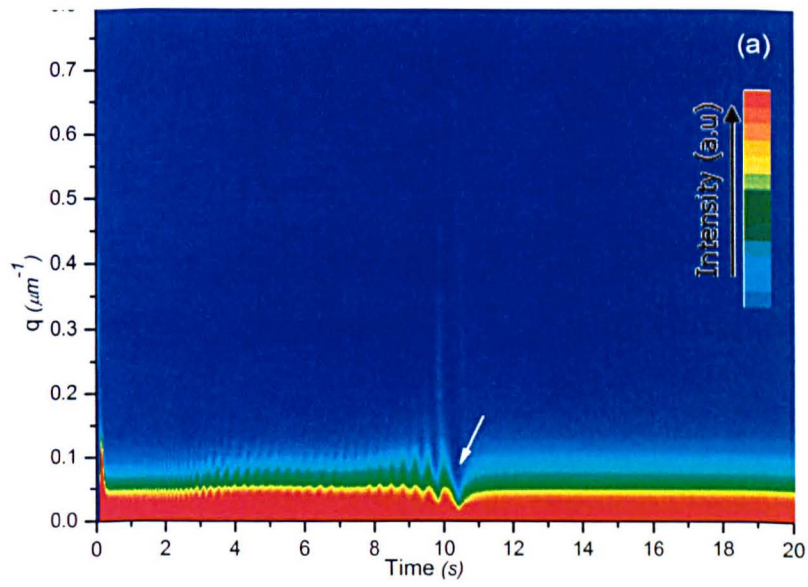


Figure (6.18) (a) Decreasing the evaporation rate, shifts the end point time (t_f) towards higher value. (b) There is no dominant structure in the centre and in (c) striations completely disappear.

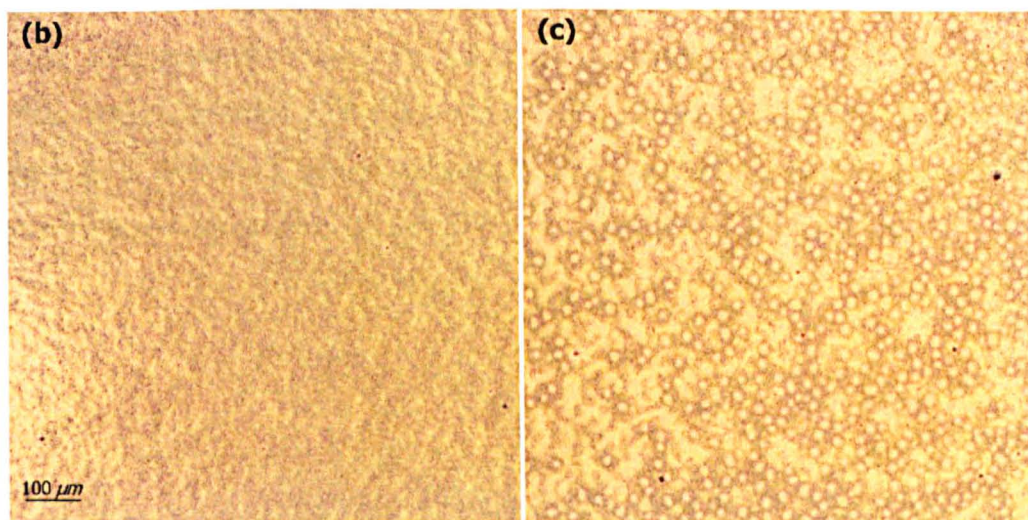
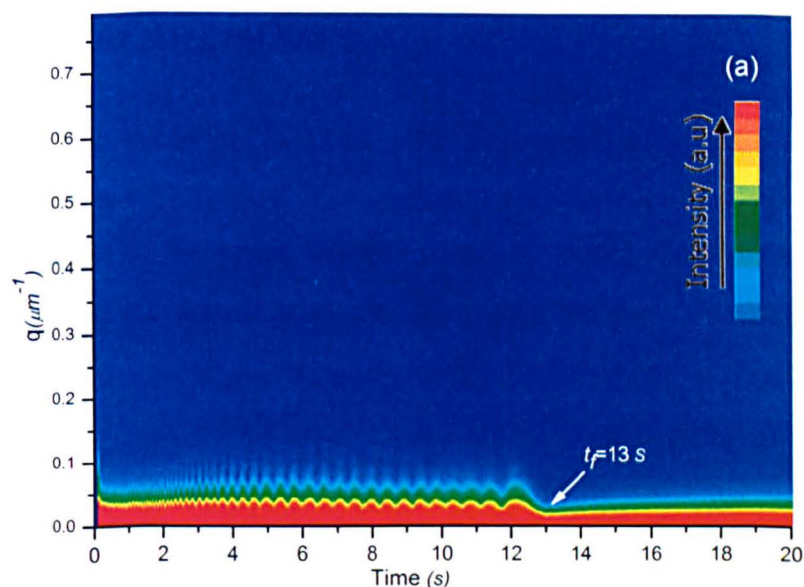


Figure (6.19) (a) The lowest evaporation rate ($e = 0.42 \mu\text{m}/\text{s}$) is applied and therefore the concentration gradient which drives the Marangoni-like instability is most suppressed. The oscillation of the scattered light is similar to the fringes in specular reflectivity. There is no dominant length scale. Perhaps the magnitude of the instability is never sufficient to break through to the surface. Micrograph (b) from the centre and (c) from the edge of the sample show neither a cellular pattern nor striations. A layered structure is believed to have been formed in this sample. See figure (6.20) and section (6.5) for more information on layer formation.

6.6 Bilayer formation

Any structure evolution in films with low evaporation rates suggests that layered structure is formed. The optical microscope images show no lateral phase separation. To prove the formation of layers, selective washing was carried out on the sample with lowest evaporation rate ($e = 0.42 \mu\text{m}/\text{s}$). The sample was first washed with acetic acid. Figure (6.20(b)) clearly shows the existence of a layer which has been detached from the substrate and partially folded (or rolled). This layer must be rich in PS to show resistance to acetic acid. Washing the sample with cyclohexane removed the remaining PS layer and clears the substrate. The fact that film has been detached from the substrate suggests PMMA is the bottom layer. Another possibility is there are 3 layers with PMMA on top and the bottom of the film and PS in between. We need more sophisticated method such as Nuclear Reaction Analysis (NRA) to characterise the order of the layers properly. In figure (6.20(b)) it seems that there is a secondary phase separation. Perhaps Raman spectroscopy could provide more information on the chemical composition of the phases.

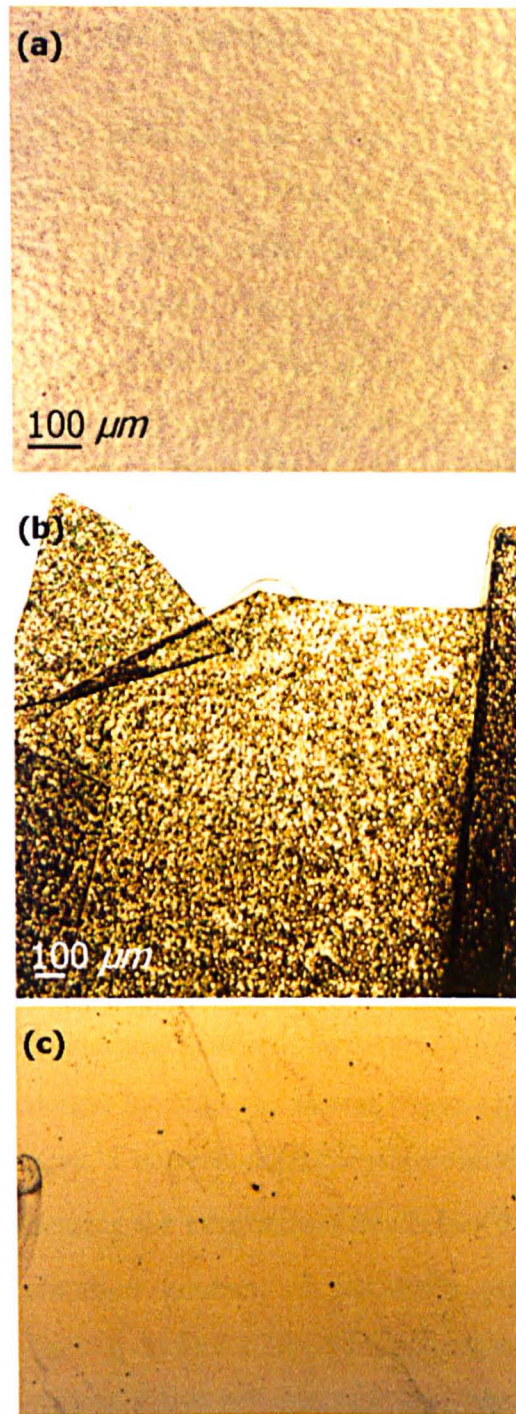


Figure (6.20) (a) As cast PS PMMA film with lowest evaporation rate (b) after washing the sample with acetic acid, PS layer is dispatched from silicon substrate and rolled (c) washing the sample with cyclohexane has removed the remaining PS layer.

6.7 Summary and conclusions

In this chapter we have addressed the origin of interfacial instability in PS/PMMA films. Films were made at controlled vapour pressure atmospheres to generate different evaporation rates. Using reflectivity-time data, the thickness-time curves were plotted. There are two dominant regions in the plot confirming that there are two mechanisms governing the structure of a spin coated film. The early stage is mostly affected by the balance between the shear force and the centrifugal force. This is followed by evaporation of the toluene from the film. At higher rates the film thins very quickly. Decreasing the evaporation rate will shift the final formation time towards a higher value. Using off-specular data and by radially averaging the intensity of the scattering images, they were converted in to length scale-time plots that provided valuable information on the structure evolution during the spin coating process. The result is summarised in figure (6.21). At high evaporation rates ($e > 1.8 \mu\text{m}/\text{s}$) where solvent evaporates from the surface of the film quicker than diffusion can re-equilibrate the concentration through the film, there will be less solvent at the surface. This can lead to a Marangoni type of instability where if the interface between the two polymers roughens, it lowers the total interfacial energy, leading to a lateral phase separation. Evaporation rates between $1.6 - 1.8 \mu\text{m}/\text{s}$ correspond to the transient region where striations start to develop. Decreasing the evaporation rate below $1.6 \mu\text{m}/\text{s}$ stabilises the structure. The concentration gradient is not steep enough to trigger the Marangoni instability, and therefore a layered structure is more likely to form. Washing the sample with selective solvents confirms that the layered structure forms during spin coating and it is possible to stabilise the interface between layers by controlling the environmental parameters.

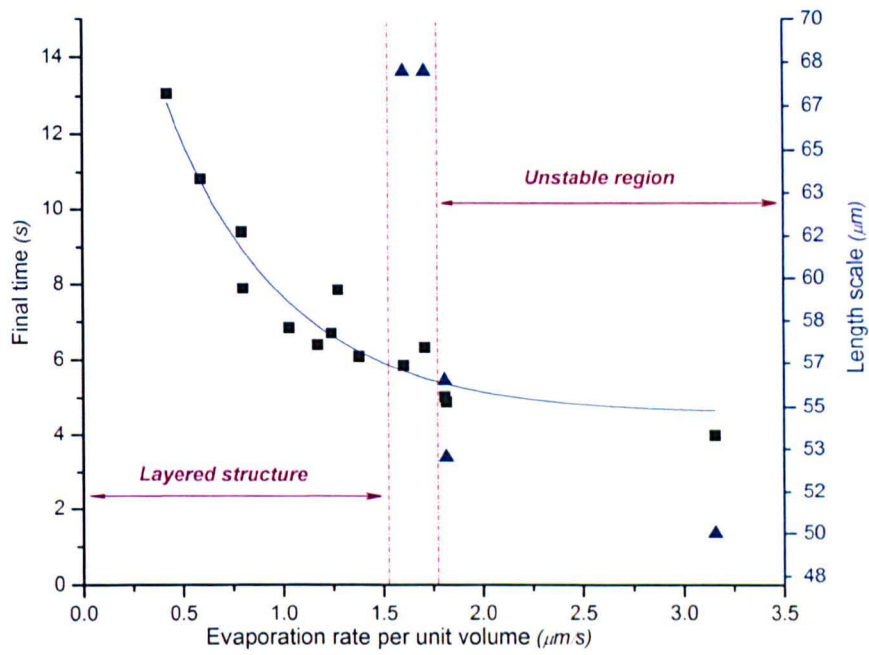


Figure (6.21) Evaporation rate can stabilise or destabilise the structure. In PS/PMMA films, evaporation rates higher than $1.8 \mu\text{m/s}$ triggers the Marangoni instability and a structure with defined length scale is formed. With lower evaporation rates ($e < 1.6 \mu\text{m/s}$) a self-stratified structure is more likely to form.

6.8 Bibliography

1. Block, M.J., *Surface Tension as the Cause of Benard Cells and Surface Deformation in a Liquid Film*. Nature, 1956. **178**(4534): p. 650-651.
2. Pearson, J.R.A., *On Convection Cells Induced by Surface Tension*. Journal of Fluid Mechanics, 1958. **4**(5): p. 489-500.
3. Pearson, J.R.A., *On convection cells induced by surface tension*. Journal of Fluid Mechanics Digital Archive, 2006. **4**(05): p. 489-500.
4. Heriot, S.Y. and R.A.L. Jones, *An interfacial instability in a transient wetting layer leads to lateral phase separation in thin spin-cast polymer-blend films*. Nature Materials, 2005. **4**(10): p. 782-786.

Chapter 7

Structure Development in Semiconducting Polymer Blends

7.1 Introduction

Blended polymer based optoelectronic devices have attracted a huge amount of interest over the last few years due to their potential application in polymer based field-effect transistors[1-3], light-emitting diodes (LEDs) [4-9] and photovoltaic devices (PVs)[10-12]. However, the efficiency of such devices, in particular the solar power conversion efficiency for all-polymer solar cells still remains well below the value of the conventional photovoltaic materials [13]. The low efficiency of solar cells is mainly due to charge transport pathways within the active layers. It is suggested that charge trapping is the main loss mechanism for charge transport [13, 14]. It has been demonstrated that the morphology of the active layer can greatly enhance the device performance [15, 16]. This can be achieved by controlling the processing parameters such as

solution and substrate temperature, spin-speed, solvent and solvent saturated atmosphere.

Using the set up I developed to control the morphology through evaporation rate, in this chapter we demonstrate a preliminary attempt to control the morphology in semiconducting polymer blends used in photovoltaics. We have used the environmental cell to make the active layer of a series of photovoltaic devices at different vapour pressure. The goal was to produce a variety of morphologies and then investigate how these variations effect the efficiency of the device. Tailoring different structures by controlling the evaporation rate only, will allow the morphology dependence of the efficiency to be studied without varying the chemical composition.

7.1.1 The effect of the morphology on device performance

In the search for alternative green energy sources, nanostructured organic materials are a potential candidate to produce low cost devices. The efficiency of opto-electronic devices is highly related to film morphology [15, 17-19]. The structure of a thin film in turn is strongly affected by process parameters during spin coating such as solvent evaporation, initial concentration, phase separation and subsequent phase coarsening [4, 20]. Therefore it is very important to have a deep understanding of the film formation process. Knowing which, we could tailor the structure providing good device efficiency. In organic optoelectronic devices, an active layer is sandwiched between two electrodes. This layer is made of conjugated polymers and provides a place for exciton dissociation or electron-hole binding (in LEDs) and also a route for charge transfer from the site of exciton dissociation to the electrodes. In photovoltaic devices, an exciton (electron-proton pair) is generated by light and then diffuses to a nearby interface where it separates into an electron and a hole. In light emitting devices, electrons and holes are injected from each electrode and need to recombine to emit light. This is schematically illustrated in figure (7.1). However, in both cases the exciton is formed far from the

interface. Excitons have a very short life time (about 10 ns) and rather short diffusion distance (≤ 10 nm) [4, 21]. They need to reach the interface within their life time. Therefore an optimum structure for the active layer should provide enough interfaces to let the exciton dissociate or recombine without being trapped in-between boundaries. Otherwise, due to the short life time it will be wasted. The laterally phase separated structure with small size domains is a good candidate for the purpose. However, after producing charges, they need to move towards electrodes.

The interconnected or bicontinuous structures can produce sufficient route for charge transfer. Vertically phase separated morphology normal to the surface provides the perfect route for charge transfer. Therefore there is an optimum structure in which both charge production and charge transfer are at their best combination.

Snaith[14, 18] and Arias and Hall and co workers [15, 17] suggested that the main reason for the low efficiency of polymeric photovoltaic devices is related to charge transfer not charge generation. They found that charge collection efficiency scales with the surface area of the interface between the mesoscale PFB-rich and F8BT-rich phases[18]. The area is marked as Δr in figure (7.2). Previous work to study the effect of the evaporation rate on morphology of the blend was done by Hall *et al* [17] by heating the spin-coater chuck with a halogen lamp immediately prior to spin coating. Due to the asymmetry of the heating process and different temperature across the substrate, a range of different morphologies were developed and studied. In another work [15] by the same group, the above method plus drop casting in a closed environment was used to control the evaporation rate. However, in these papers there is no systematic way of changing the evaporation rate. The focus is rather on changing the scale of the morphology to increase the efficiency. In this chapter we will change the evaporation rate systematically and study the effect of this change on the morphology of a PFB/F8BT blend.

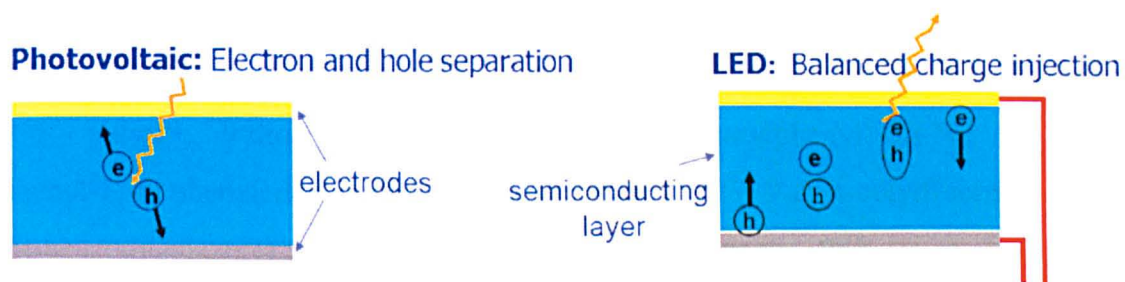


Figure (7.1) Schematic illustration of charge injection in (a) Photovoltaics and (b) Light emitting diodes.

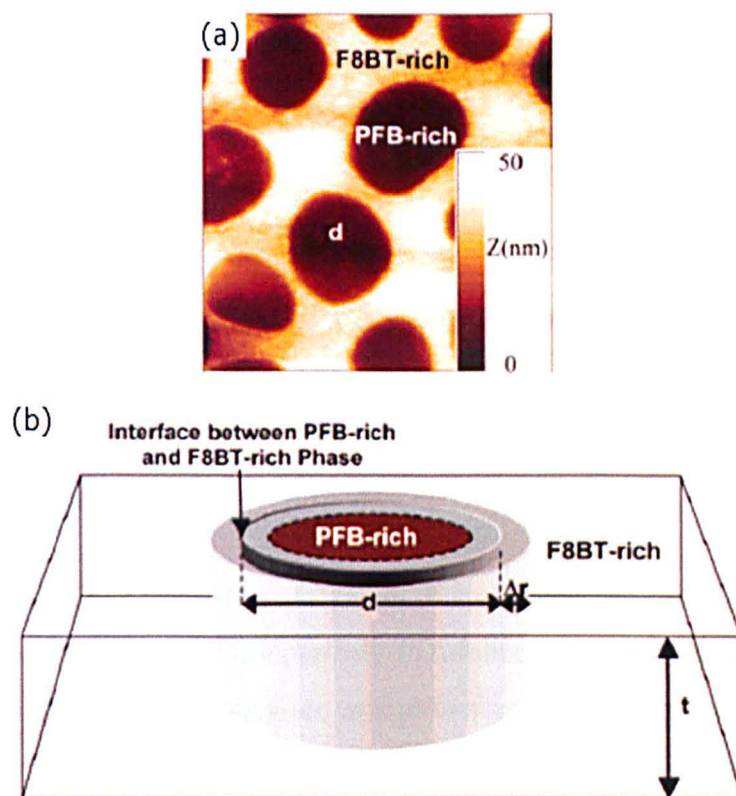


Figure (7.2) Schematic representation of blended PFB/F8BT. t is the film thickness, d is the average diameter of the circular phase, and Δr is the distance over which charge can migrate, within the minor phase, to reach the interface. H.J. Snaith *et al*, 2002 [18].

7.2 Case study: PFB/F8BT

PFB poly((9, 9-dioctylfluorene)-alt-bis-N, N-(4-butylphenyl)-bis-N, N-phenyl-1, 4- phenylenediamine) and F8BT (Poly(2, 7-(9, 9-di-n-octylfluorene)-alt-benzothiadiazole)) are both polyfluorene derivatives. PFB is a hole transporting polymer and F8BT is an electron acceptor in photovoltaic devices. Figure (7.2) shows the chemical structure of F8BT and PFB.

Different morphologies of the blend can be achieved by using different solvents such as toluene, xylene [9, 10, 15, 18, 22], chloroform [15, 23] and isodurene [10].

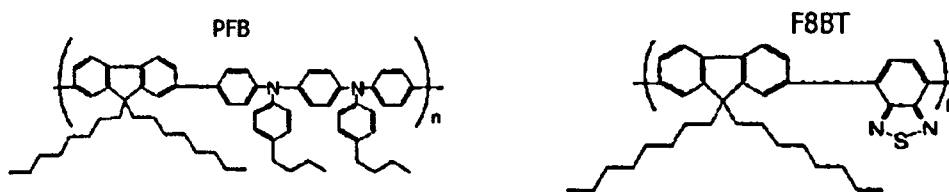


Figure (7.3) Chemical structure of PFB and F8BT

7.3 Experiments

The solution of the conjugated polymers were made by dissolving the homopolymer of PFB and F8BT separately in toluene at a concentration of 10 *ml* in 1 *ml*. The toluene solutions were mixed to form a polymer blend with a composition of 1:1 by weight. The experimental set up was similar to the one used for the PS:PMMA system.

Nitrogen gas was blown through a bubbler containing toluene placed in a water bath allowing temperature control. Silicon substrates were cleaned using the plasma cleaning technique. The films were spun cast at 2000 rpm inside the environmental cell at different vapour pressures. The distance between sample and screen was 42.4 *cm*.

A series of photovoltaic devices were also made. The active layers were made in a controlled environment atmosphere to produce different morphologies and

were thus characterised. The detail of the device making is explained later in this chapter.

7.4 Results

Toluene was produced at different vapour pressures by changing the temperature of the water bath containing a bubbler filled with solvent. Table (7.1) shows the vapour pressure and concentration at different temperatures. Reflectivity- time data and off specular scattering were collected during the spin coating and analysed. The structures of the films were studied by optical microscopy, fluorescence and atomic force microscopy.

Table (7.1) Vapour pressure and concentration of toluene at different temperature

Temperature (°C)	Vapour pressure (mmHg)	Concentration%
25	28.47	3.75
20	21.86	2.88
16	17.56	2.31
12	13.99	1.84
8	11.06	1.45

7.4.1 Reflectivity–time data

We analyse the reflectivity-time data to ensure the change in evaporation rate is consistent with applied vapour pressure. As seen in figures ((7.4)-(7-9)), by applying higher vapour pressure, the end point time (t_f) moved towards higher values. The final time (t_f) for all samples is compared in figure (7.10). This graph clearly demonstrates a good correlation between the applied vapour

pressure and final time. Evaporation rate is more suppressed at higher vapour pressures. We expect this variation in the evaporation rate to produce different morphologies.

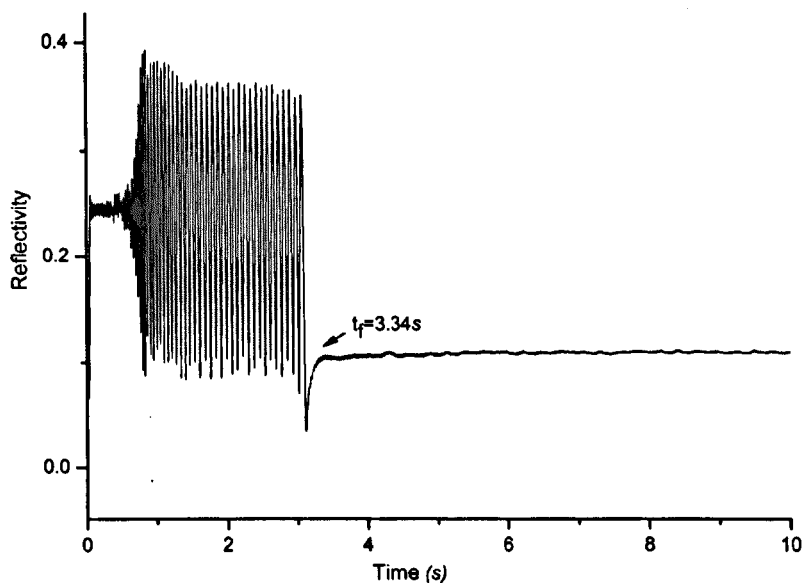


Figure (7.4) Reflectivity- time for (1:1) ratio of PFB/F8BT in toluene. The film was made at the highest evaporation rate with no toluene flow over it.

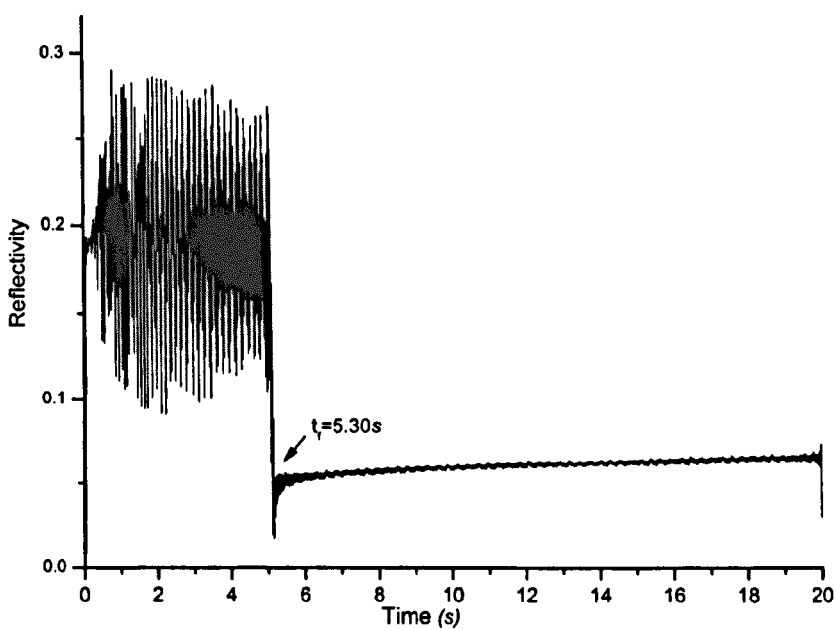


Figure (7.5) PFB/F8BT film made in environmental cell with toluene vapour pressure 11.06 mmHg.

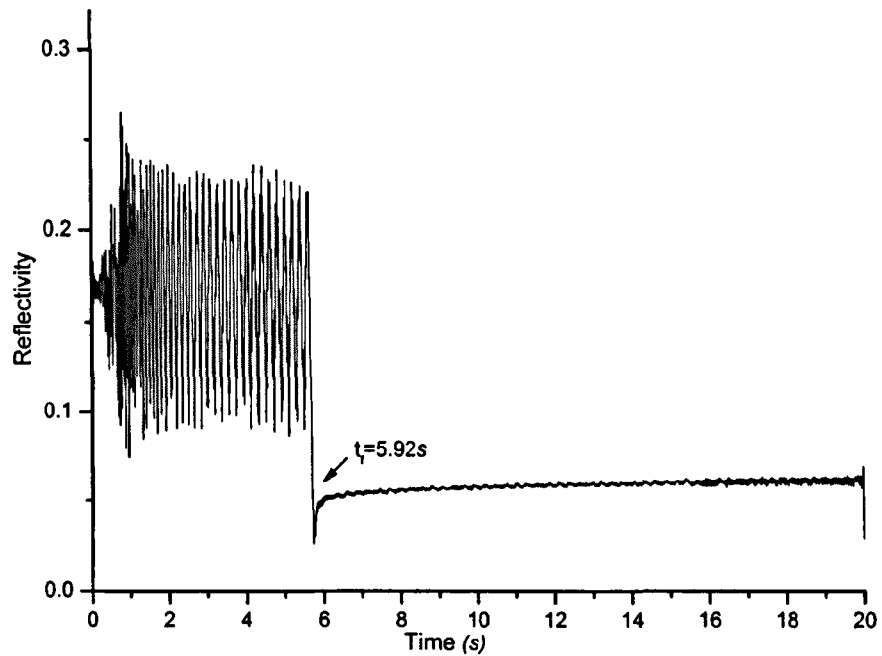


Figure (7.6) PFB/F8Bt film made in environmental cell with toluene vapour pressure 13.99 mmHg . The evaporation rate has been decreased.

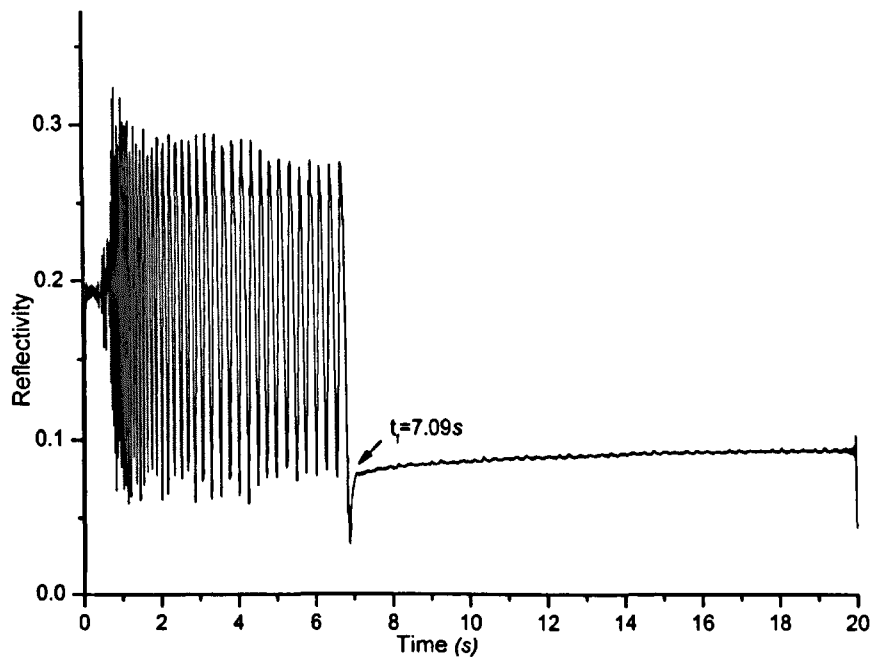


Figure (7.7) PFB/F8Bt film made in environmental cell with toluene vapour pressure 17.56 mmHg . The final time has shifted to higher value.

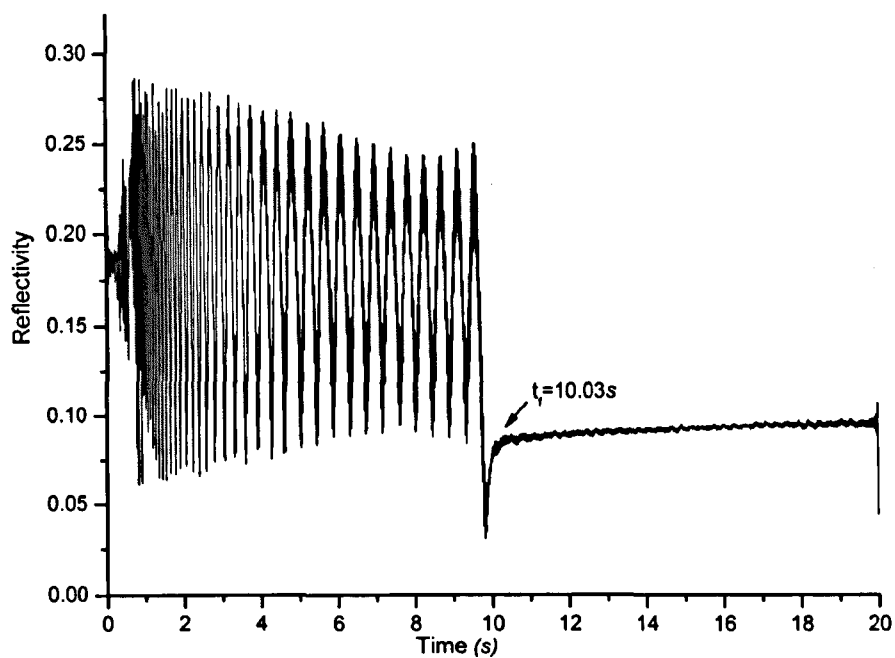


Figure (7.8) PFB/F8Bt film made in environmental cell with toluene vapour pressure 21.86 mmHg.

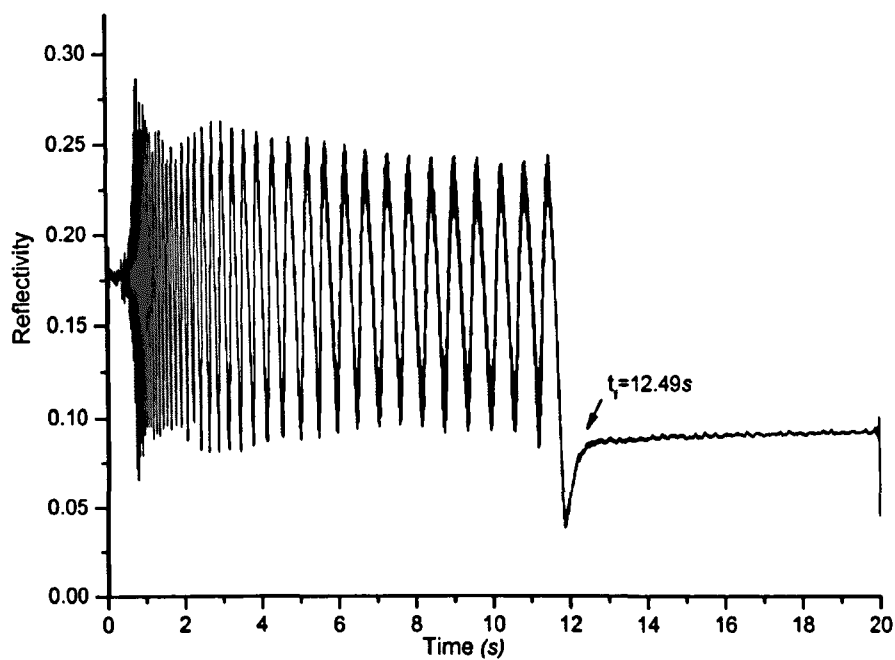


Figure (7.9) PFB/F8Bt film made in environmental cell with toluene vapour pressure 28.47 mmHg.

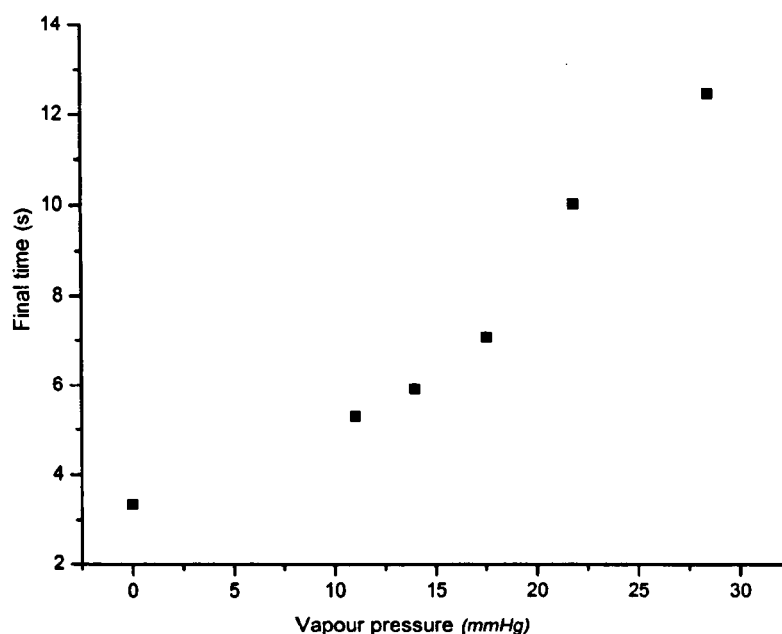


Figure (7.10) t_f as a function of applied vapour pressure of toluene for PFB/F8Bt films. Comparing the final time for the sample made at ambient atmospheric pressure ($t_f = 3.34s$) and the sample made at the highest vapour pressure ($t_f = 12.49s$) clearly shows the evaporation rate has been suppressed during film processing.

7.4.2 Structure formation in PFB:F8BT: the effect of evaporation rate

Figures (7.11)-(7.16) show the morphology of the as cast film at different vapour pressures. The morphology at ambient temperature with no flowing gas suggests two distinct phases. Small isolated islands of one component are distributed in the continuous matrix of the other phase. The fluorescence microscopy images (7.11 (b) and (c)) show the isolated particles are PFB (dark regions in (7.11(b))) and the matrix is enriched in F8BT (green regions in (7.11(b))). The isolated PFB particles have an average size of approximately $2 \mu m$. An AFM image of the same sample (figure (7.12)) shows that PFB is

the lower phase and the higher phase is rich in F8BT. Also there is a smaller length scale within the structure. The overall thickness of the film is 85 nm. Comparing the fluorescence images from this sample and the topography images, reveals that the top surface is a mixture of both materials plus distributed islands of F8BT, approximately 15 nm high.

Decreasing the evaporation rate changes the structure. In figure (7.13) where the environmental cell is filled with toluene at 11.06 mmHg (8 °C), more isolated angular regions exist (7.13(a)). However, looking at the fluorescence micrograph (figure (7.13(b))) clearly shows that PFB regions become larger in this sample. The dark PFB areas have increased and at the same time the F8BT rich phase has more defined structure and is distinctively green in (7.13 (b)) and dark in (7.13 (c)).

Decreasing the evaporation rate or increasing the vapour pressure to 13.99 mmHg (at 12 °C) makes the features more compacted (figure (7.14)). Similar to the trend above, the amount of mixed phase has decreased and the surface area fraction of PFB phase increased. AFM images (figure (7.15)) of the sample show that the F8BT rich phases are still higher than PFB.

When the evaporation in the film was more suppressed by applying higher pressure (17.56 mmHg at 16 °C) the fashion of phase separation started to change slightly. The interface between two phases (green and black area in figure (7.16)) is not as sharp as before. Going towards higher vapour pressure (22 mmHg at 20 °C and 28.47 mmHg at 25 °C), the trend of phase separation is consistent. i.e by decreasing the evaporation rate, the percentage of PFB decreases. In the fluorescence microscopy image in figure (7.18(b)) the green colour is dominant. We can not be sure that the emission of green colour (F8BT rich phase) is from surface of the film. However the weak emission of the blue colour (PFB rich phase) in image (7.18 (b)) suggests that the percentage of PFB on the surface of the film is not high. The domains in

(figure (7.18)) are more elongated and interconnected. The topography of this film (figure (7.19)) is clearly different from others for example figure (7.12). The film made at higher vapour pressure, is highly undulating on the surface. There is not a sharp interface between phases and the difference in height between high and low phases are approximately 5 *nm* (3 times smaller than the film made in atmosphere).

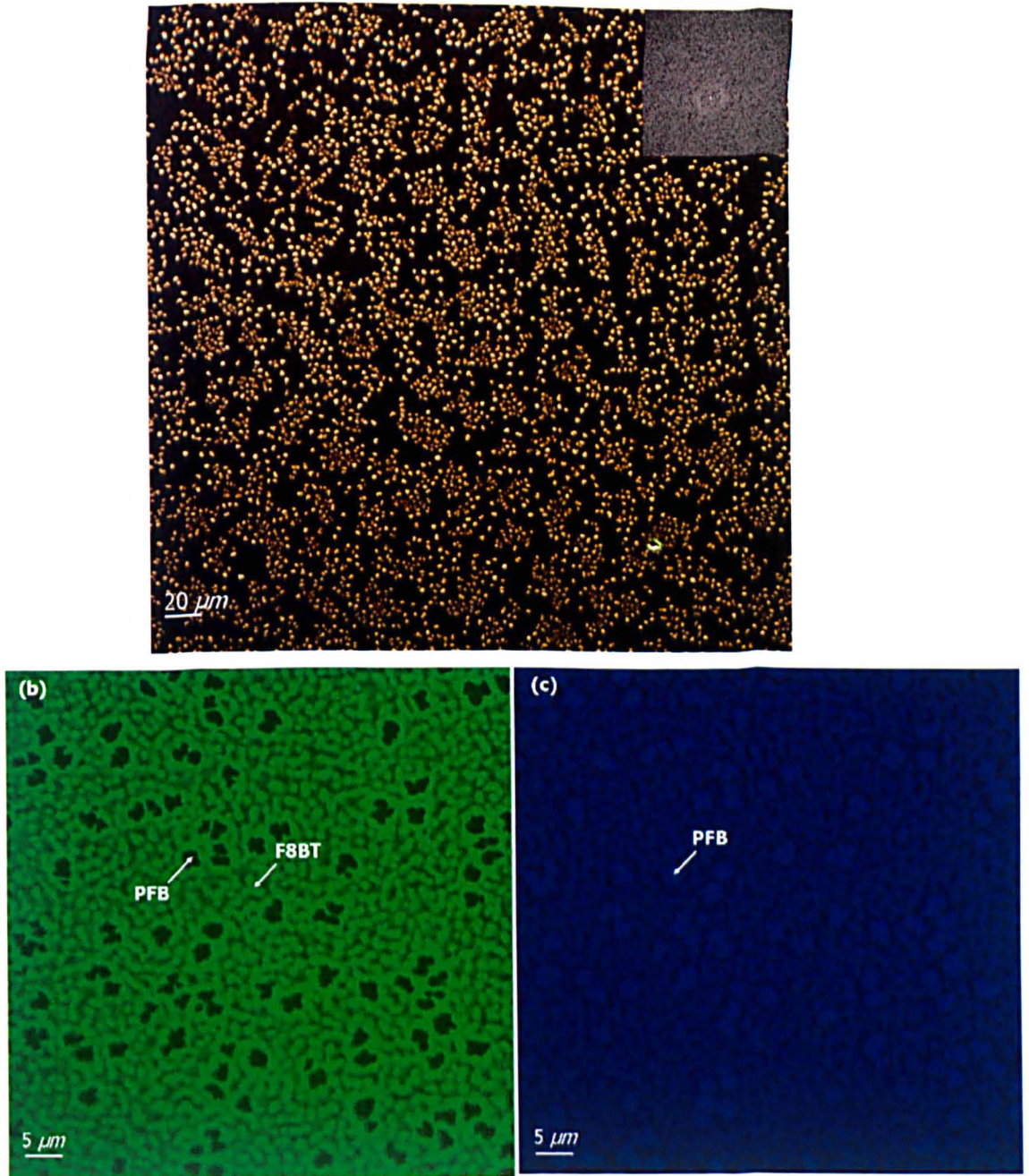


Figure (7.11) (a) Optical micrograph of the blend PFB/F8BT (1:1) spin cast from 10 mg/ml solution in toluene and in atmosphere, with isolated region having the length scale of about $2\ \mu\text{m}$. (b) The fluorescence micrograph of the film with F8BT emitting green light and (c) PFB appears blue. The higher-lying phase consists of F8BT mainly. Considering the relative composition of the phases, PFB phases have a high amount of PFB as they appear completely dark in (b) and shiny blue on (c).

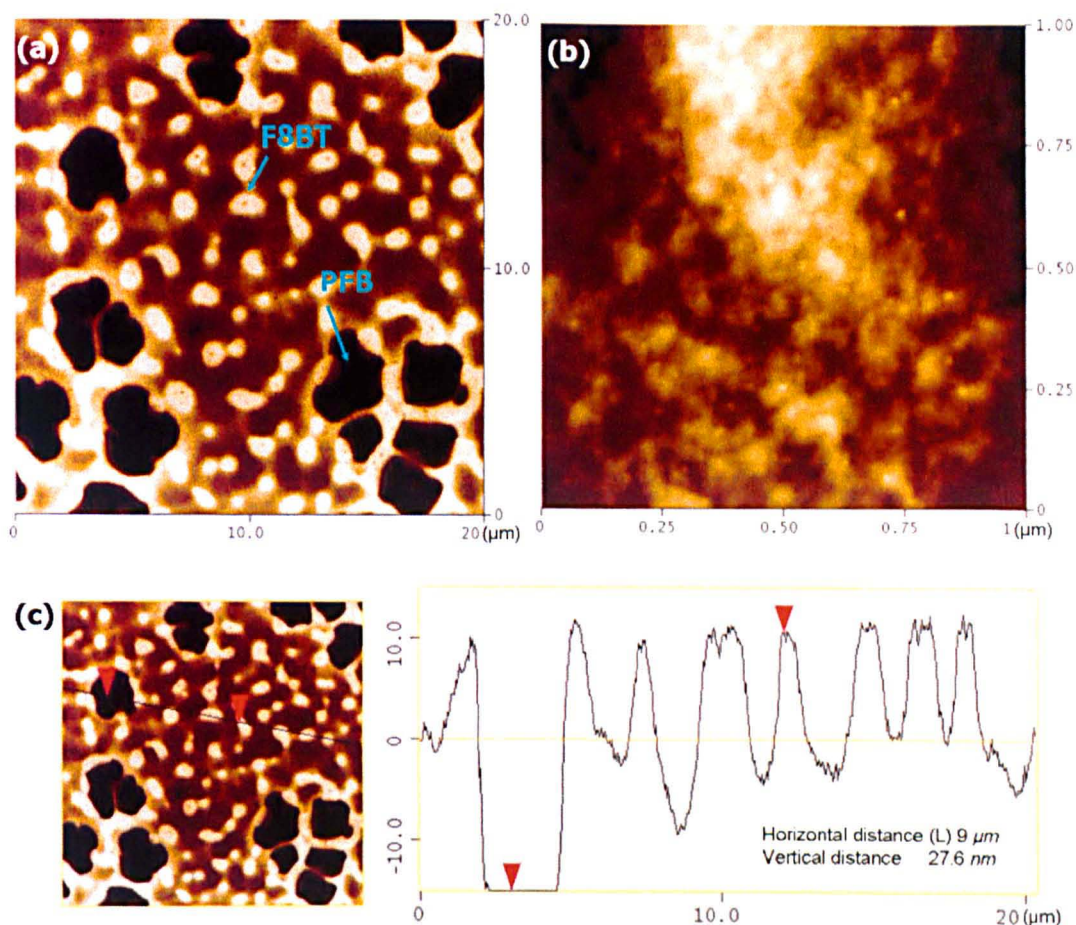


Figure (7.12) Height topography of (PFB/F8BT) film made in ambient temperature (a). The fluorescence microscopy from figure (7.11) shows that the dark regions in image above are rich in PFB. The bright regions are rich in F8BT. The dark brown areas are a mixture of both materials. (b) The smaller scan of the same sample reveals the existence of a fine length scale (about tens of nanometre) with in the structure. (c) Section analysis of the film. The height difference between lower phase (rich in PFB) and higher phase (F8BT) is about 27 nm. The thickness of the film is about 85 nm, determined by AFM measuring of the depth of a scratch in the film.

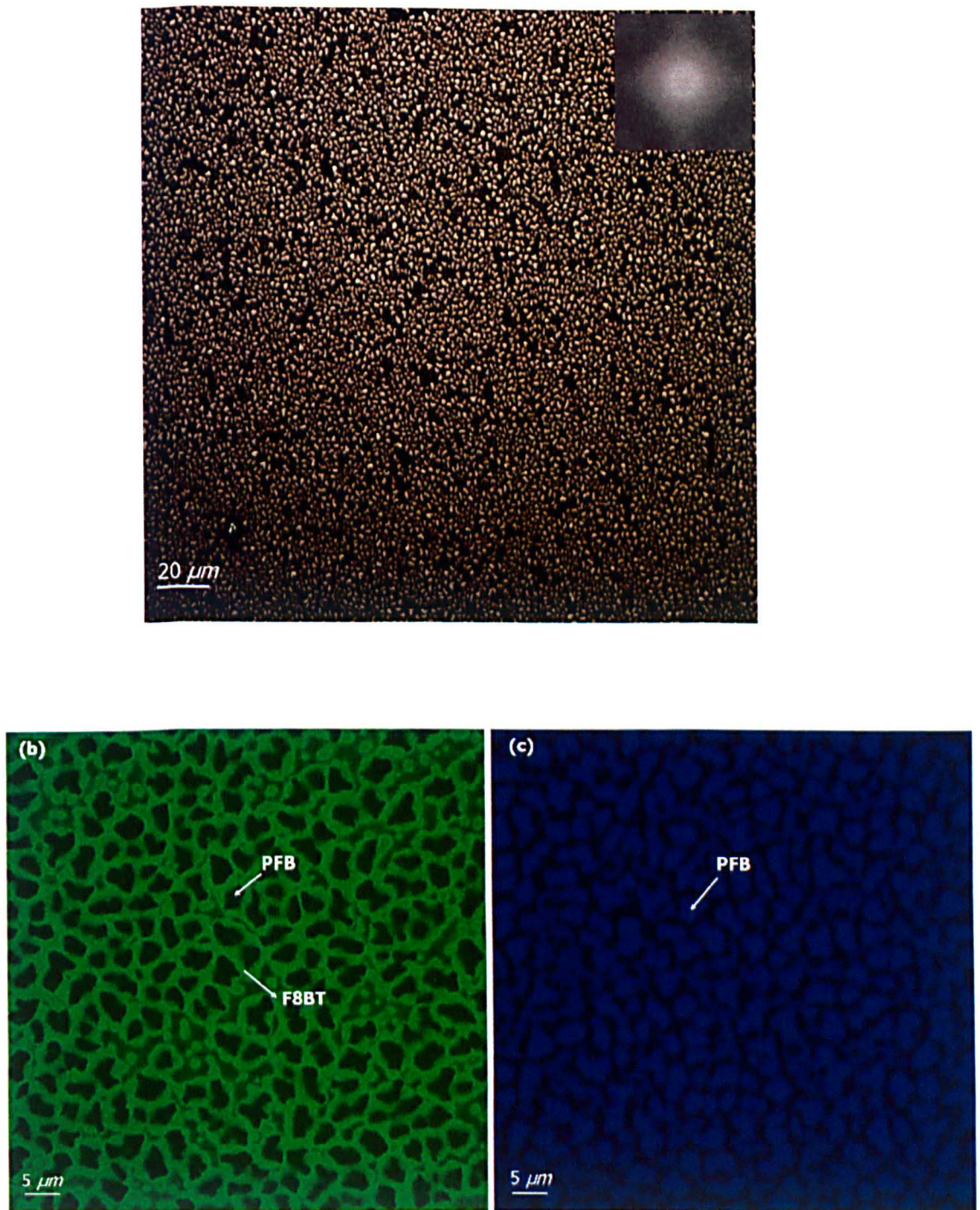


Figure (7.13) (a) Optical micrograph of the blend PFB/F8BT spin cast in saturated toluene vapour atmosphere ($v_p = 11.06 \text{ mmHg}$, $T=8^\circ\text{C}$). The PFB wells are about $4.43 \mu\text{m}$. (b) and (c) fluorescence microscopy images of the film. Decreasing the evaporation rate made the lower phase PFB wells bigger.

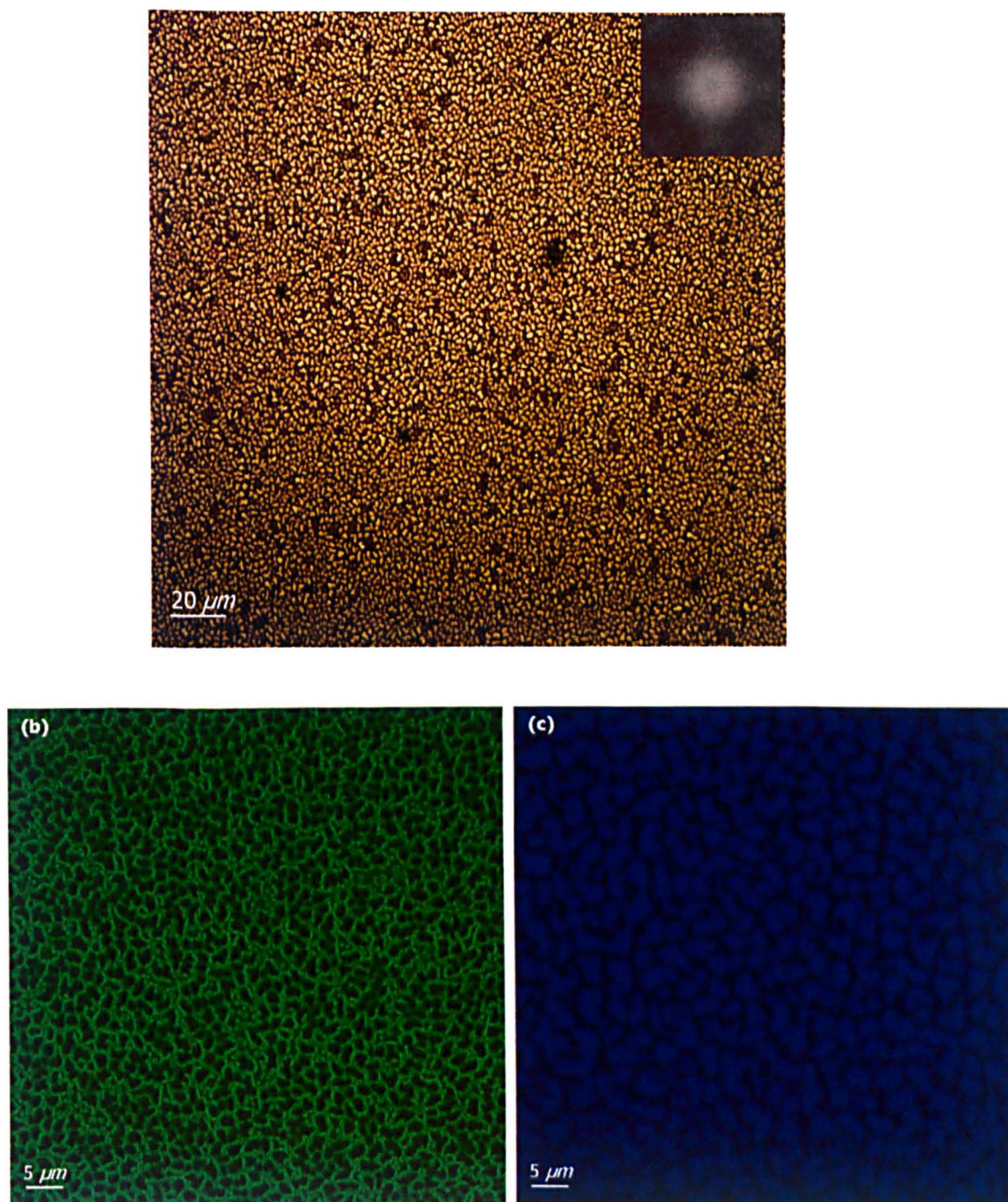


Figure (7.14) (a) Optical micrograph of the blend PFB/F8BT spin cast in saturated toluene vapour atmosphere ($v_p = 13.99 \text{ mmHg}$, $T=12^\circ\text{C}$). The length scale is $3.5 \mu\text{m}$. (b) and (c) fluorescence microscopy images of the film shows the distribution of PFB and F8BT in the film.

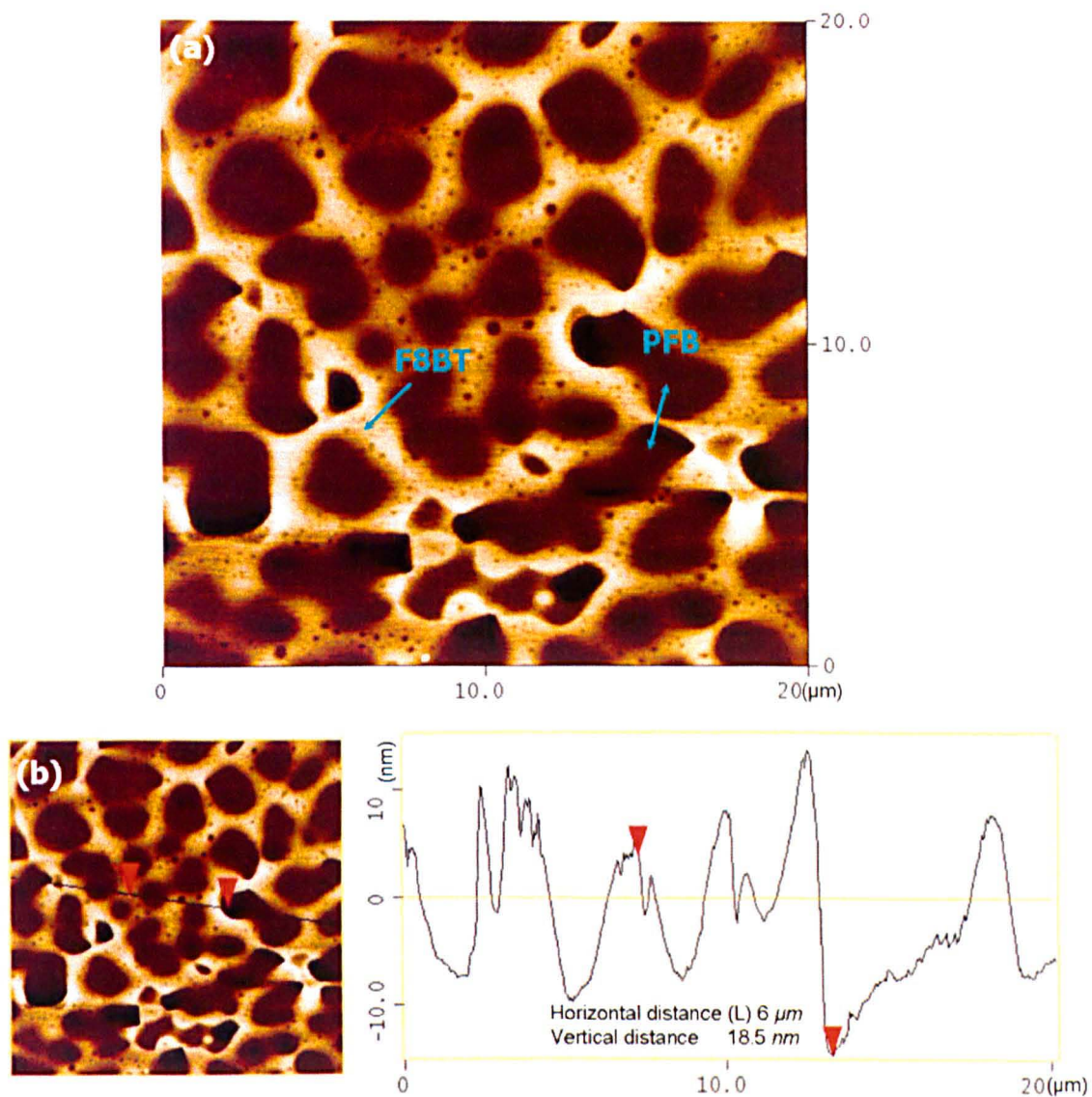


Figure (7.15) AFM topography (a) and section analyse (b) of (PFB/F8BT) film made in environmental cell with nominal toluene vapour pressure (13.99 mmHg) at 12°C . The lower phase is PFB and the higher phase rich in F8BT. The height difference between higher and lower phases has decreased to 18.5 nm and the overall film thickness is about 50 nm .

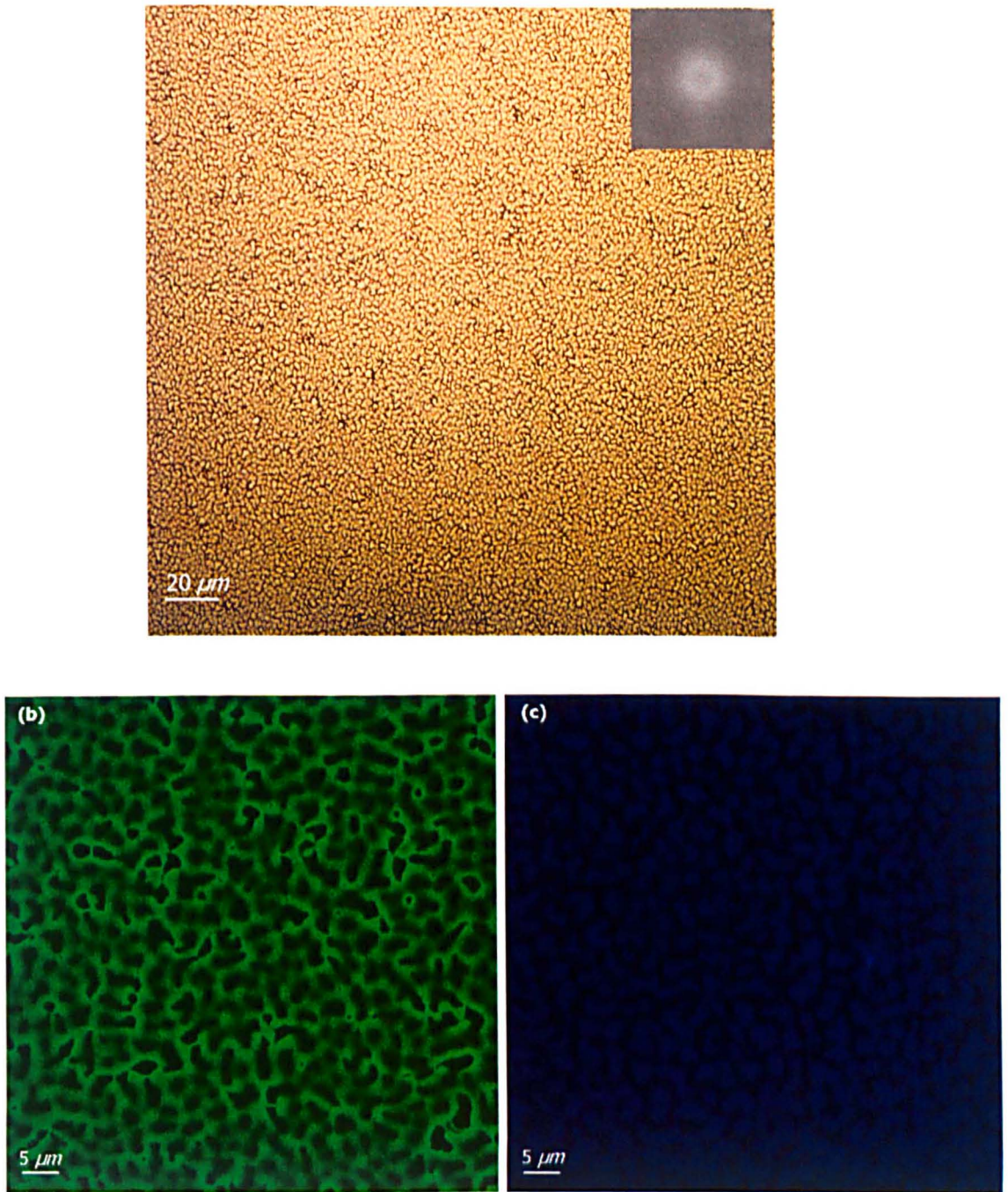


Figure (7.16) (a) Optical micrograph of the blend PFB/F8BT spin cast in saturated toluene vapour atmosphere ($v_p = 17.56 \text{ mmHg}$, $T=16^\circ\text{C}$), with length scale of $3.24 \mu\text{m}$. (b) and (c) fluorescence microscopy images of the film. The shape of the domains started to change more visibly. The PFB wells become more extended. The high phase is enrich in F8Bt and is more continuous.

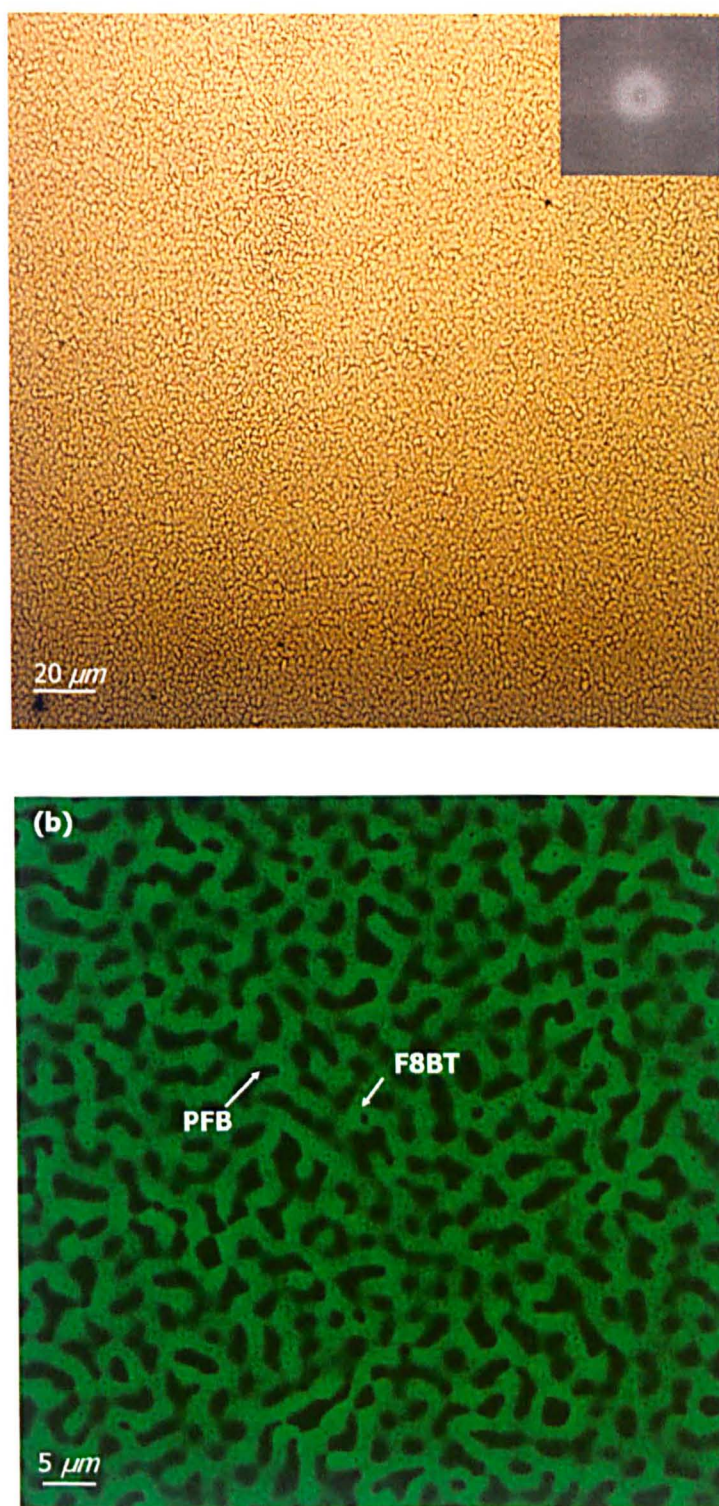


Figure (7.17) Optical micrograph of the blend PFB/F8BT spin cast in saturated toluene vapour atmosphere ($v_p = 22\ \text{mmHg}$, $T=20^\circ\text{C}$), with length scale of $3.37\ \mu\text{m}$. (b) Fluorescence microscopy images of the film. PFB lower phase has transformed to elongated domain. Higher phase becomes richer in F8BT. The surface is undulated.

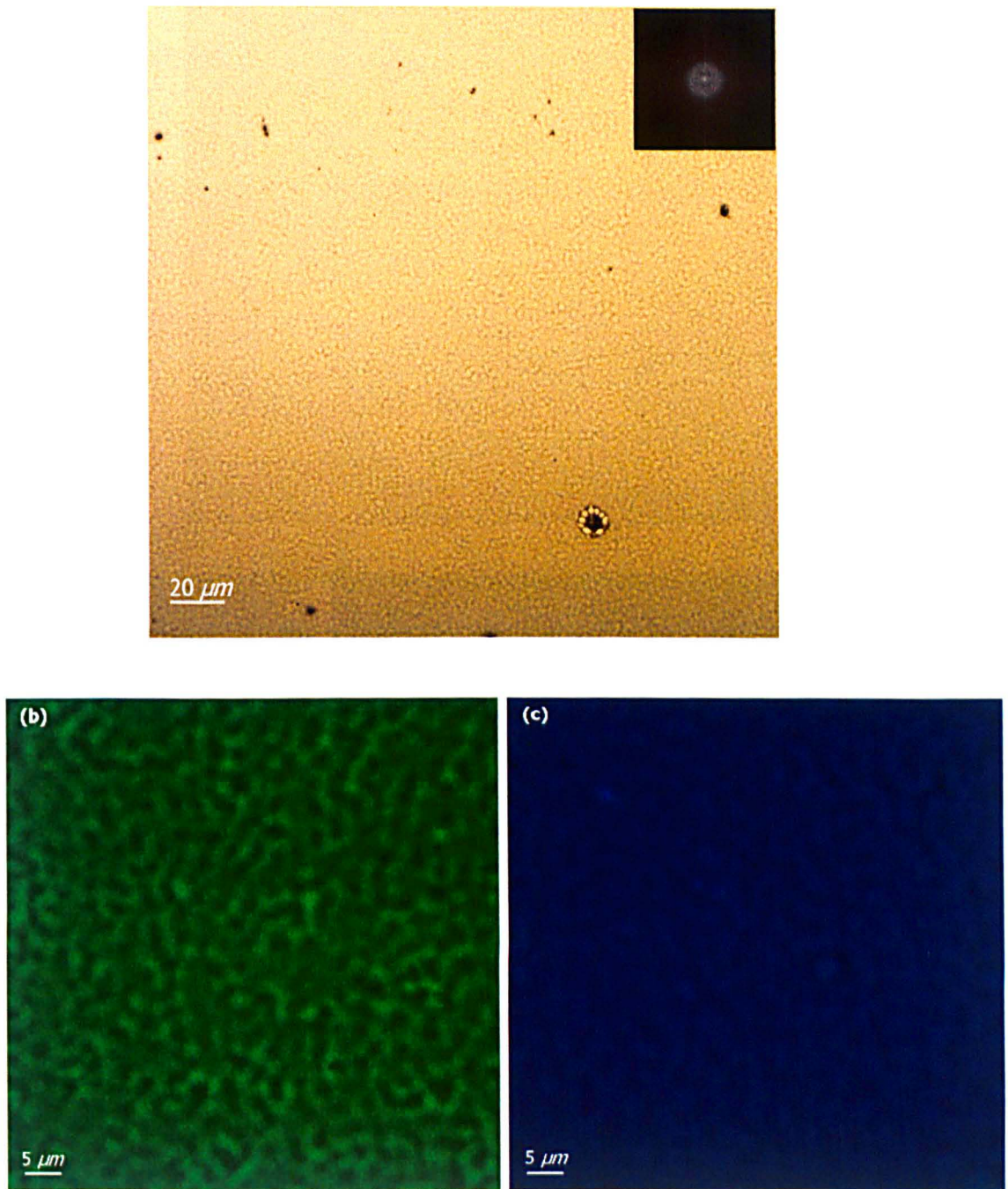


Figure (7.18) Optical micrograph of the blend PFB/F8BT spin cast in saturated toluene vapour atmosphere ($v_p = 28.47 \text{ mmHg}$, $T=25^\circ\text{C}$), with length scale of $3.47 \mu\text{m}$. (b) and (c) fluorescence microscopy images of the film show that the surface of the film mainly consists of F8BT. Undulation is very high and evaporation rate is the lowest in this sample.

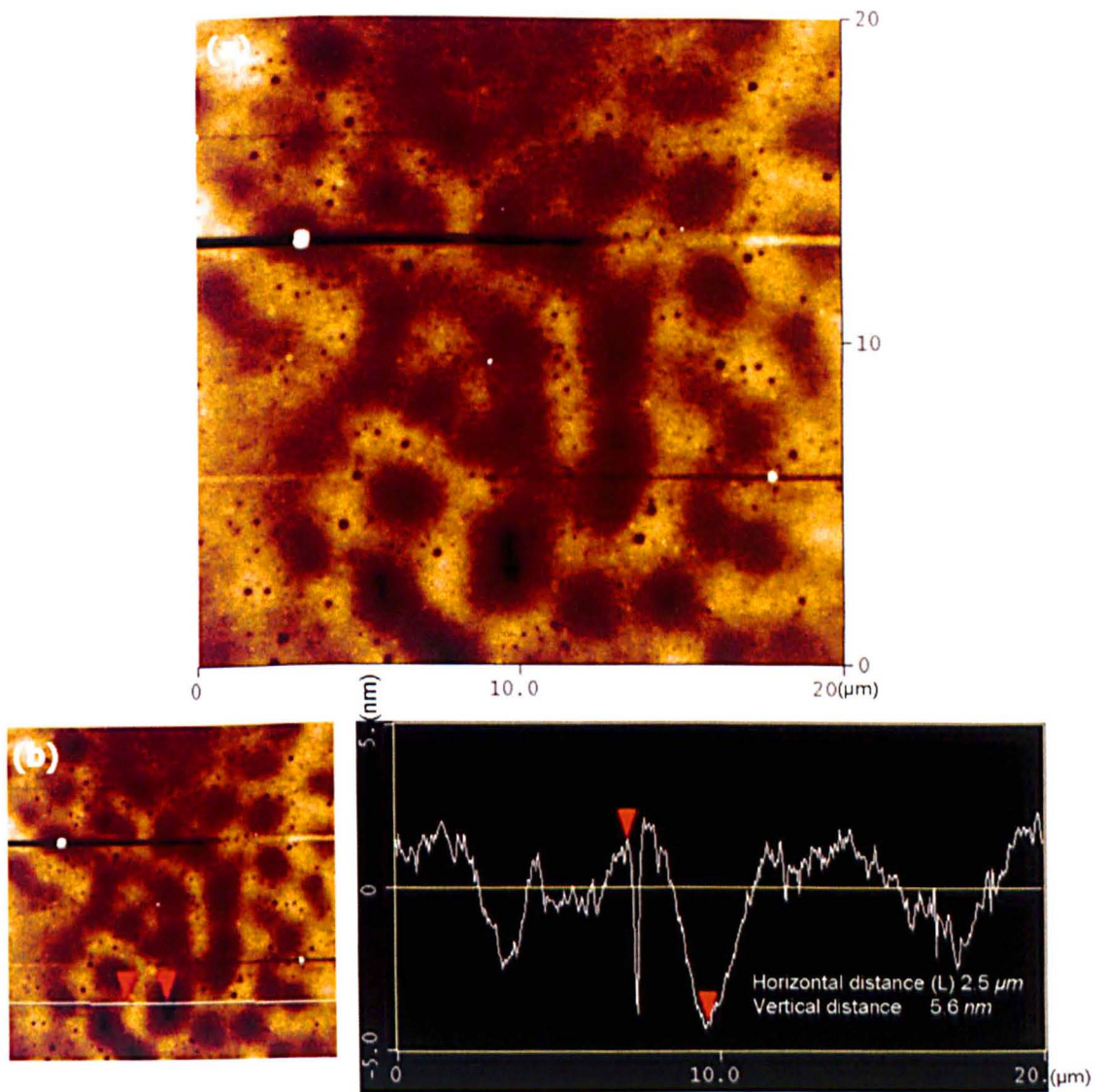


Figure (7.19) (a) Topography of a 50 nm thick PFB:F8BT film prepared from toluene solutions, with lowest evaporation rate (b) AFM section analysis of the sample. The higher layer composed of an F8BT-rich phase is approximately 6 nm thick.

7.5 Discussion and conclusion (Part I- silicon substrate)

The PFB/F8BT films were cast from a solution of toluene on a silicon substrate with different evaporation rates controlled in the environmental cell. As a result, films with different morphologies were fabricated. The aspiration of this work is to attribute the morphology development in this blend to Marangoni instability theory. If Marangoni instability is applicable to this blend, we should be able to see a clear trend; decreasing the evaporation rate should suppress the Marangoni instability. How do we detect this? Since the interface instability is suppressed, the extent of lateral phase separation should become less and perhaps at some point a layered structure will form. This means by decreasing the evaporation rate the surface composition should be enhanced with one of the polymers. This should be visible as a colour change in the fluorescence microscopy.

It should be mentioned that the intensity of the fluorescence is dependent upon the thickness of the film. Knowing this, one can argue that the dark areas for example in figure (7.13(b)) are the result of the weak signal from the lower part of the film. Our argument is the areas that appeared dark within figure (7.13(b)) emit blue light in figure (7.13(c)). The green regions in figure (7.13(b)) don't emit light in figure (7.13(c)). This suggests that the colour contrast is due to the difference in absorbance coefficient of PFB and F8BT rich phases rather than the variation in thickness. If the colour contrast were related to thickness only, the lower phase should have appeared dark with both 550nm and 480 band pass filters.

How do we know that the dark region (PFB rich phases) has a lower thickness and is less abundant on the surface? While analysing the data, the fluorescence and AFM images should be considered together. To make it clear, we discuss figures (7.11) and (7.12) which are related to the same sample. The PFB rich

phases (dark region in (7.11(b)) and blue areas in (7.11(c))) have a distinctive shape. AFM images (figure (7.12)) show that these areas are lower in height. The matrix phase (dark and light brown) in figure (7.12) corresponds to the dark green and light green area in figure (7.11 (b)). The variation in the thickness in the AFM image follows the variation of green spectrum in the fluorescence microscopy image. This suggests that the different spectrums of green colour in figure (7.12(b)) are more likely to be due to the variation in the thickness of the film.

Based on our observation we suggest that the difference between the two colours (blue and green) in the fluorescence images are more likely to be due to the difference in the absorption coefficient of the two materials. This is based on the evidence that the area emitting blue light with one filter doesn't emit any light with the other filter. Similarly, the green emitting areas do not emit light with the blue filter.

On the other hand the different spectrums of one colour are more likely to be due to variations in thickness rather than richness of the phases.

A first glance at the system using optical and fluorescence microscopy images doesn't reveal any clear trend. The variation in composition along with the evolution of domains from round to elongated shaped domains, makes it very difficult to extract a clear trend with the naked eye.

However, we employed image processing software (ImageJ) to obtain quantitative information about the development of structure. Figure (7.20) shows how the images were processed. A threshold was applied to the image and two major phases were marked by different colours. The marked districts were treated as particles and the area fraction of the marked phase was calculated. A plot of the surface area fraction of the lower-lying phase (which appeared rich in PFB) at different vapour pressures, along with the relevant morphologies, is shown in figure (7.21). There is a peak in the graph. We name the area before and after the peak, region I and region II respectively. In region I, initially the percentage of PFB increases and after reaching the peak in

region II, it starts to decrease. The trend in region II can be explained by Marangoni theory. At the PFB peak, a steep composition gradient is created by the high evaporation rate. Therefore there is a high driving force for Marangoni instability to take place and make the interface between the layers unstable. The result is a lateral phase separation of one phase in the matrix of the other phase. At the peak we have 41% PFB on the lower-lying phase. The rest of the composition is mainly F8BT and some mixed phase domains. By going towards lower evaporation rate in region II, the polymers remain in the solvent for longer, the composition gradient diminishes and the Marangoni effect becomes weaker. Therefore, there is a good chance for bilayer formation. In region II, by going towards the right end of the plot (suppressing the evaporation rate), the area fraction of PFB goes down consistently and as the blend is 50:50 by weight, we postulate the F8BT percent goes up on the surface of the film. The dominant green colour in the fluorescence images confirms our hypothesis. Therefore, the Marangoni instability theory is in agreement with the structure development.

The question is, why does region I show a different trend? One possible explanation could be, the faster solvent evaporates, the less time the polymer components have to rearrange themselves into separate phases whilst the transient wetting layer is being forming. Since the initial layers are less pure, the subsequent phase separated domains will also be less pure and the composition is a mixture of both components. Two different shades of dark and bright green area in the fluorescence image of a film made at atmospheric pressure may suggest the presence of a very rich F8BT phase in the vicinity of less rich F8BT phase. However, as mentioned before, the change in intensity could be due to variation in the thickness. More sophisticated techniques such as XPS are needed to study the composition change.

By decreasing the evaporation rate in region I (increasing the vapour pressure), the polymers have more time to segregate towards the specific layer in the bilayer. As a result, each layer will be more enhanced with its main component. The subsequent Marangoni instability will break the interface (of the already

enhanced phases) to the surface and a laterally phase separated structure will form.

Therefore we may consider a threshold evaporation rate, *which when above a transient bilayer made of highly enhanced layers is formed. Further Marangoni instability will lead the structure formation (region II). Below the threshold vapour pressure, there might be a composition variation in each layer within the transient wetting layer, and therefore the subsequent structure (as a result of Marangoni effect) will have mixed phases. One would expect that the solubility of the polymer in the solvent plays an important role.*

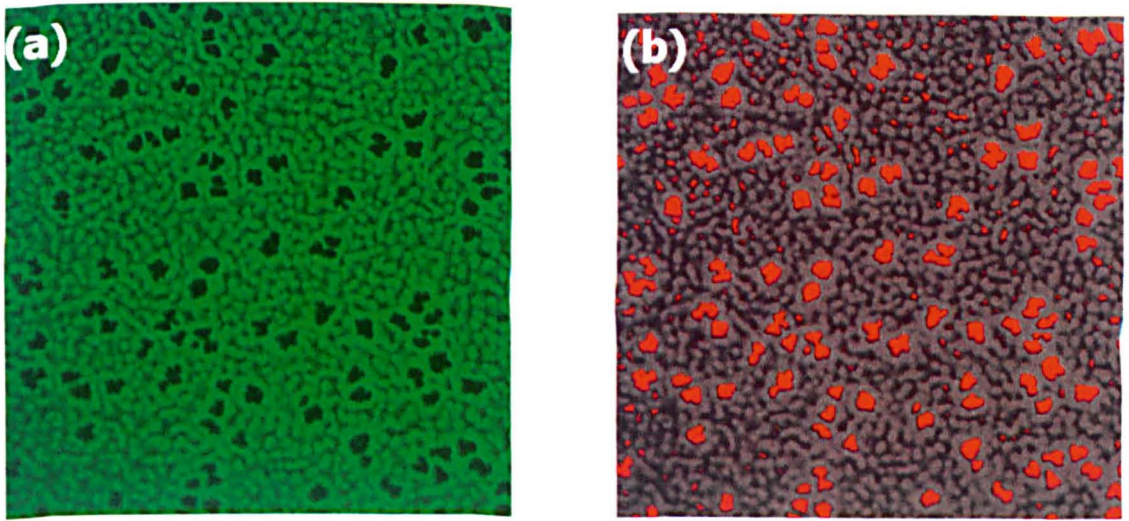


Figure (7.20) (a) Fluorescence microscopy image of the sample with F8BT emitting green light and PFB appear dark. (b) By applying a threshold colour, PFB areas have been marked by red colour and the area fraction of the red regions is calculated by the software.

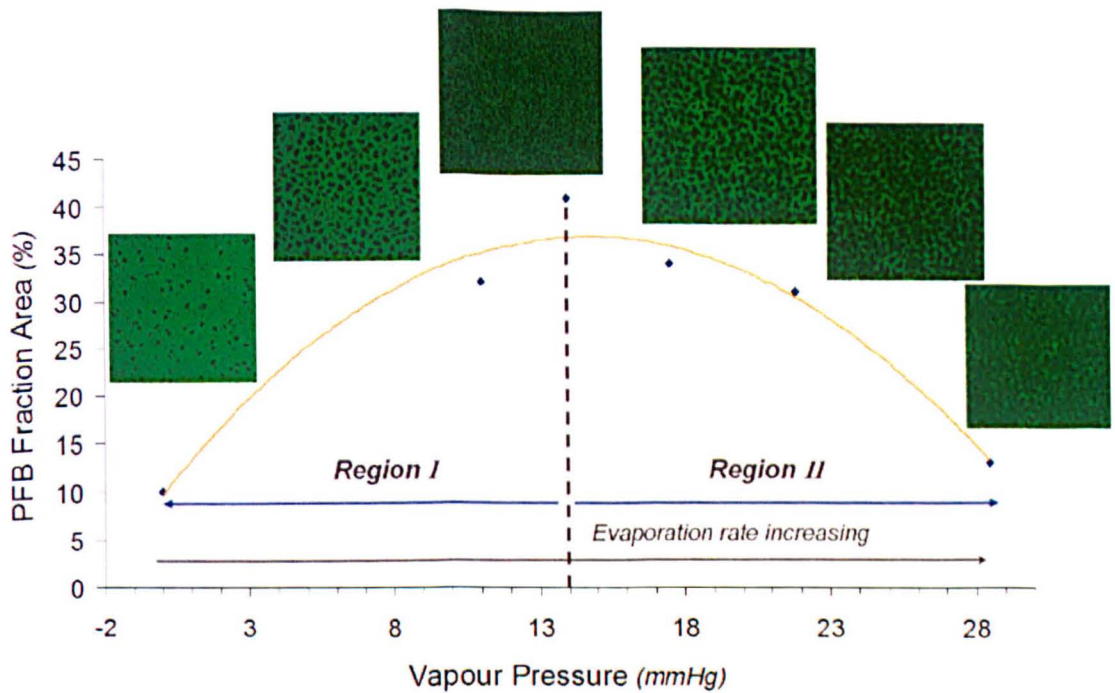


Figure (7.21) PFB fraction area at different vapour pressures along with the relevant morphology. There are two different regions with a threshold evaporation rate. Either side of this threshold the film evolves differently. The PFB rich regions appear as the dark recessed regions in the above AFM images. The PFB regions emit blue light. The curve is a guide to the eye.

7.6 Photovoltaic devices

We made a preliminary attempt to make photovoltaics by controlling a process parameter, in this case evaporation rate. A range of morphologies were produced as a result. We then studied the effect of the morphology on device efficiency. Photovoltaic devices were fabricated in the architecture Glass/ITO (50nm)/PEDOT:PSS (60nm)/Active Layer/Ca(20nm)/Ag(40nm). The active layer was spin cast from a blend of (1:1) PFB and F8BT (PFB/F8BT). Solutions were prepared at 10 *mg/ml* concentration in toluene. The active layer was made in environmental cell under saturated toluene atmosphere at different vapour pressures to produce different morphologies. The calcium and silver cathode metals were supplied by Testbourne with purities of 99.5% and 99.99% and were deposited on the active layer by a vapour deposition technique. Then the devices were sealed with glue and a glass sheet in a nitrogen glove box and later on were characterised by fluorescence microscopy, Atomic force microscopy and Photoluminescence.

7.6.1 The result of fluorescence microscopy and AFM

Fluorescence images (100x) taken through an optical microscope using a 550nm band pass filter (figures (7.22(a-f))) and 480nm band pass filter (figures (7.23 (a-f))) show the distribution of PFB and F8BT rich phases on the substrate. Going from image (a) to image (f), the evaporation rate is decreasing. Initially when there is no toluene vapour pressure, the amount of (dark) PFB phase over the matrix of (green) F8BT phase is visibly higher. Figure (7.22 (a)) shows the isolated PFB domains have polygonal shape. Increasing the vapour pressure changes the PFB domains from round to elongated shape (figure (7.23 (b))). The occurrence of isolated regions in films with slower evaporation rate is smaller than in films with higher evaporation rate, as illustrated in Figures ((7.22) and (7.23)). i.e. A more continuous F8BT high phase is obtained when the film is prepared via spin coating under a

higher vapour pressure atmosphere (lower evaporation rate). This suggests that the lower evaporation rate induces the layered type structure as expected.

However, the rate of the structure development is not the same at different stages. Initially, applying the vapour pressure (suppressing the evaporation rate), has a strong effect on the morphology. The percent of F8BT in the form of a continuous phase on the higher-lying phase increases noticeably. It covers the majority of the lower PFB phase. The build up of continuous F8BT on the polymer/air surface will more or less continue but with a much smaller rate at lower evaporation rate. However in most samples there is a smaller length scale within big length scales. AFM images show the topography of the film and more details about the morphology. When the evaporation rate is high, the structure consists of a dark phase of PFB wells with micron sized domains in a homogeneous phase of F8BT. By decreasing the evaporation rate, the morphology of F8BT evolves to a more rough structure. In figure (7.30) we can see a mesoscale (tens to hundreds of nanometre) structure in the F8BT phase which is reminiscent of spinodal decomposition. Alternatively it could be due to a secondary phase separation.

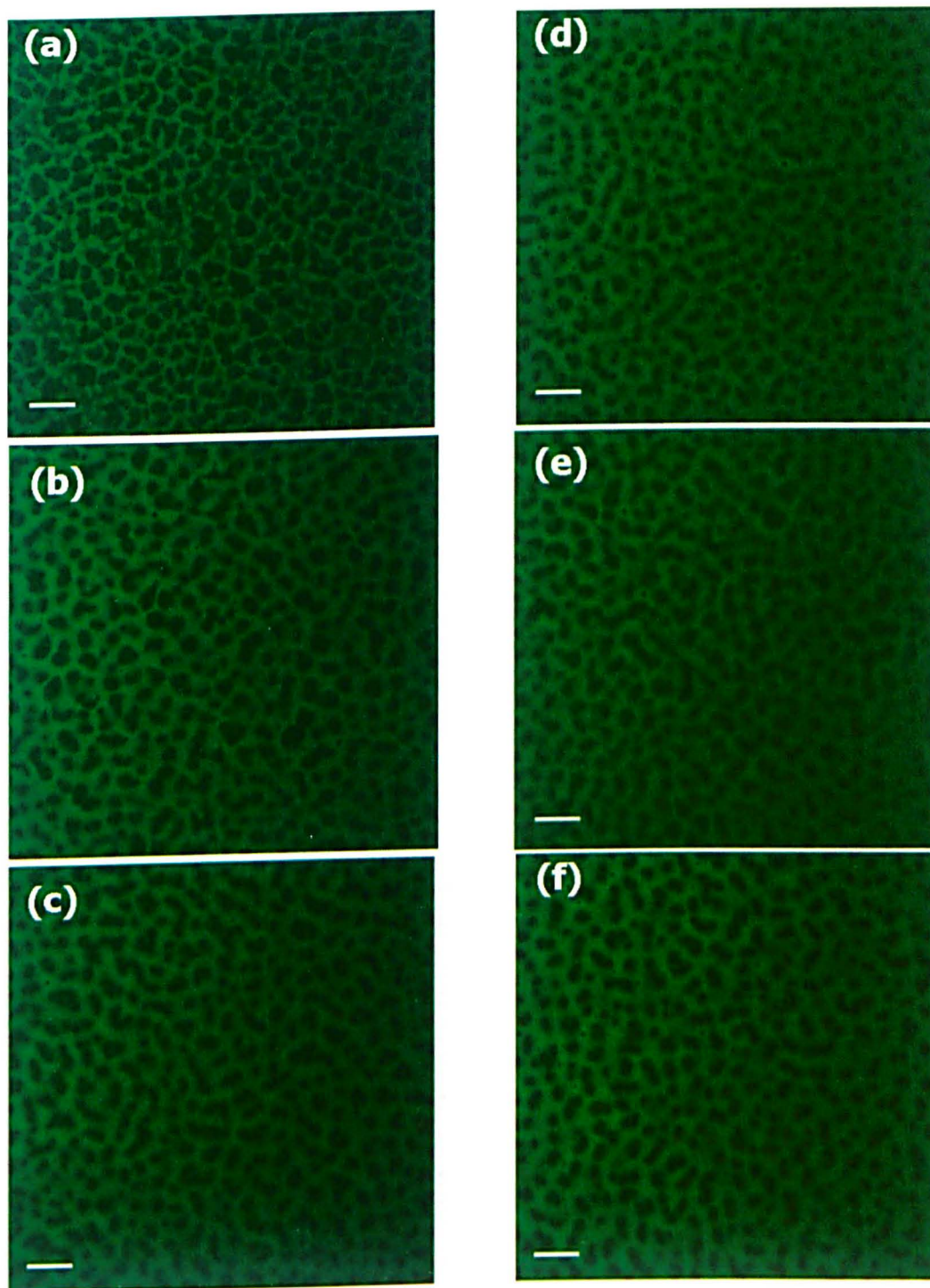


Figure (7.22) Fluorescence microscopy images of thin films of the blend F8BT:PFB (1:1) spin-coated from a 10 mg/ml solution in toluene on a substrate of ITO, pre-coated with 60 nm PEDOT:PSS. With (a) having the highest evaporation rate made in atmosphere and (f) having the lowest evaporation rate. Dark areas are PFB wells in the matrix of green F8BT phase. The scale bars are $5\ \mu\text{m}$.

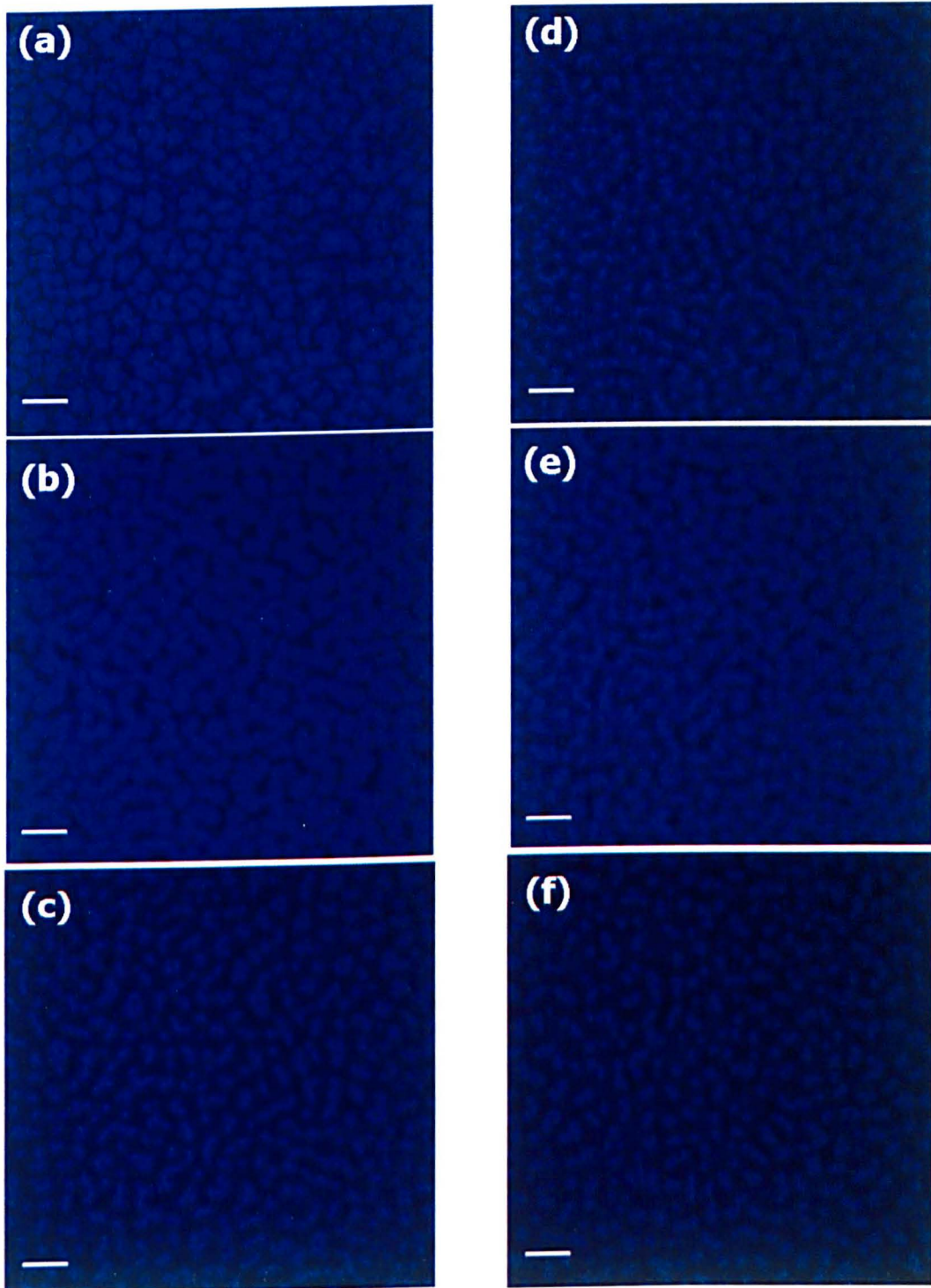


Figure (7.23) Fluorescence microscopy images of thin films of the blend F8BT:PFB (1:1) spin-coated from a 10 mg/ml solution in toluene on a substrate of ITO, pre-coated with 60 nm PEDOT:PSS. With (a) having the highest evaporation rate made in atmosphere and (f) having the lowest evaporation rate. Blue emission is done by PFB. The scale bars are $5 \mu\text{m}$.

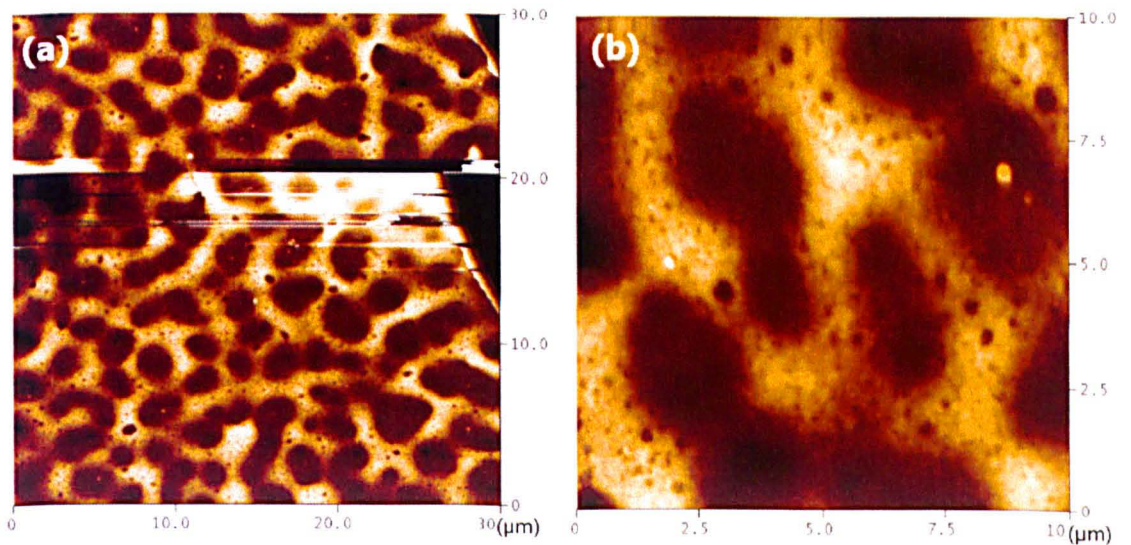


Figure (7.24) (a) Tapping-Mode AFM images of a thin film of the blend F8BT:PFB (1:1) spin-coated on ITO substrate at toluene saturated atmosphere ($v_p = 11.06 \text{ mmHg}$, $T=8^\circ\text{C}$). (b) The same sample with more details.

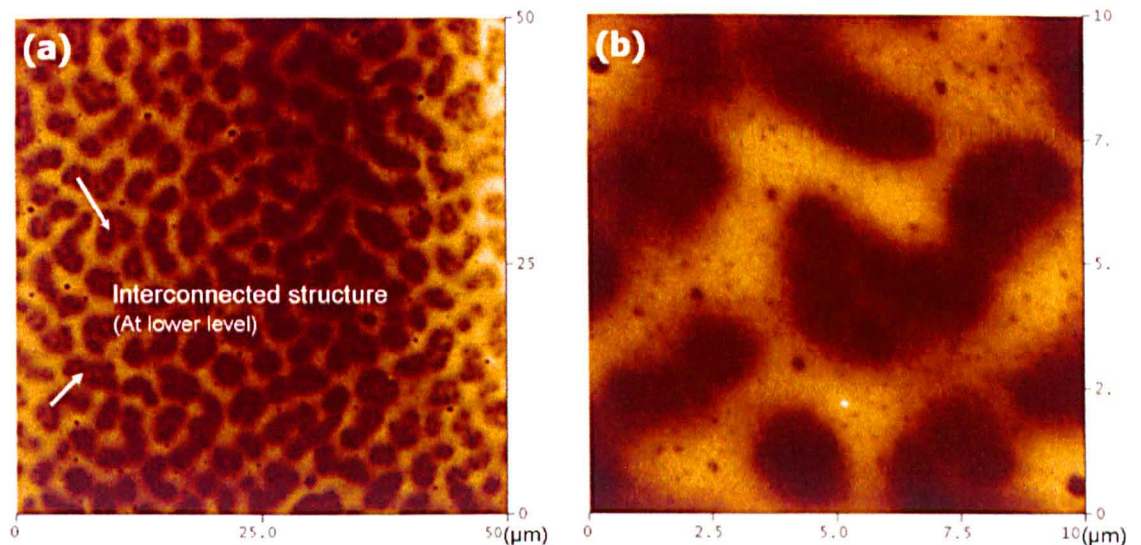


Figure (7.25) Tapping-Mode AFM images of a thin film of the blend F8BT:PFB spin-coated with lower evaporation rate ($v_p = 13.99 \text{ mmHg}$, $T=12^\circ\text{C}$). (a) The laterally phase separated structure with interconnected lower phase structure (b) F8BT phase is more uniform than PFB.

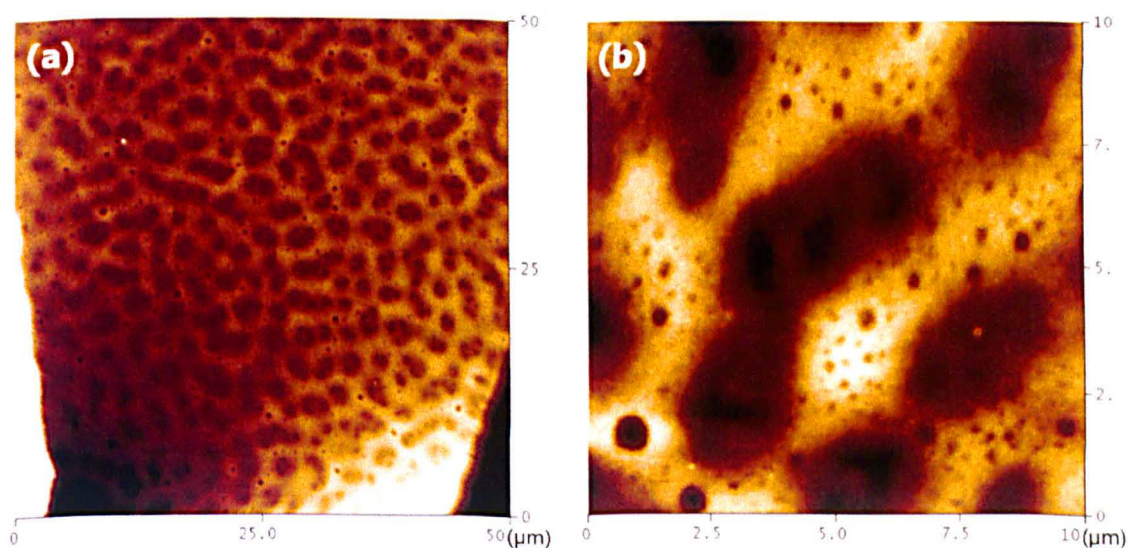


Figure (7.26) (a) Tapping-Mode AFM images of a thin film of the blend F8BT:PFB spin-coated with lower evaporation rate ($v_p = 17.56 \text{ mmHg}$, $T=16^\circ\text{C}$). (b) The roughness of the F8BT has increased.

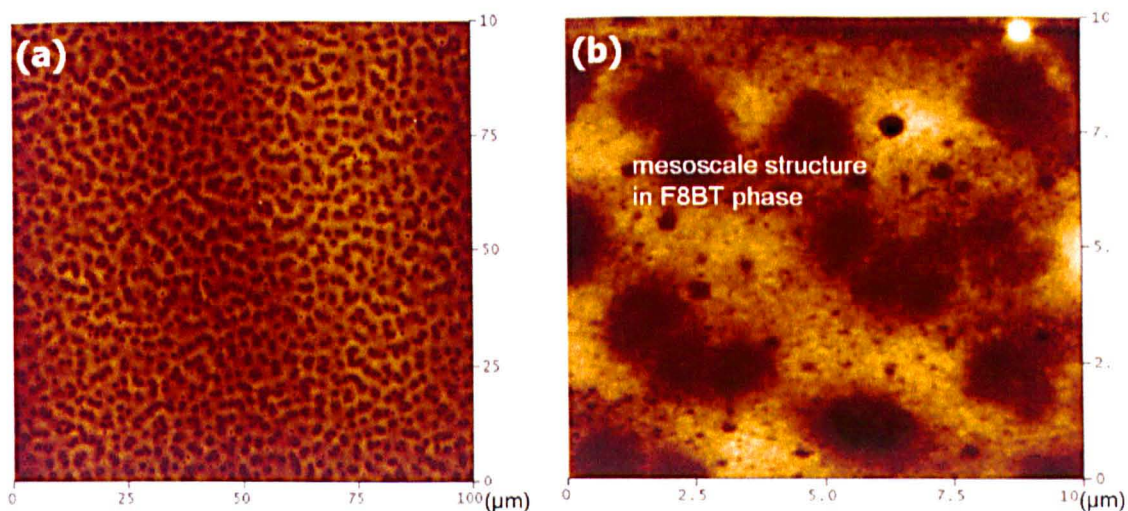


Figure (7.27) Tapping-Mode AFM images of a thin film of the blend F8BT:PFB spin-coated with lower evaporation rate ($v_p = 28.47 \text{ mmHg}$, $T=25^\circ\text{C}$) (a) the interconnected structure at lower phase has reduced, perhaps due to slower evaporation rate and longer transformation time. (b) There is a mesoscale structure within F8BT domains.

7.6.2 Photovoltaic device characterisation

Power conversion efficiency (PCE) is a standard way to measure the efficiency of photovoltaic devices. There are 6 pixels on the substrate, each makes a device. The PCE reported here for samples prepared at each vapour pressure is the average value of all 6 pixels. The length scale of the samples with different morphologies was measured by using atomic force microscopy images and employing Nanoscope 5.12 software. Figure (7.28) is a plot of normalized PCE via length scale. As expected increasing the length scale decreases the efficiency of the device. However, it is not well understood why the micron size domains can perform as a device. Perhaps this is due to the smaller mesoscale structures inside the micron sized domains.

When a photovoltaic device is exposed to a photon, the absorbed energy will excite the electron. The excited electron will go to a higher energy level. This creates an unstable state. Therefore the electron will return to the ground state and as a result different phenomena can happen. It can re-emit light (this is called photoluminescence) or it can produce charges or some non-radiative recombination (which is not easy to measure) can occur. Efficiency of the device can be characterised by measuring these outcomes. For example PLQY (photoluminescence quantum yield) is the ratio of number of photons excited to the number of photons incident on the sample (PLQY= number of photons out/number of photons in). Another quantity which is commonly used for device performance is EQE (External quantum efficiency) which is the ratio of produced charges to the incident photons (EQE= number of charges out/number of photons in).

Figure (7.29) shows the photoluminescence quantum yield efficiency of samples prepared at different vapour pressure. The sample made with the lowest evaporation rate shows a high PL quantum efficiency which usually means low charge generation. The sample made at ambient pressure along with the sample made at ($v_p = 17.56 \text{ mmHg}$, $T=16^\circ\text{C}$), have low photoluminescence

quantum yield efficiency which means higher probability for charge generation. Overly it seems that there is an optimum morphology with the best possible domain size and shape that affect the efficiency of the device.

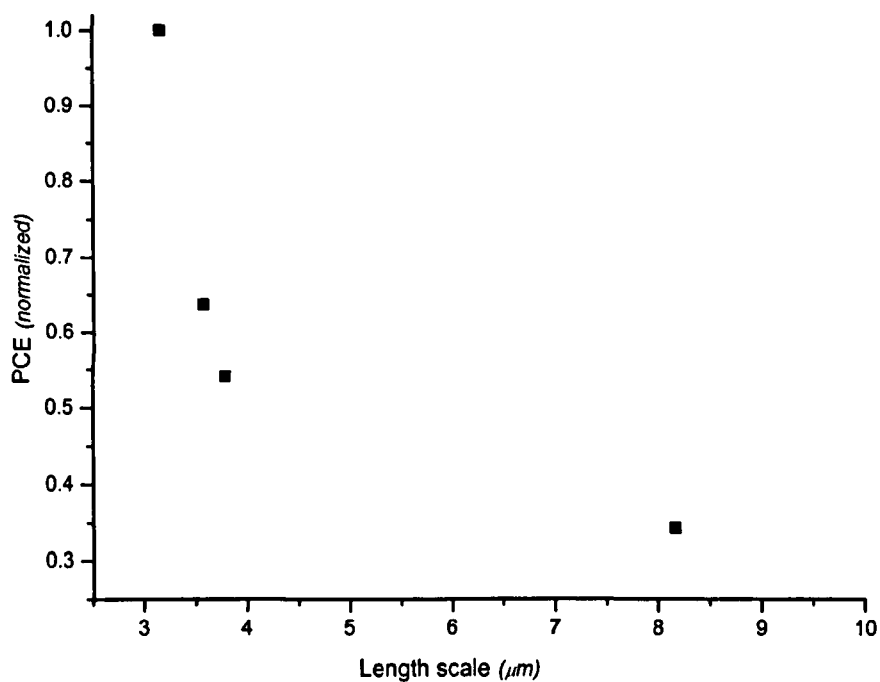


Figure (7.28) Normalised power conversion efficiency of PVs with active layer made of the a thin film of the blend F8BT:TFB (1:1) spin-coated from a 10 mg/ml solution in toluene on a substrate of ITO, via length scale calculated from AFM images.

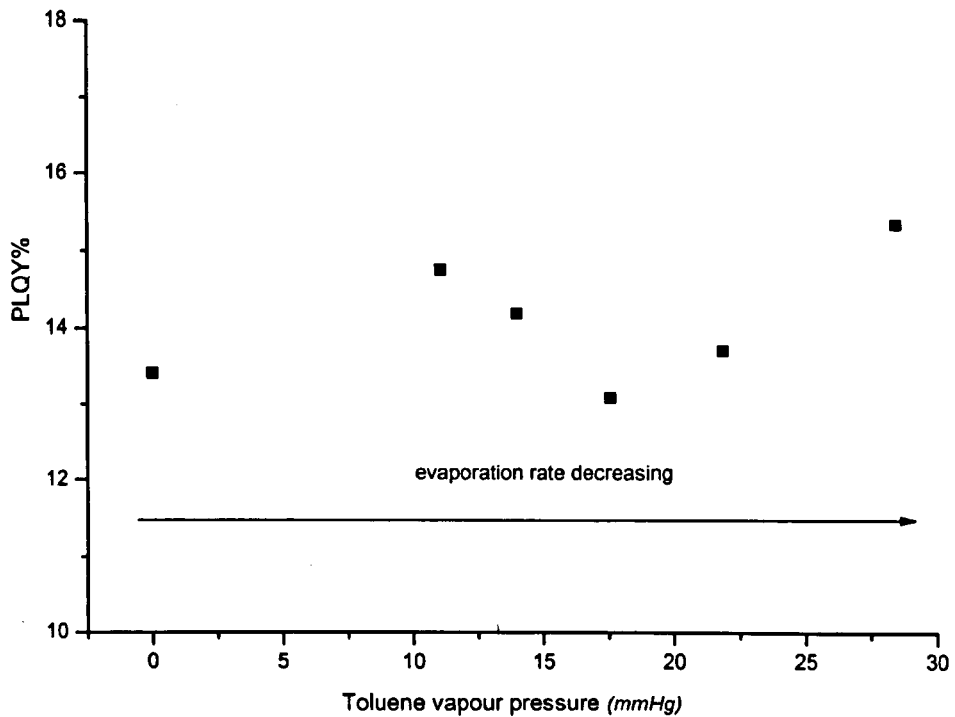


Figure (7.29) Photoluminescence quantum yield efficiency (PLQY) of PVs at different toluene vapour pressures. The active layer is made of a thin film of the blend F8BT:TFB (1:1) spin-coated from a 10 mg/ml solution in toluene on a substrate of ITO.

7.7 Discussion and Conclusion (Part II- photovoltaics)

Controlling the evaporation rate during spin coating in our environmental cell enables us to produce different morphologies of PFB/F8BT without changing the composition of the blend. While the morphology of the film responds to variations in evaporation rate more or less systematically, understanding the device efficiency seems to be more complicated. Suppressing the evaporation rate makes the F8BT phase be the dominant component in the higher-lying phase. This suggests the formation of self-stratified layers as a result of suppressing the Marangoni instability by decreasing the evaporation rate. However, our results show that the layered structure doesn't necessarily lead to higher device efficiency. The efficiency of the device which is related to charge generation and charge transfer (and the latter is believed to be more

important) is far more complicated. The architecture and composition of the layers along with finer structure in the matrix of the uniform phases and also the shape and size of the domains should all be considered together to study the device performance.

However, our method of controlling evaporation rate during spin coating seems to be a good way to study this area of science more systematically. More samples are required to minimise any error arising from experimental conditions like faulty substrates etc. An *extensive study* of the photovoltaic devices made in our lab is beyond the scope of this thesis. However employing more characterisation methods could enable us to gain a better understanding of the performance of these devices.

7.8 The effect of substrate on the morphology of PFB/F8BT

The nature of the substrates and the interaction between these and a specific polymer is very important in controlling the architecture of optoelectronic devices. In this section we compared the morphology of PFB/F8BT deposited on silicon substrate and a ITO/PDOT:PSS substrate. For the matter of simplicity, the fluorescence images of PFB/F8BT, solution cast at highest evaporation rate are compared in figure (7.30). The fluorescence microscopy shows that the higher phase observed in both substrates correspond to F8BT emitting phases. However, a more continuous F8BT layer is observed on silicon substrate than on ITO. This could possibly be related to the extent of hydrophilicity of the surface. Perhaps both of these substrates are hydrophilic after plasma cleaning, but with a different degree of hydrophilicity. It is clear that PFB is more hydrophilic than F8BT as in both cases it wets the hydrophilic substrate. Initial contact angle measurements of the surface energy of these polymers measured elsewhere [10] show that the surface energy of PFB is

higher than that of F8BT and indicate that PFB interacts more favourably with ITO and PEDOT:PSS surfaces. As a lower surface energy component, F8BT migrates to the polymer/air surface to decrease the total energy of the system. However, the first investigation of figure (7.30) shows that the relative composition of the F8BT (and consequently PFB) phase is different on the two substrates. F8BT is more continuous and more pure on the silicon substrate. In other words, the F8BT rich phase on the silicon substrate has higher percentage of F8BT than on the ITO substrate. However, more experimental techniques such as Raman spectroscopy or XPS are needed to fully characterise the composition of these phases. Never the less, it is an interesting consequence that even different degree of hydrophilicity can change the kinetics of film formation, perhaps by affecting the formation of a transient wetting layer. It would be interesting to use substrates with completely opposite properties (hydrophilic and hydrophobic) and study the structure of the resulting film. Does F8BT wet a hydrophobic surface? *How does the domain shape change?* How pure will different phases be? The answer to these questions are not clear yet, but applying the experimental method developed in my project, provides numerous opportunities for systematic study of morphology formation which is the key role defining the efficiency of polymer based optoelectronic devices.

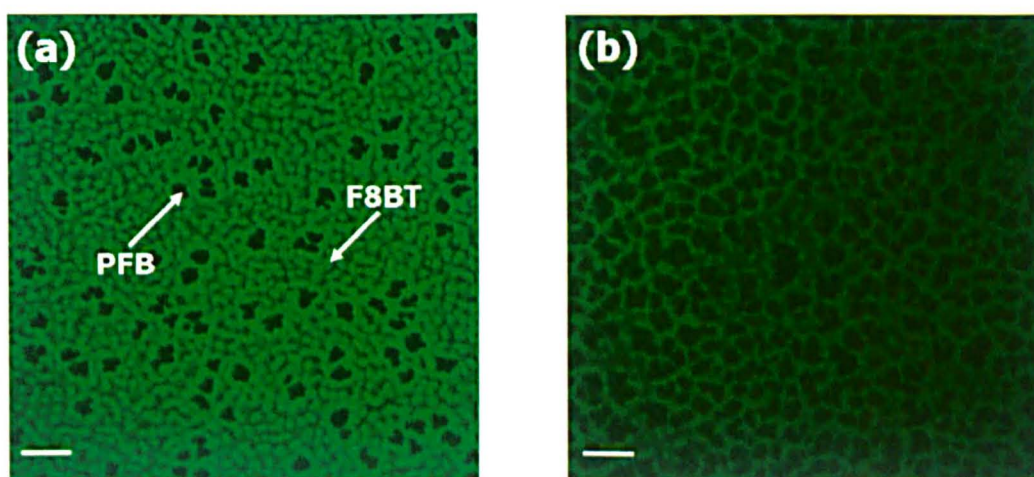


Figure (7.30) Comparing the morphology formation of PFB/F8BT on (a) silicon substrate and (b) ITO/PDOT:PSS. Scale bars are 5 μm .

7.9 Bibliography

1. Sirringhaus, H., N. Tessler, and R.H. Friend, *Integrated optoelectronic devices based on conjugated polymers*. Science, 1998. **280**(5370): p. 1741-1744.
2. Garnier, F., et al., *All-Polymer Field-Effect Transistor Realized by Printing Techniques*. Science, 1994. **265**(5179): p. 1684-1686.
3. Yang, Y. and A.J. Heeger, *A New Architecture for Polymer Transistors*. Nature, 1994. **372**(6504): p. 344-346.
4. Chappell, J., et al., *Correlating structure with fluorescence emission in phase-separated conjugated-polymer blends*. Nature Materials, 2003. **2**(9): p. 616-621.
5. Bernius, M.T., et al., *Progress with light-emitting polymers*. Advanced Materials, 2000. **12**(23): p. 1737-1750.
6. Morgado, J., R.H. Friend, and F. Cacialli, *Improved efficiency of light-emitting diodes based on polyfluorene blends upon insertion of a poly(p-phenylene vinylene) electron-confinement layer*. Applied Physics Letters, 2002. **80**(14): p. 2436-2438.
7. Wilkinson, C.I., et al., *Enhanced performance of pulse driven small area polyfluorene light emitting diodes*. Applied Physics Letters, 2001. **79**(2): p. 171-173.
8. Friend, R.H., et al., *Electroluminescence in conjugated polymers*. Nature, 1999. **397**(6715): p. 121-128.
9. Coffey, D.C. and D.S. Ginger, *Time-resolved electrostatic force microscopy of polymer solar cells*. Nature Materials, 2006. **5**(9): p. 735-740.
10. Arias, A.C., et al., *Vertically segregated polymer-blend photovoltaic thin-film structures through surface-mediated solution processing*. Applied Physics Letters, 2002. **80**(10): p. 1695-1697.
11. Halls, J.J.M., et al., *Efficient Photodiodes from Interpenetrating Polymer Networks*. Nature, 1995. **376**(6540): p. 498-500.
12. Chen, L.C., et al., *Excitation transfer in polymer photodiodes for enhanced quantum efficiency*. Advanced Materials, 2000. **12**(15): p. 1110-+.

13. Granstrom, M., et al., *Laminated fabrication of polymeric photovoltaic diodes*. Nature, 1998. **395**(6699): p. 257-260.
14. Snaith, H.J., N.C. Greenham, and R.H. Friend, *The origin of collected charge and open-circuit voltage in blended polyfluorene photovoltaic devices*. Advanced Materials, 2004. **16**(18): p. 1640-+.
15. Arias, A.C., et al., *Photovoltaic performance and morphology of polyfluorene blends: A combined microscopic and photovoltaic investigation*. Macromolecules, 2001. **34**(17): p. 6005-6013.
16. Greenham, N.C., X.G. Peng, and A.P. Alivisatos, *Charge separation and transport in conjugated-polymer/semiconductor-nanocrystal composites studied by photoluminescence quenching and photoconductivity*. Physical Review B, 1996. **54**(24): p. 17628-17637.
17. Halls, J.J.M., et al., *Photodiodes based on polyfluorene composites: Influence of morphology*. Advanced Materials, 2000. **12**(7): p. 498-+.
18. Snaith, H.J., et al., *Charge generation kinetics and transport mechanisms in blended polyfluorene photovoltaic devices*. Nano Letters, 2002. **2**(12): p. 1353-1357.
19. Moons, E., *Conjugated polymer blends: linking film morphology to performance of light emitting diodes and photodiodes*. Journal of Physics-Condensed Matter, 2002. **14**(47): p. 12235-12260.
20. Higgins, A.M., et al., *Surface segregation and self-stratification in blends of spin-cast polyfluorene derivatives*. Journal of Physics-Condensed Matter, 2005. **17**(8): p. 1319-1328.
21. Halls, J.J.M., et al., *Exciton diffusion and dissociation in a poly(p-phenylenevinylene)/C-60 heterojunction photovoltaic cell*. Applied Physics Letters, 1996. **68**(22): p. 3120-3122.
22. Cadby, A., et al., *Mapping exciton quenching in photovoltaic-applicable polymer blends using time-resolved scanning near-field optical microscopy*. Journal of Applied Physics, 2008. **103**(9).
23. Snaith, H.J. and R.H. Friend, *Photovoltaic devices fabricated from an aqueous dispersion of polyfluorene nanoparticles using an electroplating method*. Synthetic Metals, 2004. **147**(1-3): p. 105-109.

Chapter 8

Conclusions and Future work

In this thesis I have studied how to control the morphology of solution cast polymer thin films by means of process variables such as evaporation rate. This parameter was selected based on a fundamental model that explains the mechanism of film formation. It is suggested that during the spin coating, due to preferential attraction of one component to the substrate, a transient layered structure is formed. A subsequent interfacial instability destroys the transient wetting layer and forms the well-known laterally phase separated structure. The origin of this instability which is the main interest of this project is related to the Marangoni type instability, which we believe is driven by a gradient of solvent evaporation from the substrate to the surface of the film.

I examined this hypothesis by changing the concentration gradient in the film. During the spin coating, the solvent is removed from the system by evaporation which creates a concentration gradient. This happens when the rate of evaporation is greater than the time scale of solvent diffusion to make the concentration uniform through the film. As a result an interfacial tension profile is formed in the film.

To control the evaporation rate, we first built an environmental chamber mounted on the optospinometer apparatus. I have shown that it is possible to control the evaporation rate by filling the cell with controlled vapour pressure of the same solvent as in the film solution. The vapour pressure was systematically controlled by changing the temperature. To extract the evaporation rate, we solved Meyerhofer's equation for the thinning rate of a spin cast film. By fitting the solution to the thickness-time profile modelled from reflectivity-time data, we extracted the value of evaporation rate for toluene at different vapour pressures. The results provide direct evidence in favour of Meyerhofer's theory; this suggests that film thinning happens in two different stages with at least two different mechanisms. At the beginning, the film thinning is governed by hydrodynamic flow in which shear and centrifugal forces compete until a viscously static layer is formed. Evaporation becomes the main player at the second stage. The thickness-time profile shows that at the beginning of the spin coating, the thinning rate is almost the same for all films regardless of evaporation rate (hydrodynamic thinning). When the evaporation takes place, the rate of thinning is proportional to evaporation rate. The higher the evaporation rate is, the quicker the layer thins.

Future work (1): We have extracted the evaporation rate for toluene at different vapour pressure. This can be done for different solvents such as Chloroform, xylene, MEK, THF etc.

Future work (2): Different substrates with different surface energy or properties can be used with the evaporation rate experiment. The interest could be how the property of the substrate can affect the hydrodynamics of the solution. Does the substrate affect the evaporation rate?

Future work (3): In our experiments we were unable to test higher vapour pressures due to the effect of condensation. It is possible to avoid condensation by modifying the experimental set up. One suggestion is to wrap the

connecting tubes and the cell in a heating mantle with a controller to change the temperature. Is there also any threshold, which when below, the evaporation rate has no significant effect on the system?

To study the Marangoni type instability in liquid-liquid interface of PS/PMMA film, we spin cast the films in an environmental cell exposed to toluene gas at various vapour pressures. The reflectivity-time and also off specular scattering data were collected during the spin coating. We radially averaged the intensity of light scattered from the specular direction from the blended film in order to study the structure evolution during its formation. The results show the formation of different length scales during the evolution of the film. We were able to alter the structure evolution and final morphology by changing the evaporation rate. This provides strong support for our hypothesis that the Marangoni instability is the main origin of interfacial instability. Suppressing the evaporation rate gives a chance for diffusion to re-equilibrate and suppress the solvent concentration gradient in the film. As a result a less dominant interfacial tension profile will form. If the strength of the interfacial tension is weak enough, the Marangoni instability can not break the transient wetting layer to the surface and therefore a layered structure is formed. Washing PS/PMMA with selective solvents confirms there are layers.

Future work (4): To characterise the layers properly, it is suggested nuclear reaction analysis (NRA) or Ion beam experiments with deuterated components are carried out. However, we have performed a preliminary experiment with d-PS/PMMA samples. The sample which was made at the lowest evaporation rate, consisted of a PS layer on top with a thickness of approximately 150 nm, followed by a diffusion layer of roughly 30-40 nm on top of a PMMA layer. Studying samples with different evaporation rates shows that the diffusion layer (interface) is moving with evaporation rate. How will the interface move? Does the thickness of diffusion intermediate layer change with evaporation rate? How? How does the evaporation rate affect the thickness of layers? The answers to these questions lie in future work.

Another outcome of the evaporation experiments is striation formation. It seems that striations are a direct result of evaporation and they disappear when the evaporation is suppressed. Evaporation rates between $(1.6-1.8) \mu\text{m}/\text{s}$ correspond to the transient region where striations start to develop. Decreasing the evaporation rate below $1.6 \mu\text{m}/\text{s}$ stabilises the structure. The formation and disappearance of the striation is analogous to the formation of the cellular pattern and disappearance of it at high and low evaporation rate respectively. They also have the same lengthscale. This suggests that the formation of striations is not independent of the factors that control the overall film structure. Hydrodynamics simply break the symmetry of the instability when the shear field is large without affecting the physics that underlie the selection of a length scale.

Future work (5): However, one interesting way of studying the striation is modifying the optospinimeter by installing an additional laser and detector photodiode and CCD camera (parallel to the existing one). The new line should be aligned near the edge of the sample where the striations form. The evolution of the structure both at the centre and the edge could then be studied at the same time.

There are still some unanswered questions. By decreasing the evaporation rate, one expects to see thickness increases. But both studied systems (PS/PMMA and PFB/F8BT) show the opposite. Decreasing the evaporation rate decreases the film thickness! One possible explanation could be high evaporation rate forms a crust which beneath it is trapped solvent. This blocks further evaporation from the film. At low evaporation rate films have longer time to reach equilibrium conditions. Perhaps most of the solvent is evaporated.

Future work (6): Annealing the samples may change the film thickness.

Using the set up I developed to control the morphology through evaporation rate, we made preliminary photovoltaic devices. The active layer was made of (1:1) PFB/F8BT blend spin cast from a 10 *mg/ml* solution in toluene at different vapour pressures. The first series of different morphologies were made on silicon substrates. The results show by means of our experimental set up, we were able to suppress the evaporation rate and change the morphology during the spin coating. Fluorescence microscopy and AFM images suggest that the higher phase is mainly composed of F8BT with the thickness of approximately 15 *nm* and the lower-lying phase is rich in PFB. By suppressing the evaporation rate, the area fraction of PFB transforms with a Gaussian shape distribution. To make the analysis clear, we divided the (area fraction of PFB%-vapour pressure) plot into two different areas. The structure evolution above the peak can be explained by the Marangoni type instability. Decreasing the evaporation rate weakens the instability and a layered structure is more likely to form. However, below the peak (41% PFB), the trend is different. We relate this to the formation of a less pure transient wetting layer. Due to high evaporation rate the components don't have enough time to segregate to two layers with completely distinctive compositions. Therefore, the subsequent Marangoni instability which leads to the interfacial instability at the surface will create mixed phases. However, suppressing the evaporation rate provides enough time for this decomposition to happen and makes the following transient bilayer more pure. As a result the phase separated phases will be purer.

Future work (7): To study the compositional evolution of the phases properly, more sophisticated techniques like Raman spectroscopy are needed. It would be interesting to know how evaporation rate changes the balances of the different components in each phase.

Future work (8): We need to modify the experimental system in order to suppress the evaporation rate even more. We have to increase the temperature

to produce a higher vapour pressure. This means that we need to overcome the condensation problem. The suggested way to do that is described earlier in this chapter.

The effect of morphology on device efficiency was studied after making the photovoltaic devices on ITO/(PDOT:PSS) substrate. Although the active layers were not made under nitrogen atmosphere, the devices perform as photovoltaics. The overall structure is similar to the ones deposited on silicon substrate, i.e. the higher phase being F8BT, although the surface area fraction of PFB is considerably higher on the samples spin cast on ITO substrate. This highlights the effect of the substrate. The preferential attraction of the substrate for a favourable component can play an essential role in the order of the transient bilayer. In our experiment, despite both substrates being hydrophilic, the morphology and perhaps the relative composition of phases are different. This is possibly due to the fact that one substrate is more hydrophilic than the other.

Future work (9): Substrates with different surface properties could be made, to investigate how the morphology evolution with evaporation rate is altered as a result. Can this modification enable us to have a better control of layer formation? Is it possible to swap the order of the layers? Or even change the composition ratio of the phases? How do these variations improve the efficiency of device?

We have performed some tests to measure the efficiency of these devices. The device performance is strongly related to the lengthscale of the structure. However, while we are mostly able to explain the evolution of morphology of the active layer in photovoltaic device by controlling the evaporation rate, predicting the device efficiency seems more complicated. It seems that the mesoscale features which form inside the micron size domains have a big effect on device efficiency. Proper analysis of the device efficiency and related phenomena is beyond the scope of this thesis. However, our technique of

systematically controlling the morphology without changing the ratio of the blend, by means of evaporation rate, provides a methodical procedure for designing more efficient devices.

Future work (10): More experiments like SNOM etc are needed to correlate the observed trend in device efficiency to a particular factor like charge generation or charge transfer etc.

Other researchers usually create different morphologies by changing the ratio of the blend or solvent or modifying the substrate. While all these methods are interesting in their own right, we believe that comparing the result of these different experiments is not the ideal way of studying the system. Changing each parameter will change the kinetics of the film formation.

The advantage of our method and the overall conclusion of this work is that we are able to control the morphology of spin-coated polymer blend films by controlling a process variable such as evaporation rate. The core of this work which explores the origin of interfacial instability during the spin coating of polymer thin films provides a deeper insight into the mechanism of film formation.

Appendix I

Light scattering in discrete media

The amplitude $E_s(R, t)$ of the electric field of the radiation scattered to a point detector at position R in the far field is given by [1]:

$$E_s(\vec{R}, t) = -E_0 \frac{\exp[i(kR - \omega t)]}{R} \sum_{j=1}^N b_j(\vec{q}, t) \exp[-i\vec{q} \cdot \vec{R}_j(t)] \quad (1)$$

R : The distance of arbitrary origin O to detector

\vec{q} : Scattering vector

$\vec{R}_j(t)$: The position of the centre of mass of particle j at time t

$b_j(\vec{q}, t)$: Scattering length of particle j

The scattering length of particle j is defined by:

$$b_j(\vec{q}, t) = \int_{V_j} \Delta\rho(\vec{r}_j, t) \exp(-i\vec{q} \cdot \vec{r}_j) d^3r_j \quad (2)$$

$\Delta\rho(\vec{r}_j, t)$: Measure of the local "density of scattering material" and is defined as:

$$\Delta\rho(\vec{r}_j, t) = \frac{k^2}{4\pi} \left[\frac{\varepsilon_p(\vec{r}_j, t) - \varepsilon_L}{\varepsilon_0} \right] \quad (3)$$

$\varepsilon_p(\vec{r}_j, t)$: The local dielectric constant at position \vec{r}_j in particle j

- ε_L : The average dielectric constant of the liquid
 ε_0 : The average dielectric constant of the medium

Scattering is caused by the fluctuations in the medium. Usually these fluctuations are associated with the variation in the “density of scattering material”. The quantity of $\Delta\rho(\vec{r}_j, t)$ can be regarded as measure of the local “density of scattering material”. $\Delta\rho(\vec{r}_j, t)$, in X-ray is related to scattering length. In neutron scattering it is related to the density of the electron and in light scattering is due to fluctuation in reflective index. Dielectric constants and reflective index are related through equation (4)

$$\varepsilon = n^2 \quad (4)$$

Replacing ε with n^2 in equation (3), gives us:

$$\Delta\rho(\vec{r}_j, t) = \frac{k^2}{4\pi} \left[\frac{n^2(\vec{r}_j, t) - n^2_L}{n_0^2} \right] \quad (5)$$

- n_L : The average refractive index of the liquid
 n_0 : The average refractive index of the medium

As the difference between refractive indices of the solution and the film is not too large, equation (5) becomes:

$$\Delta\rho(\vec{r}_j, t) = \frac{k^2}{4\pi} \left[\frac{n^2(\vec{r}_j, t) - n^2_L}{n_0^2} \right] \quad (6)$$


$$\Delta\rho(\vec{r}_j, t) = \frac{k^2}{4\pi} [n(\vec{r}_j, t) - n_L] \quad (7)$$

Thus from equation (7) and (2), we have:

$$b_j(\vec{q}, t) = \frac{k^2}{4\pi v_j} \int [n(\vec{r}_j, t) - n_L] \exp(-i\vec{q} \cdot \vec{r}_j) d^3 r_j \quad (8)$$

So as it is observed in equation (1-below), the total scattered electric field is the sum of the fields scattered by the individual particles.

$$E_s(\vec{R}, t) = -E_0 \frac{\exp[i(kR - \omega t)]}{R} \sum_{j=1}^N b_j(\vec{q}, t) \exp[-i\vec{q} \cdot \vec{R}_j(t)]$$



Scattering length determined by the instantaneous distribution of material within the particle

Phase factor determined by the instantaneous position the particle in the sample

1. P.Lindner, Th. Zemb., *Neutrons, X-rays and Light: Scattering Methods Applied to Soft Condensed Matter*. 2002: North Holland.